

**Fundamental Symmetry Tests Using
a $^{129}\text{Xe}/^3\text{He}$ Dual Noble Gas Maser**

A thesis presented

by

David Chaiyarat Bear

to

The Department of Physics

in partial fulfillment of the requirements

for the degree of

Doctor of Philosophy

in the subject of

Physics

Harvard University

Cambridge, Massachusetts

July 2000

©2000 by David Chaiyarat Bear

All rights reserved

**Fundamental Symmetry Tests Using
a $^{129}\text{Xe}/^3\text{He}$ Dual Noble Gas Maser**

Abstract

We report the development and operation of the Harvard-Smithsonian $^{129}\text{Xe}/^3\text{He}$ dual noble gas maser. The dual noble gas maser (DNGM) is the first device to sustain simultaneous active maser oscillations on distinct transitions in two intermingled atomic species, and it allows sensitive differential measurement of the ^{129}Xe and ^3He nuclear spin-1/2 Zeeman transition frequencies [1–3]. We used the DNGM to test Lorentz and CPT symmetry with unprecedented precision. Specifically, a search for sidereal variations in the frequency difference between the DNGM’s co-located ^{129}Xe and ^3He maser ensembles has placed an upper bound of 47 nHz on Lorentz and CPT violating parameters in a standard-model extension that allows violation of these symmetries. Our measurement sets the most stringent limit to date on leading-order Lorentz and CPT violations of the neutron: $\sim 10^{-31}$ GeV. We also report in this thesis progress in a search for a permanent electric dipole moment (EDM) of the ^{129}Xe atom. Our preliminary result of $d_{Xe} < 1 \times 10^{-26}$ e-c.m. sets a direct bound on time-reversal (T) symmetry violating interactions in the ^{129}Xe nucleus.

Contents

Acknowledgments	viii
List of Figures	xi
List of Tables	xvi
1 Introduction	1
2 Theoretical Principles	13
2.1 Preliminaries	13
2.2 Polarization of ^{129}Xe and ^3He	15
2.2.1 Optical Pumping of Rubidium	16
2.2.2 Spin Exchange	20
2.2.3 Longitudinal Spin Relaxation	21
2.3 Transverse Spin Relaxation	24
2.4 Bloch Equations and Masing	26
2.4.1 Modified Bloch Equations	27
2.4.2 Equilibrium Solutions and Near Equilibrium Oscillations	31
2.5 Characterizations of Stability	35
2.5.1 Extraction of Phase and Frequency Data	35

2.6	Frequency Stability of the DNGM	40
2.6.1	Thermal Noise Limits to Frequency Stability	40
2.6.2	Measured DNGM Frequency Stability	43
2.6.3	Systematic Limits to Frequency Stability	44
3	Experimental Realization	54
3.1	Cells	54
3.1.1	Cell cleaning, coating and endplate attachment	56
3.1.2	Cell filling	59
3.2	DNGM Oven Assembly: Design and Illustrations	61
3.3	Blown Air Temperature Control	72
3.4	Optical Pumping System	77
3.4.1	Overview	77
3.4.2	Measuring the Relative Rb Magnetization in the Pump Bulb	79
3.4.3	Stabilizing the Optical Pumping Light	83
3.4.4	Future Work	85
3.5	Magnetic Field Environment	87
3.5.1	Magnetic Shielding	87
3.5.2	Main Solenoid	90
3.5.3	Estimate of Solenoid B_z Homogeneity	91
3.5.4	Gradient Trim Coils	93
3.5.5	Maximization of the Transverse Coherence Time in the Ab- sence of Masing	94
3.5.6	B_z Inhomogeneity Induced by Noble Gas Magnetizations	97
3.5.7	Choke Coils	102
3.5.8	Magnetic Field Stabilization	103

3.6	Co-magnetometer Effectiveness	105
3.6.1	Theoretical Description	106
3.6.2	Experimental Measurements	107
3.7	Signal Detection System	111
3.7.1	Measuring Coil Q , L , and R_{ac}	113
3.7.2	Cabling and Grounding	116
3.7.3	Design and Construction of Pickup Coil and External Resonator Circuit	118
3.7.4	Resonator Tuning	123
3.7.5	Effect of Temperature Fluctuations on the Double Resonator .	124
3.7.6	Pulse Coil Operation and an Estimate of B_1 Homogeneity . .	127
3.7.7	Signal Processing and Data Storage	128
3.8	Appendix to Chapter 3: Assembly and Optimization	129
4	Measurement of Operational Parameters and Verification of the Bloch Theory	134
4.1	Rb Frequency Shift Measurement of ^{129}Xe Polarization in the Pump Bulb	134
4.2	Measurement of Noble Gas Decoherence	136
4.3	Measurement of the Radiation Damping Time and Estimation of the Resonator Fill Factor	138
4.4	Measurement of the Longitudinal Polarization Lifetime in the Maser Chamber	138
4.5	Measurement of the Ratio $P_{z,o}/P_o$	139
4.6	Measurement of the Equilibrium Orientation Angle of the Maser Polarization	141

4.7	Verification of the Bloch Theory for Near-Equilibrium Oscillations of the ^{129}Xe Maser	146
5	Testing Lorentz and CPT Symmetry Using a Two-Species Noble Gas Maser	149
5.1	Overview	149
5.2	Limit on Lorentz and CPT Violation Using the DNGM	153
5.3	Addendum to Chapter 5	165
6	Toward a Test of Time Reversal Symmetry Using the DNGM	167
6.1	Theoretical Overview and Motivation	168
6.2	Experimental Procedure and Apparatus	172
6.3	Preliminary Results	175
A	Extended Bloch Theory of the Dual Zeeman Maser	A.1

Acknowledgments

First and foremost, I would like to thank my parents for their love and support, which have been unfailing over the past twenty-nine years. They have made everything possible. To my late grandparents Prachoom and Chinda Chaiyarat, and to my Uncle F.T. I dedicate this thesis: I will miss you always.

I am very thankful to my advisor, Ronald Walsworth, for giving me the chance to work on the dual noble gas maser experiment and for providing such patient and caring guidance during my time at the CFA. I am also very grateful to Richard Stoner, whose creativity and technical prowess made things possible. I owe a great deal as well to Mark Rosenberry at the University of Michigan. Mark taught me cell-making, introduced me to the world of high voltage, and shared many of my frustrations and successes while we worked together on the DNGM.

I have learned much during my time in graduate school, some of it from books and articles, but most of it from the people in and around the CFA. Don Graveline and Dick Nicoll shared indispensable knowledge as well as an incredible array of tools and instruments. Along with Robert Vessot and Ed Mattison, they also provided the DNGM experiment with the most stable timebase in the world. Larry Knowles and Charlie Hughes made sure that I was always safe and well set-up in Building E – I'm not sure how I would have fabricated half the parts for the DNGM without their assistance. David Phillips and Glenn Wong shared scientific knowledge, Mexican food, and – most important – friendship, for which I am extremely thankful.

I cannot imagine having completed this program without the support of the best and most caring group of friends a person could have. Rebecca, Tony, Dave, Ben, Claudine, Angelina and Cara were far away but somehow always present. Ruben, Nora, James, Nien-he, Terri, Kristin, Alix, and Terry: it took approximately 150

trips to Casablanca, 500 bottles of red wine, and a whole lot of learning and laughing, but you made my life outside lab a real joy. Thank you, and always remember to leave town at the right time, or as Kenny Rogers opined so tunefully: “You gotta know when to hold ’em, know when to fold ’em, know when to walk away, and know when to run.”

Everything should be made as simple as possible, but no simpler.

Albert Einstein, 1879 - 1955

List of Figures

1.1	Schematic depiction of the Harvard-Smithsonian dual noble gas maser (DNGM).	3
1.2	A figure emphasizing that a coherent frequency measurement can achieve greater precision than the incoherent average of a set of shorter measurements made during an equivalent period of time [1].	7
2.1	Elementary depiction of optical pumping of Rb by circularly polarized σ^+ light.	18
2.2	Zeeman maser polarization and magnetization vectors as seen in the frame rotating at the Larmor precession frequency	32
2.3	Phase evolution of the free-running ^3He maser over a 40,000 second timescale.	37
2.4	Linear regression has removed the (relatively) rapid linear evolution from the free-running ^3He phase trace.	38
2.5	Typical short-term ^3He phase residuals after least squares regression has removed the linear beat-note evolution.	39
2.6	The Allan deviation of a generic precision oscillator as a function of τ [22].	44

2.7	Example of free-running ^3He maser Allan deviation as a function of measurement interval for typical DNGM runs of $\approx 50,000$ seconds. . .	45
2.8	Figure showing the cumulative effect of short-term polarization dependent frequency shifts.	46
2.9	Figure showing the cumulative effect of long-term polarization dependent frequency drift.	47
3.1	Schematic diagram of the dual noble gas maser used to make the measurements reported in this thesis.	55
3.2	A photograph of the DNGM laboratory, circa 1997.	56
3.3	Typical manifold used to make three EDM-capable cells.	58
3.4	Machine drawing of the DNGM pump block, fabricated from 2" thick Nylatron GS sheet.	63
3.5	Machine drawing of the DNGM maser block, fabricated from 2" thick Nylatron GS sheet.	64
3.6	Machine drawing of the spacer connecting the pump and maser blocks, fabricated from 3" diameter Nylatron rod stock.	65
3.7	View of the assembled DNGM oven components, as viewed along the direction traveled by the optical pumping laser beam.	66
3.8	A design drawing of the DNGM shroud assembly. Notice the grooves for gradient trim coils cut on the outer surface.	67
3.9	A photograph of the DNGM shroud and oven block assembly.	68
3.10	End-on view of DNGM oven, shroud, and solenoid assembly.	69
3.11	Side view of DNGM oven, shroud, and solenoid assembly.	70
3.12	Drawing of the plate sealing the downstream end of the DNGM shroud assembly.	71

3.13	Temperature of the DNGM laboratory environment over a typical 24 hour period.	73
3.14	General schematic of the DNGM's blown air temperature control systems.	74
3.15	A photograph of the optics used in the DNGM experiment.	78
3.16	(a) A schematic of the optical components used in the DNGM experiment. (b) Typical observed improvement in maser amplitude stability of more than an order of magnitude when the two-loop LDA stabilization techniques are employed.	80
3.17	Plot of the relative value of M_{rb} versus temperature in the diode bar of the Coherent LDA, for fixed $I = 37$ amperes. DNMG 17, page 119.	82
3.18	Measured variation in the pump bulb Rb magnetization (M_{rb}) with and without the two optical feedback loops engaged.	86
3.19	Scale drawing of the μ -metal shields used in the DNGM experiment. .	88
3.20	Schematic drawing of the y -trim coil used in the DNGM experiment.	94
3.21	Plot of the measured $^{129}\text{Xe } T_2$ vs. z	95
3.22	Example of the measured $^{129}\text{Xe } T_2$ as a function of the current in each gradient trim coil.	96
3.23	Measured $^{129}\text{Xe } T_2$ as a function of the relative levels of ^3He and ^{129}Xe polarization.	99
3.24	Measured $^{129}\text{Xe } T_2^{-1}$ as a function of the relative ^{129}Xe polarization. .	100
3.25	Photograph of a typical DNGM EDM cell, with "choke coils" installed, as described in Section 3.5.7.	103

3.26	A photograph of DNGM cell S3, wired in such a way as to permit generation of a magnetic field at least as inhomogeneous as that which would result from the flow of leakage currents from the high voltage supply.	110
3.27	A schematic of the DNGM signal detection system.	112
3.28	Plot of Q_{coil} and R_{ac} as a function of frequency for the external resonator coil ($L = 104$ mH, $R_{dc} = 21.4\Omega$) presently in use (Section 3.7.3). DNGM-15, page 108.	115
3.29	A photograph of the aluminum junction box described in Section 3.7.2.	117
3.30	A design drawing of the pickup coil form, fabricated from Nylatron GSM.	120
3.31	A design drawing of the external resonator form, fabricated from Nylatron GSM.	122
3.32	A plot of the radiation damping rate τ_{rd}^{-1} for the ^{129}Xe and ^3He species as a function of detuning from their associated resonator peaks. . . .	125
4.1	A typical free-induction-decay (FID) ringdown for the ^{129}Xe species in EDM cell SE3.	137
4.2	Typical measurements of the ratio $P_z(t)/P_{z,max}$, used to determine T_1^* .	140
4.3	A figure depicting the maser polarization vector \mathbf{P}	143
4.4	The R -trace of the phase-locked ^{129}Xe maser before and after a proper tip α was applied at $t = 0$	145
4.5	^{129}Xe plot of the measured ratio $P_{\perp,+}/P_{\perp,o}$ as function of varying pulse durations τ for fixed drive voltage.	146

5.1	Bounds on CPT- and Lorentz-violation can be obtained by comparing the frequencies of co-located clocks as they rotate with respect to the fixed stars.	151
5.2	Typical residuals for the ^3He phase data from one sidereal day, calculated using the fit model given in Eq. (3).	162
5.3	Values of the Lorentz-violating parameter $\delta\nu_X$ obtained with cell SE3 in the E1 orientation. The horizontal line indicates the mean value for that data set.	164
5.4	A plot of the R -distribution probability function.	166
6.1	Illustration of how for an atom, molecule, or elementary particle to have a permanent EDM, T symmetry must be violated.	169
6.2	Schematic of the DNGM high voltage system used to create the applied electric field necessary for a ^{129}Xe EDM search.	173
6.3	Method of achieving electrical connection between the high voltage supplies and an EDM cell.	174
6.4	Estimated mean values and standard errors of the 25 usable single-day EDM runs.	180

List of Tables

1.1	Typical dual noble gas maser operating parameters.	11
1.2	Typical dual noble gas maser operating parameters in the maser bulb.	12
1.3	Typical dual noble gas maser operating parameters in the pump bulb.	12
2.1	Values for the spin-rotation rate constants k_{rb-a} and typical gas densities $[a]$	19
2.2	Typical DNGM values for the maser bulb parameters in Equation 2.19. The value of $T_{2,\nabla B_z}$ is inferred using Equation 2.19 and the other values in the table.	26
2.3	Common designations for the noise processes associated with values of μ in the expression $\sigma(\tau) \propto \tau^\mu$	43
2.4	RMS phase noise residuals for the phase-locked ^{129}Xe maser and free-running ^3He maser at three different total flow rates (DNGM-15, page 20).	53
3.1	Gas fill pressures (at 298 K) for the cells used to make measurements reported in this thesis.	57
3.2	Dimensions of the cells used to make measurements reported in this thesis.	57
3.3	Properties of Nylatron GS, available from AIN Plastics, Norwood, MA.	62

3.4	Typical parameters for the three DNGM temperature control subsystems.	77
3.5	Typical operational parameters for the Optopower and Coherent LDAs used in the DNGM experiment.	79
3.6	Characteristics of the solenoid used in the DNGM experiment.	91
3.7	The best attainable values of T_2 for DNGM cell 37, with and without choke coils installed, DNGM 10, pages 117, 124, and 127.	104
3.8	Example measurements of the standard deviation of ^{129}Xe maser phase residuals over a 500 second interval as a function of adjustable magnetic field lock-loop parameters.	106
3.9	Results of co-magnetometer measurements carried out in April, 1999.	108
3.10	Room-temperature characteristics of the pickup and external resonator coils presently used in the DNGM, depicted in Figures 3.30 and 3.31.	120
3.11	Normalized ^3He maser frequency shifts $\Delta\nu_{he}/\Delta T$ when controlled temperature changes were applied to the DNGM pickup coil, external resonator, coaxial cables, and junction box.	126
3.12	Upper bounds on the limitations imposed by thermal fluctuations of the resonator system on the LLI and EDM tests described in this thesis.	127
3.13	Table of typical settings for SRS 830 and 850 lockin amplifiers, as of June 2000.	132
3.14	Table of typical settings for PID boxes, as of June 2000.	132
3.15	Settings for the temperature monitor/control bridges depicted in Figure 3.14.	133

4.1	Comparison of the ratios $P_{z,o}/P_o$ and τ_{rd}/T_2 for cell S1 data, DNGM-14, pages 1, 19, 61, 66, and 67.	141
4.2	Summary of the values θ_o and α , as well as the near-equilibrium ring-down parameters γ_{ring} and ω_{ring} that were deduced from the ensemble of measurements performed with cell S1 in December, 1998.	145
5.1	Means and standard errors for $\delta\nu_X$ and $\delta\nu_Y$. Results are displayed for each of the three cells (S3, E9, and SE3) with both east (E) and west (W) orientations of the magnetic field. Two runs were performed for cell SE3.	163
5.2	Leading experimental bounds on Lorentz violation for the electron, proton and neutron.	165
6.1	Table of the most stringent present experimental limits on the T -violating parameters in Equation 6.1.	171
6.2	Table enumerating the 25 usable single-day EDM results, with estimated errors.	179

Chapter 1

Introduction

In the field of precision measurements, atomic frequency standards play a privileged role. This is due to several characteristics such as: accuracy, reproducibility, [and] stability with time.

Jacques Vanier, 2000

This thesis reports the development and operation of the Harvard-Smithsonian $^{129}\text{Xe}/^3\text{He}$ dual noble gas maser. The dual noble gas maser (DNGM) is the first device to sustain simultaneous active maser oscillations on distinct transitions in two intermingled atomic species, and it allows sensitive differential measurement of the ^{129}Xe and ^3He nuclear spin-1/2 Zeeman transition frequencies [1–3]. We used the DNGM to test Lorentz and CPT symmetry with unprecedented precision. Specifically, a search for sidereal variations in the frequency difference between the DNGM’s co-located ^{129}Xe and ^3He maser ensembles has placed an upper bound of 47 nHz on Lorentz and CPT violating parameters in a standard-model extension that allows violation of these symmetries. Our measurement sets the most stringent limit to date on leading-order Lorentz and CPT violations of the neutron: $\sim 10^{-31}$ GeV. We also report in this thesis progress in a search for a permanent electric dipole

moment (EDM) of the ^{129}Xe atom. Our preliminary result of $d_{Xe} < 1 \times 10^{-26}$ e-c.m. sets a direct bound on time-reversal (T) symmetry violating interactions in the ^{129}Xe nucleus.

Introduction to Operational Principles of the DNGM

Precision measurement of the Zeeman splitting in a two-state system is important for magnetometry [4, 5], as well as for searches for physics beyond the standard model [6–17]. The most precise tests of new physics are often realized in differential experiments which compare the transition frequencies of two co-located clocks, typically radiating on their Zeeman or hyperfine transitions. The advantage of differential measurements is that they render the experiment insensitive to common-mode systematic effects, such as uniform magnetic field fluctuations [18].

The DNGM was first proposed by Walsworth in 1991, and has been developed at the Harvard-Smithsonian Center for Astrophysics in collaboration with researchers at the University of Michigan [1–3]. It is the first device to sustain simultaneous active maser oscillations on distinct transitions in intermingled atomic species, and it allows sensitive differential measurement of the ^{129}Xe and ^3He nuclear spin-1/2 Zeeman transition frequencies: ~ 4.8 kHz for ^3He and ~ 1.7 kHz for ^{129}Xe in a static magnetic field of ~ 1.5 gauss. The maser population inversions for the ^{129}Xe and ^3He ensembles are created by spin exchange collisions between the noble gas atoms and optically-pumped Rb vapor [18, 19]. The DNGM has two chambers, one acting as the spin exchange “pump bulb” and the other serving as the “maser bulb.” This two chamber configuration permits the combination of physical conditions necessary for a high flux of spin-polarized noble gas atoms into the maser bulb, while also maintaining ^{129}Xe and ^3He maser oscillations with good frequency stability.

A schematic diagram of the dual noble gas maser is given in Figure 1.1, with

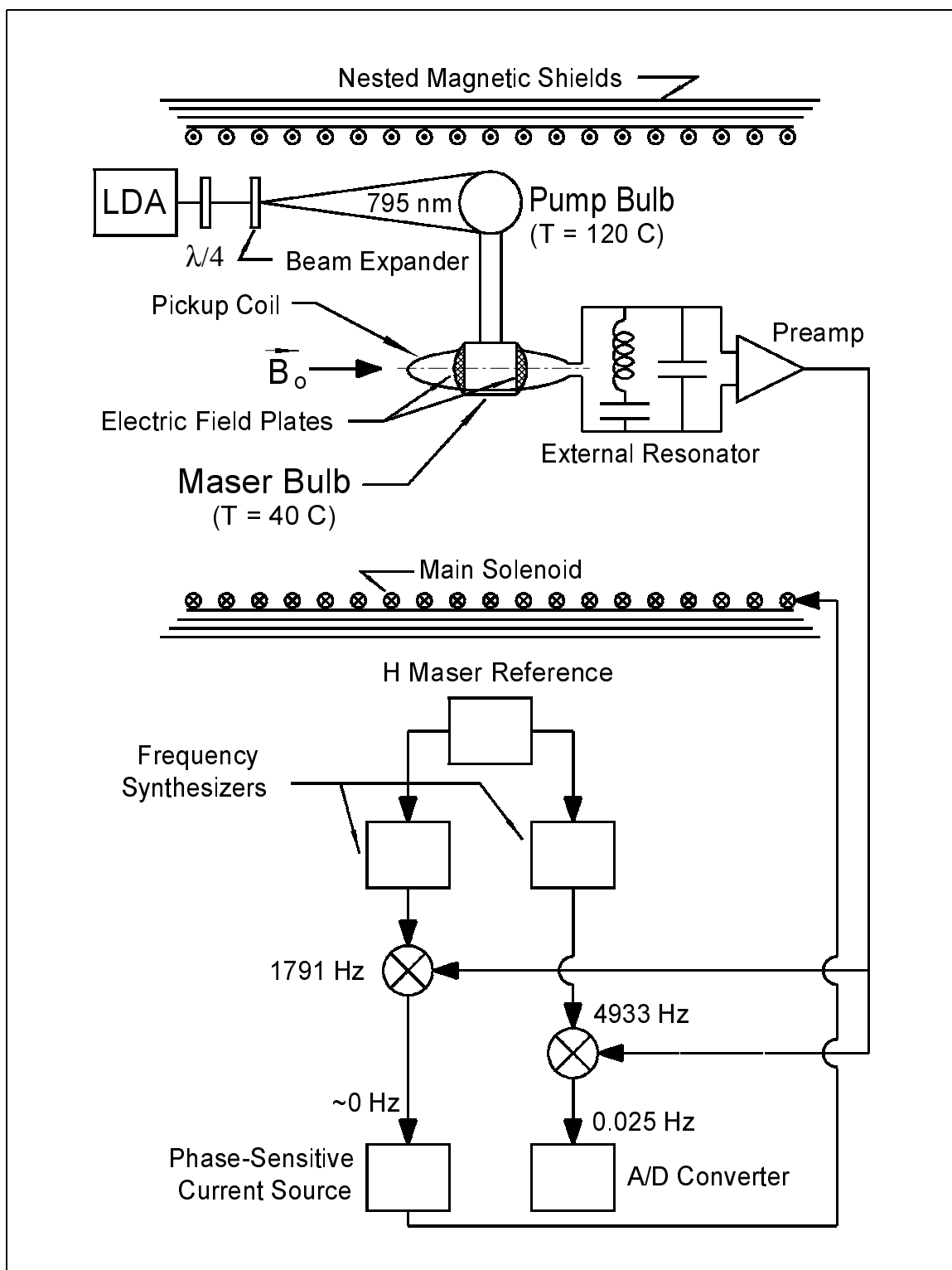


Figure 1.1: Schematic depiction of the Harvard-Smithsonian dual noble gas maser (DNGM).

typical system parameters listed in Tables 1.1, 1.2, and 1.3. A mixture of ^{129}Xe , ^3He , and N_2 gases is contained in a two-chambered cell (Figure 3.3) blown from Corning 7056 borosilicate glass. The inner surface of the cell is treated with a silane coating to minimize spin relaxation of the ^{129}Xe atoms at the walls [20]. A cell consists of a roughly spherical pump bulb (spin-exchange optical pumping region) joined by a straight transfer tube to a roughly cylindrical maser bulb (interaction region). In cells capable of searches for a ^{129}Xe electric dipole moment (EDM), molybdenum discs epoxied to the ends of the maser bulb seal the cell and serve as high voltage electrodes used in the EDM measurement described in Chapter 6 of this thesis. The pump bulb also contains a small amount of Rb metal, and is maintained at a temperature of approximately 115 °C. Thus there is a moderate number density of Rb vapor ($\sim 10^{13} \text{ cm}^{-3}$) present in the pump bulb. In the maser bulb the Rb vapor density is low ($\sim 10^{10} \text{ cm}^{-3}$) because of the relatively cool temperature ($\sim 41 \text{ °C}$) of this chamber. The low Rb density in the maser bulb prevents unwanted Rb-induced spin exchange relaxation and frequency shifts from adversely affecting the masing ^3He and ^{129}Xe ensembles.

The DNGM is housed inside three concentric cylindrical magnetic shields which screen the experiment from inhomogeneous DC magnetic fields and ambient RF noise. A homogeneous and stable field of ~ 1.5 gauss is used to split the noble gas Zeeman sublevels. This field is created with a single-layer solenoid located inside the magnetic shields together with field-gradient correction coils mounted around the maser bulb. The resultant field homogeneity ($\nabla B \sim 20 \mu\text{G}/\text{cm}$) allows spin coherence relaxation times (T_2) of the ^{129}Xe and ^3He ensembles of ~ 330 and ~ 170 seconds, respectively, in the DNGM.

Light from a high power laser diode array is circularly polarized and focused onto the pump bulb. Such light is resonant with the Rb D1 transition ($\lambda = 795 \text{ nm}$) and

induces an electron spin polarization in the Rb vapor via a standard optical pumping process [21]. The N_2 gas in the pump bulb promotes collisional de-excitation of the optically pumped Rb atoms. This prevents radiation trapping, which would otherwise limit the efficiency of the optical pumping process [21]. Spin exchange collisions between the ^{129}Xe and ^3He atoms and optically-pumped Rb vapor [18, 19] polarize the noble gas nuclei and provide the population inversion necessary for continuous (i.e., active) maser oscillation.

The polarized ^{129}Xe and ^3He atoms diffuse out of the pump bulb and down the transfer tube into the maser bulb. The maser bulb is located at the center of a single pickup coil tuned simultaneously to the ^{129}Xe and ^3He Larmor precession frequencies. This double-resonant circuit provides positive feedback to the noble gas Zeeman transitions, and under proper conditions the ^{129}Xe and ^3He ensembles each perform continuous and independent maser oscillations. After making radiative transitions in the maser bulb, the noble gas atoms diffuse back to the pump bulb where they are re-polarized by spin-exchange. Thus active maser oscillation of both species can continue indefinitely.

It should be emphasized that operation of the two species maser requires a two chamber design to separate the spin-exchange pump and maser operations. The ^{129}Xe -Rb spin-exchange rate is two orders of magnitude greater than that of ^3He -Rb. Thus in a single bulb, a Rb density adequate to maintain a ^3He population inversion that will sustain ^3He maser oscillation will also induce excessive de-coherence of the ^{129}Xe ensemble and prevent ^{129}Xe maser oscillation. Moreover, the differential frequency resolution of a single-chamber DNGM would be severely limited by noble gas Zeeman frequency shifts induced by the magnetization of, and the collisional contact hyperfine interaction with, optically pumped Rb.

The ^{129}Xe and ^3He maser signals from the pickup coil (typically ~ 3 to $5 \mu\text{V}$)

are amplified and sent to a pair of digital lockin detectors. All reference frequencies used in the experiment are derived from the same hydrogen maser clock to eliminate concerns about unstable phase and frequency shifts among the reference oscillators. Active feedback to the solenoid’s magnetic field locks the phase of the ^{129}Xe (or ^3He) maser to that of a 1.7 kHz (or 4.8 kHz) reference signal, thereby isolating the experiment from common-mode systematic effects (such as stray magnetic field fluctuations) which would otherwise shift the frequencies of the noble gas masers in proportion to the ratio of their magnetic moments. The short and long-term frequency stability [3] of the phase-locked maser is typically several orders of magnitude better than that of the free-running maser; hence the Zeeman frequency of the phase-locked maser is treated as a constant in all DNGM data analysis. Because magnetic field variations in the maser bulb are only compensated for at the level of the phase-locked maser’s intrinsic frequency stability, it is always better to lock the higher SNR maser. Under our typical operating conditions, this has always been the ^{129}Xe maser. In principle, however, the same physics can be tested with either maser phase-locked. Any frequency shift mechanism acting on the phase-locked maser would change the magnetic field required to maintain a constant phase-locked maser frequency; this alteration of the magnetic field would cause a frequency shift in the free-running maser. Any frequency shift mechanisms acting on the free-running maser would, of course, be directly observable.

Continuous oscillation in the DNGM permits long coherent measurements of the noble gas Zeeman frequencies (on timescales $\sim 5,000$ seconds). In a regime where phase noise processes dominate frequency noise processes [2, 22], a coherent frequency measurement can achieve greater precision than the incoherent average of a set of shorter measurements made during an equivalent period of time [1], as illustrated in Figure 1.2.

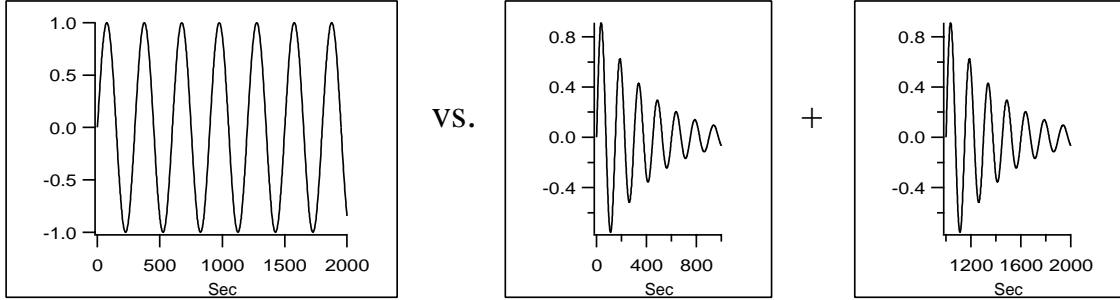


Figure 1.2: A figure emphasizing that a coherent frequency measurement can achieve greater precision than the incoherent average of a set of shorter measurements made during an equivalent period of time [1].

Chapters 5 and 6 of this thesis describe two tests of fundamental physical symmetries that have been and will be performed using the DNGM. In Chapter 5, a search for sidereal variations in the relative frequency of the co-located ^{129}Xe and ^3He masers limits the size of Lorentz and CPT symmetry violating interactions involving the neutron. Chapter 6 reports on progress toward a search for a permanent electric dipole moment (EDM) of the ^{129}Xe atom, as a probe of time reversal (T) symmetry violation in elementary particle interactions. We now provide a brief overview of each of these experiments.

A Test of Lorentz and CPT Symmetry Using the DNGM

Lorentz symmetry is a fundamental feature of modern descriptions of nature, including both the standard model of particle physics and general relativity. However, these realistic theories are believed to be the low-energy limit of a single fundamental theory at the Planck scale. Even if the underlying theory is Lorentz invariant, spontaneous symmetry breaking might result in small apparent violations of Lorentz invariance at an observable level [6]. Experimental investigations of the validity of Lorentz symmetry therefore provide valuable tests of the framework of modern

theoretical physics.

Kostelecký and co-workers have recently developed a standard model extension that treats the effects of spontaneous Lorentz symmetry breaking in the context of a low-energy effective theory, in which terms can be induced which appear to violate Lorentz invariance explicitly [6, 23–30]. Lorentz symmetry remains a property of the underlying fundamental theory, because the breaking is spontaneous. This leads to the effective low energy theory possessing many desirable properties, such as microcausality, energy positivity, and momentum and energy conservation. Also, standard quantization methods are retained, so that Dirac and Schrödinger equations emerge at the appropriate limits.

We used the $^{129}\text{Xe}/^3\text{He}$ maser to search for a Lorentz-violation signature by monitoring the relative phases and Larmor frequencies of the co-located ^3He and ^{129}Xe masers as the laboratory reference frame rotated with respect to the distant stars. The DNGM was operated with the ^{129}Xe maser phase-locked, the ^3He maser free-running, and the quantization axis of the experiment directed east-west in the Earth’s reference frame. To leading order, the standard-model extension [6] of Kostelecký et al. predicts that the Lorentz-violating frequency shifts for the ^3He and ^{129}Xe maser are the same size and sign. We thus searched for a sidereal variation of the ^3He maser frequency of the form

$$\delta\nu_{He} = A \cos(\Omega_s t) + B \sin(\Omega_s t), \quad (1.1)$$

where Ω_s is the angular frequency of the sidereal day ($T_{sidereal} \approx 23.93$ hours), and the parameters (A, B) represent the net effect of Lorentz- and CPT-violating couplings on the ^3He maser frequency with the ^{129}Xe maser phase-locked. With 90 days of data taking, we found no such sidereal variation of the ^3He maser frequency

at the one-standard-deviation level of 47 nHz.

In the context of the standard model extension, the parameters (A, B) are predominantly associated with neutron couplings. Thus the experiment described in Chapter 5 sets the most stringent limit to date on leading order Lorentz and CPT violation of the neutron: about 10^{-31} GeV, or more than six times better than the best previous measurements [6].

A Test of T Symmetry Using the DNGM

Time reversal was long assumed to be a fundamental, perfect symmetry of elementary particle interactions. In 1964, however, a single, indirect¹ example of a violation of T -symmetry was discovered in the decay of neutral K -mesons [31]. During the past 30 years much theoretical effort has been devoted to understanding T -symmetry violation in nature, and many experiments have been performed to search for failures of T -symmetry beyond that originally observed in the K -meson system. The theoretical work has posited various possible sources of T -asymmetry beyond the standard model, but no new experimental examples have been found, thus preventing confirmation of a correct theory and leaving T -symmetry violation as an important problem in elementary particle physics. In addition, the inferred matter/antimatter asymmetry in the universe may be a consequence of T -asymmetry in the laws of elementary particle interactions [32]. Thus an understanding of T -symmetry violation is important both for high energy physics and cosmology.

Composite systems like atoms and molecules may also be probed for evidence of T -symmetry violation due both to intrinsic T -violation of their sub-atomic constituents as well as T -odd interactions among these constituents [17,33]. We used the

¹This experiment measured CP violation, which implies T violation if CPT holds. Recent work on the CPLEAR experiment at CERN has made direct observation of T -symmetry violation in same system.

DNGM to test T -symmetry violation by searching for a possible permanent electric dipole moment (EDM) of the ^{129}Xe atom. For any atom, molecule, or elementary particle to have an EDM, both T and P (parity) symmetry must be violated. In the absence of degeneracies, Wigner-Eckart [34] selection rules require an EDM \mathbf{d} to be parallel or antiparallel to the system's angular momentum vector \mathbf{J} . But \mathbf{d} results from an effective separation of charge and is thus a polar vector (T -even, P -odd) while \mathbf{J} is an axial vector (T -odd, P -even). Thus the relative orientations of \mathbf{d} and \mathbf{J} change under either time reversal or spatial inversion. Calculations indicate that atomic EDM magnitudes increase rapidly with atomic number Z [35]. Thus precision experimental EDM searches using high- Z atoms such as ^{129}Xe serve as good testbeds for physics beyond the standard model.

In Chapter 6 we provide motivation for, and progress on, a search for a permanent electric dipole moment (EDM) of the ^{129}Xe atom. Our preliminary EDM search consisted of sequential applications of an electric field across the interaction region. The electric field was oriented parallel to the experiment's static magnetic field, and its direction was reversed regularly. Coupling to a ^{129}Xe EDM would produce a maser frequency shift linear in the magnitudes and signs of both the ^{129}Xe EDM and the electric field. The static magnetic field was stabilized by phase-locking the ^{129}Xe maser to a stable frequency standard. The free-running ^3He maser was monitored for electric-field-proportional frequency shifts. A ^{129}Xe EDM coupling would change the magnetic field required to maintain a constant ^{129}Xe maser frequency: this EDM-induced alteration of the magnetic field would cause a frequency shift in the free-running ^3He maser. As will be detailed in Chapter 6, no effect was found at the level of $|\mathbf{d}_{xe}| \leq 1 \times 10^{-26}$ e-c.m. ($1\text{-}\sigma$ statistical level).

Tabulation of Typical DNGM Parameters

We conclude this introduction with three tables containing typical values for DNGM operating parameters which are important throughout this thesis. The last column of each table indicates the section of the thesis where the reader should look for further discussion of the parameter of interest.² Note that much of the information in the following tables is cell-specific. We have taken parameters from cell SE3, whose gas fill-pressures and geometry are provided in Tables 3.1 and 3.2.

Parameter	Description	Typical Value	Section
T_p	pump bulb temperature	115 °C	3.3
T_m	maser bulb temperature	41 °C	3.3
P_{xe}	¹²⁹ Xe fill pressure	120 Torr	3.1
P_{he}	³ He fill pressure	1100 Torr	3.1
P_{nit}	N ₂ fill pressure	80 Torr	3.1
$[Rb]_p$	pump bulb Rb density	$2.0 \times 10^{13} \text{cm}^{-3}$	3.4
$[Rb]_m$	maser bulb Rb number density	$8.2 \times 10^{10} \text{cm}^{-3}$	2.6
P_{rb}	pump bulb Rb polarization	0.5	2.2.1
B_z	static magnetic field	1.5 G	3.5
η	resonator fill factor	.02	A

Table 1.1: Typical dual noble gas maser operating parameters.

²Note that there is a list of tables before the introductory chapter. Also note that footnotes and figure captions often provide contact information for vendors, and refer to the DNGM logbooks in which extensive details of relevant experimental procedures may be found. For instance, the citation “DNGM-13, pages 13-23” indicates that more information, including cross-references to computer data files, can be found in the DNGM logbook number 13, pages 13-23.

Parameter	Description	^{129}Xe value	^3He value	Section
Q_{eff}	effective dual resonator Q	9.9	9.3	3.7.3, A
$[ng]$	noble gas density	$4.0 \times 10^{18}\text{cm}^{-3}$	$4.2 \times 10^{19}\text{cm}^{-3}$	3.1
$T_{1,meas}$	polarization relaxation time	1000 sec	8 hr	2.4, 4.4
D_{ng}	noble gas diffusion constant	$.17\text{ cm}^2\text{s}^{-1}$	$.84\text{cm}^2\text{s}^{-1}$	3.5.5
G_m	polarization transfer rate	$4 \times 10^{-4}\text{s}^{-1}$	$2.5 \times 10^{-3}\text{s}^{-1}$	2.4, [36]
T_2	transverse coherence time	333 sec	170 sec	2.3
τ_{rd}	radiation damping time	76 sec	16 sec	4.3
ν_{ng}	operating frequency	1710 Hz	4710 Hz	–

Table 1.2: Typical dual noble gas maser operating parameters in the maser bulb.

Parameter	Description	^{129}Xe value	^3He value	Section
$[ng]$	noble gas density	$3.2 \times 10^{18}\text{cm}^{-3}$	$3.3 \times 10^{19}\text{cm}^{-3}$	3.1
γ_{se}^{-1}	spin exchange time	.08 hr	173 hr	2.2.2
$T_{1,meas}$	polarization relaxation time	500 sec	8 hr	2.4, [36]
D_{ng}	noble gas diffusion constant	$.24\text{ cm}^2\text{s}^{-1}$	$1.2\text{ cm}^2\text{s}^{-1}$	3.5.5
G_p	polarization transfer rate	$4 \times 10^{-4}\text{s}^{-1}$	$2.5 \times 10^{-3}\text{s}^{-1}$	2.4, [36]

Table 1.3: Typical dual noble gas maser operating parameters in the pump bulb.

Chapter 2

Theoretical Principles

This chapter introduces the main theoretical principles of the $^{129}\text{Xe}/^3\text{He}$ dual noble gas maser. Longitudinal and transverse polarization creation and relaxation mechanisms are described, and a modified Bloch theory of the DNGM is presented. Also introduced are the methods by which maser phase and frequency data are analyzed in order to assess the performance of the DNGM as a precision oscillator. The chapter concludes with a description of frequency shift mechanisms in the DNGM.

2.1 Preliminaries

The interaction Hamiltonian for a noble gas atom with nuclear magnetic moment \mathbf{m}_{ng} in a magnetic field $\mathbf{B}(\mathbf{r}, t)$ is

$$\hat{H} = -\mathbf{m}_{\text{ng}} \cdot \mathbf{B}(\mathbf{r}, t). \quad (2.1)$$

The value of \mathbf{m}_{ng} is given by

$$\mathbf{m}_{\text{ng}} = g_{ng} \left[\frac{e\hbar}{2m_p c} \right] \mathbf{I}, \quad (2.2)$$

where \mathbf{I} is the nuclear spin ($I_z = \pm 1/2$), and the quantity in braces is the nuclear magneton μ_N , which has value $0.5050824 \times 10^{-27}$ J/T [37]. The value of the Landé g -factor is -2.13 for ${}^3\text{He}$ and -0.770 for ${}^{129}\text{Xe}$; and the gyromagnetic ratio ($h\gamma_{ng} \equiv g_{ng}\mu_N$) has values -3243.4 Hz/G and -1178.0 Hz/G for ${}^3\text{He}$ and ${}^{129}\text{Xe}$, respectively. The ratio γ_{he}/γ_{xe} appears frequently in this thesis, and has the approximate value 2.7541.

The expectation value of \mathbf{m}_{ng} evolves according to the von Neumann equation

$$i\hbar \frac{\partial}{\partial t} \langle \mathbf{m}_{\text{ng}} \rangle = \langle [\mathbf{m}_{\text{ng}}, \hat{H}] \rangle. \quad (2.3)$$

After expansion of the commutator and re-arrangement of terms, Equation 2.3 can be written as

$$i\hbar \frac{\partial}{\partial t} \langle m_i \rangle = \langle [\mathbf{m}_{\text{ng}}, \hat{H}]_i \rangle = \gamma i \hbar \sum_{j,k} \langle m_j \rangle B_k \varepsilon_{ijk}. \quad (2.4)$$

where ε_{ijk} is the completely antisymmetric Levi-Civita density. In terms of the vector cross-product, this relation takes the more familiar form

$$\frac{\partial}{\partial t} \langle \mathbf{m}_{\text{ng}} \rangle = \gamma \langle \mathbf{m}_{\text{ng}} \rangle \times \mathbf{B}(\mathbf{r}, t). \quad (2.5)$$

It is thus permissible to treat the quantum dynamics of the ${}^{129}\text{Xe}$ and ${}^3\text{He}$ spins classically as long as \mathbf{m}_{ng} is understood to be a quantum mechanical expectation value.¹ Consistent with conventions found in most of the maser literature [1–3], we

¹This result holds true for spin systems of any dimensionality, as long as the energy coupling to the magnetic field is dipolar. It is thus possible to create masers from noble gas species with

will equate the noble gas magnetic moment at each point in space with a magnetization density in a small volume dV :

$$\mathbf{m}_{\text{ng}} = \mu_{ng}[ng]\mathbf{P}_{\text{ng}}, \quad (2.6)$$

where \mathbf{P}_{ng} is the expectation value of the noble gas polarization vector in dV , $[ng]$ is the noble gas number density, and $\mu_{ng} = g_{ng}\mu_N$ refers to the numerical value of the noble gas magnetic moment.

The mean magnetization \mathbf{M}_{ng} of each ensemble can then be expressed as the volume integral of \mathbf{m}_{ng} over the interaction region:

$$\mathbf{M}_{\text{ng}} = \int \mathbf{m}_{\text{ng}}(\mathbf{r})dV. \quad (2.7)$$

When referring to magnetization in the DNGM, M_z indicates longitudinal magnetization along the direction of the static magnetic field, and M_{\perp} indicates magnetization which lies in the plane transverse to the z -axis. Note that the polarization and magnetization vectors for both ^{129}Xe and ^3He are oppositely directed because of their negative g -factors.

2.2 Polarization of ^{129}Xe and ^3He

In the DNGM experiment, the ^{129}Xe and ^3He nuclei are polarized by spin-exchange interactions with optically pumped Rb vapor [21, 38, 39]. This process occurs in two stages. First, Rb is polarized by optical pumping with circularly polarized light tuned to the Rb D1 transition. Second, polarization from the Rb valence electrons

spin $> 1/2$, provided that quadrupole and higher-order couplings can be suppressed. For example, a demonstration of a dual $^3\text{He}/^{21}\text{Ne}$ Zeeman maser (using the nuclear spin-3/2 ^{21}Ne species) has recently been performed in our laboratory.

is transferred to the ^{129}Xe and ^3He nuclei during collisions between the Rb and noble gas atoms. The spin-exchange process is similar for both noble gas species, but the angular momentum transfer rate from the Rb to the ^{129}Xe atoms is ~ 2300 times the transfer rate from the Rb to the ^3He atoms. In this section we present a brief summary of the physics of the spin-exchange optical pumping process, and conclude with a discussion of the polarization relaxation mechanisms that are most important in the DNGM. References [20,21,36] develop more thoroughly the topics reviewed here.

2.2.1 Optical Pumping of Rubidium

The two naturally occurring isotopes of Rb, ^{85}Rb ($S = 1/2, I = 5/2$) and ^{87}Rb ($S = 1/2, I = 3/2$), have ground state hyperfine splittings of 3036 MHz and 6835 MHz, respectively. A typical DNGM cell contains a gas mixture of ~ 1000 Torr ^3He , ~ 100 -200 Torr ^{129}Xe , and ~ 50 -100 Torr N_2 . The presence of these gases broadens the Rb D1 line to a width of ~ 20 GHz, which is much larger than the hyperfine splitting of either isotopic ground state.² Figure 2.1 thus shows a simplified level diagram for both isotopes of Rb, with the (unresolvable) hyperfine levels not depicted. The $m_s = +1/2$ and $m_s = -1/2$ Zeeman sublevels are split by the experiment's solenoidal magnetic field: $\Delta\nu_z = 466$ kHz/G. This Zeeman splitting is also not resolved for typical DNGM magnetic fields ~ 1 G because of collisional broadening. However, such collisions cause insignificant spin depolarization in the Rb ground electronic state; hence the two m_s sublevels are resolved in angular momentum space. Circularly polarized σ^+ light selectively drives the D1 transition $^2S_{1/2} \rightarrow ^2P_{1/2}$, with $\Delta m = +1$. Spontaneous radiative decay from the excited state

²The pressure broadening coefficients for the Rb D1 transition are approximately 14 GHz/atm for N_2 and 18 GHz/atm for ^{129}Xe and ^3He [20].

occurs with a probability of $2/3$ to return to the $m_s = -1/2$ ground state and a probability of $1/3$ to return to the $m_s = +1/2$ ground state, which is the desired, spin-polarized state.

When a Rb atom undergoes such radiative decay, it emits a photon that in general will have neither the same polarization nor propagation direction as the optical pumping light. Re-absorption of these emitted photons by ground state $m_s = 1/2$ Rb atoms limits the efficiency of the optical pumping process. The addition of ~ 80 Torr of N_2 buffer gas to each DNGM cell provides a mechanism for radiationless de-excitation of the Rb valence electron. The Rb- N_2 cross-section for collisional Rb de-excitation is several orders of magnitude larger than the Rb- ^3He and Rb- ^{129}Xe cross-sections, with a decay time of ~ 2 nanoseconds [40]. The spontaneous radiative decay time is ~ 30 nanoseconds; thus $\sim 94\%$ of the Rb atoms decay non-radiatively [40]. Collisional mixing between the Rb and ^{129}Xe , ^3He , and N_2 atoms also rapidly populates the two $^2P_{1/2}$ m_s states equally. Hence non-radiative decay to either ground state m_s level occurs with equal probability. In this simple picture, and in the absence of spin-destruction mechanisms that connect the two m_s ground states, it requires an average of two σ^+ photons to polarize one Rb valence electron.

The rate equation governing the Rb polarization represents the competition between the optical pumping rate, γ_{opt} , and the rate of spin-relaxation of the Rb atom between the ground state sublevels, Γ_{rb} . We can write the optical pumping rate as

$$\gamma_{opt}(z) = \eta \int \Phi(\nu, z) \sigma_{abs}(\nu) d\nu \quad (2.8)$$

where $\Phi(\nu, z)d\nu$ is the (position-dependent) laser σ^+ photon flux in the interval $(\nu, \nu + d\nu)$, $\sigma_{abs}(\nu)$ is the absorption cross-section for σ^+ light (dependent on the Rb

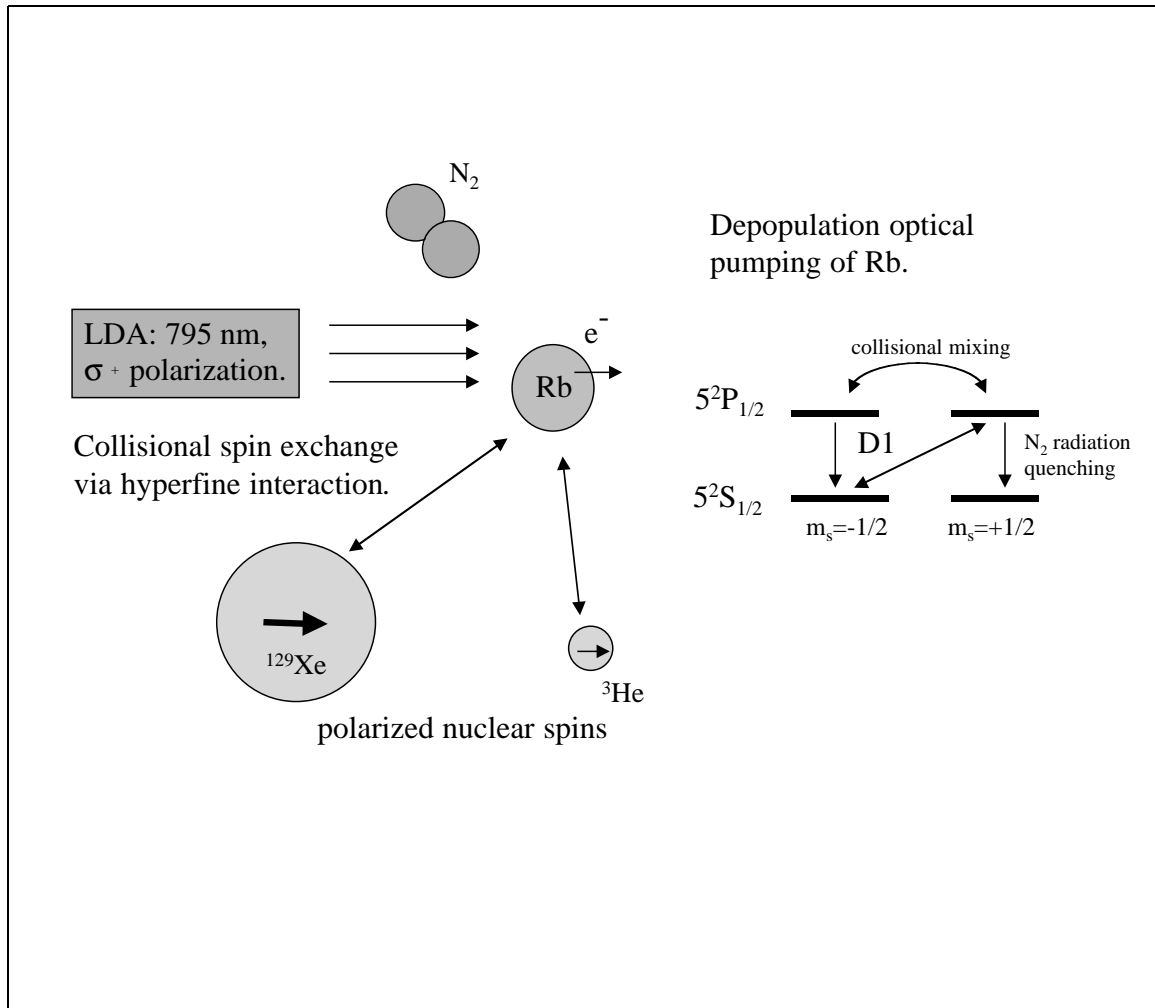


Figure 2.1: Elementary depiction of optical pumping of Rb by circularly polarized σ^+ light. In a pressure-broadened cell the hyperfine levels cannot be energetically resolved and are not shown. The $m_s = 1/2$ and $m_s = -1/2$ Zeeman sublevels are split by the experiment's solenoidal magnetic field in both the $5^2S_{1/2}$ and $5^2P_{1/2}$ electronic states, and are resolved in angular momentum space.

species a	k_{rb-a} cm ³ s ⁻¹	$[a]$ cm ⁻³
³ He	1.0×10^{-18}	3×10^{19}
¹²⁹ Xe	4.7×10^{-15}	3×10^{18}
Rb	4.2×10^{-13}	1×10^{13}
N ₂	9.0×10^{-18}	1×10^{18}

Table 2.1: Values for the spin-rotation rate constants k_{rb-a} and typical gas densities $[a]$.

density and polarization), and η is the probability that an unpolarized Rb atom will end up in the target $m_s = +\frac{1}{2}$ state per photon absorbed (including the “slowing down” effect due to the internal Rb hyperfine interaction [20]). For simplicity, we will ignore the position dependence of the photon flux and the Rb polarization in the discussions that follow.

The Rb spin-destruction rate Γ_{rb} is due mainly to spin-rotation interactions³ between Rb and other atoms in the optical pumping region [40]:

$$\Gamma_{rb} = k_{rb-he}[^3He] + k_{rb-xe}[^{129}Xe] + k_{rb-rb}[Rb] + k_{rb-nit}[N_2], \quad (2.9)$$

where the $k_{rb-a} = \langle v_a \sigma_{rb-a} \rangle$ are velocity dependent rate constants resulting from collisions of Rb atoms with atoms of type a . Table 2.1 gives values for the relevant k_{rb-a} ; it is clear that Γ_{rb} is dominated by spin-rotation interactions of the Rb and ¹²⁹Xe atoms [36]. The time dependence of the Rb polarization is

$$\frac{dP_{rb}}{dt} = \gamma_{opt}(1 - P_{rb}) - \Gamma_{rb}P_{rb}, \quad (2.10)$$

³Recall that spin-rotation interactions are of the form $\hat{H}_{sr} = \alpha \mathbf{L}_{\text{pair}} \cdot \mathbf{S}$ where \mathbf{L}_{pair} is the angular momentum associated with the center of mass motion of a Rb and second atom. Spin rotation can transform spin angular momentum to kinematic angular momentum and is thus a mechanism for polarization loss only.

which has the following solution for the initial condition $P_{rb}(0) = 0$:

$$P_{rb}(t) = \frac{\gamma_{opt}}{\gamma_{opt} + \Gamma_{rb}} \left(1 - e^{-(\gamma_{opt} + \Gamma_{rb})t}\right) \quad (2.11)$$

For typical DNGM operating conditions, P_{rb} reaches its equilibrium value of $\sim 50\%$ in ~ 1 msec.

2.2.2 Spin Exchange

The polarization of a Rb valence electron can be transferred to a noble gas nucleus by a spin-exchange interaction⁴ of the form

$$\hat{H} = -2g_{ng}\mu_B\mu_{ng} \sum_{i=1}^N \left[\frac{\mathbf{S}_i \cdot \mathbf{I}}{r_i^3} - 3 \frac{(\mathbf{I} \cdot \mathbf{r}_i)(\mathbf{S}_i \cdot \mathbf{r}_i)}{r_i^5} + \frac{8\pi}{3} \delta(r_i) \mathbf{S}_i \cdot \mathbf{I} \right] \quad (2.12)$$

where \mathbf{I} represents the nuclear spin of the noble gas and \mathbf{S}_i is summed over the Rb valence electron and all the noble gas electrons [41, 42]. The last term in the Hamiltonian represents the Fermi contact interaction between the electrons and the noble gas nucleus, and it is this interaction that dominates the spin exchange process [41]. The sum over all noble gas electrons can best be understood by considering the exchange enhancement process [42], in which the Rb valence electron can be exchanged with one of the noble gas electrons. This effectively brings the polarized Rb electron spin closer to the noble gas nucleus and increases the cross-section for angular momentum transfer to the nuclear spin. The total gas pressure in a typical DNGM cell is approximately 1.5 atmosphere. This is low enough to permit the formation of transient Rb-¹²⁹Xe Van der Waals molecules during three-body collisions between Rb and noble gas atoms. The third atom serves as a sink for

⁴This interaction also leads to a noble gas polarization-induced shift of the Rb Zeeman frequency. This “contact shift” effect will be discussed in greater detail in Section 2.6.

the energy and momentum of the Rb-¹²⁹Xe pair, and the resultant formation of a Van der Waals molecule increases the Rb-¹²⁹Xe hyperfine interaction time, thereby enhancing the Rb-¹²⁹Xe spin-exchange rate [19].

As with the polarization of Rb, the polarization of ³He and ¹²⁹Xe can be characterized by a spin-exchange source term $\gamma_{se} = k_{se}[Rb]$ and a relaxation term Γ_{ng} . Mechanisms for noble gas relaxation will be discussed in Section 2.2.3. Under typical operating conditions in the DNGM pump bulb, $k_{se-he} \approx 7 \times 10^{-20}$ (binary collisions only) and $k_{se-xe} \approx 4 \times 10^{-16} + 1 \times 10^{-15}$, where the second term arises from the three-body interactions described above [36]. Estimated values of the spin-exchange rates for the DNGM parameters used in recent measurements are thus $\gamma_{se-he} \approx 1 \times 10^{-6}$ s⁻¹ and $\gamma_{se-xe} \approx 0.020$ s⁻¹ in the pump bulb.⁵ The rate equation for P_{ng} is given by

$$\frac{dP_{ng}}{dt} = \gamma_{se}(P_{rb} - P_{ng}) - \Gamma_{ng}P_{ng} \quad (2.13)$$

In the DNGM, typical Rb polarization times are ~ 1 ms; those for ¹²⁹Xe are ~ 10 minutes; and those for ³He are ~ 3 hours. It is thus safe to solve the P_{ng} rate equation treating P_{rb} as a constant on the scale of both noble gas pumping times. For the initial condition $P_{ng}(0) = 0$ we have:

$$P_{ng}(t) = \frac{P_{rb}\gamma_{se}}{\gamma_{se} + \Gamma_{ng}} \left(1 - e^{-(\gamma_{se} + \Gamma_{ng})t} \right). \quad (2.14)$$

2.2.3 Longitudinal Spin Relaxation

Ignoring polarization loss in the transfer tube and in the absence of masing, the steady-state longitudinal noble gas magnetization density can be written as the

⁵This estimated rate is larger than our measured rate of ¹²⁹Xe polarization by a factor of 10 or so. The discrepancy is probably due to inaccuracy in determining $[Rb]$ and uncertainty in the constants contributing to k_{se} .

product

$$m_{ng} = \mu_{ng}[ng] \left(\frac{\gamma_{opt}}{\gamma_{opt} + \Gamma_{rb}} \right) \left(\frac{\gamma_{se}}{\gamma_{se} + \Gamma_{ng}} \right), \quad (2.15)$$

where $[ng]$ is the noble gas number density and μ_{ng} is the magnetic moment of the noble gas nucleus. Here we summarize mechanisms that contribute to the longitudinal relaxation rates Γ_{ng} of the noble gas atoms. References [21, 40] develop these topics in much greater detail. In the discussions that follow, it is helpful to keep in mind that measured DNGM polarization lifetimes ($1/T_1 = \gamma_{se} + \Gamma_{ng}$) for ^{129}Xe are $T_{1,p} \sim 500$ s in the pump bulb and $T_{1,m} \sim 1000$ s in the maser bulb; and for ^3He are $T_{1,p} \approx T_{1,m} \sim 8$ hours. For ^{129}Xe , the longitudinal polarization relaxation rate Γ_{xe} includes the effects of polarization transport from the region under consideration (parameterized by transport rates G_p and G_m for the pump and maser bulbs, respectively) and assumes that polarization is lost when it leaves either bulb (i.e., $\Gamma_{xe} > G_p, G_m$). For ^3He , G_p and G_m are much greater than all sources of polarization relaxation. Thus ^3He polarization is not lost through inter-bulb exchange (in the absence of masing), and G_p and G_m do not contribute to Γ_{he} . Section 4.4 describes measurements of $T_{1,m}$. The parameters $T_{1,p}$, G_p , and G_m have been measured by our collaborators at the University of Michigan [36] in cells and under operating conditions almost identical to those in our laboratory.

One way noble gas atoms may become depolarized is through interactions (spin-exchange and dipole-dipole) with other atoms in the cell volume. In the maser chamber the Rb density is approximately $8 \times 10^{10} \text{ cm}^{-3}$, and there is effectively no relaxation of noble gas polarization through spin-exchange with polarized Rb atoms: i.e., $1/T_1 = \Gamma_{ng}$. For ^{129}Xe the measured depolarization rate Γ_{xe} in the maser chamber is thus due largely to wall relaxation effects, as described in Section 3.1 and references [20, 21], with lesser contributions from escape from the maser

bulb and other processes. The OTS coating used in DNGM cells increases the ^{129}Xe relaxation time from tens of seconds on bare borosilicate glasses [20] to the value of $T_{1,m} \sim 1000$ seconds observed under typical running conditions with properly coated cells. Assuming only a slight temperature dependence of the wall relaxation time, the typical observed ^{129}Xe $T_{1,p}$ of ~ 500 seconds indicates that ^{129}Xe -Rb spin-exchange and perhaps transport mechanisms contribute an amount $\sim 0.001 \text{ s}^{-1}$ to the overall relaxation rate $1/T_{1,p}$ in the pump chamber.

For ^3He Romalis [40] reports that the rate of ^3He - ^3He dipole relaxation is given by

$$\Gamma_{he,dipole} = \frac{[{}^3\text{He}]}{744} \text{hrs}^{-1}, \quad (2.16)$$

where $[{}^3\text{He}]$ is in amagats. Because the typical measured ^3He polarization lifetime is ~ 8 hours, the above dipole-dipole relaxation mechanism is clearly not a limiting factor in the DNGM. The ^{129}Xe - ^{129}Xe dipole relaxation rate is even smaller and is not a contributor to ^{129}Xe spin-destruction in the DNGM [21]. The limiting relaxation rate for ^3He in both chambers is thus due to wall interactions, which are poorly understood [21].⁶

It bears mentioning that noble gas atoms can also become depolarized through interactions with magnetic field inhomogeneities of the form $\nabla\mathbf{B}_\perp$, where \mathbf{B}_\perp is the component of the static magnetic field transverse to the DNGM Zeeman field $B_z \sim 1$ G [21]:

$$\Gamma_{\nabla B,ng} = \frac{D_{ng} |\nabla\mathbf{B}_\perp|^2}{B_z^2}. \quad (2.17)$$

The noble gas diffusion constants D_{ng} are largest in the hot pump chamber, with rough values $D_{xe} \sim 0.2$ and $D_{he} \sim 1.0 \text{ cm}^2/\text{sec}$. Even in the presence of polarization-

⁶It should be noted that wall relaxation times scale as volume/(surface area). Thus in large cells such as those used for polarized ^3He target work and biomedical imaging, ^3He dipole-dipole relaxation can become the dominant ^3He spin-destruction mechanism [40].

induced field gradients, the homogeneity of ∇B_z is of order $10 \mu\text{G}/\text{cm}$ (Sections 3.5.3 and 3.5.6). Suppose the gradients in the static transverse field were 10x as large (an extremely conservative estimate). The resulting relaxation rates would be $\Gamma_{\nabla B,xe} \sim 10^{-7}/\text{s}$ and $\Gamma_{\nabla B,he} \sim 10^{-8}/\text{s}$. As we have seen, these values are much smaller than the contributions to Γ_{ng} from other sources.

2.3 Transverse Spin Relaxation

Longitudinal noble gas polarization P_z is created in the DNGM pump chamber, as described in Section 2.2, and diffuses through the transfer tube into the interaction region (maser chamber). Atomic polarization which is tipped away from the quantization axis will precess about the static magnetic field B_0 that splits the noble gas Zeeman sublevels: $\hbar\omega_{zeeman} = 2\mu_{ng}B_0$. The voltage induced across the DNGM pickup coil (Section 3.7.3) by precessing transverse polarization P_{\perp} is used to search for signatures of possible new physics (Lorentz symmetry violation and a ^{129}Xe EDM). In this section we summarize the mechanisms that deplete transverse polarization in the DNGM maser chamber.

The dominant mechanism for transverse spin relaxation in the maser bulb arises from interactions of the noble gas atoms with axial magnetic field inhomogeneities of the form ∇B_z . The detected magnetization signal is actually the weighted volume average of signals produced by individually precessing noble gas dipoles in the interaction region. Dipoles at different locations will experience slightly different magnetic fields B_z , and will thus precess at slightly different rates. Motional averaging (i.e., diffusion) of the dipoles about the maser chamber will tend to reduce the effective inhomogeneity of B_z sampled by individual atoms. Nevertheless, phase differences in $P_{\perp,i}$ among the dipoles accumulate, and the bulk transverse magne-

tization will relax with a phenomenological decay time T_2 as e^{-t/T_2} [1, 22, 43]. In a cylindrical cell the dephasing rate takes the form [44]

$$\frac{1}{T_{2,\nabla B_z}} = \frac{L^4 \gamma_{ng}^2}{120 D_{ng}} \left| \frac{\partial B_z}{\partial z} \right|^2 + \frac{7a^4 \gamma_{ng}^2}{96 D_{ng}} \left(\left| \frac{\partial B_z}{\partial x} \right|^2 + \left| \frac{\partial B_z}{\partial y} \right|^2 \right), \quad (2.18)$$

where D_{ng} is the total diffusion constant, γ_{ng} is the gyromagnetic ratio, L is the cell length, and a is the cell radius (in typical EDM cells, 2 cm and .64 cm respectively). The components of ∇B_z include contributions from the solenoid field, from residual magnetization of the μ -metal shields, and from fields produced by the polarized noble gas atoms. Section 3.5 describes and quantifies these effects further.

To obtain a complete expression for T_2 , we must add to Equation 2.18 terms to account for escape of noble gas atoms from the interaction region, and also to account for the polarization loss mechanisms described in Section 2.2.3. T_2 is then given by

$$\frac{1}{T_2} = \frac{1}{T_{2,\nabla B_z}} + \frac{1}{T_{storage}} + \frac{1}{T_1}, \quad (2.19)$$

where $T_{storage} = G_m^{-1}$ is the noble gas storage time in the maser chamber. Typical DNGM values for the parameters in Equation 2.19 are given in Table 2.2. For ^3He measured T_2 values are ~ 150 seconds, and T_1 relaxation is clearly not a significant contributor. For ^{129}Xe , typical T_2 values are ~ 300 seconds, which indicates that the T_1 relaxation time of ~ 1000 seconds contributes at the $\sim 25\%$ level. As indicated by the values in Table 2.2, the T_2 of the more rapidly diffusing ^3He species is field-gradient and escape-time limited (estimated $T_{storage} \sim 390$ s), whereas atom escape contributes only about 15% to the ^{129}Xe T_2 , a sub-optimal condition discussed more in Section 3.1.

The transverse coherence time establishes a threshold condition for active maser

parameter	${}^3\text{He}$ (s)	${}^{129}\text{Xe}$ (s)
T_1 (measured)	2.8×10^4	1000
T_2 (measured)	150	300
$T_{storage}$ (estimated)	390	2000
$T_{2,\nabla B_z}$ (inferred)	245	545

Table 2.2: Typical DNGM values for the maser bulb parameters in Equation 2.19. The value of $T_{2,\nabla B_z}$ is inferred using Equation 2.19 and the other values in the table.

oscillation and figures prominently in determining the total maser output power (Section 2.4). It also places fundamental limits on the optimal frequency resolution of the DNGM in a measurement interval τ (Section 2.6.1). Subsequent sections in this thesis describe this impact of T_2 on DNGM performance in some detail, and also provide methods for improving the T_2 of both species. The experimental procedure for determining T_2 is presented in Section 4.2.

2.4 Bloch Equations and Masing

Combining Equations 2.5 and 2.6 with the phenomenological relaxation times T_1 and T_2 introduced in the previous sections, we can write the well-known Bloch equations [22, 43] for noble gas polarization dynamics in the maser chamber:

$$\begin{aligned}
\dot{P}_x &= \gamma_{ng}(P_y B_z - P_z B_y) - \frac{P_x}{T_2} \\
\dot{P}_y &= \gamma_{ng}(P_z B_x - P_x B_z) - \frac{P_y}{T_2} \\
\dot{P}_z &= \gamma_{ng}(P_x B_y - P_y B_x) - \frac{P_z}{T_1}
\end{aligned} \tag{2.20}$$

If $\mathbf{B} = B_0 \hat{z}$ only, initial components of transverse polarization will precess about the z -axis and decay exponentially with a $1/e$ time T_2 (Section 2.3). Similarly, in

the absence of a source of longitudinal polarization, P_z will decay at a rate of $1/T_1$ from its initial value.

In the DNGM, however, P_z is replenished by a flux of polarized atoms from the pump bulb, and the magnetic field has a transverse component due to current flow in the pickup coil induced by the precessing spins. Under conditions of sufficient polarization influx and sufficient coupling of the DNGM dual resonator (Section 3.7.3) to the transverse polarization P_\perp , steady-state maser oscillation can occur for each species. Appendix A describes in detail an extended Bloch theory of dual Zeeman masers,⁷ modified to incorporate the effects of inter-bulb polarization transport and off-resonant spin-circuit coupling. Here we present a summary. Experimental verification of the basic Bloch theory for small perturbations and on-resonant spin-circuit coupling is presented in Section 4.7.

2.4.1 Modified Bloch Equations

As detailed in Appendix A and described in References [1,2], the modified Bloch equations for each noble gas species take the form

$$\begin{aligned}
\dot{P}_\perp &= \frac{P_z P_\perp}{P_o \tau_{rd}} \frac{\rho(\omega)}{Q} \sin \alpha - \frac{P_\perp}{T_2} \\
\dot{P}_z &= -\frac{P_\perp^2}{P_o \tau_{rd}} \frac{\rho(\omega)}{Q} - \frac{P_z}{T_1} + G_m (\beta P_p - P_z) \\
\dot{P}_p &= P_{rb} \gamma_{se} - P_p \left(\frac{1}{T_{1,p}} + \gamma_{se} \right) + G_p (\beta P_z - P_p) \\
\omega &= \gamma_{ng} B_z - \frac{P_z}{P_o \tau_{rd}} \frac{\rho(\omega)}{Q} \cos(\alpha),
\end{aligned} \tag{2.21}$$

where P_p refers to longitudinal polarization in the pump bulb, P_z refers to longitudinal polarization in the maser bulb, ω is the frequency of the voltage induced

⁷I am extremely grateful to Richard Stoner for writing the paper included in Appendix A.

across the resonator by the coupled noble gas/resonant circuit system, and we have switched from Cartesian to polar coordinates via the equations

$$\begin{aligned}
P_x &= P_{\perp} \cos(\Phi(t)) \\
P_y &= P_{\perp} \sin(\Phi(t)) \\
\omega &= \dot{\Phi}(t).
\end{aligned} \tag{2.22}$$

G_m and G_p are transport rates from the maser and pump bulbs, respectively; β is a parameter to account for noble gas depolarization in the transfer tube; $T_{1,p}$ is the polarization lifetime in the pump chamber; and P_o is the equilibrium value of noble gas polarization in the maser chamber in the absence of spin-circuit coupling. We have assumed that the resonator acts for each noble gas species as if it is a simple $R - L - C$ series circuit with resonant frequency $\omega_o = (LC)^{-1/2}$ and quality factor $Q = \omega_o L/R$. The resonator response is described in terms of an amplitude function $\rho(\omega)$ and a phase function $\alpha(\omega)$ (Appendix A):

$$\begin{aligned}
\rho(\omega) &= \frac{Q}{\sqrt{Q^2 (1 - (\omega_o/\omega)^2)^2 + (\omega_o/\omega)^2}} \\
\cos \alpha &= \rho(\omega) (1 - (\omega_o/\omega)^2) \\
\sin \alpha &= \frac{\omega_o \rho(\omega)}{\omega Q}
\end{aligned} \tag{2.23}$$

Here, $\pi/2 - \alpha$ is the phase angle between the resonator voltage and current, so that the resonance condition $\omega = \omega_o$ implies $\sin \alpha = 1$, $\cos \alpha = 0$, and $\rho(\omega) = Q$. Note that although the frequency ω is a dynamical variable (of great interest) in this theory, it may be treated as a constant $\omega \approx \gamma_{ng} B_0$ in all but the last of Equations 2.21.

Note also that in the actual DNGM resonator system, the pickup coil is part of

a dual resonance circuit, described in detail in Section 3.7.3 and Appendix A. The Bloch equations as written above still hold, but Q must be replaced by the effective quality factor Q_{eff} , as discussed in Appendix A (Equation E5). This effective quality factor measures the current gain provided by the DNGM resonator system, and of course reduces to $Q_{eff} = \omega_o L/R$ when the dual resonator is replaced by a simple $R - L - C$ series circuit. Section 3.7.1 outlines methods for measuring Q and Q_{eff} .

Radiation Damping Time

The radiation damping time τ_{rd} is defined as

$$\frac{1}{\tau_{rd}} = \frac{1}{2} \frac{\hbar \gamma_{ng}^2}{2} \mu_o \eta Q [ng] P_o, \quad (2.24)$$

where μ_o is the permeability of free space, η is the so-called “filling factor,” which quantifies the average geometrical coupling between the pickup coil and the maser cell volume, and $[ng]P_o$ is the maser chamber noble gas magnetization in the absence of any spin-circuit coupling. The radiation damping time is an easily measured quantity. With the resonator tuned far off the noble gas Zeeman frequency, $\dot{P}_\perp = -P_\perp/T_2$. With the resonator tuned to the Zeeman frequency, $\omega = \omega_o = \gamma_{ng}B_o$, $|P_z| = P_o$ at early times, and the first of Equations 2.21 becomes

$$\dot{P}_\perp = P_\perp \left(\frac{\pm 1}{\tau_{rd}} - \frac{1}{T_2} \right), \quad (2.25)$$

where the $+/-$ refers to whether the noble gas atoms have been pumped into the positive/negative energy state. (The positive energy state, i.e., and a population inversion, is needed for active maser oscillation.) The difference of the transverse decay times with and without the resonator tuned to the Zeeman frequency thus

yields the value of τ_{rd} , as described further in Section 4.3.

Estimating Polarization Loss in the Transfer Tube

In writing Equations 2.21, we have made the simplifying approximation (see Appendix A for the complete theory) that transport effects can be accounted for solely by a transfer tube loss-parameter β . The probability that an atom diffusing down the transfer tube becomes depolarized is proportional to τ , the time spent in the transfer tube, multiplied by the wall relaxation rate in the transfer tube. This transfer tube wall relaxation rate can be estimated by multiplying the maser chamber relaxation rate by the ratio of the wall collision rates in the transfer tube and maser chamber. β is then given by

$$\begin{aligned}\beta &= \exp\left[-\frac{\gamma_{w,tube}\tau}{T_{1,wall}\gamma_{w,maser}}\right] \\ &\approx \exp\left[-\frac{L^2 \cdot l_m^2}{2DT_{1,wall} \cdot l_t^2}\right],\end{aligned}\tag{2.26}$$

Here, $T_{1,wall}$ is the wall depolarization time in the maser chamber and γ_w is the wall collision rate in the region of interest. The collision rate is given by $\gamma_w = 2D/l^2$, where D is the diffusion coefficient of the noble gas species under consideration and l is the mean wall spacing in the region of interest. τ , the time spent by an atom in the transfer tube, can be approximated from the first diffusion mode as $\tau \approx L^2/2D$, where L is the length of the transfer tube. For ^3He , the $T_{1,wall}$ time is so long that $\beta_{he} \approx 1$. For ^{129}Xe , inserting typical values of $L = 4.1$ cm, $l_m = 1.5$ cm, $l_t = .4$ cm, $T_{1,wall} \approx 800$ sec, and $D_{xe} \approx .17$ cm²/sec yields $\beta \approx 0.42$.

Schematic Illustration of Zeeman Maser Dynamics

Figure 2.2 summarizes the different dynamical effects acting on the noble gas polarization vector and magnetization vectors in the maser chamber, as seen in the frame rotating at the Larmor precession frequency. For ^{129}Xe and ^3He the magnetization and polarization vectors are oppositely directed. P_z is replenished by diffusive loading and dissipated by wall loss, escape from the bulb and radiation damping. P_\perp is replenished by radiation damping and destroyed by magnetic field gradients, wall loss, and escape from the interaction region.

2.4.2 Equilibrium Solutions and Near Equilibrium Oscillations

To obtain the equilibrium solutions of the modified Bloch equations for the DNGM (Equations 2.21), we set all time derivatives to zero. For the steady-state maser frequency and longitudinal polarizations, the results are

$$\begin{aligned}\omega_{ss} &= \gamma_{ng}B_z - \frac{\cot \alpha}{T_2} \\ P_{z,o} &= \frac{P_o\tau_{rd}}{T_2} \frac{Q}{\rho \sin \alpha}.\end{aligned}\tag{2.27}$$

For both noble gas species $Q \ll \omega_{ss}T_2$. Defining the line quality factor as $Q_{line} = \gamma_{ng}B_zT_2$, and assuming the resonator is tuned close to the atomic Zeeman frequency, we can rewrite the expression for the steady-state maser frequency as

$$\omega_{ss} = \gamma_{ng}B_z - \frac{Q}{Q_{line}}(\gamma_{ng}B_z - \omega_o),\tag{2.28}$$

which is clearly the cavity-pulling frequency shift present in any generic active atomic oscillator [22]. Because $P_{z,0} \leq P_o$, the second of Equations 2.27 defines a threshold

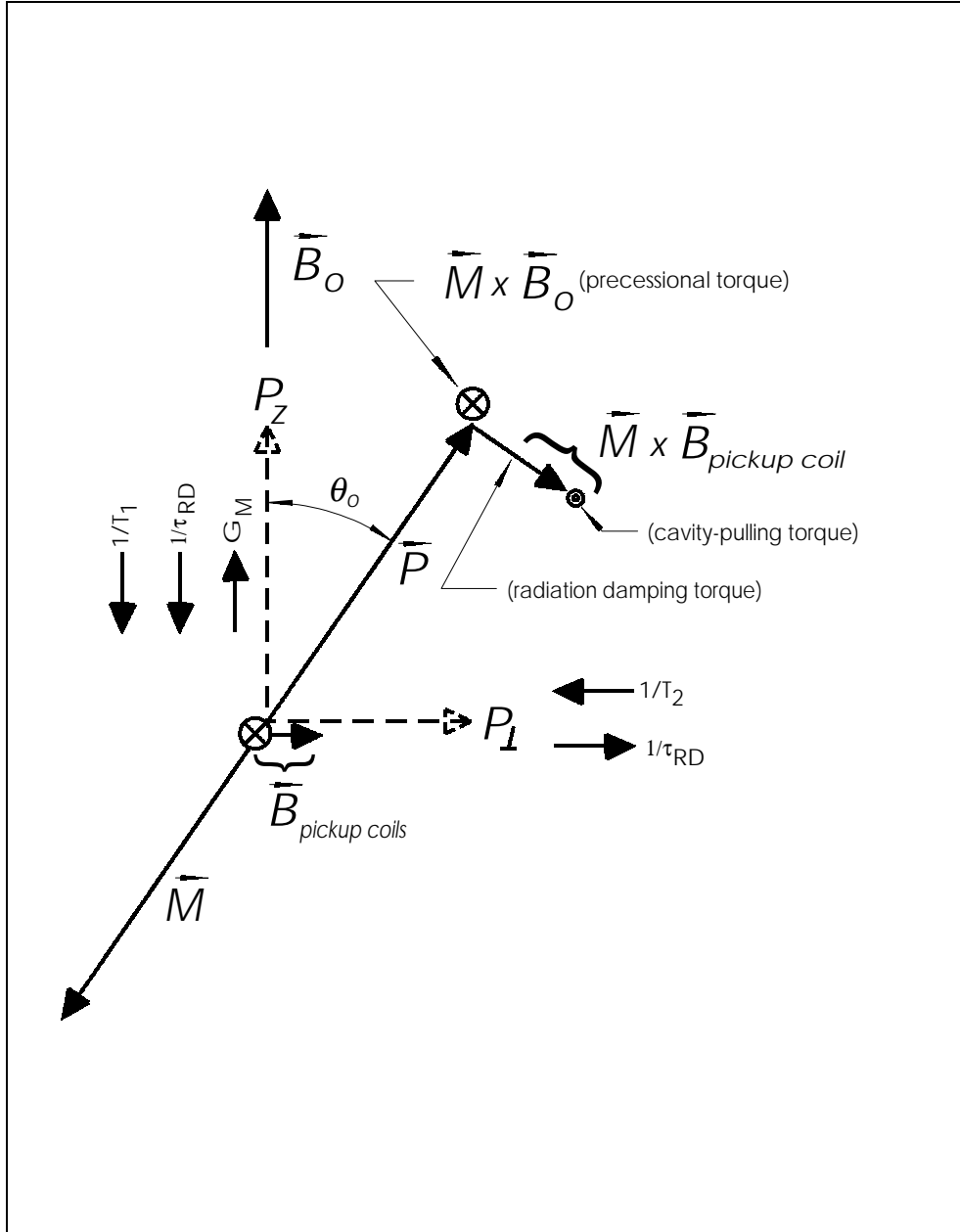


Figure 2.2: Zeeman maser polarization and magnetization vectors as seen in the frame rotating at the Larmor precession frequency. For both ^{129}Xe and ^3He the magnetization and polarization vectors are oppositely directed. P_z is replenished by diffusive loading and dissipated by wall loss, escape from the maser chamber, and radiation damping. P_\perp is replenished by radiation damping and destroyed by magnetic field gradients, wall loss, and escape from the interaction region. Also indicated is the cavity-pulling torque described in Equation 3.20.

condition for maser oscillation:

$$\tau_{rd} \leq T_2 \left(\frac{\rho \sin \alpha}{Q} \right). \quad (2.29)$$

If the maser is operated with the resonator tuned to $\omega_o = \omega_{ss}$, this condition reduces to the familiar form $\tau_{rd} \leq T_2$ [1].

Solving Equations 2.21 for $P_{\perp,o}$ and $P_{p,o}$ is done in Appendix A. The values are obtained easily but are somewhat unwieldy; also, linearized solutions for the coupled near-equilibrium oscillations of $P_p(t)$, $P_z(t)$, and $P_{\perp}(t)$ cannot be expressed in closed, analytic form. A great deal of insight into DNGM behavior can be gained, however, by ignoring polarization transport effects and proceeding as though the maser dynamics all occurred in a single bulb cell. As will be shown in Section 4.7, this approximation is quite good for the slowly diffusing ^{129}Xe species (transfer tube loss parameter $\beta \approx .4$; $T_1, T_2 < T_{storage}$) and quite poor for the rapidly diffusing ^3He species ($\beta \approx 1$; $T_2 \approx T_{storage} \ll T_1$). Without loss of insight we will also assume $\omega_{ss} = \omega_o$ until Section 2.6, in which we discuss frequency shift mechanisms in the DNGM. Under these approximations, the modified Bloch Equations 2.21 become [1]

$$\begin{aligned} \dot{P}_{\perp} &= \frac{P_z P_{\perp}}{P_o \tau_{rd}} - \frac{P_{\perp}}{T_2} \\ \dot{P}_z &= -\frac{P_{\perp}^2}{P_o \tau_{rd}} + \gamma_{se} P_{rb} - \left(\gamma_{se} + \frac{1}{T_1} \right) P_z. \end{aligned} \quad (2.30)$$

The equilibrium values for the polarizations are given by

$$\begin{aligned} P_{z,o} &= \frac{P_o \tau_{rd}}{T_2} \\ P_{\perp,o} &= \sqrt{P_o \tau_{rd} \left(\gamma_{se} P_{rb} - \frac{P_o \tau_{rd}}{T_2} \frac{1}{\gamma_{se} + 1/T_1} \right)} \end{aligned} \quad (2.31)$$

The second of these equations illustrates that all other parameters being held constant, increasing T_2 always increases the equilibrium maser amplitude (and hence output power). It should also be noted that with T_2 fixed, decreasing the radiation damping time τ_{rd} does not necessarily increase the maser output power.

Because many of the subsequent sections in this thesis refer to the near-equilibrium behavior of the maser polarizations, it is useful at this point to linearize Equations 2.30 about their equilibrium values. Before doing so, however, we can make some general statements about the relationships between near-equilibrium oscillations of the more complete set of Equations 2.21. Let us define small deviations of the dynamical variables from their equilibrium values via

$$\begin{aligned}\omega &= \omega_{ss} + \delta\omega(t) \\ P_{\perp} &= P_{\perp,o} + \delta P_{\perp}(t) \\ P_z &= P_{z,o} + \delta P_z(t).\end{aligned}\tag{2.32}$$

Plugging into Equations 2.21, neglecting terms higher than first order in the deviations, and using the steady state solutions, it is easy to show that

$$\begin{aligned}\delta\omega &= -\frac{\delta P_z}{P_o\tau_{rd}} \left(\frac{\rho}{Q} \cos \alpha \right) \\ \delta\dot{P}_{\perp} &= \left(\frac{P_{\perp,o}}{P_o\tau_{rd}} \frac{\rho}{Q} \sin \alpha \right) \cdot \delta P_z(t).\end{aligned}\tag{2.33}$$

We will return to Equations 2.33 in Section 2.6.

Linearization of the simplified Bloch Equations 2.30 yields

$$\delta\dot{P}_{\perp} = \left(\frac{P_{\perp,o}}{P_o\tau_{rd}} \right) \cdot \delta P_z(t)$$

$$\delta\dot{P}_z = -\left(2\frac{P_{\perp,o}}{P_o\tau_{rd}}\right)\delta P_{\perp} - \frac{\delta P_z}{\gamma_{se} + 1/T_1}. \quad (2.34)$$

The solutions for δP_{\perp} and δP_z for the simplified Bloch equations are thus exponentially damped sinusoids. The decay time and oscillation frequency are given by

$$\begin{aligned} \tau_{decay} &= \frac{1}{\gamma_{se} + 1/T_1} \\ \omega_{osc} &= \sqrt{2}\frac{P_{\perp,o}}{P_o\tau_{rd}}. \end{aligned} \quad (2.35)$$

In Chapter 4 we will experimentally probe the predictions of the simplified Bloch equations.

2.5 Characterizations of Stability

Section 2.6 presents frequency shift mechanisms in the DNGM; and most sections that follow describe the implementation and performance of maser subsystems in reference to how they affect the fundamental performance of the DNGM as a stable oscillator. It thus seems sensible to give at this point a brief summary of the laboratory realization of the DNGM data collection scheme (described in Section 3.7.7), and then develop in some detail the methodology by which DNGM phase and frequency data are used to characterize maser performance.

2.5.1 Extraction of Phase and Frequency Data

The maser output signals from an inductive pickup coil are buffered, amplified and sent to a pair of digital lockin detectors. Typical raw signal levels are ~ 3 to $5 \mu\text{V}$. All reference signals used in the DNGM are derived from the same hydrogen maser

clock, thus eliminating concerns about unmeasurable electronic phase shifts between the reference oscillators. Active feedback to the solenoid’s magnetic field locks the phase of one of the masers to that of a reference signal to isolate the experiment from common-mode systematic effects (such as stray magnetic field fluctuations) which would otherwise shift the frequencies of the noble gas masers. The effectiveness of the phase-lock loop and co-magnetometer system will be discussed in Section 3.6. Because both the LLI and EDM measurements performed with the DNGM are differential in nature, it is in principal possible to lock the solenoidal field using either species. In practice, the greater signal-to-noise of the ^{129}Xe channel favors locking this species and letting the ^3He free-run. Without loss of generality, the discussion that follows assumes this to be the case.

The in-quadrature and out-of-quadrature portions of each maser signal are recorded at regular intervals, typically once every four seconds. As with most heterodyne detection methods [45], these traces take the form

$$\begin{aligned} x(t) &= R \cos(2\pi\nu_b t + \phi_0) \\ y(t) &= R \sin(2\pi\nu_b t + \phi_0) \end{aligned} \tag{2.36}$$

where the maser amplitude is given by $R(t) = \sqrt{x(t)^2 + y(t)^2}$, and $\nu_b(t) = \nu_{ng}(t) - \nu_{ref}$ represents the beat frequency between the detected maser signal and the signal from the ultra-stable reference oscillator. Implicit in the time-dependence of the parameter $R(t)$ are the effects of noise and systematic drift. These effects are also implicit in $\nu_{ng}(t)$, whose time evolution is to be analyzed for evidence of signatures arising from EDM and LLI-violating interactions. The effects of noise processes and drift will be quantified in Section 2.6.1.

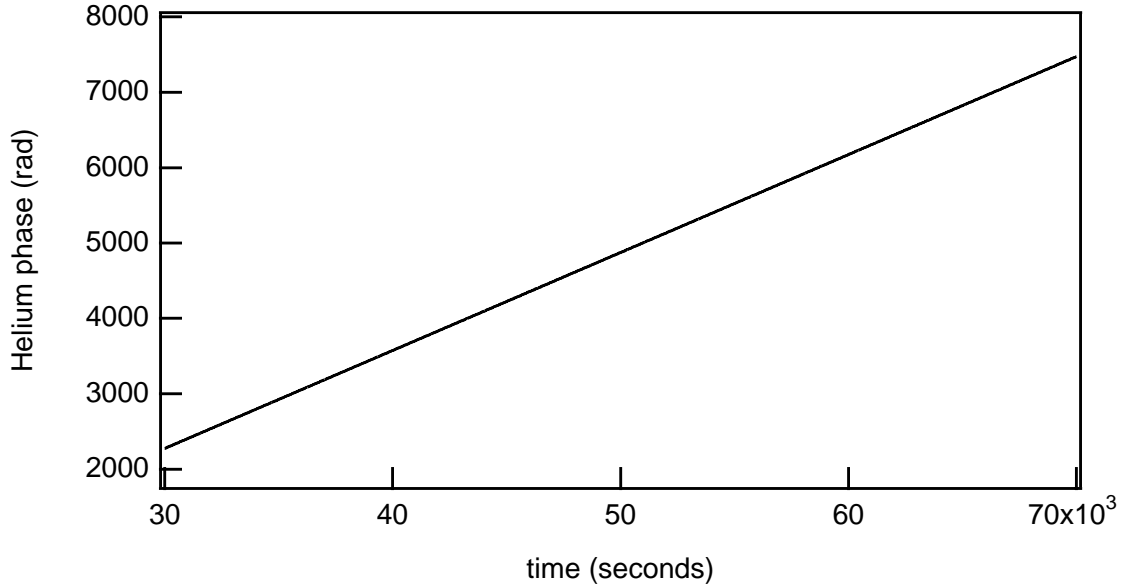


Figure 2.3: Phase evolution of the free-running ^3He maser over a 40,000 second timescale. The 25 mHz beat-note evolution makes noise and systematic fluctuations, as well as possible new physics, visually unresolvable. Cell SE3, May 2000.

The phase evolution of each maser, from which its frequency dependence can be derived,⁸ is given by

$$\phi(t) = \text{arctangent} \left(\frac{y(t)}{x(t)} \right) = 2\pi\nu_b t + \phi_0 \quad (2.37)$$

The beat frequency of the free-running ^3He maser is typically adjusted to be $\simeq 25$ mHz. Because variations in the free-running frequency are $\leq 1 \mu\text{Hz}$ on timescales ≥ 1000 seconds, visual inspection of maser phase traces is most instructive following a linear regression which removes the (relatively) rapid beat-note evolution. Figures 2.3 and 2.4 show the phase evolution of the free-running ^3He maser over a 40,000 second timescale.

⁸In [46] Stein writes: “It has been suggested that measurement techniques for frequency and time constitute a hierarchy (Allan and Daams, 1975), with the measurement of the total phase of the oscillator at the peak ... The total phase has this status owing to the fact that all other quantities can be derived from it.”

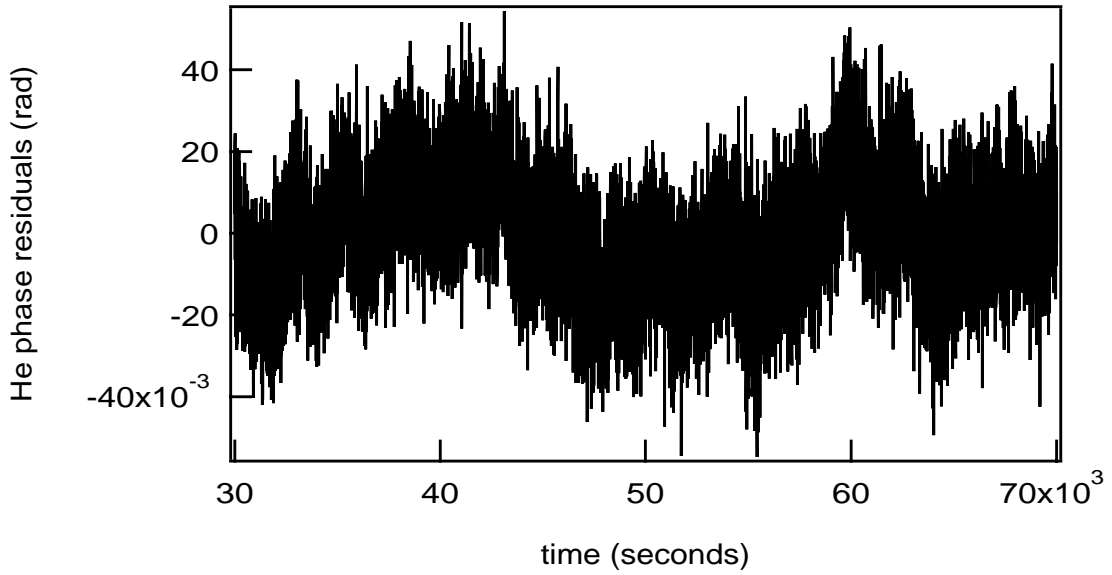


Figure 2.4: Linear regression has removed the (relatively) rapid linear evolution from the free-running ^3He phase trace shown in Figure 2.3. Clearly visible now are manifestations of phase noise, frequency noise, and other systematic drift effects. Cell SE3, May 2000.

Short-term maser phase noise is assessed by computing the RMS deviation of the residual phase data after least-squares regression has removed the dominant, linear evolution (see Figure 2.5). This figure of merit is typically established on timescales between 500 and 1,000 seconds, and will be written as σ_ϕ in subsequent sections and chapters.

From oscillator phase data (Equation 2.37), it is possible to produce over a time interval τ a minimum variance estimate of the oscillator frequency. Reference [47] explores several different frequency estimation methods. The method applied to the DNGM phase data is perhaps the most common. All detected phase points are assumed to have the same error σ_ϕ , and the phase data are fit to a function of a form

$$\phi(t) = c_0 + c_1 t \quad (2.38)$$

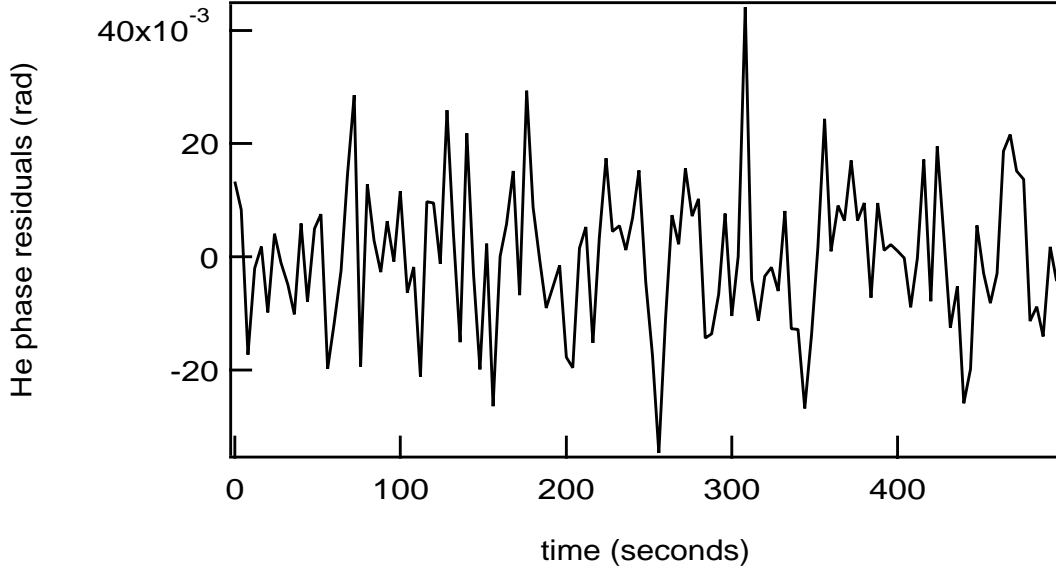


Figure 2.5: Typical short-term ^3He phase residuals after least squares regression has removed the linear beat-note evolution. The ^3He phase noise is given by $\sigma_\phi \approx 10$ mrad. Data taken from cell SE3, May 2000.

In the limit $N \gg 1$, the maser frequency over the interval τ is given by

$$\nu(\tau) = \frac{c_1}{2\pi} = \frac{12}{2\pi\tau^2 N^2} \left(N \sum_{i=1}^N \phi_i t_i - \sum_{i=1}^N \phi_i \sum_{i=1}^N t_i \right). \quad (2.39)$$

The statistical error in the estimated value of c_1 reflects the contribution of phase noise to the uncertainty in frequency, and is given by

$$\sigma_\nu^2(\tau) = \frac{12\sigma_\phi^2}{(2\pi)^2 N \tau^2} \quad (2.40)$$

where $N \gg 1$ is the number of points in the fitting range. For a constant data sampling rate, $N \sim \tau$, and for a fixed level of white phase noise $\sigma(\phi) = \sigma_\phi$ (see Section 2.6.1 and Table 2.3), $\sigma(\tau) \propto \tau^{-3/2}$, and uncertainties due to phase noise average away rapidly with increasing τ .

A proper measure of the frequency stability of a clock or oscillator must incorporate the effects of frequency as well as phase noise processes [46]. We used the Allan (or two-sample) deviation, one of two measures recommended by the IEEE, to assess the quality of DNGM frequency data. To compute the Allan deviation, a stream of phase data of total duration T_0 is divided into m adjacent intervals, each of length $\tau = \frac{T_0}{m}$. The best frequency estimate ν_i is extracted for each interval, and a set of $(m - 1)$ difference frequencies is formed:

$$y_i(\tau) = \nu_{i+1}(\tau) - \nu_i(\tau) \tag{2.41}$$

The Allan deviation is then the RMS spread in the points $\{y_i\}$, divided by $\sqrt{2}$ to correct for cross-correlations between adjacent $\{y_i\}$:

$$\sigma_{Allan}(\tau) = \frac{\sigma_y(\tau)}{\sqrt{2}} \tag{2.42}$$

2.6 Frequency Stability of the DNGM

In [22] Jacques Vanier and Claude Audoin present a thorough discussion of noise processes that affect the frequency measurement precision of devices such as the DNGM. We now describe the primary sources of frequency and phase noise in the DNGM, typical measurements of the DNGM’s frequency stability, and likely causes of systematic frequency variations.

2.6.1 Thermal Noise Limits to Frequency Stability

Even under ideal operating conditions, the DNGM frequency resolution is fundamentally limited by two independent manifestations of thermal noise: white frequency

noise, and added white phase noise.

White frequency noise is caused by thermal radiation inducing a random walk in time of the phase of the coherent electromagnetic field produced by each noble gas maser.⁹ The limit on frequency stability arising from the effects of white frequency noise is given by:

$$\Delta\nu_{freq} = \frac{1}{\pi T_2} \sqrt{\frac{k_B T}{2W_{ng}\tau}} \propto \tau^{-1/2}, \quad (2.43)$$

where T_2 is the transverse decoherence time of the atomic ensemble in the absence of masing, T is the temperature of the masing region in degrees Kelvin, and W_{ng} is the steady state radiated maser power.

The second form of thermal noise, added white phase noise, arises from the external amplification of the maser signals. The signal amplifiers multiply thermal noise present in the resonant signal detection circuits, and also add noise due to their own finite temperature. The frequency deviation due to this added white phase noise is given by

$$\Delta\nu_{phase} = \frac{1}{2\pi\tau} \sqrt{\frac{k_B(T_{coil} + T_{amp})B}{W_{ng}}} \propto \tau^{-3/2}, \quad (2.44)$$

where $B \approx (\pi\tau)^{-1}$ is the measurement bandwidth and T_{coil} and T_{amp} are the pickup coil and amplifier noise temperatures, respectively.

For typical operational parameters (listed in Tables 1.1, 1.2, and 1.3), the calculated limits on DNGM performance due to these two thermal noise processes are given by

$${}^3He : \quad \Delta\nu_{freq} \approx 9 \times 10^{-7} \tau^{-1/2}$$

⁹Other intrinsic frequency noise processes in the DNGM arise from unstable collisional and wall-induced shifts as well as imperfect operation of the magnetic field lock loop [1]. An accurate model that predicts the size of such effects has not yet been completed.

$$\begin{aligned}
& \Delta\nu_{phase} \approx 4 \times 10^{-4} \tau^{-3/2} \\
^{129}\text{Xe} : & \quad \Delta\nu_{freq} \approx 2 \times 10^{-7} \tau^{-1/2} \\
& \Delta\nu_{phase} \approx 2 \times 10^{-4} \tau^{-3/2} \tag{2.45}
\end{aligned}$$

For the phase measurement technique we employ with the DNGM,¹⁰ $B = (\pi\tau)^{-1}$ is given by the data analysis software, and thus the “cross-over” time at which the contributions of thermal white phase and white frequency noise become equal is a function of T_2 only:

$$\tau_{cross} = T_2 / \sqrt{\pi}, \tag{2.46}$$

where we have assumed $T_{coil} = T_{amp}$.

These thermal noise sources place intrinsic limits on the sensitivity of any frequency measurement made with the DNGM. For example, using the stability numbers given in Equations 2.44 and 2.45 (instability in the phase-locked species also affects the measured free-running frequency), a 60 day search for sidereal variations in the frequency of the free-running ^3He maser would yield a sensitivity to LLI-violating interactions of the neutron corresponding to $\Delta\nu_{he} \approx 1$ nHz; this is approximately $40\times$ better than the limit of ~ 40 nHz reported in this thesis. For an EDM search in ^{129}Xe , the two above thermal noise sources limit the net ^{129}Xe maser frequency measurement precision in a 10,000 second observation interval to be $\Delta\nu_{xe} \approx 3.8$ nHz. Making two consecutive such measurements with the applied electric field set at values of ± 2.5 kV/cm, the two-standard-deviation sensitivity to a ^{129}Xe EDM would be $\approx 3.2 \times 10^{-27}$ e-cm, in 2×10^4 seconds of data taking. If 250 of these EDM measurements were made, one would have $\Delta\nu_{xe} \approx 480$ pHz and

¹⁰The frequency stability of atomic clocks and other stable oscillators is often determined by measuring the beat period ($= \nu_b^{-1}$) as a function of time [22]. This technique uses a fixed bandwidth $\geq \nu_b$, implying that $\Delta\nu_{phase} \sim \tau^{-1}$.

μ	<i>Designation</i>
-1.5	White noise of phase
-1	Flicker noise of phase
-.5	White noise of frequency
0	Flicker noise of frequency
.5	Random walk of frequency

Table 2.3: Common designations for the noise processes associated with values of μ in the expression $\sigma(\tau) \propto \tau^\mu$. In systems like the DNGM, the software bandwidth scales inversely with averaging time τ , which allows differentiation between white noise of phase and flicker noise of phase.

a two-standard-deviation ^{129}Xe EDM sensitivity $\approx 2 \times 10^{-28}$ e-cm, in 1400 hours of data taking. From these estimates one concludes that the DNGM has not yet been developed to the point where its performance is limited by fundamental thermal noise.

2.6.2 Measured DNGM Frequency Stability

Figure 2.6 shows a plot of the Allan deviation of a generic precision oscillator as a function of measurement interval: $\sigma(\tau) \propto \tau^\mu$. Shown for each regime are typical values of the exponent μ . Table 2.3 associates with each value of μ its common designation in the literature [22, 46].

A typical plot of the measured Allan deviation for an early and current configuration of the DNGM is shown in Figure 2.7. System engineering has improved the frequency stability of the DNGM by an order of magnitude over the past three years for measurement intervals $\sim 1 - 3$ hours [3]; nevertheless, the frequency resolution of the DNGM is still limited by systematic sources of phase and frequency noise that are not thermal in origin. In the next section we outline leading candidates for such systematic effects. In Chapter 3 we describe the optical, thermal and magnetic

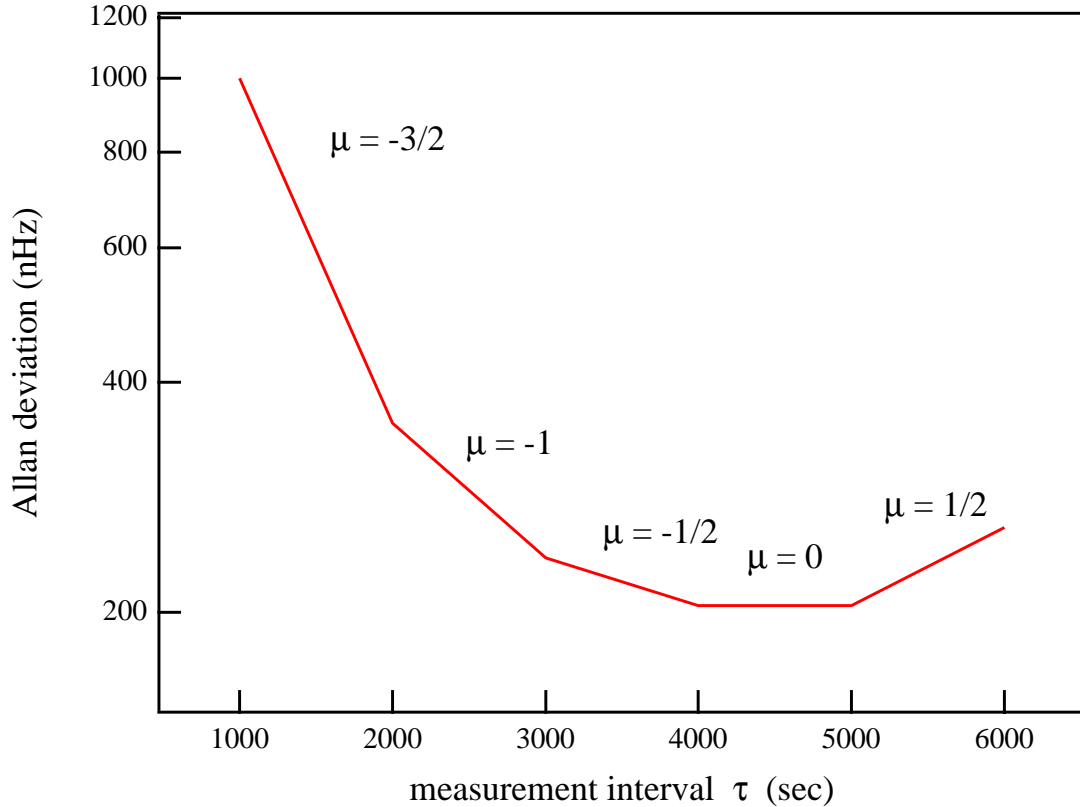


Figure 2.6: The Allan deviation of a generic precision oscillator as a function of τ [22]. Shown are typical values of the exponent μ in the expression $\sigma(\tau) \propto \tau^\mu$.

field control systems we have implemented to minimize these sources of frequency instability.

2.6.3 Systematic Limits to Frequency Stability

Calculations and measurements indicate that the three most important sources of systematic maser frequency deviation are: (i) variation of the magnetic fields created by longitudinal ^3He and ^{129}Xe magnetizations; (ii) imperfect co-magnetometry due to changes in the transverse polarization distributions of the maser ensembles; and (iii) blown-air induced noise, which contributes measurably to maser phase noise

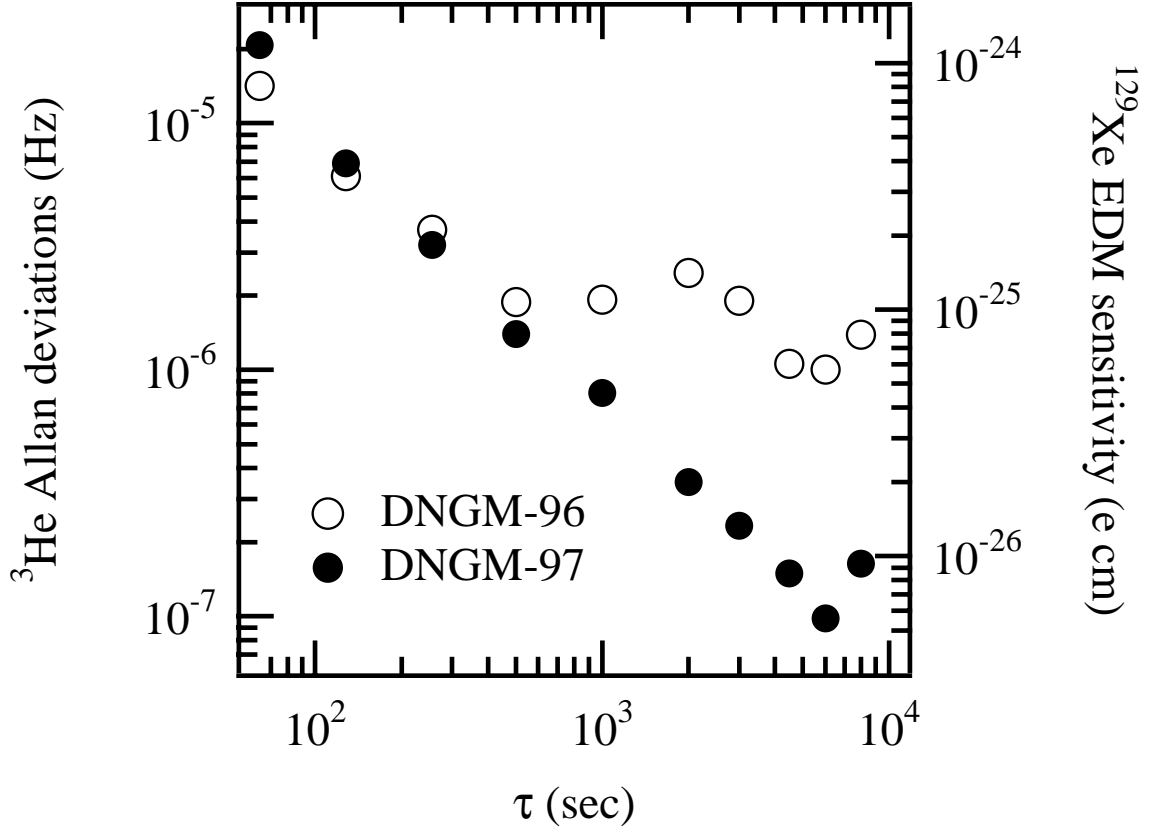


Figure 2.7: Example of the free-running ^3He maser Allan deviation as a function of measurement interval for typical DNGM runs of $\approx 50,000$ seconds. The DNGM-96 data are from an early configuration of the DNGM for which systematic variation set an Allan deviation floor of $\sim 1 \mu\text{Hz}$. The DNGM-97 data are from the current configuration of the experiment: upgrades in system engineering and environmental control improved the Allan deviation to $\sim 100 - 300 \text{ nHz}$ for measurement intervals beyond about 4,000 seconds. The right ordinate axis gives the ^{129}Xe EDM sensitivity that would result from the plotted ^3He maser Allan deviation and an electric field of $\pm 5 \text{ kV/cm}$ applied across the maser chamber.

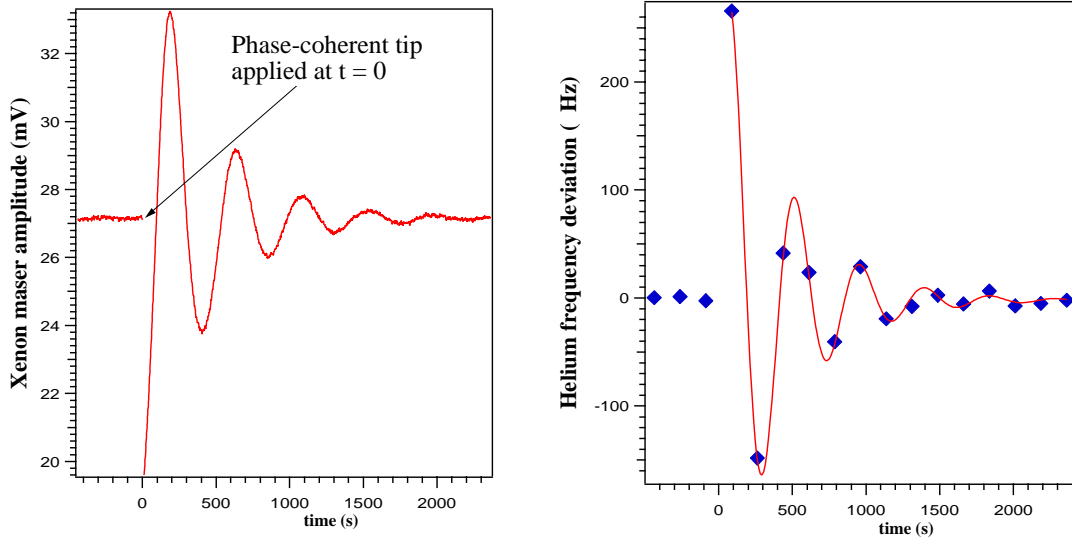


Figure 2.8: Figure showing the cumulative effect of short-term polarization dependent frequency shifts. The ^{129}Xe maser was perturbed with an on-resonant Rabi pulse at $t = 0$ to create an unmistakably observable variation in both the ^{129}Xe maser amplitude and ^3He maser frequency. Note that the displayed ^{129}Xe P_{\perp} oscillations are related to ^{129}Xe P_z oscillations as described by Equations 2.33.

and hence to short-term frequency instability. In particular, we have observed maser frequency variations that are strongly correlated to maser amplitude changes. These can result from P_z -proportional dipolar field shifts and imperfect magnetometry as described below. Sorting out the individual contributions has thus far proven intractable. We present two figures illustrating the cumulative effect, both for short-term oscillations of P_{\perp} (Figure 2.8), which in turn is related to P_z oscillations as described by the Bloch model of Chapter 2, and long-term drift of P_{\perp} (Figure 2.9).

We also discuss below four additional frequency shift mechanisms that are commonly addressed in the literature [20, 36] and thus merit consideration. We will show, however, that these effects do not limit the frequency stability of the DNGM as it is currently configured. Note that in order to keep this chapter generally applicable to the DNGM, we have deferred to Section 3.6 discussion of leakage current

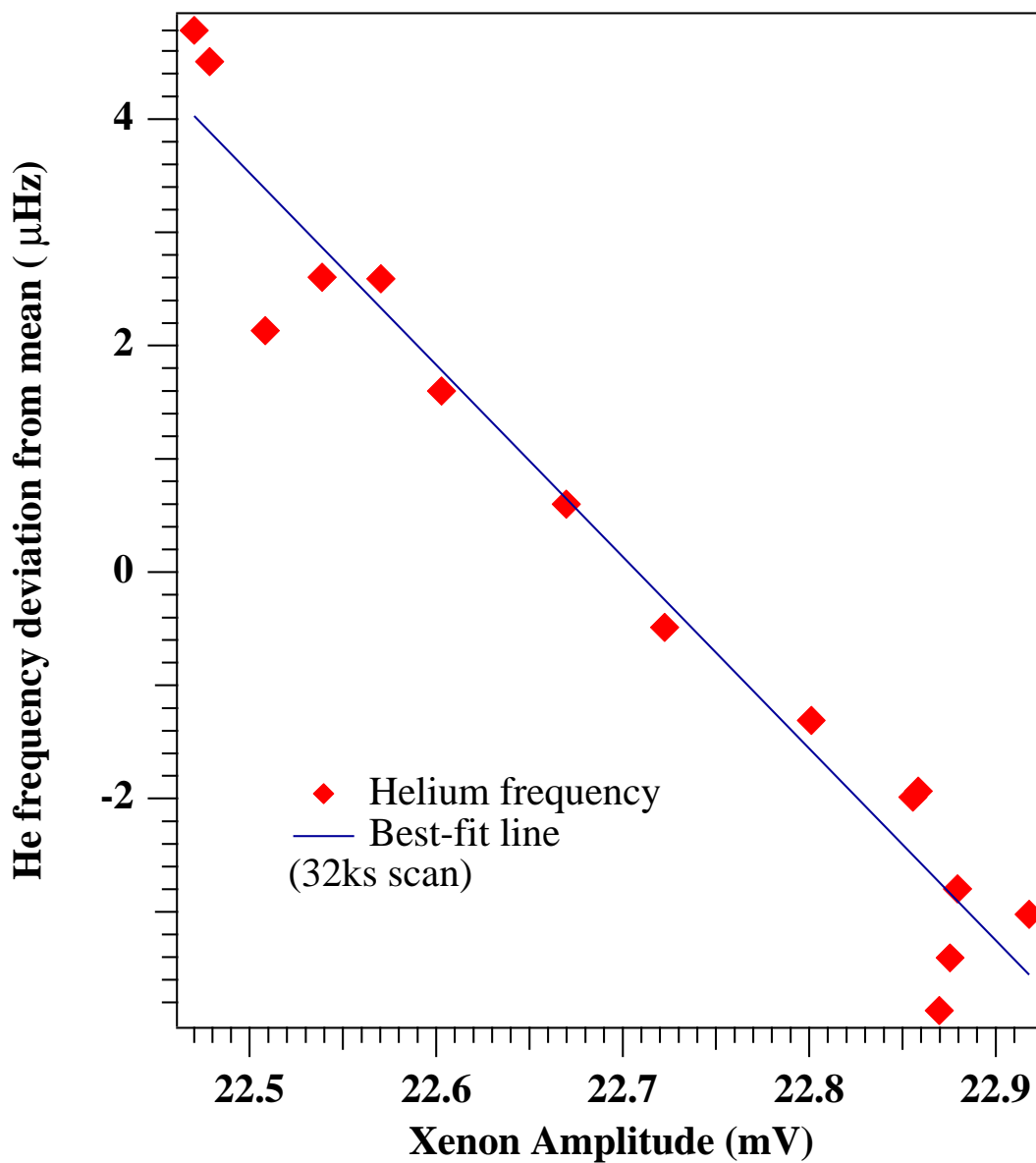


Figure 2.9: Figure showing the cumulative effect of long-term polarization dependent frequency drift. Note that the displayed ^{129}Xe maser amplitude drift (i.e., $^{129}\text{Xe } P_{\perp}$ drift) is related to P_z drift as described by Equations 2.33.

frequency shifts, which are important only for the search for a ^{129}Xe permanent electric dipole moment (EDM).

Polarized Rb frequency shifts

Schaefer [48] describes the shift of noble gas Zeeman frequencies induced by polarized Rb atoms (the collisional contact shift and the bulk Rb magnetization shift). In a spherical cell (we will use this approximation for the cylindrical maser chamber) this shift takes the form

$$2\pi \cdot \delta\nu_{ng} = (\kappa_{ng} - 1)\gamma_{ng} \cdot \frac{8\pi}{3}\hbar\gamma_{rb}[Rb]P_{rb}, \quad (2.47)$$

where $[Rb]$ is the Rb number density in the maser bulb, γ_{rb} and γ_{ng} are the Rb and noble gas gyromagnetic ratios, P_{rb} is the average longitudinal Rb polarization in the maser bulb, and κ_{ng} is the contact shift enhancement factor: $\kappa_{xe} \approx 726$ and $\kappa_{he} \approx 5.0$ [48].

In the maser bulb $T_m \approx 41$ °C, and $[Rb] \approx 8 \times 10^{10}$ cm $^{-3}$. This yields shifts in the maser bulb given by $\delta\nu_{he} \approx (190 \mu\text{Hz})P_{rb}$ and $\delta\nu_{xe} \approx (10 \text{ mHz})P_{rb}$. P_{rb} in the maser chamber is due almost entirely to Rb repolarization via spin-exchange with polarized ^{129}Xe atoms [20, 36]. Numerical estimates performed in our laboratory indicate $P_{rb} < .0001$ in the maser chamber. Limits on noble gas frequency shifts are thus given by $\delta\nu_{he} < 19$ nHz and $\delta\nu_{xe} < 1$ μHz . Assuming an RMS temperature stability of ~ 10 mK in the maser chamber, $[Rb]$ will have a fractional stability of $\sim .1\%$. Similarly, the noble gas polarizations in the maser bulb which contribute to P_{rb} are stable to $\sim .1\%$ over a typical DNGM run. The estimated bounds on DNGM frequency instability due to polarized Rb atoms in the maser bulb are thus $\delta\nu_{he} < 19$ pHz and $\delta\nu_{xe} < 1$ nHz, or well below the limits set by other sources of

frequency instability.

Off-resonant magnetic field frequency shifts

In [49] Ramsey shows that the Larmor precession frequency of an atom may be shifted in the presence of a magnetic field rotating a rate different from the Larmor precession frequency. Therefore, in the DNGM, the ^3He maser's magnetic field can shift the ^{129}Xe maser frequency and vice versa. This shift takes the form

$$\delta\nu_{ng} \approx \frac{(\gamma_{ng}B_{\perp})^2}{8\pi^2(\nu_{ng} - \nu_{\perp})}, \quad (2.48)$$

where γ_{ng} is the noble gas gyromagnetic ratio, ν_{ng} is the Larmor precession frequency of that same species, and B_{\perp} and ν_{\perp} are the magnitude and frequency of the non-resonant magnetic field created by the other species.

In the DNGM, numerical estimates for B_{\perp} are $B_{\perp,he} \sim 100$ nG and $B_{\perp,xg} \sim 1000$ nG. In its present configuration, the DNGM is operated with $\nu_{xe} \sim 1.7$ kHz and $\nu_{he} \sim 4.7$ kHz. This results in frequency shifts of $|\delta\nu_{xe}| \sim 2 \times 10^{-9}$ Hz and $|\delta\nu_{he}| \sim 2 \times 10^{-12}$ Hz. The temporal stability of such shifts is clearly not a concern for the measurements reported in this thesis.

Static magnetic field gradient frequency shifts

In [50] Cates et al. show that Zeeman frequency shifts can arise from the presence of static magnetic field gradients. To approximate the size of such shifts in the DNGM, we take the expression for a spherical cell:

$$\delta\nu \approx \frac{\gamma_{ng}a^2}{20\pi} \frac{|\nabla B_x|^2 + |\nabla B_y|^2}{B_z}, \quad (2.49)$$

where γ_{ng} is the noble gas gyromagnetic ratio and a is the cell radius. In Section 3.5.3 we estimate $\nabla B_z \sim 20 \mu\text{G}/\text{cm}$. The gradients appearing in Equation 2.49 must also include the effects of noble gas induced field gradients (Section 3.5.6). Assuming that $|\nabla B_x| \sim |\nabla B_y| \sim 20 \mu\text{G}/\text{cm}$, we obtain $\delta\nu_{xe} \sim 34 \text{ nHz}$ and $\delta\nu_{he} \sim 94 \text{ nHz}$ for $a \approx 2 \text{ cm}$.

If we conservatively assume a temporal stability of 1% for the ratio of magnetic field quantities in Equation 2.49, the resultant maser frequency instabilities are $\delta\nu_{xe} \sim .34 \text{ nHz}$ and $\delta\nu_{he} \sim .94 \text{ nHz}$, which are well below the present performance of the DNGM. We note further that the above shifts scale as γ_{ng} and thus should be largely nulled-out by the magnetic field phase-lock loop.

Cavity-pulling frequency shifts

Good temperature control of the DNGM signal detection circuits is needed to prevent significant variations in the cavity pulling of the the maser frequencies (see Equation 3.20). As will be shown in Section 3.7.5, the present level of resonator temperature control is sufficient to prevent cavity-pulling from being an appreciable source of frequency instability in the DNGM.

P_z -proportional frequency shifts

The noble gas maser frequencies are shifted by the static magnetic fields created by longitudinal magnetizations of the ^3He and ^{129}Xe ensembles, which are proportional to their longitudinal polarizations (P_z). The magnitudes of the magnetic fields due to the longitudinal ^3He and ^{129}Xe magnetizations are $\sim 100 \text{ nG}$ for the present configuration of the DNGM. A 1% change in P_z can thus shift the ^{129}Xe frequency by $\sim 4 \mu\text{Hz}$ and the ^3He frequency by $\sim 11 \mu\text{Hz}$. For active maser oscillation, the steady-state longitudinal magnetizations of the atomic ensembles depend directly

on system parameters such as the characteristics of the dual resonator system and the flux of polarized atoms into the interaction region, as set by the pump laser power, atomic densities, and system temperature and geometry.

Thus stabilization of the longitudinal ^3He and ^{129}Xe magnetizations translates practically into: (i) stabilization of the DNGM’s resonator circuitry by proper construction techniques, choice of components, and temperature control (see Section 3.7.5); (ii) stabilization of the gas densities and diffusion via good design and construction of the oven assembly and blown air system (see Sections 3.2 and 3.3); and (iii) control of the on- and off-resonant power of the laser diode array (see Section 3.4.3). In practice, the various control systems in the DNGM do not operate ideally. We estimate there are P_z variations of $\sim 1 - 5$ parts in 10^4 over timescales ~ 1 hour, which will induce free-running ^3He maser frequency instability of $\sim 100 - 500$ nHz. Data analysis can account partially but not entirely for these drift effects (see Chapters 5 and 6), because P_z -induced drifts that have a component parallel to the exotic physics under consideration cannot be subtracted from DNGM phase (or frequency) data.

P_\perp -proportional frequency shifts

Variations in the transverse polarization distributions of the masing ensembles can affect the DNGM’s co-magnetometry and thereby induce frequency instability in the free-running maser. This effect is described in detail in Section 3.6 and Appendix A. We summarize the discussion here.

The effective Larmor frequency of a noble gas maser is given by

$$2\pi\nu_{ng} = \frac{\int \gamma_{ng}\eta(\mathbf{r})B_z(\mathbf{r})P_\perp(\mathbf{r})dV}{\int \eta(\mathbf{r})P_\perp(\mathbf{r})dV}, \quad (2.50)$$

which is proportional to the volume average of the total longitudinal magnetic field (from all sources), weighted by the transverse polarization distribution of the masing ensemble and the pickup coil filling factor. Even a small change of $2 \mu\text{m}$ in the “center of ensemble” position of the P_{\perp} distribution would induce a $\sim 1 \mu\text{Hz}$ frequency shift for typical DNGM parameters and B_z gradients. Such “center of ensemble” shifts occur in a 2-bulb noble gas maser system when there is a change in the flux of polarized noble gas atoms into the interaction region. The shifts are larger for a smaller diffusion constant and a larger wall loss rate, so that they would be larger for a ^{129}Xe maser than for a ^3He maser. Nevertheless, shifts on either species will induce frequency instability on the free-running maser.

Blown-air induced noise

Temperature control of the DNGM is maintained by a blown-air heating system, as described in Section 3.3. A minimum total flow rate of $\approx 45 - 50 \text{ slm}$ is required to maintain reasonable ($\approx 10 \text{ mK}$) temperature control of the pump, maser, and external resonator regions. Increasing the flow rate decreases the thermal time constants and permits better temperature control, but vibrational excitations of the pickup coil, external resonator, and oven and cell components increase the phase noise and hence degrade the frequency stability of the DNGM. Table 2.4 gives measured RMS phase noise residuals for the phase-locked ^{129}Xe maser and free-running ^3He maser at three different total flow rates (DNGM-15, page 20). A careful study of the DNGM frequency stability as a function of air flow rates has not yet been performed.

Flow rate (slm)	$\sigma_{\phi,xe}$ rad	$\sigma_{\phi,he}$ rad
60	.000320	.00836
50	.000296	.008188
40	.0002397	.00682

Table 2.4: RMS phase noise residuals for the phase-locked ^{129}Xe maser and free-running ^3He maser at three different total flow rates (DNGM-15, page 20).

Chapter 3

Experimental Realization

Chapters 1 and 2 of this thesis have provided an overview of the DNGM experiment as well as a description of the theory of two-species Zeeman masers. This chapter describes the fabrication and experimental implementation of the major DNGM subsystems, depicted schematically in Figure 3.1. A photograph of the DNGM laboratory is shown in Figure 3.2.

3.1 Cells

The mixture of ^{129}Xe , ^3He , and N_2 gases and Rb metal used in the DNGM is contained in a two-chambered cell (Figure 3.3) blown from Corning 7056 borosilicate glass.¹ Each cell consists of a roughly spherical pump chamber (optical pumping region) joined by a straight transfer tube to a roughly cylindrical maser chamber (interaction region). In EDM cells, molybdenum discs epoxied to the ends of the maser chamber seal the cell and serve as the high voltage electrodes used in the EDM measurement described in Chapter 6 of this thesis. This section describes

¹Good cells have also been produced from Corning 7052 glass.

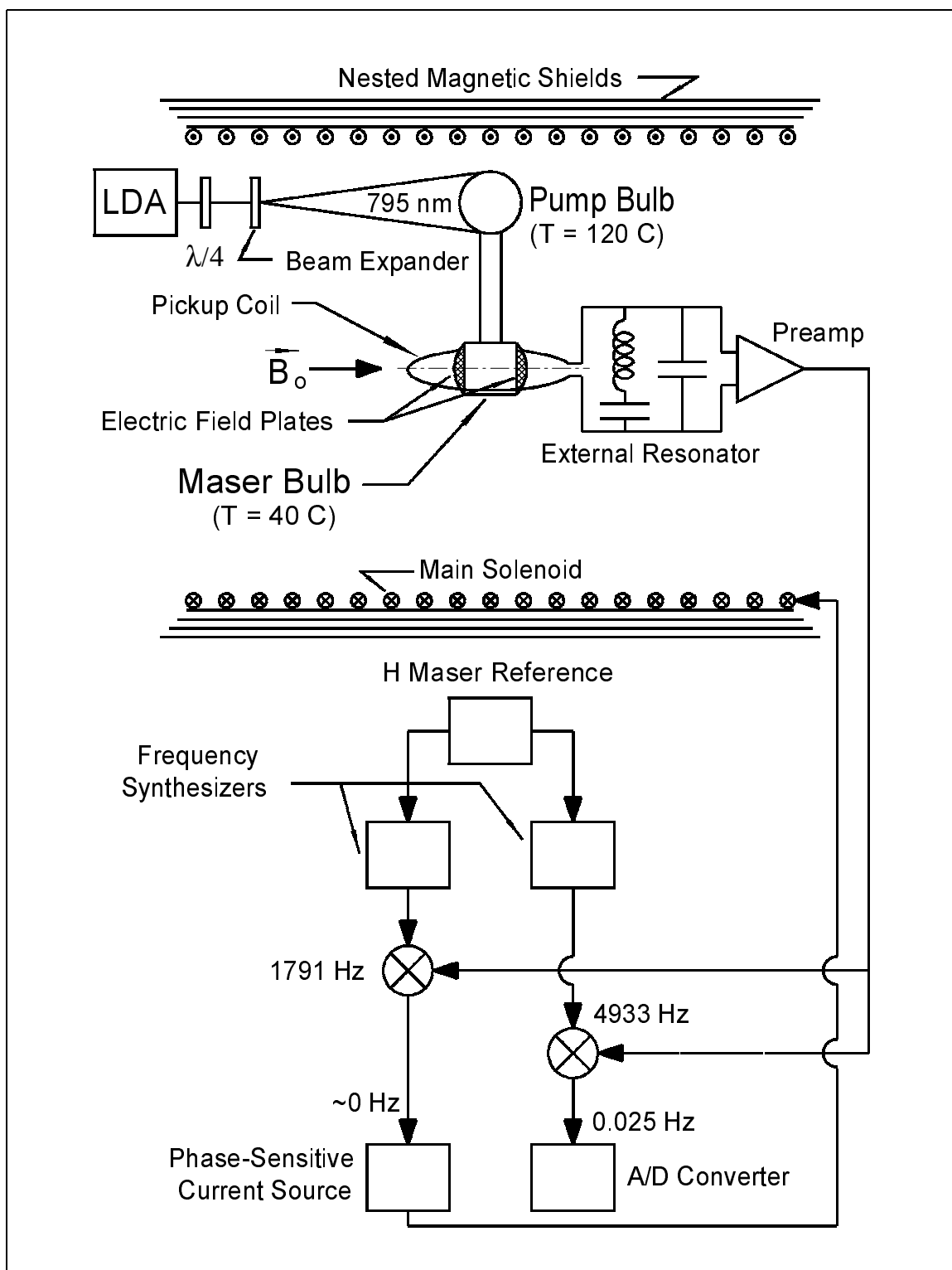


Figure 3.1: Schematic diagram of the dual noble gas maser used to make the measurements reported in this thesis.

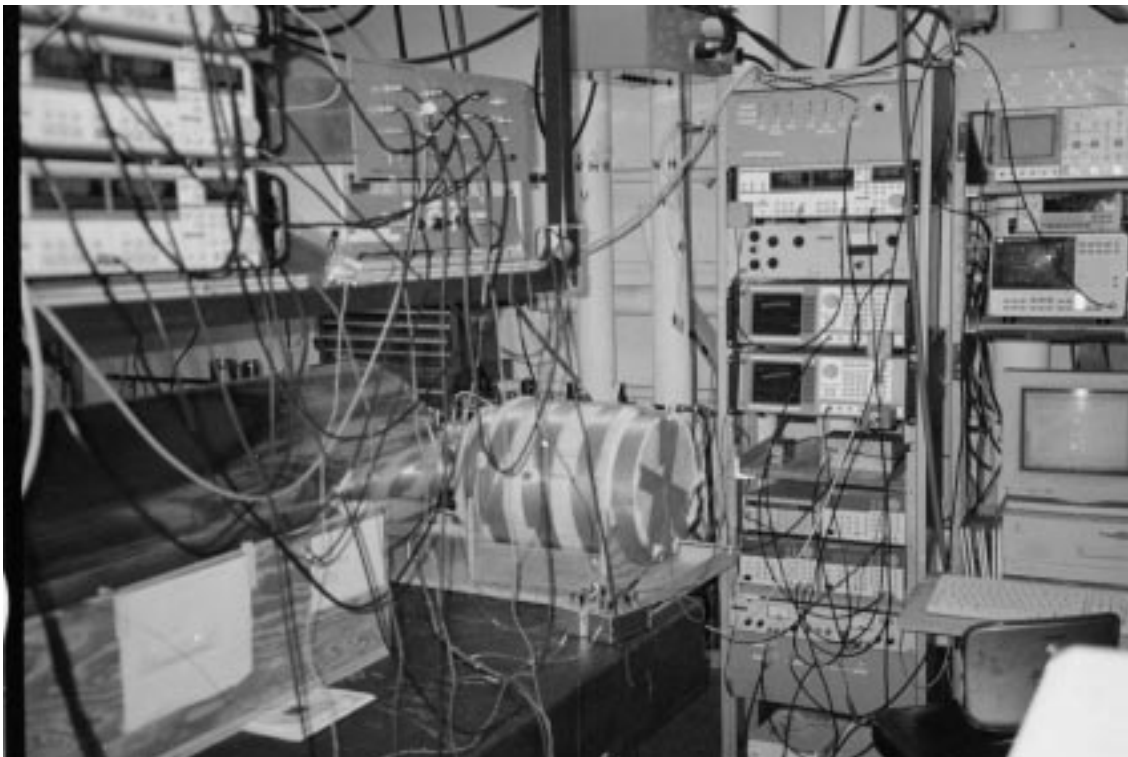


Figure 3.2: A photograph of the DNGM laboratory, circa 1997. Pictured are the magnetic shield and solenoid assembly, the heavily insulated external resonator assembly, many of the lockin amplifiers and function generators used in the experiment, and custom-built control electronics.

the cell making process and concludes with a brief discussion on cell aging. Table 3.1 lists the gas fill pressures (at 298 K) for the cells used to make measurements reported in this thesis. Table 3.2 lists the cell dimensions.

3.1.1 Cell cleaning, coating and endplate attachment

Cells are generally prepared in groups of three from a manifold such as that shown in Figure 3.3. In order to reduce the rate of nuclear spin relaxation caused by interactions of the ^{129}Xe nuclei with magnetic impurity sites on the glass walls, the cells are coated with $\text{CH}_3-(\text{CH}_2)_{17}-\text{SiCl}_3$, otherwise referred to as octadecyltrichlorosilane, or

Cell	P_{xe} (Torr)	P_{he} (Torr)	P_{nit} (Torr)
37 – glass	186	2059	77
S1 – glass	99	1158	80
S3 – glass	107	1265	59
E9 – EDM	210	2411	97
SE3 – EDM	110	1100	80

Table 3.1: Gas fill pressures (at 298 K) for the cells used to make measurements reported in this thesis.

Cell	t-tube length (in.)	t-tube i.d. (in.)	maser bulb length (in.)	maser bulb i.d. (in.)
37 – glass	1.62	.133	.890	.468
S1 – glass	1.66	.093	.820	.468
S3 – glass	1.66	.093	.870	.468
E9 – EDM	1.60	.133	.880	.468
SE3 – EDM	1.53	.093	.890	.468

Table 3.2: Dimensions of the cells used to make measurements reported in this thesis. Each cell had a cylindrical maser chamber and a spherical pump bulb with outer diameter 3/4 inches.

OTS. A properly formed coating consists of a covalently bonded monolayer of OTS molecules, each oriented perpendicular to the glass surface. The coating decreases the mean sticking time of the ^{129}Xe atoms to the cell walls and also increases the mean distance of closest approach of the atoms to paramagnetic impurities on the borosilicate surface [51, 52]. A good coating will last indefinitely as long the cell is run at temperatures below 190 °C [20], a limit which is safely removed from the ~ 114 °C operating temperature of the DNGM. The longitudinal relaxation time T_1 of the ^3He atoms is unchanged by the presence (or absence) of the OTS coating, although a burned or damaged coating will negatively impact the T_1 of both noble gas species. The cell coating procedure which follows is based in large part upon

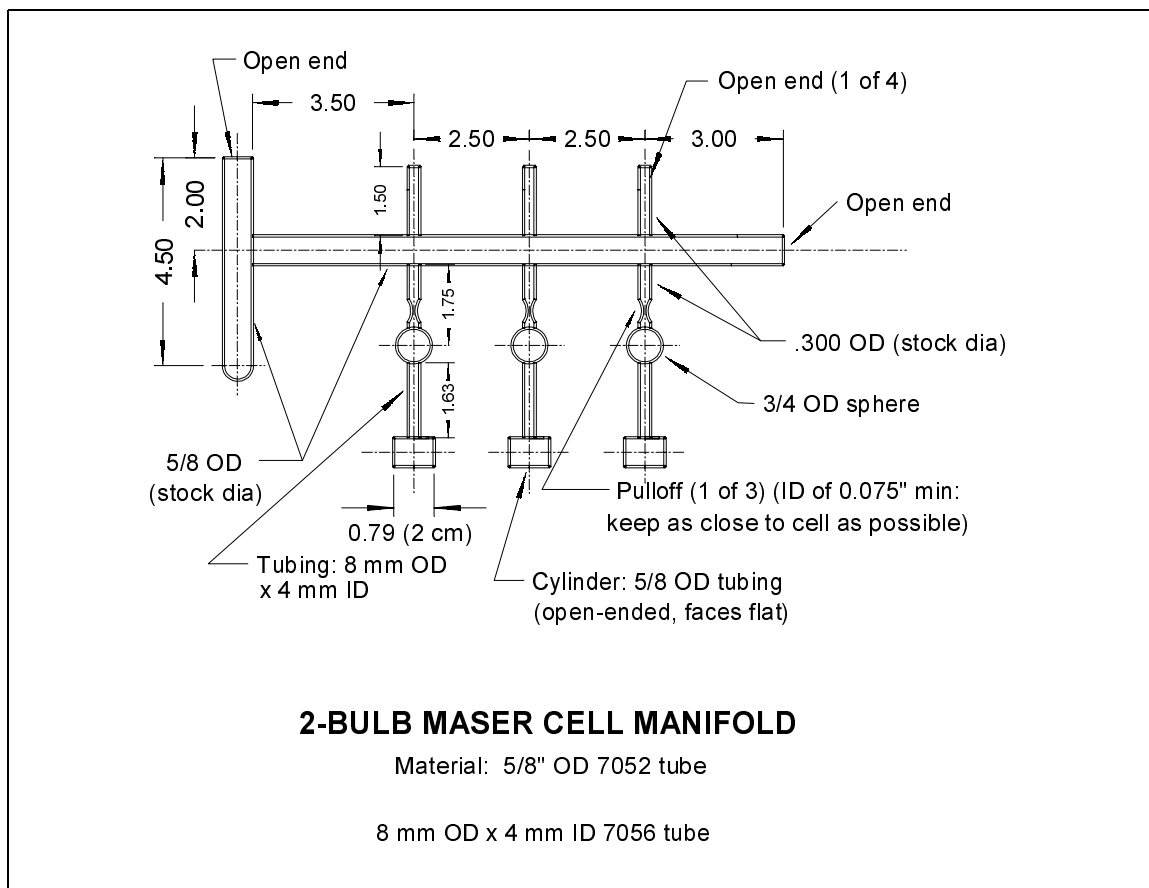


Figure 3.3: Typical manifold used to make three EDM-capable cells. The pieces are blown from annular stock of Corning 7056 borosilicate glass, which has a helium permeability of 1.8×10^{-11} ($\text{cm}^3 \text{ mm} / (\text{sec cm}^2 \text{ torr})$) at 130°C and a volume resistivity of $\sim 6 \times 10^{18} \Omega \text{ cm}$ at 40°C . The glass-blowing for this experiment was performed by Harold W. Eberhardt, Scientific Master Glassblower, University of Michigan, Ann Arbor.

the work outlined in references [20, 36, 53].

Before the cells are coated, surface contaminants are removed from the glass by immersing the cells in a “piranha” mixture of 30% H_2O_2 (hydrogen peroxide) stock solution and 97% H_2SO_4 (sulfuric acid) stock solution (3:7 ratio by volume). After soaking in the piranha mixture for ~ 1 hour, the cells are removed and rinsed three times each with distilled water and then three times each with methanol. They are then rinsed once more with distilled water and allowed to air dry for one hour.

Once dry, each cell is dipped into a silane coating solution consisting of five drops (about 200 μL) of OTS mixed with a base solution of C_6H_{14} (hexane) and C-H-Cl_3 (chloroform, 9:1 ratio by volume). After soaking in the solution for five minutes, each cell is allowed to air dry for five minutes before unreacted OTS is removed using a rinse of pure chloroform. Finally, the cells are each rinsed with methanol and baked at 180 $^\circ\text{C}$ for ~ 12 hours in order to drive residual hexanes from the glass surface.

In EDM cells, the high voltage endplates used to seal the maser chamber are fabricated from .020" thick molybdenum sheet.² To ensure good surface preparation, the endplates are sanded with oiled 600 grade sandpaper, polished with Brasso, dipped in piranha solution for 30 seconds, rinsed with distilled water, and then polished with methanol soaked wipes. The ends of the maser chamber are sanded with an emery board to remove OTS coating, which is known to prevent proper adhesion of metal plates to the glass surface. The components are then joined using EPO-TEK 35ND³ epoxy and cured according to schedule. Before filling with noble gases is undertaken, the cells are placed on the vacuum system and thermally cycled to liquid nitrogen temperatures. They are also filled with nitrogen gas to a higher pressure than that to which they will be subjected under actual running conditions.⁴

3.1.2 Cell filling

Cells that demonstrate helium leak test integrity following the above procedures are ready to be filled. First, the manifold is removed from the vacuum system. A

²Available from Alfa Aesar Metals, War Hill, Massachusetts, www.alfa.com.

³10 parts A and 1 part B (hardener) by weight, available from Epoxy Technology, Inc. Billerica, Massachusetts.

⁴These thermal cycling and overpressure tests are performed to ensure that the cells will not fail during the filling procedures described in the following section. Cells which leak at this stage in the process can generally be repaired, re-cleaned, and re-coated. Such is not the case after Rb has been chased into the cells (Section 3.1.2).

sealed glass ampule containing 1 gram of naturally occurring Rb (72% ^{85}Rb and 28% ^{87}Rb) is chilled in liquid nitrogen⁵, cracked open, and placed in the sidearm of the cell manifold. The sidearm is sealed off using a dual propane/oxygen torch, and the manifold is placed under vacuum and baked at 120 °C for 48 hours. The pressure in the manifold should be $\sim 2 \times 10^{-7}$ Torr at the end of the bakeout process.

After baking, Rb is chased from the sidearm into the pump chamber of each cell using a cool propane flame. Care is taken to avoid damaging the OTS by inadvertently applying heat to the coated glass surfaces. To reduce this risk, each cell is wrapped with damp strips of cloth and covered in aluminum foil. Toward the end of the chasing process, the protective wrapping must be removed in order to verify that Rb has been chased successfully into the pump chamber. After the chasing is complete, the manifold is pumped on until the pressure returns to its value before Rb was driven into the cells. This usually takes ~ 24 hours, at which time the cells are ready for gas filling. The gases (loaded in the order ^{129}Xe , N_2 , and ^3He) consist of mixtures of 90% isotopically enriched ^{129}Xe (99.999% purity), 99.95% CP grade enriched ^3He , and 99.9999% pure N_2 , each of which is gettered [54] before loading into the cells. After loading is complete and the N_2 and ^3He are allowed to mix for ~ 30 minutes, the glass cells are pulled off and sealed using a dual oxygen/propane flame while the pump bulb and everything below it are immersed in liquid nitrogen. The LN_2 freezes the ^{129}Xe into the cells and keeps the total N_2 and ^3He gas pressures below 1 atmosphere, an essential condition for the glass to collapse inward and form a vacuum seal when the cell is pulled away from the manifold. At room temperature, typical partial pressures of the gases used in recent DNGM cells are $P_{\text{Xe}} \approx 150$ Torr, $P_{\text{He}} \approx 1100$ Torr, and $P_{\text{N}_2} \approx 80$ Torr. Section 3.5.6 describes some important considerations in choosing noble gas fill pressures.

⁵Cooling reduces the rate of Rb oxidation while the unsealed ampoule is exposed to air.

New cells are installed in the maser system and tested by measuring the longitudinal polarization of ^{129}Xe , ^3He , and Rb gases under canonical operating conditions (see Table 1.1). A new cell generally needs to sit under heat for ~ 2 days before it is ready for use. Over longer periods of time, it has been found that the attainable levels of Rb, ^3He , and ^{129}Xe polarizations within a particular cell slowly decrease, with other operational parameters being kept constant. Although this loss mechanism is not well understood, it is believed that over long timescales Rb is driven from the hot pump chamber and plates out in the much cooler transfer tube and maser chamber, thus causing cells which are used for ≥ 6 months to suffer irreversible deterioration in performance.

3.2 DNGM Oven Assembly: Design and Illustrations

The double bulb cells used in the DNGM reside in an oven assembly fabricated from Nylatron GS, an easily machined nylon-molybdenumdisulfide composite material whose salient properties are given in Table 3.3, below. The DNGM oven consists of a “pump block” joined to a “maser block” by an annular Nylatron spacer. The assembly is designed to provide structural support for the double bulb cell as well as for the maser chamber pickup coil (Section 3.7.3) and pump chamber Zeeman drive coil (Section 3.4.2). Optical access to the pump bulb is provided by anti-reflective coated optical flats (Section 3.4) glued into detents cut in the pump block. The multi-block design allows the necessary thermal isolation of the hot pump chamber ($\sim 110^\circ\text{C}$) from the cooler maser chamber ($\sim 40^\circ\text{C}$); and blown air access to each chamber provides a means of achieving the temperature control required for stable

property	value
continuous service temperature in air (maximum)	120 °C
coeff. of linear thermal expansion (inch/inch-°F)	3.5×10^{-5}
volume resistivity	$2.5 \times 10^{13} \Omega\text{-cm}$
melting point	260 °C

Table 3.3: Properties of Nylatron GS, available from AIN Plastics, Norwood, MA.

maser operation.

Figures 3.4 and 3.5 give detailed machine drawings of the pump and maser blocks, and Figure 3.6 shows a machine drawing of the connecting Nylatron spacer. 1/4" NPT holes are tapped in both the pump and maser blocks to accommodate compressed air fittings. Also note that the bore of the maser block is designed to accommodate the resonant pickup coil form depicted in Figure 3.30. Small, 1 inch diameter detents on the pump block provide recesses for the forms on which are wound the Zeeman depumping drive coils (Section 3.4.2). Figure 3.7 shows a view of the assembled oven components, as viewed along the direction traveled by the optical pumping laser beam.

The assembled oven rests inside a Nylatron "shroud," machined to fit snugly inside the bore of the DNGM solenoid (Section 3.5). A machine drawing of the shroud is given in Figure 3.8. The gradient trim coils described in Section 3.5.4 are wound in grooves cut into the surface of the shroud, as shown. A photograph of the oven and shroud assembly is given in Figure 3.9, and front and side views of the oven, shroud, and solenoid assembly are provided in Figures 3.10 and 3.11. Note

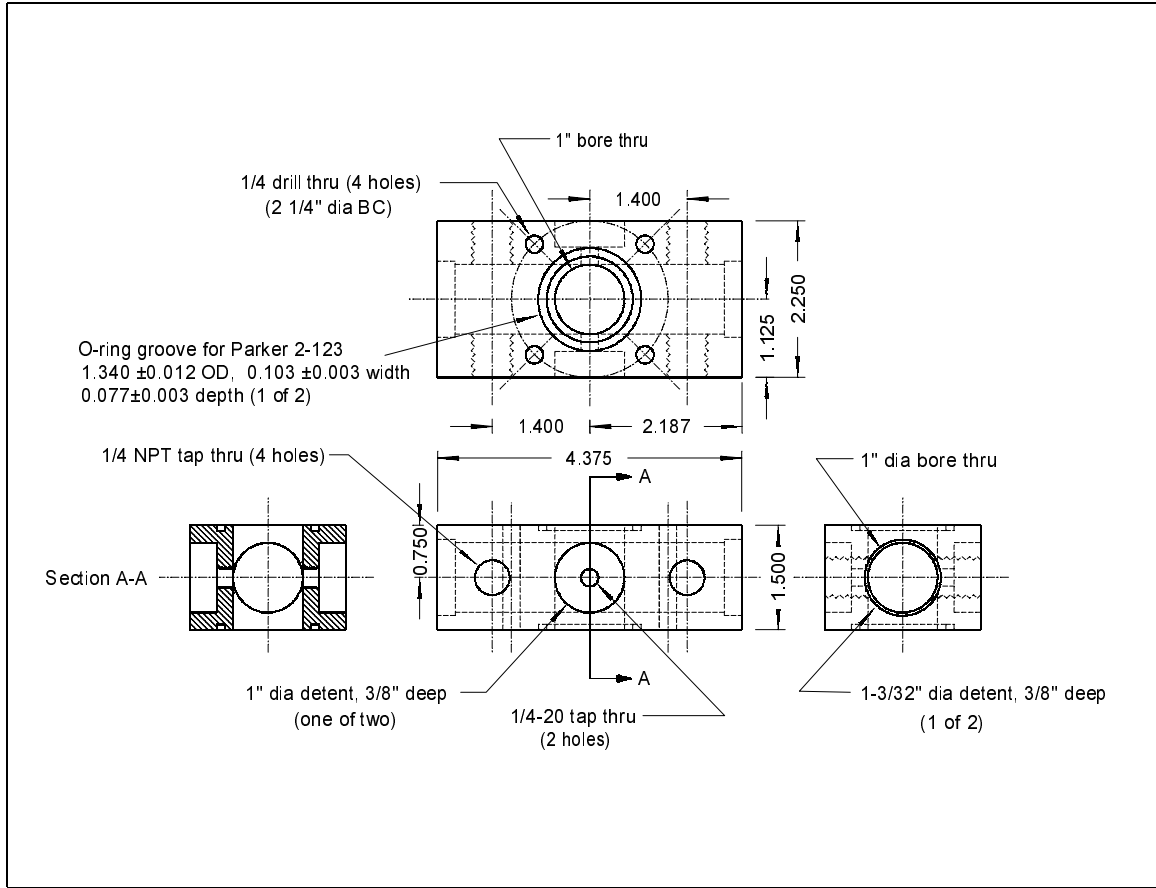


Figure 3.4: Machine drawing of the DNGM pump block, fabricated from 2" thick Nylatron GS sheet.

that the ends of the shroud are sealed by 1/4" thick Nylatron plates. The plates have optical access holes cut into them, as well as holes and strain relief points for compressed air tubing, electrical wires, etc. A machine drawing of the front plate downstream from the optical pumping laser is shown in Figure 3.12.

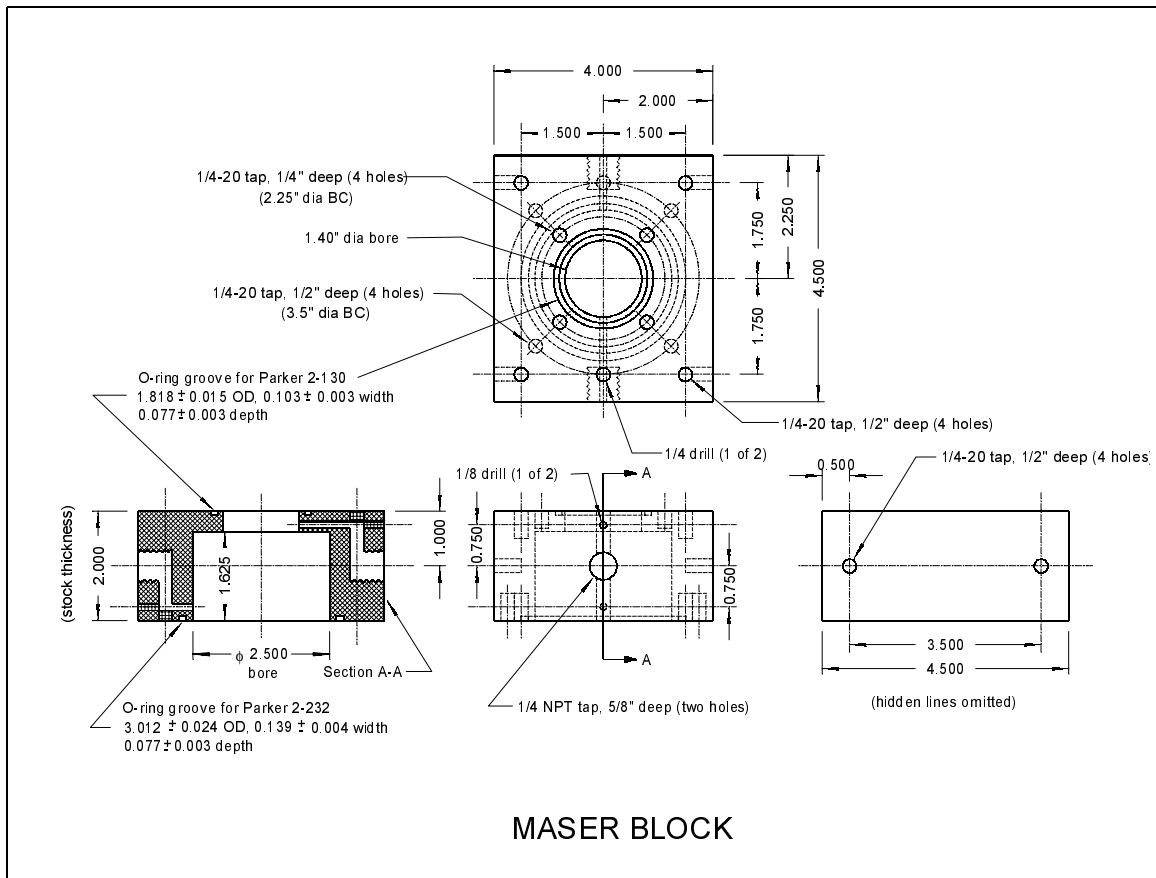


Figure 3.5: Machine drawing of the DNGM maser block, fabricated from 2" thick Nylatron GS sheet.

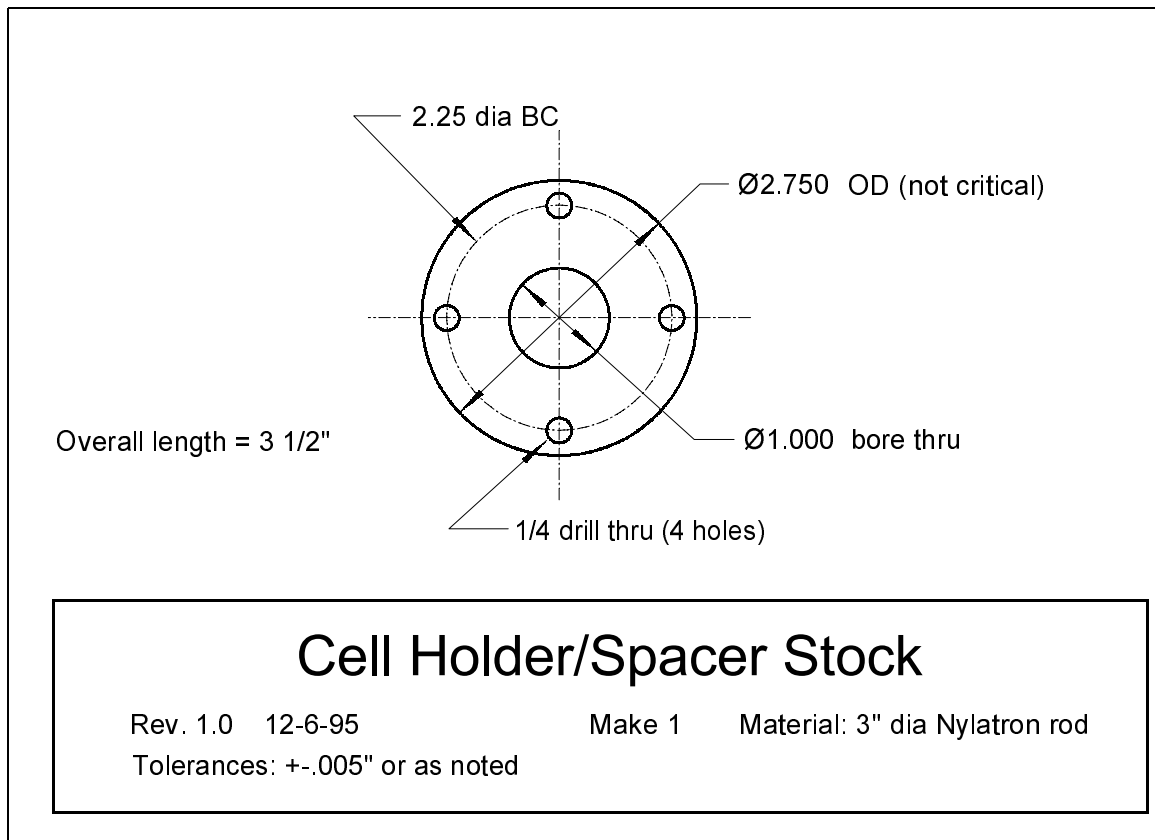


Figure 3.6: Machine drawing of the spacer connecting the pump and maser blocks, fabricated from 3" diameter Nylatron rod stock.

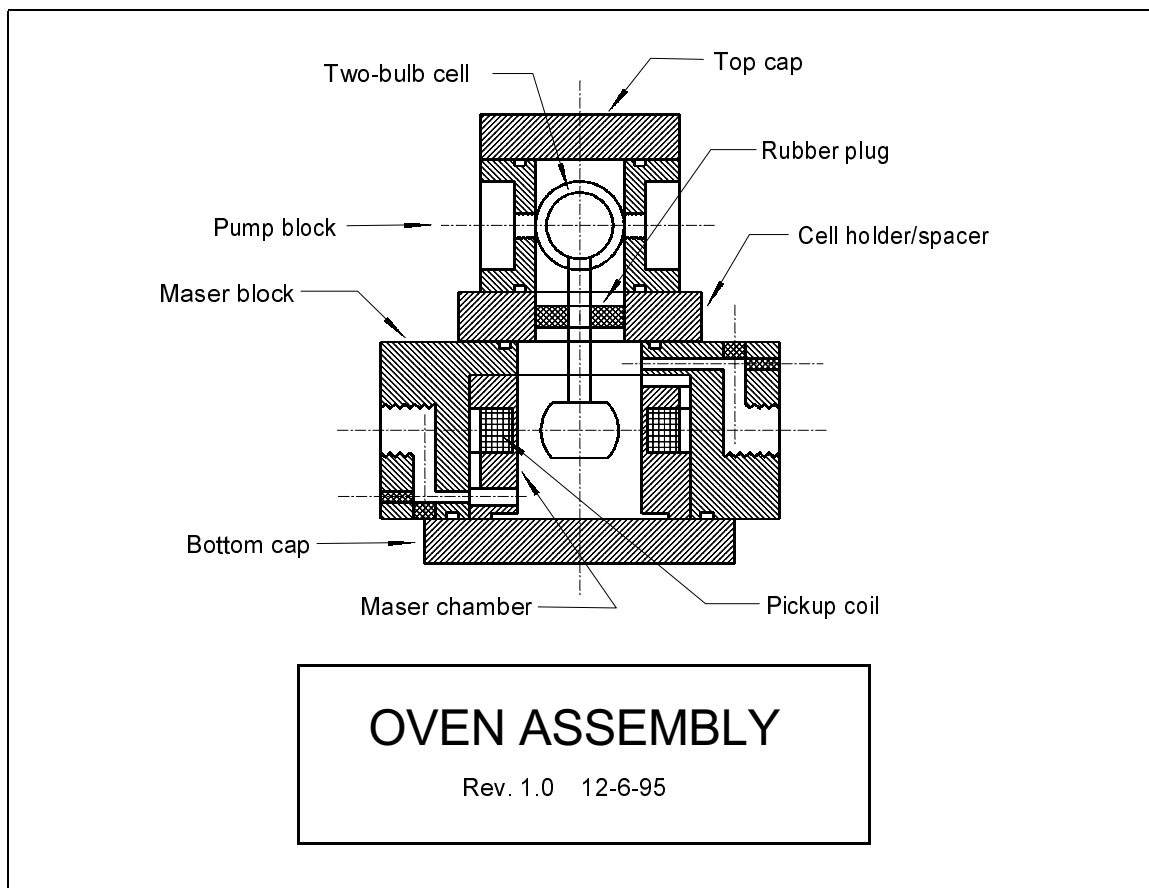


Figure 3.7: View of the assembled DNGM oven components, as viewed along the direction traveled by the optical pumping laser beam.

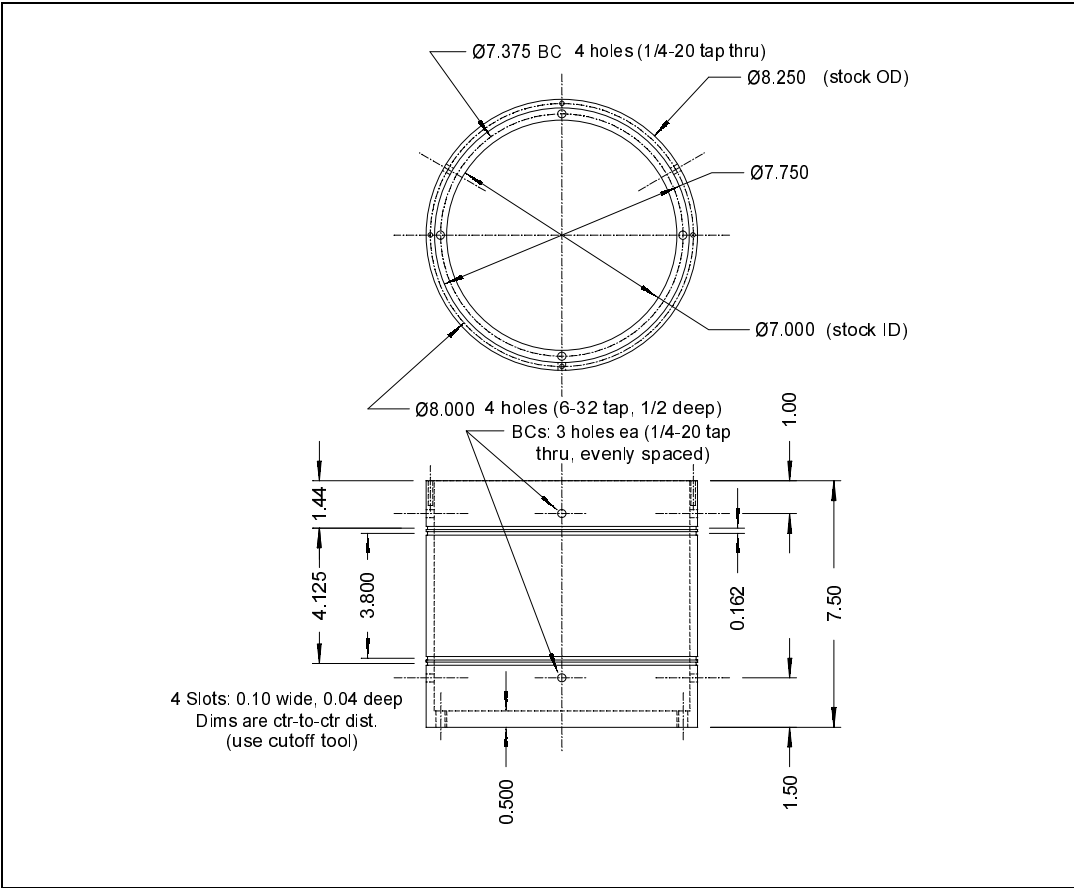


Figure 3.8: A design drawing of the DNGM shroud assembly. Notice the grooves for gradient trim coils cut on the outer surface.

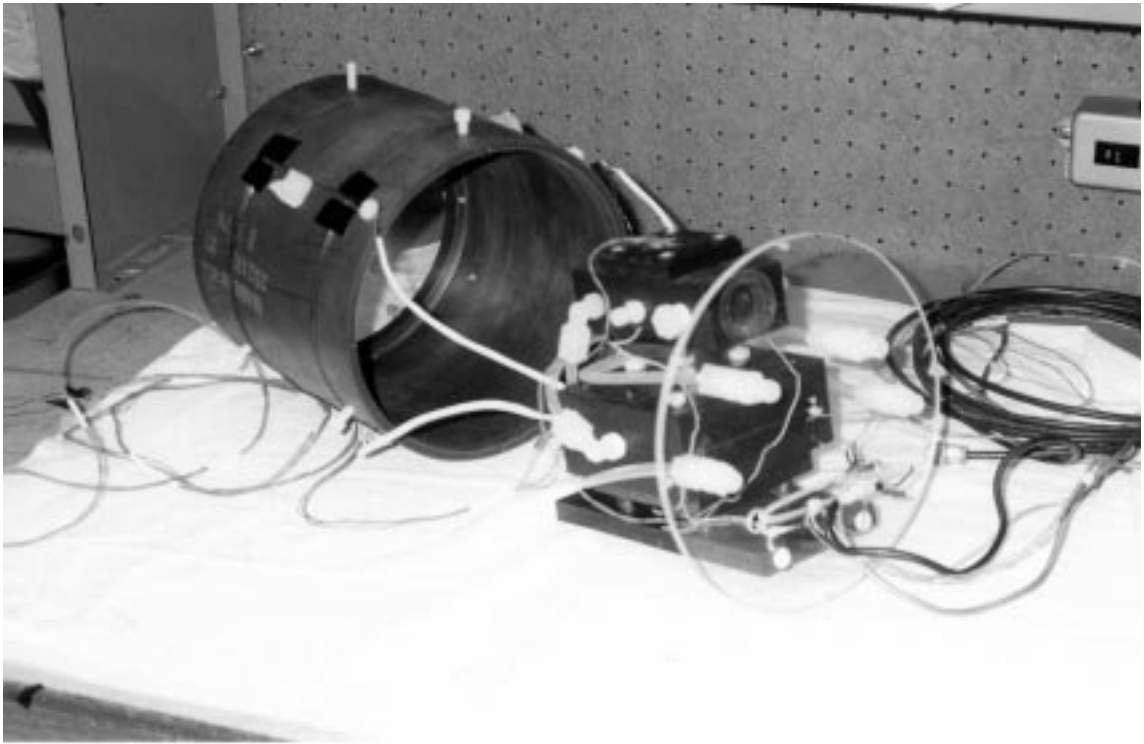


Figure 3.9: A photograph of the DNGM shroud and oven block assembly.

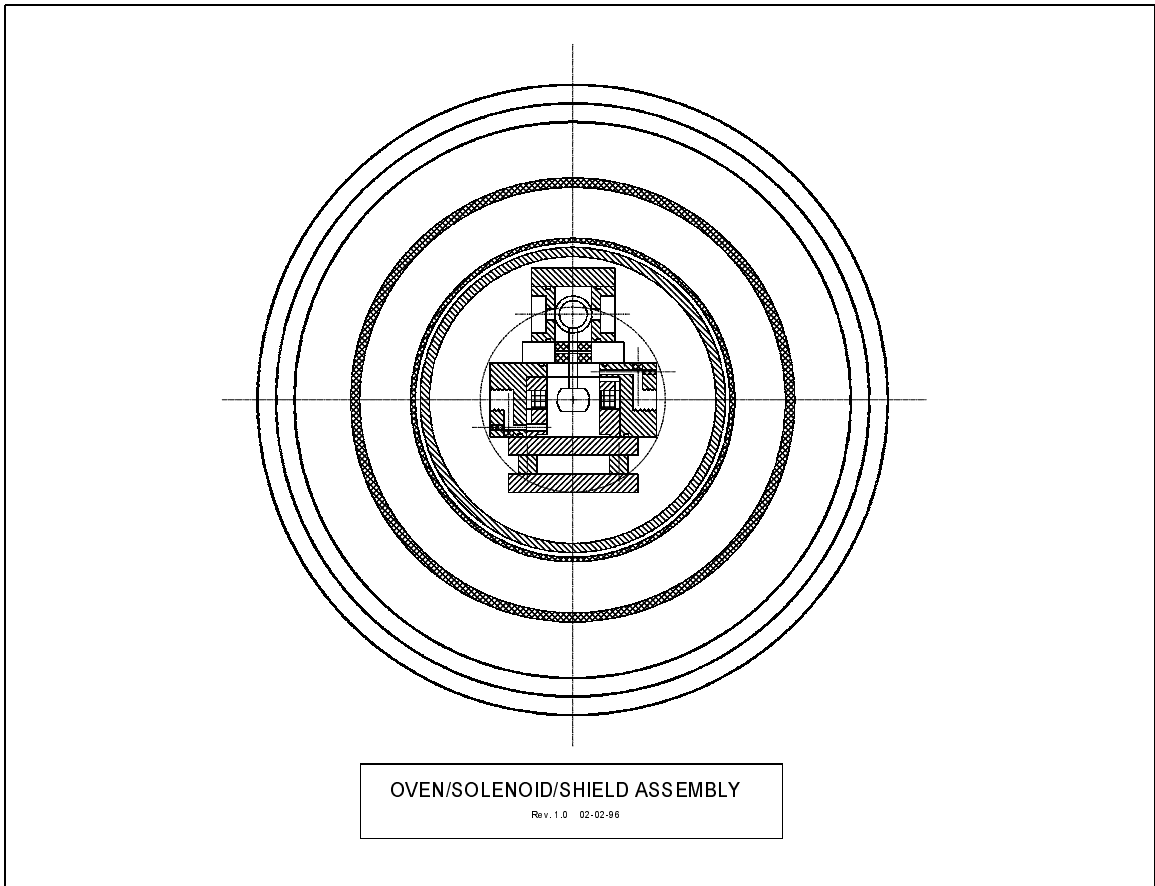


Figure 3.10: End-on view of DNGM oven, shroud, and solenoid assembly.

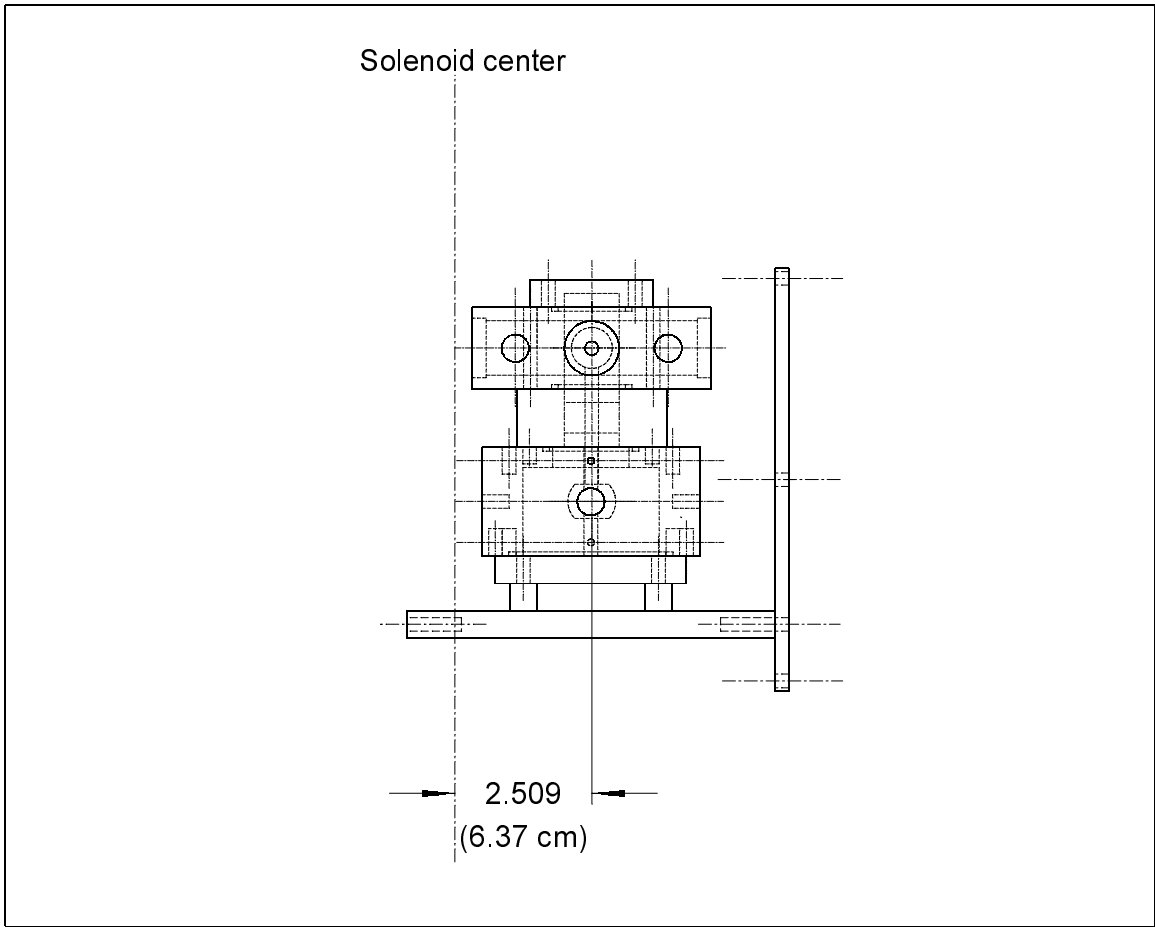


Figure 3.11: Side view of DNGM oven, shroud, and solenoid assembly.

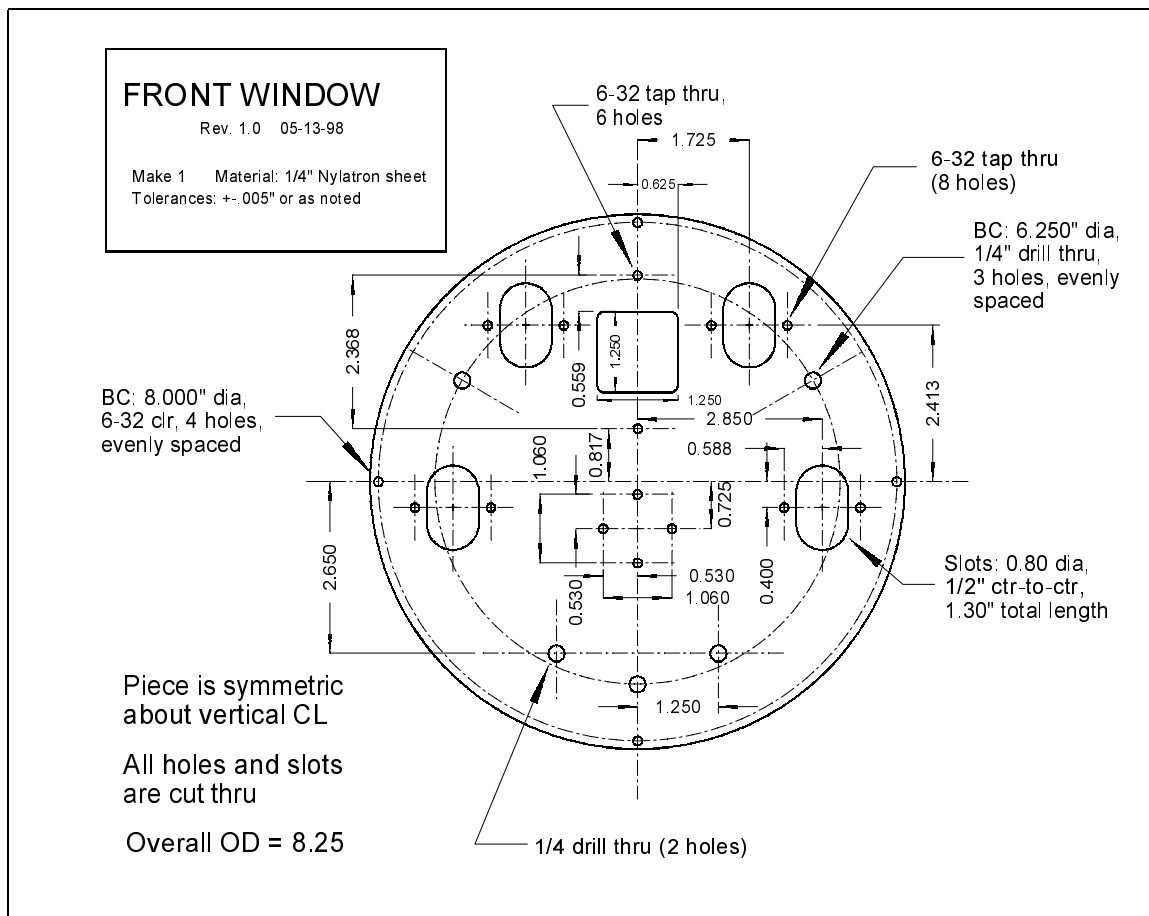


Figure 3.12: Drawing of the plate sealing the downstream (from the optical pumping LDA) end of the DNGM shroud assembly. Notice the large square hole at the height of the pump chamber for optical access, as well as the various holes and strain relief points for compressed air tubing, electrical wires, etc.

3.3 Blown Air Temperature Control

Stable frequency operation of the DNGM requires precise temperature control of the optical pumping and masing regions, and also of the double resonator circuit components (Section 3.7.3). Cell temperature instability causes changes in Rb magnetization in the optical pumping region (Section 3.4.2) as well as changes in the density distributions of the noble gases ensembles, thereby affecting ^{129}Xe and ^3He magnetization levels throughout the cell. Temperature fluctuations also affect the noble gas polarization lifetimes T_1 and T_2 and the DNGM's co-magnetometry, both by changing the interactions between the atoms and the cell walls [55], and by changing the noble gas diffusion constants (Section 2.3). Temperature fluctuations in the double resonator circuit components degrade the performance of the DNGM by changing the cavity pull frequency shift (Equation 3.20). The effects of temperature-dependent frequency shifts on the measurement resolution of the DNGM are discussed thoroughly in Sections 2.6 and 3.7.5. We describe now the implementation of the DNGM's blown air temperature control systems. Note that the temperature environment of the DNGM laboratory is maintained at ≈ 24 °C, with characteristic oscillations of $\approx \pm 0.1$ °C (due to the on-off nature of the air conditioning unit) at 1.6 mHz, as shown in Figure 3.13.

The DNGM pump bulb and maser bulb are contained in thermally separated pump and maser blocks, as described in Section 3.2. Temperature control of these regions, as well as of the external resonator,⁶ is achieved using standard bridge measurement techniques, combined with PID feedback control to a heated airflow system (Figure 3.14). As the methodology for controlling temperature is the same in each region, we first discuss the general aspects of the control system, and afterward

⁶The external resonator is contained in separate, thermally and electrically isolated enclosure, as described in Section 3.7.3.

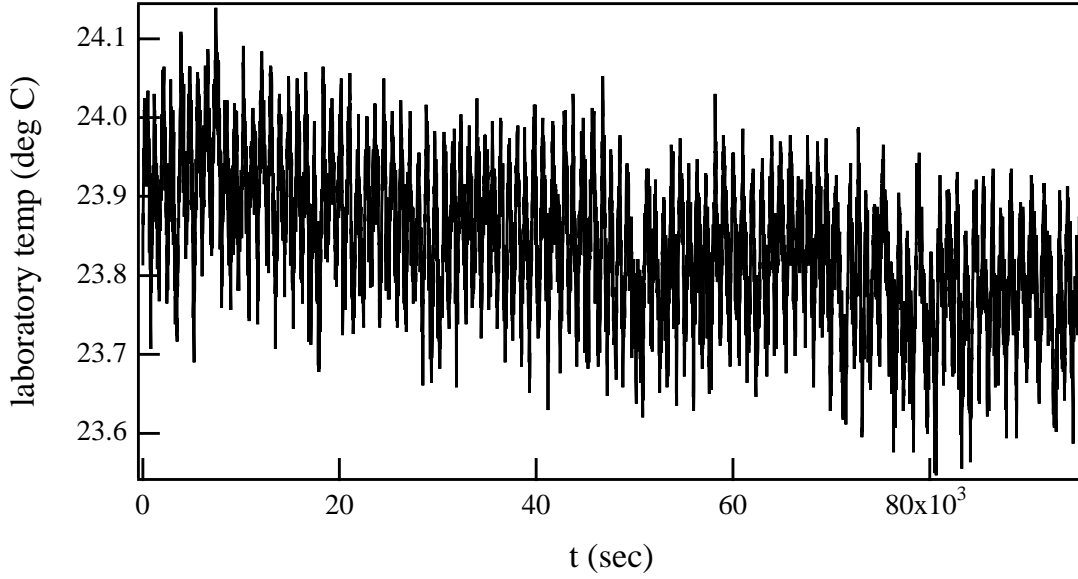


Figure 3.13: Temperature of the DNGM laboratory environment over a typical 24 hour period. The thermal sensor (RTD) was located near the maser signal processing pre-amplifier. The room’s air conditioning unit induces temperature oscillations of $\approx \pm 0.1$ °C at 1.6 mHz.

comment briefly on issues distinct to each individual region. Table 3.4 summarizes salient characteristics of the temperature control systems in each region. Note that an excellent description of how to measure and control temperature can be found in [56].

Figure 3.14 shows a schematic of the DNGM temperature control system. The temperature sensors are three-lead, 100 Ω non-magnetic, platinum resistance thermometers (RTDs⁷), with lead-resistances r shown in the diagram. The resistance of each sensor is a linear function of temperature: $R = 100 + .384 \cdot T$, where R is in Ω and T is in °C. In order to allow sensitive temperature resolution ($\sim .1$ mK) with small bridge currents⁸($\sim 2 \times 10^{-5}$ A), each RTD is part of a standard, balanced

⁷Available from Omega Engineering, www.omega.com.

⁸Larger currents produce self-heating of the RTDs and, more important, produce associated noise fields which are picked up by the maser detection coils in proximity to the RTDs.

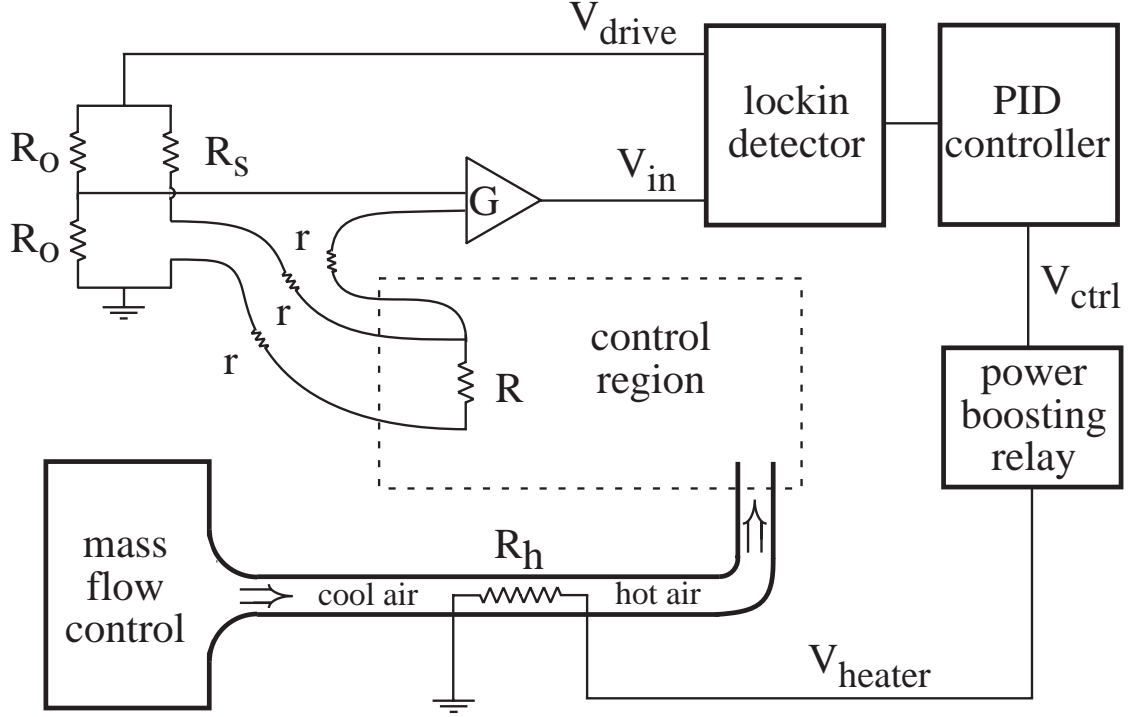


Figure 3.14: General schematic of the DNGM's blown air temperature control systems. The input voltage lockin detector, V_{in} , is the bridge output voltage multiplied by the pre-amplifier gain G .

temperature bridge energized by an AC drive voltage (typically 4 mV RMS at 950 Hz) provided by the internal reference of an SRS 830 digital lockin amplifier. The buffered and pre-amplified bridge output voltage is given by

$$V_{in} = G \cdot V_{drive} \left(\frac{R}{R + R_s} - \frac{1}{2} \right), \quad (3.1)$$

where G is the amplifier gain, V_{drive} is the drive voltage provided by the lockin, R is the resistance of the temperature sensor, R_s establishes the temperature setpoint of the control loop, and the lead resistances r (approximately equal for each lead) are assumed to be much smaller than R , with one lead resistance on each arm of the bridge. Bridge resistors R_o and R_s have temperature coefficients smaller than 10

ppm/°C.⁹ Typical values for these resistors are: $R_o = 120 \Omega$, $R_s = 144.2 \Omega$ (pump bulb), $R_s = 115.9 \Omega$ (maser bulb), $R_s = 111.3 \Omega$ (external resonator).

Lockin detection of the voltage V_{in} produces a DC error signal which is passed to a high performance PID (proportional-integral-differential) temperature controller. The output voltage from the PID controller (V_{ctrl}) is amplified by a voltage controlled power relay and then passed to an air process heater. (V_{ctrl} typically includes a DC offset to maintain rough temperature control, plus a variable correction voltage to account for system temperature deviations.) A precisely regulated flow¹⁰ of air through the process heater and into the region to be controlled supplies the variable heating power required to maintain temperature control. A higher flow rate into the control region reduces the thermal time constant¹¹ of the temperature lock loop and thus permits more stable control of the temperature [56]; but as detailed in Section 2.6, phase and frequency noise on the maser increase with larger air flow rates, primarily because of mechanical jitter induced on resonant circuit elements. The DNGM is presently operated with a total of 100 slm (standard liters per minute) of air flowing through all three chambers, with approximately 55% going to the pump block, 27% going to the maser block, and 18% going to the external resonator (see Table 3.4 for typical thermal time constants and other important parameters).

We now enumerate important aspects of the DNGM blown-air temperature control system that have not yet been discussed, and summarize in a concluding table parameters that may be of interest to the reader.

- **Pump chamber:** Absorption of near-infrared light from the optical pump-

⁹Vishay type S102K .1% resistors, available from Vishay Precision Resistors, 63 Lincoln Highway, Malvern, PA 19355.

¹⁰The air flow is regulated by an MKS Type 1500 Series Mass-Flow Controller, 200 slm maximum capacity. MKS Industries, 6 Shattuck Road, Andover, MA 01810.

¹¹The thermal time constant is measured by setting the integration and differentiation times of the PID loop to zero, while setting the DC gain to as high a value as possible. The system will then exhibit an oscillatory temperature with period $\tau_{thermal}$.

ing laser contributes substantially to heating of the pump chamber. Feedback control to the total output power of the laser stabilizes this contribution (Section 3.4). Romalis estimates in [40] that for a thermal configuration similar to that of the DNGM, gas temperature inside the target cell may be as much as 10 °C warmer than the air temperature sensed ~ 1 cm outside the cell. The pump chamber RTD is located in the top cap of the pump block, shielded from optical pumping light. Estimates of thermal gradients across the interior of the pump block, but outside the pump bulb, are $\nabla T \sim .1$ °C/cm. In spite of these large gradients, the RMS fluctuations on a monitor RTD placed in the pump chamber ~ 10 cm from the control RTD are approximately the same as the RMS fluctuations of the control thermometer (~ 20 mK, see Table 3.4).

The operational temperature of 114 °C is essentially the maximum temperature attainable in the pump chamber with the present system configuration and a pump block air flow rate of 55 slm. The dependence of maser amplitudes and frequency performance on pump bulb operating temperature have not been carefully studied.

- **Maser chamber:** The control RTD is heat-sunk to the pickup coil. It is found that the temperature of the coil, in the presence of pump chamber heating only, is ≈ 37 °C. A temperature setpoint of ≈ 41 °C provides ample dynamic range for the feedback loop.
- **External resonator:** The control RTD is heat-sunk directly to the outer layer of the external resonator coil. As described in Section 3.7.3, the coil is contained in a separate blown air oven which is placed inside thermally insulated metallic shields. Because of the large thermal mass of the copper coil and the relatively modest air flow rate to the oven, the thermal time

constant for this region is quite large (~ 200 sec).

parameter	pump block	maser block	external resonator
air flow rate (slm)	55	27	18
thermal time constant	30 s	100 s	200 s
operating temperature	114 °C	41 °C	29 °C
RMS temp. fluctuations	20 mK	11 mK	3 mK
sidereal temp. variations	–	.8 mK	.04 mK

Table 3.4: Typical parameters for the three DNGM blown-air temperature control subsystems. The integration time constant of each PID loop is set as close as possible to the measured intrinsic thermal time constant of the system.

3.4 Optical Pumping System

As described in Section 2.2, the ^{129}Xe and ^3He nuclei are polarized by spin-exchange interactions with optically pumped Rb vapor. This section describes the lasers, optical components, and control systems used to produce stable σ^+ light resonant with the pressure-broadened Rb D1 line (794.8 nm).

3.4.1 Overview

We first note that all DNGM data gathered before December, 1999 were obtained while using an Optopower¹² OPC-A015-FCPS laser diode array (LDA). A detailed characterization of the properties of eleven such Optopower arrays, including presentation of a method for stabilizing the spectral output of the particular unit used to take DNGM data, is presented in our group’s paper [57]. In December, 1999 the Optopower array was replaced with a higher-power Coherent¹³ FAP-I array. The

¹²Optopower Corporation, 3321 E. Global Loop, Tucson, AZ 85706.

¹³Coherent, Semiconductor Group, 5100 Patrick Henry Drive, Santa Clara, CA 95054-1112.



Figure 3.15: A photograph of the LDA optical fiber, collimating lenses, $\lambda/4$ plates, and polarizing beam splitter cube used in the DNGM experiment. The optical setup is situated approximately 1 foot from the end of the outer μ -metal shield.

operational principles of both LDA models are similar. The Coherent unit, however, has twice the total on- (and off-) resonant output power and has exhibited better intrinsic stability than the Optopower arrays. We thus describe the DNGM optical pumping system as it is presently configured, with the Coherent unit as the source of optical pumping light.

Table 3.5 gives operational parameters for the Coherent (and Optopower) LDA under typical conditions. The line-shape and total power of the LDA spectrum are adjusted by controlling the injected current to the diode bar and the operating temperature of the bar. Light emitted from the LDA is coupled to an optical fiber bundle (5 m in length), and then passed through a pair of collimating lenses to produce a spot size roughly the same diameter as the target pump cell. The

Operating parameter	Optopower LDA	Coherent LDA
total broadband power	15 W	30 W
spectral width	1.8 nm	1.5 nm
operating current	25 Amps	38 Amps
diode bar temperature	24.5 °C	18 °C
length of fiber bundle	3 m	5 m

Table 3.5: Typical operational parameters for the Optopower and Coherent LDAs used in the DNGM experiment.

initially unpolarized beam is imparted σ^+ helicity by passage through a polarizing beam splitter cube followed by passage through a $\lambda/4$ -plate plate.¹⁴ AR coated windows (reflection coefficient for resonant light $\leq 1\%$) provide optical access to the DNGM oven assembly and DNGM pump bulb. Figure 3.16 shows a schematic diagram of the optical components described above.

3.4.2 Measuring the Relative Rb Magnetization in the Pump Bulb

In this section we describe a method for measuring the relative level of Rb magnetization ($M_{rb} = [Rb] \cdot P_{rb}$) in the pump bulb. Knowledge of M_{rb} is extremely important, as it provides a real-time diagnostic used to optimize laser steering, laser fiber orientation, and the operating temperature of the laser diode bar. The relative value of M_{rb} also provides one of the two signals used to stabilize (indirectly) the noble gas polarization in the pump bulb (Section 3.4.3). The techniques described in these sections can be generally applied to monitor and stabilize the Rb magnetization in any cell being optically pumped by a tunable, broadband LDA.

To monitor the relative level of Rb magnetization, a weak, transverse oscillating

¹⁴The use of a wave plate with variable retardance (LCVR) will be discussed in Section 3.4.3.

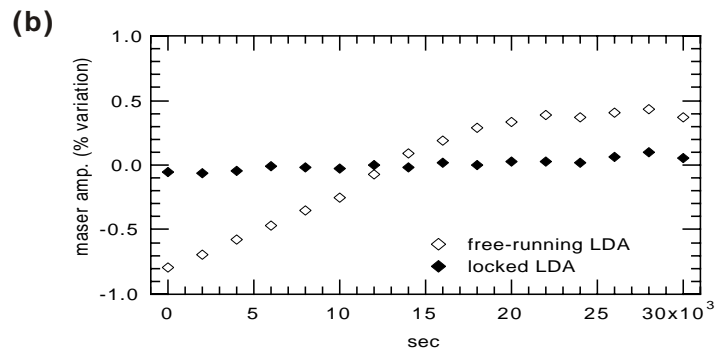
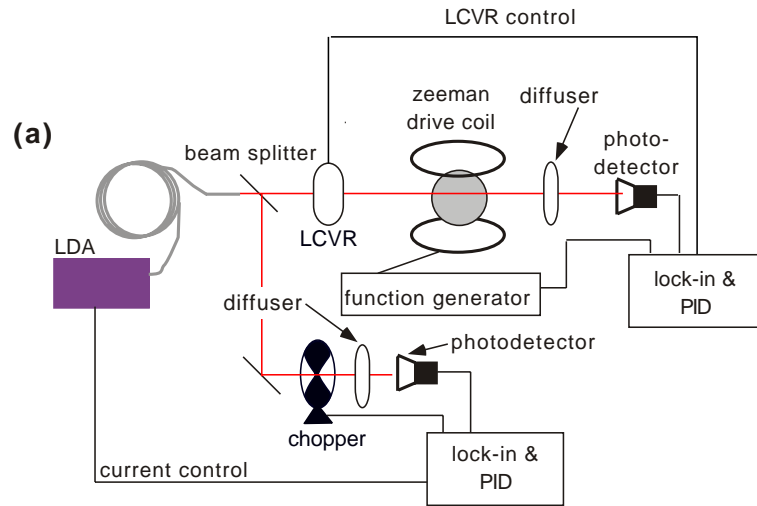


Figure 3.16: (a) A schematic of the optical components used in the DNGM experiment. (b) Typical observed improvement in maser amplitude stability of more than an order of magnitude when the two-loop LDA stabilization techniques are employed.

(Rabi) magnetic field is applied to the cell at the Rb Zeeman frequency, ~ 700 kHz under typical running conditions (Section 2.2.1). In the absence of such a field, the Rb polarization is given by

$$P_{rb,off} = \frac{\gamma_{opt}}{\gamma_{opt} + 1/T_1}, \quad (3.2)$$

where γ_{opt} is the optical pumping rate (Equation 2.8), T_1 is the polarization lifetime of the Rb atoms (Section 2.2.1), and the subscript “off” indicates the Zeeman drive is inactive. If the Zeeman drive is turned on, however, the Rb polarization takes the form [34, 37, 43]

$$P_{rb,on} = \frac{\gamma_{opt}}{\gamma_{opt} + 1/T_1 + \left(\frac{\gamma_1 B_1}{2}\right)^2 T_2}, \quad (3.3)$$

where $\left(\frac{\gamma_1 B_1}{2}\right)$ measures the average strength of the co-rotating component of the Zeeman drive. (Note that the Rb polarization reaches equilibrium with the Zeeman drive in ~ 1 msec, a timescale much shorter than all dynamic processes of interest in the DNGM.)

The applied Zeeman field thus reduces the Rb magnetization, assuming the Rb density (a function of the pump bulb temperature) is stable. In the DNGM we typically use a Zeeman drive that reduces M_{rb} by $\leq 5\%$, which in turn proportionally increases the absorption of the LDA optical pumping light. The LDA light transmitted through the pump bulb passes through a ground-glass diffuser and is then incident upon a photodiode detector (PDD).¹⁵ The diffuser both reduces the beam intensity (to prevent potential saturation of the photodetector) and performs

¹⁵We stabilize the temperature of all photodetectors used in the DNGM experiment to approximately 50 mK RMS. The fractional temperature coefficient of each photodetector’s output voltage has been measured to be approximately $10^{-4}/^\circ\text{C}$. Temperature stability of 50 mK thus yields fractional optical detection resolution of $\sim 5 \times 10^{-6}$, well below the limitations imposed by intrinsic noise sources in the detection system.

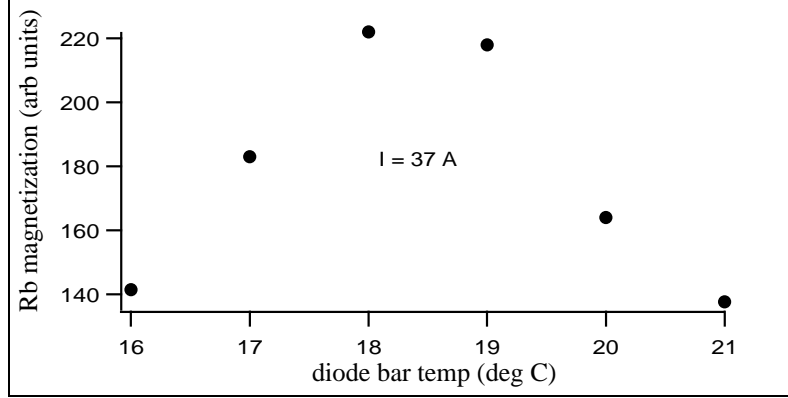


Figure 3.17: Plot of the relative value of M_{rb} versus temperature in the diode bar of the Coherent LDA, for fixed $I = 37$ amperes. DNMG 17, page 119.

a spatial average over the light from various fibers of the LDA and over refractive distortions introduced by the glass cell. The amplitude of the Zeeman drive is modulated slowly¹⁶ ($\nu_{mod} \sim 400$ Hz). Lock-in detection at ν_{mod} permits extraction from the photodiode detector a signal proportional to the Rb magnetization in the pump bulb.

Knowledge of the relative value of M_{rb} provides several means for improving the optical pumping rate γ_{opt} (Equation 2.8). Most simply, fine adjustments to the LDA steering and fiber-bundle orientation can be carried out to increase the detected Rb signal. For the Coherent LDA, the total optical pumping power increases monotonically with the value of the current through the diode bar; hence the laser is typically operated with I very near its maximum value. To tune the light to the Rb D1 transition (794.8 nm), the temperature of the diode bar is adjusted until the Rb magnetization signal is maximized. For example, figure 3.17 shows a plot of the relative value of M_{rb} versus diode bar temperature for fixed $I = 37$ amperes.

¹⁶“Slow” being in comparison to the Rb polarization lifetime, which is typically ~ 1 msec.

3.4.3 Stabilizing the Optical Pumping Light

Temporal drifts in the resonant LDA optical pumping power can lead to significant changes in the Rb polarization (P_{rb}). Changes in the total LDA power incident upon the cell can also affect the cell temperature and thus the Rb vapor density ($[Rb]$, see Equation 3.5). These two parameters determine the noble gas nuclear spin polarization (P_{ng}) induced by spin exchange collisions with the Rb vapor. P_{ng} is given approximately by (Section 2.2.2)

$$P_{ng} = \frac{P_{rb}\gamma_{se}}{\gamma_{se} + 1/T_1}, \quad (3.4)$$

where T_1 is the polarization lifetime of the noble gas set by interactions with cell walls, etc., and γ_{se} is the Rb–noble gas spin–exchange rate, which is proportional to $[Rb]$. Drifts in both the resonant and total LDA power can thus lead to significant changes in the noble gas polarization. This polarization drift will also change the net magnetic field created by the noble gas spin ensembles and the functioning of the two-species magnetometry, thereby affecting the frequency stability of the DNGM, as described in Section 2.6. To reduce these sources of frequency instability, we employ a two–loop feedback technique to stabilize both the total output power of the LDA and the power on the Rb D1 resonance. A schematic depiction of the feedback system is shown in Figure 3.16.

The first feedback loop monitors the total power from the LDA with a chopper, a temperature–stabilized photodetector, a lockin amplifier, and a PID controller. A small portion of the laser beam is picked off using a microscope slide, and a ground–glass diffuser in the light path between the chopper and photodetector reduces the sensitivity of the measured LDA power to beam steering drifts. The current injected into the LDA is adjusted by the feedback loop to maintain constant power on the

photo-diode. By this technique we control the total emission power of the LDA with a fractional stability of a few parts in 10^4 , roughly an order of magnitude more stable than in free-running operation. This feedback loop maintains a constant heat load on the Rb/noble gas sample cell due to illumination by the LDA, reducing fluctuations in the cell temperature and thus the Rb density.

A second feedback loop directly controls the Rb magnetization in the pump bulb, thereby indirectly controlling the LDA power on the Rb D1 resonance, and hence P_{rb} . The Rb magnetization is measured with the Zeeman drive technique described in Section 3.4.2. With a slight sacrifice in total Rb magnetization, the feedback loop stabilizes the Rb magnetization by adjusting the degree of circular polarization imparted to the LDA light by the waveplate bearing the moniker “LCVR” in Figure 3.16. The LCVR is a Liquid Crystal Variable Retarder, manufactured by Meadowlark Optics (www.meadowlark.com). The LCVR functions as a standard birefringent waveplate over a wide wavelength range (~ 200 nm), with the added property that the refractive indices of the fast and slow optical axes can be changed by applying an electrical waveform at frequency $\nu = 2$ kHz. For example, for light at $\lambda = 850$ nm, the retardance can be tuned over the range $\lambda/20$ to λ , thus enabling easy production of right- or left-circularly polarized light. If the LCVR is initially set such that its retardance results in $\approx 10\%$ less Rb magnetization than maximally possible, the second lock loop can correct for all reasonable temporal variations in M_{rb} .

This two-loop feedback technique produces a fractional stability of the Rb magnetization of $\sim 1 \times 10^{-3}$ as measured by a monitor lockin amplifier sensing M_{rb} in parallel with the control lockin. This is an improvement in Rb magnetization stability of roughly a factor of 10 over the free running LDA. Figure 3.18 compares the relative Rb magnetization levels without and with the two feedback loops engaged.

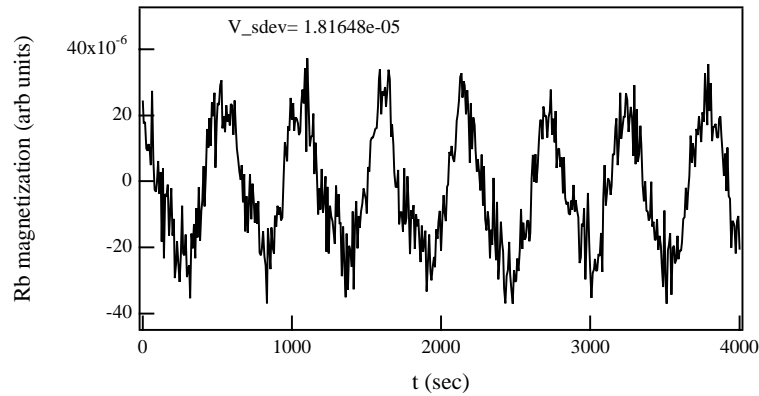
With the loops engaged, there is no discernible drift on the magnetization trace over timescales of several days.

Independent confirmation of stable Rb magnetization is provided by the improved amplitude stability of the DNGM ^{129}Xe and ^3He amplitudes. Figure 3.16 shows the typical observed improvement in maser amplitude stability of more than an order of magnitude when the LDA stabilization technique is employed. As a reminder, the importance of maser amplitude stability to DNGM performance is discussed in Section 2.6.

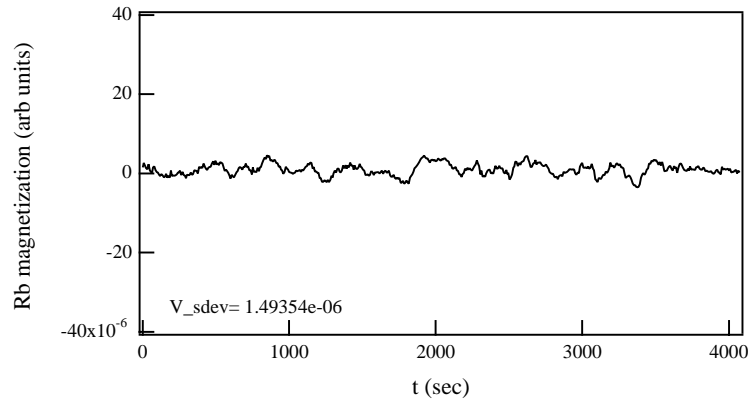
3.4.4 Future Work

While the optical control systems implemented to date have improved the amplitude and frequency stability of the DNGM substantially (Section 3.4.3), the addition of a spectrally stable, narrow-band probe laser (with requisite optical isolator) could improve the stability of the DNGM even further.

Recall that the level of longitudinal noble gas polarization in the DNGM pump bulb depends on both the Rb density, $[Rb]$; and the Rb polarization, P_{rb} (Equation 3.4). A single mode diode laser at the D1 resonance of Rb has a typical linewidth of ≤ 4 MHz [57], much less than the 16-18 GHz pressure-broadened Rb line in a typical DNGM cell. The beam from such a laser could be split into a linearly polarized portion and a circularly polarized portion, each optically chopped at different rates, passed through the DNGM cell, and detected with a photodiode. The linearly and circularly polarized beams would probe in real-time the density and polarization, respectively, of Rb in the pump chamber. Both signals could then be normalized by the total output power (now entirely on resonance) of the narrowband laser. Feedback to the pump chamber temperature control system would lock the Rb



Optical pumping light feedback loops not engaged.



Optical pumping light feedback loops engaged

Figure 3.18: Measured variation in the pump bulb Rb magnetization (M_{rb}) with and without the two optical feedback loops engaged. The mean value of the photodiode detector output voltage (≈ 1 mV) has been subtracted from both traces. The 1.4 mHz oscillations correlate with room temperature cycling of ~ 300 mK RMS, although the causality is not well understood. DNMG 17, page 120-138.

density, and feedback to the LCVR would lock the Rb polarization. This scheme has the additional benefit of providing knowledge of the mean temperature inside the pump bulb, via the formula:

$$[Rb] = \frac{10^{(9.318 - \frac{4040}{T})}}{1.38 \times 10^{-17} \cdot T}, \quad (3.5)$$

where $[Rb]$ is the Rb number density in cm^{-3} and T is the temperature in Kelvin [58].

3.5 Magnetic Field Environment

In this section we describe the implementation of the magnetic shields, solenoid and gradient trim coils used to produce the homogeneous magnetic field required for operation of the DNGM. For an excellent reference on some of the topics discussed here, the reader is referred to Hanson and Pipkin's paper of 1964 [59]. Note that a thorough discussion of the effectiveness of the ^{129}Xe co-magnetometer is presented in Section 3.6.

3.5.1 Magnetic Shielding

To provide isolation from inhomogeneous DC magnetic fields and ambient audio-frequency noise, the DNGM oven and solenoid assembly are housed inside three concentric, cylindrical magnetic shields (Figure 3.19). The shields are rolled from .062 inch thick μ -metal¹⁷, which was shaped, seam-welded and annealed prior to delivery.¹⁸ The effectiveness of the shields in screening out quasi-static magnetic fields was assessed in March, 1999. A fluxgate magnetometer probe [61] ($\sim 1 \mu\text{G}$

¹⁷The skin depth of μ -metal is .019" at 60 Hz and .003" at 1 kHz [60].

¹⁸CoNetic AA Alloy, available from Magnetic Shield Corp. 740 North Thomas Drive, Bensenville, Illinois.

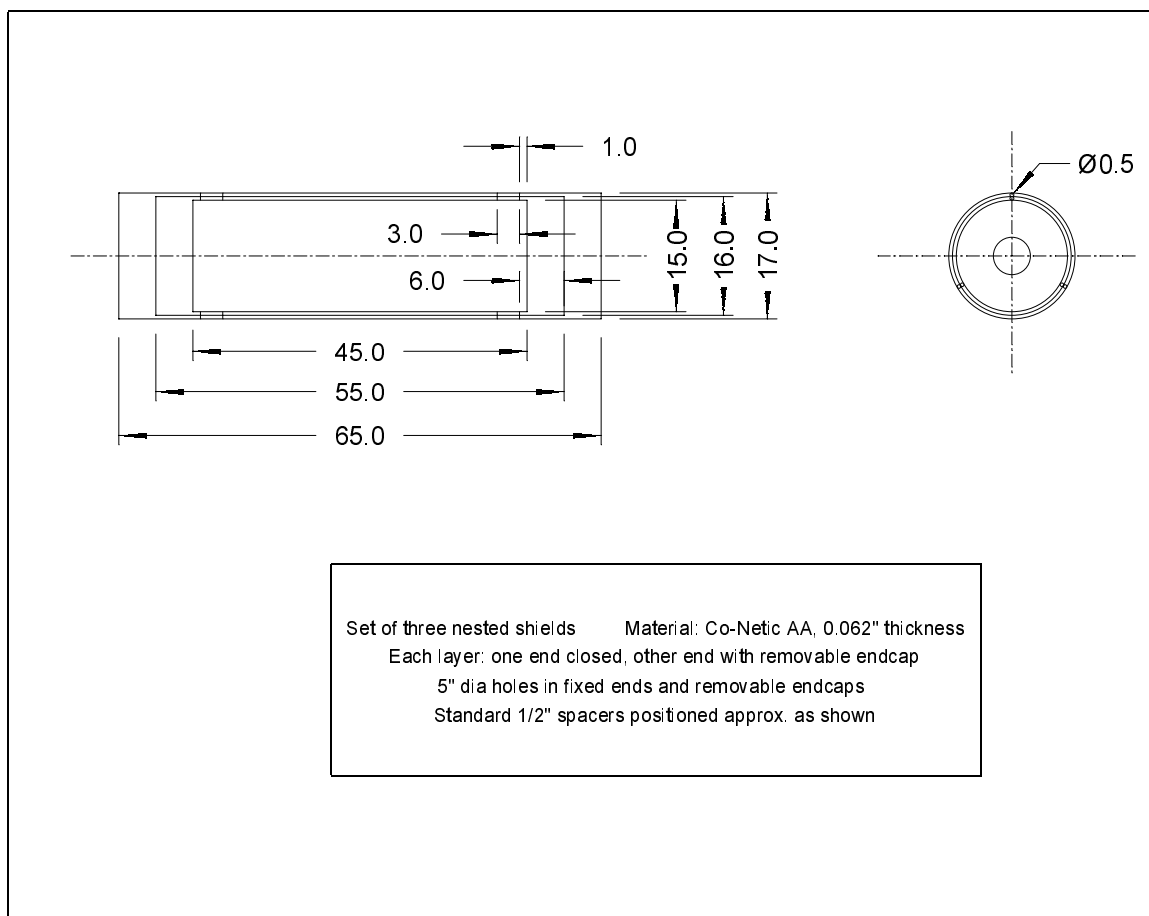


Figure 3.19: Scale drawing of the μ -metal shields used in the DNGM experiment. The ends of each shield feature 5.0 inch diameter holes to provide electrical, optical and blown air access to the DNGM oven assembly. The shields are oriented east-west in the laboratory frame, with the removable endcaps at the end farther from the optical pumping laser.

sensitivity) was placed in the center of the three nested shields. A hexagonal coil with a circumference of 25 feet was placed on each side the shield setup. The coil centers were separated by a distance of 90" and had area moments which were parallel to each other but perpendicular to the shield symmetry (z) axis. A current of 2 Amperes was passed through each coil and the z -component of the magnetic field at the probe location was recorded. The shields were then removed, and the measurement was repeated. The ratio of the measured field values $B_{noshields}/B_{shields}$ yielded a transverse shielding factor of $\approx 20,000$. To measure the longitudinal shielding factor, a similar measurement was carried out using a single square coil of circumference 25 feet, centered on the shield symmetry axis. The longitudinal shielding factor was measured to be ≈ 900 . To estimate the spatial dependence of shielding factors, the above measurements were performed with the probe at several different z -positions inside the shields, with the result that the transverse and longitudinal shielding factors varied by less than 10% when the probe was moved ± 10 inches along the z -axis.

After prolonged exposure to an ambient magnetic field (~ 1 gauss for both the DNGM solenoid field and the earth's field in the laboratory), μ -metal may acquire a degree of magnetization which degrades its ability to screen out external magnetic fields. To restore shielding effectiveness, a de-gaussing procedure was implemented following every re-assembly of the DNGM and after every reversal of the solenoidal magnetic field. De-gaussing was always done with the solenoid field on and with the system at its expected operating temperature. A large 60 Hz axial current ($I_z \approx 200 \cos(2\pi \cdot 60 \cdot t)$ A) was passed along a copper cable through the center of the shields, thereby saturating the magnetic domains in the μ -metal. Such a current reverses the field direction 60 times per second, forming a hysteresis loop. By increasing and then reducing the amplitude of the applied current to zero

in ~ 30 seconds, the area enclosed by such a loop shrinks to zero adiabatically, effectively demagnetizing the μ -metal. It should be noted that as of the writing of this thesis, the demagnetization procedure outlined above has produced only minimal improvements in the best-attainable values of the noble gas transverse coherence times (T_2). Because the skin depth of μ -metal is .019" at 60 Hz, it is likely that only the innermost annular portion of the inner shield (thickness .062") was de-gaussed effectively using available 60 Hz wall current. An alternating current source of frequency .5 Hz would produce a magnetic field with skin-depth $\approx .20$ ", which should be large enough to allow effective de-gaussing of all three shield layers at currents substantially less than 200 A, albeit with a very slow ramp-up/ramp-down cycle. Future work on the DNGM should incorporate such a current source.

3.5.2 Main Solenoid

The static field used to split the ^{129}Xe and ^3He nuclear Zeeman sublevels is produced by a single layer solenoid magnet wound from 25 AWG copper wire.¹⁹ The magnet was wound on an a hollow aluminum cylinder which was turned at approximately 10 rpm by one person while a second person laid wire with great precision onto the aluminum surface. The completed layer was painted with marine spar varnish (lacquer) to prevent small excursions of the windings due to vibrations and mechanical stress. Table 3.6 summarizes salient properties of the completed solenoid.

It should be mentioned that the first DNGM magnet (circa 1997) was a two-layer solenoid, designed primarily to reduce the effects of unpaired line-currents flowing to and from the ends of a single-layer solenoid. Laying wire on the surface of the first layer proved quite difficult, resulting in a systematic irregularity in the windings of

¹⁹25 HAPT polyester-amide wire, available from MWS Wire Industries, 31200 Cedar Valley Drive, Westlake Village, CA 91362, (818) 991-8553. Wire thickness = .020", including insulation.

solenoid parameter	value
diameter of windings	9.375 "
wall thickness	.060"
length	44.5"
turns density	50/inch
DC resistance	182.2 Ω
in-situ inductance	287 mH
vacuum inductance	\approx 250 mH

Table 3.6: Characteristics of the solenoid used in the DNGM experiment. The DC resistance was measured at room temperature. The in-situ inductance value refers to the measured inductance with the solenoid installed in its canonical location (in proximity to the magnetic shields and other metallic objects). The vacuum inductance is the rough estimated value for an isolated solenoid with the same geometry and turns density as the DNGM solenoid.

the second layer. Not surprisingly, the resultant field homogeneity when both layers were energized was ~ 3 times worse than when only the inner layer was energized (based on measurements of the best-attainable ^{129}Xe T_2 , logbook DNGM-3). The solenoid described in Table 3.6 (fabricated in 1999) was thus crafted with only one layer. Adverse effects on the maser T_2 arising from axial end-currents have not been observed, even when the current-carrying end leads (one lead at each end of the solenoid) are deformed and flexed during FID measurements. This is perhaps not surprising, as the DNGM cell resides approximately 5 solenoid diameters from either end of the magnet.

3.5.3 Estimate of Solenoid B_z Homogeneity

The presence of axial magnetic field gradients inside the DNGM, from any source, will reduce the transverse coherence times T_2 of the ^{129}Xe and ^3He ensembles and thus degrade the frequency measurement precision of the DNGM. Transport effects between pump and maser bulbs, as well as contributions from noble gas dipolar

fields to the dephasing time, made it unfeasible to use a standard two-bulb DNGM cell to assess the basic performance capabilities of the completed solenoid. Instead, such tests were performed (without shim coils) using a single bulb near-spherical cell which contained a mixture of 266 Torr of ^3He , 228 Torr of ^{21}Ne , and 31 Torr of N_2 buffer gas. The expression for T_2 in a spherical cell of radius R is given by [20]

$$\frac{1}{T_2} = \frac{8R^4 |\gamma \nabla B_z|^2}{175D} \quad (3.6)$$

where γ is the gyromagnetic ratio and D is the total diffusion constant, which under our operating conditions was given by

$$\begin{aligned} D_{he} &= \left(\frac{1}{D_{he-he}} + \frac{1}{D_{he-he}} + \frac{1}{D_{he-n2}} \right)^{-1} \\ &= \left(\frac{1}{6.96} + \frac{1}{4.936} + \frac{1}{27.51} \right)^{-1} \\ &= 2.61 \text{ cm}^2 \text{ sec}^{-1} \end{aligned}$$

With this test set-up $\gamma_{he} = 2\pi \cdot 3243.4 \text{ Hz/G}$, $R = .290 \text{ inches}$, and we measured a ^3He $T_2^{-1} = 8.2 \times 10^{-4} \text{ sec}^{-1}$ at a field of 1.5 Gauss. We thus determined a volume average estimate for the field inhomogeneity produced by the solenoid: $|\nabla B_z| \approx 20 \mu\text{G/cm}$. It should be noted that the laser was turned off during this measurement to eliminate the effect of Rb magnetization fields on the measured value of T_2 .

3.5.4 Gradient Trim Coils

To first order, axial magnetic field gradients induce the following relaxation rate for transverse noble polarization in a cylindrical cell [20]:

$$\frac{1}{T_2} = \frac{L^4 \gamma^2}{120D} \left| \frac{\partial B_z}{\partial z} \right|^2 + \frac{7a^4 \gamma^2}{96D} \left(\left| \frac{\partial B_z}{\partial x} \right|^2 + \left| \frac{\partial B_z}{\partial y} \right|^2 \right), \quad (3.7)$$

where D is the total diffusion constant, γ is the gyromagnetic ratio, L is the cell length, and a is the cell radius (in DNGM cells, ≈ 2 cm and .64 cm respectively). Recall that in our geometry \hat{z} points along the applied static magnetic field (quantization) axis and \hat{y} points along the direction of the transfer tube.

To provide a means for reducing the size of the components of ∇B_z , trim (also called “shim”) coils were laid into grooves on the DNGM oven shroud (Figures 3.8 and 3.9). Reference [59] discusses in some detail the theory and design of gradient trim coils. In the DNGM, the $\partial B_z/\partial x$ and $\partial B_z/\partial y$ coil pairs each have diameter 7.75”, center to center spacing 3.80”, and are wound from 25 AWG single-strand wire in a Golay (saddle) configuration. Figure 3.20 shows a schematic of the coil used to trim $\partial B_z/\partial y$. The x -trim coil is identical, but rotated by $\pi/2$. $\partial B_z/\partial z$ is of course trimmed by using a Maxwell pair,²⁰ with diameter 7.75” and center to center spacing 3.80 inches.

²⁰A Maxwell pair coil has only odd powers of z in the Taylor expansion of $B_z(z)$, thus producing no net field at $z = 0$. When separated by the anti-Helmholtz spacing (center to center spacing $\sqrt{3}$ times the coil radii), the coefficient of z^3 vanishes at $z = 0$. Clearly future work with the DNGM should incorporate properly spaced grooves for the Maxwell pair, as the present configuration yields a non-vanishing coefficient of z^3 at $z = 0$.

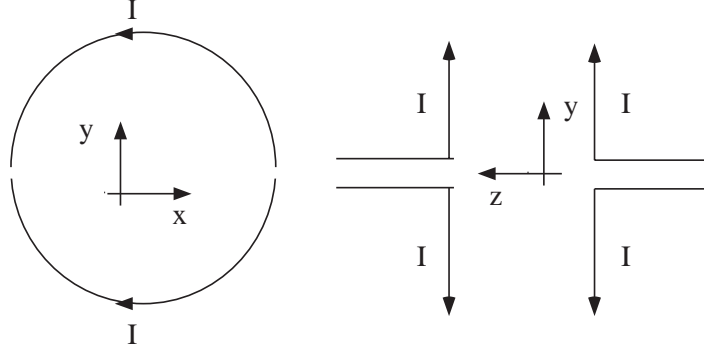


Figure 3.20: Schematic drawing of the y -trim coil used in the DNGM experiment. The x -coil is identical, but rotated by $\pi/2$. The trims are wound of 25 AWG wire in grooves whose dimensions are shown in Figure 3.8.

3.5.5 Maximization of the Transverse Coherence Time in the Absence of Masing

Maximization of T_2 for both ^3He and ^{129}Xe in a double-bulb cell consists of minimizing the components of the gradient of B_z (Equation 3.7). To do this, the oven is initially placed in the center of the solenoid. With both species fully polarized, the ^{129}Xe T_2 is measured from a free induction decay (FID, Section 4.2) using a small tip angle, $\theta_{tip} \approx 10^0$ (^{129}Xe is used because of its more rapid polarization. We generally found similar results if ^3He was used.) For recent cells, raw detected signal levels have been $\sim .2 \mu\text{V}$ just after the tip was applied. The oven is then moved ~ 1 cm in the $\pm z$ -direction and the measurement repeated. After four or five data at different z -positions are gathered, a curve fit to the function $T_2^{-1} = \gamma_0 + k(z - z_0)^2$ is performed. The oven is then placed at z_0 , the empirically determined “sweet-spot” of the solenoid, i.e., the position of maximum ^{129}Xe T_2 . Figure 3.21 shows a plot of the ^{129}Xe T_2 vs. z for an installation of cell SE3 (lab book DNGM-18, page).

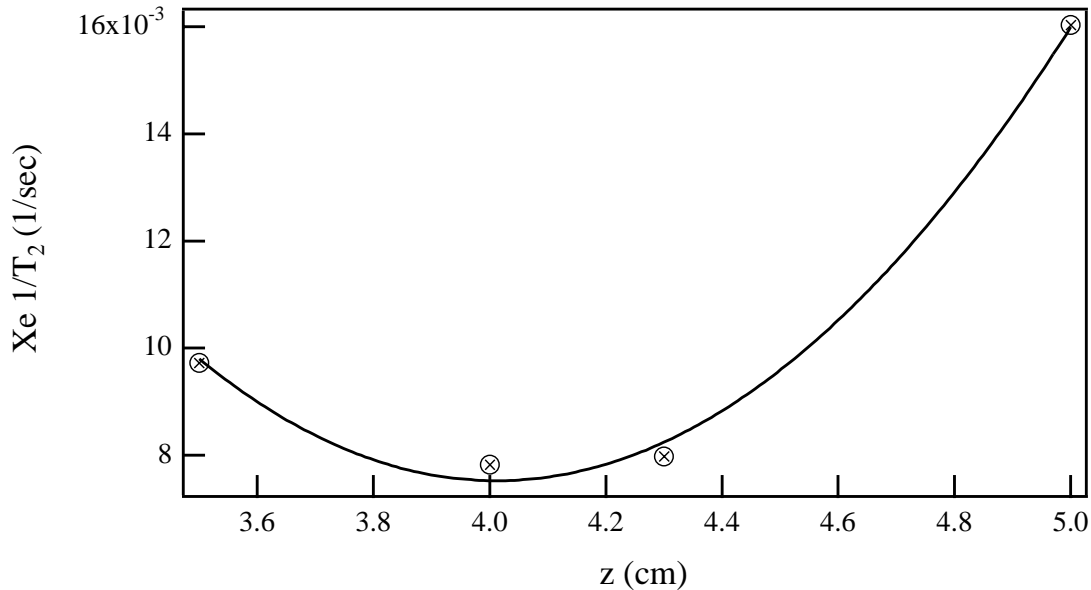


Figure 3.21: Plot of the measured $^{129}\text{Xe } T_2$ vs. z (the distance in cm of the maser cell center from the geometrical center of the solenoid; $+\hat{z}$ points away from the optical components and toward the cell). Cell SE3, DNGM-18, page 30.

After locating the oven at its optimal z -position, the current through each of the gradient trim coils (Section 3.5.4) is adjusted independently to further increase the measured $^{129}\text{Xe } T_2$ (i.e., to reduce the size of the gradient terms in Equation 3.7). The procedure followed is almost always the same for each installation. The trims are generally adjusted in the order y, z, x , corresponding to the fact that the y -trim generally has the largest effect on improving T_2 because of the dominant effect of field gradients created by noble gas magnetization in the transfer tube. Figure 3.22 shows a plot of the increased $^{129}\text{Xe } T_2$ as a function of the current in each gradient trim coil for a recent installation of cell SE3.

After adjustment of the gradient trim coils is complete, a final FID measurement extracts the optimized ^{129}Xe and $^3\text{He } T_2$ values. For example, results from the trimming effort shown in Figure 3.22 were $^{129}\text{Xe } T_2 \approx 330$ seconds, and $^3\text{He } T_2 \approx 170$ seconds.

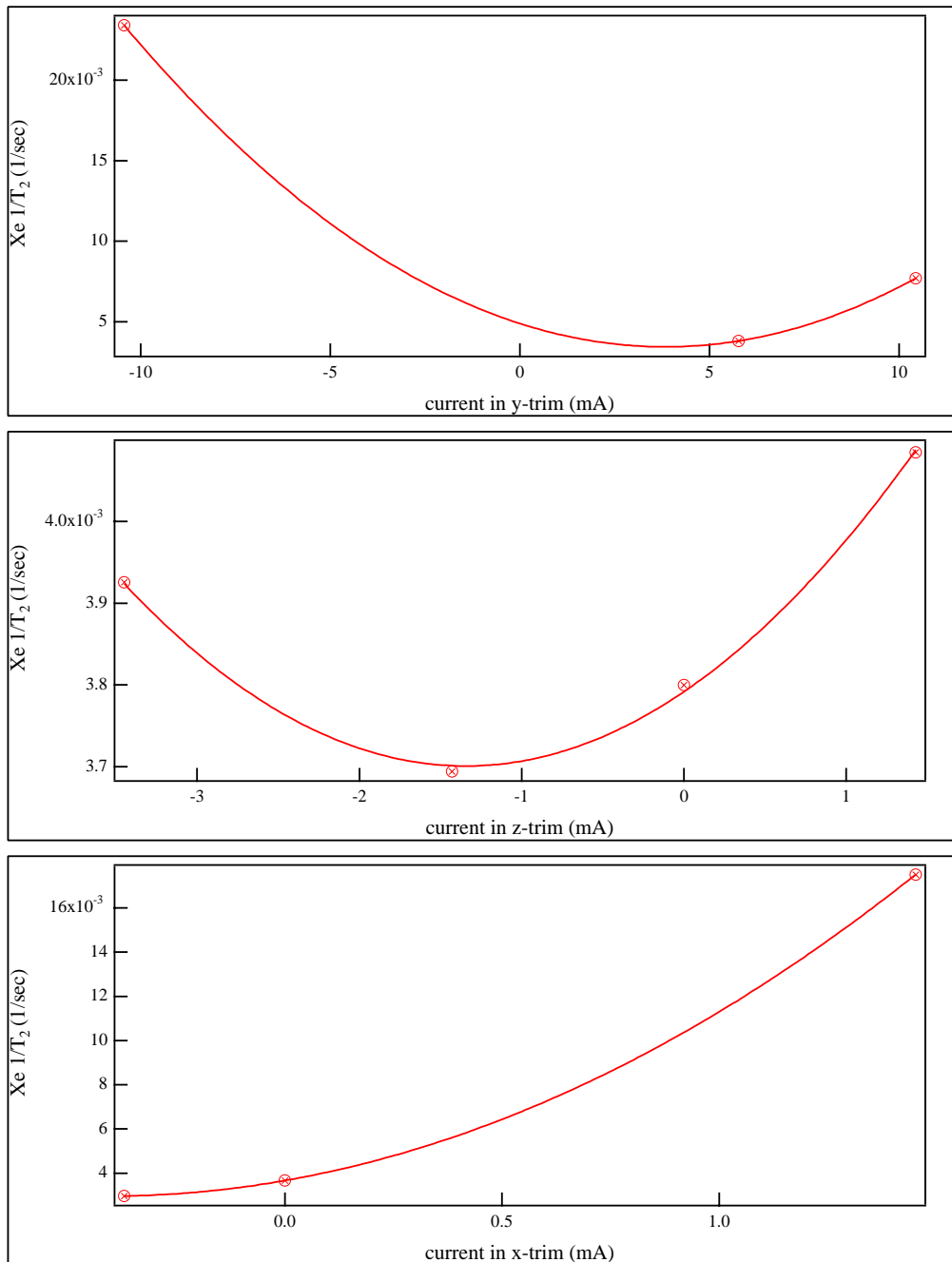


Figure 3.22: Example of the measured $^{129}\text{Xe } T_2$ as a function of the current in each gradient trim coil for a recent installation of cell SE3. Note that after the first trim is adjusted, its current is left at the optimum value and the second trim is optimized, and so forth. The trims were adjusted in the order y, z, x . DNGM-18 page 29.

3.5.6 B_z Inhomogeneity Induced by Noble Gas Magnetizations

It is well-known that the field inside a sphere of uniform magnetization is itself uniform.²¹ In a double-bulb maser cell, however, the noble gas magnetizations are non-uniform because of wall relaxation and spatially asymmetric input of magnetization into the maser chamber. In addition, the double-bulb geometry is far from spherical. The presence of noble gas magnetization can thus contribute to measurable inhomogeneities in the Zeeman field B_z . Here we describe a method (assuming a spherical maser cell geometry and ignoring inter-bulb transport as well as T_1 effects) which estimates the relative size of such noble gas-induced field gradients. We also describe how reduction of noble gas fill pressures since the fall of 1998 has largely eliminated the contribution of magnetization-induced field gradients to the observed noble gas T_2 s.

Effect of Noble Gas Induced Field Gradients in Early DNGM Cells

The transverse coherence time for an ensemble of noble gas atoms in a spherical cell is given by Equation 3.6. Let us write $\nabla B_z = \alpha \nabla B_{ng} + \nabla B_0$, where B_{ng} is the z -component of the dipolar field produced by the noble gas species under consideration at maximum polarization, and α ranges from 1 to -1, depending on the polarization.²² B_0 is the axial field from all other sources. Equation 3.6 can then be re-written as a quadratic function of α :

$$\frac{1}{T_2} = f(\alpha) = \frac{8R^4\gamma^2}{175D} \left[|\nabla B_0|^2 + 2 \cos(\theta_{rel}) |\nabla B_{ng}| |\nabla B_0| \alpha + |\nabla B_{ng}|^2 \alpha^2 \right], \quad (3.8)$$

²¹This result actually holds for any ellipsoid of revolution with a uniform magnetization.

²²We mean by $\alpha = 1$ that polarization is at its maximum practical value for the current system configuration, not that the polarization level is 100%.

where θ_{rel} is the mean angle between the gradient fields. If data are taken for several values of α and a curvefit is performed to extract the coefficients from the expression $f(\alpha) = c_0 + c_1\alpha + c_2\alpha^2$, the ratio of the size of the noble gas induced field gradient to other system gradients can be extracted:

$$\frac{|\nabla B_{ng}|}{|\nabla B_0|} = \sqrt{\frac{c_2}{c_0}} \quad (3.9)$$

Figure 3.23 shows plots of the measured ^{129}Xe T_2 as a function of the relative levels of ^3He and ^{129}Xe polarizations for an older, “full-pressure” DNGM cell ($P_{xe} = 200$ Torr and $P_{he} = 2300$ Torr). Notice the change in the value of T_2 as the longitudinal polarization level of either species varies. Figure 3.24 shows data from the same measurement, plotting the ^{129}Xe T_2^{-1} as a function of the relative ^{129}Xe polarization (i.e., α). An analogous result holds when the ^3He polarization is varied. Shown also in Figure 3.24 is the best fit parabola used to extract the coefficients c_j from Equation 3.9. For these gas pressures (typical for all early DNGM cells), the relative strength of the ^{129}Xe magnetic field gradient to gradients from other sources was $\sqrt{\frac{c_2}{c_0}} \approx 1.24$.

Amplitude-Based Trimming of the Transverse Coherence Time

Recall from Section 2.4 that the equilibrium values for P_\perp and P_z of a noble gas maser ensemble depend strongly on the transverse coherence time T_2 . But as shown above, the value of T_2 is itself a potentially strong function of noble gas longitudinal polarization, which is altered by active maser oscillation. The optimized settings of the gradient trim coils obtained by the FID methods of Section 3.5.5 are thus not necessarily the optimal values for operation under masing conditions. To improve system performance, it was necessary when using older, full-pressure DNGM cells

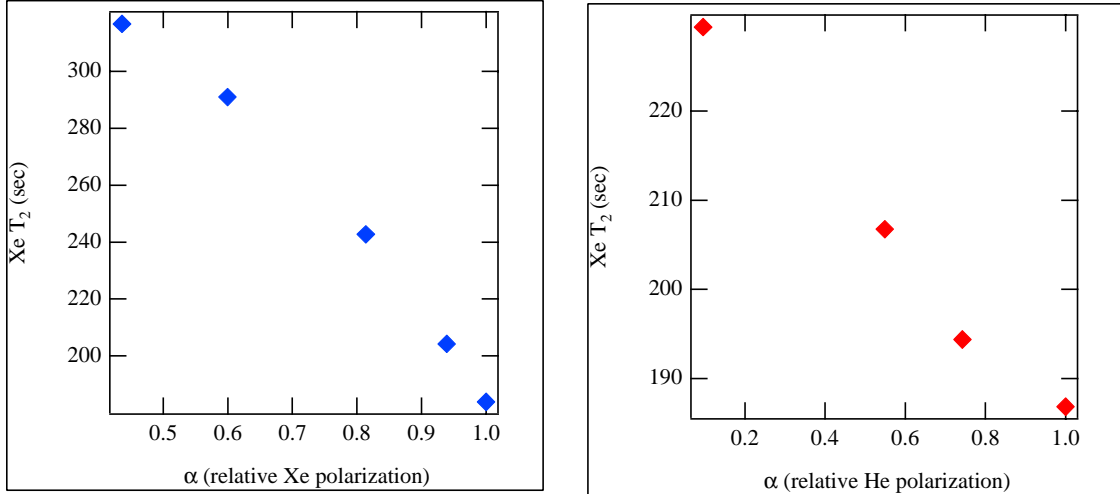


Figure 3.23: Measured ^{129}Xe T_2 as a function of the relative levels of ^3He and ^{129}Xe polarization. These data were gathered using an older, “full-pressure” cell, with a ^{129}Xe pressure of 200 Torr and ^3He pressure of 2300 Torr.

to implement also a program of maser-amplitude based T_2 trimming.

Under all operating conditions, the equilibrium maser amplitude is an increasing function of T_2 , all other parameters being held constant (Section 2.4). Amplitude-based T_2 trimming consists of making discrete adjustments to the current passing through each gradient trim coil until the ^{129}Xe maser amplitude is maximized, thereby implicitly improving the value of T_2 under masing conditions, while also explicitly increasing the maser output signal. Re-equilibration times for a slightly perturbed ^{129}Xe maser are typically ~ 2500 seconds. Adjusting all three gradient coils (done independently) typically required 12 hours; and in full pressure DNGM cells (pre-1999) this procedure increased both the ^{129}Xe and ^3He maser amplitudes by $\sim 5 - 10\%$.

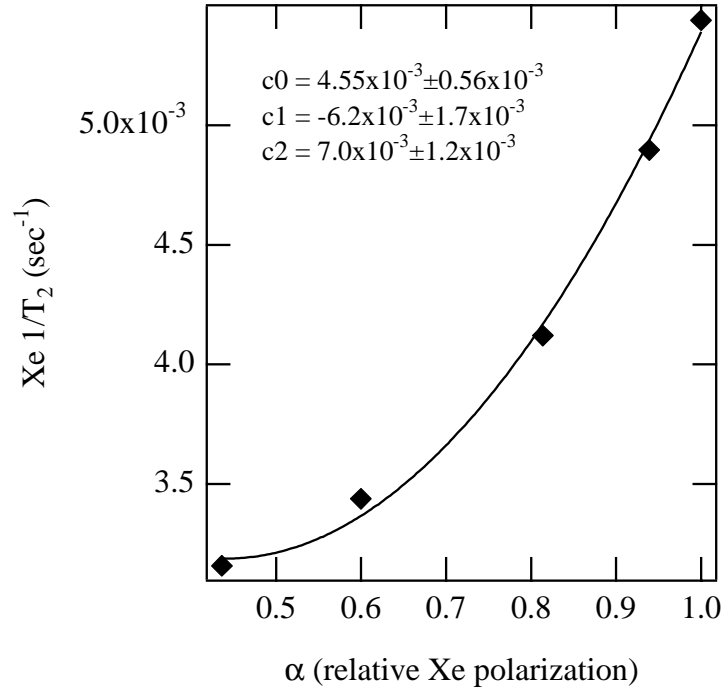


Figure 3.24: Measured $^{129}\text{Xe } T_2^{-1}$ as a function of the relative ^{129}Xe polarization. Shown also is the best fit parabola used to extract the coefficients c_2 and c_0 from Equation 3.9. These data were gathered using an older, “full-pressure” cell, with a ^{129}Xe pressure of 200 Torr and ^3He pressure of 2300 Torr.

Reduction of Noble Gas Fill Pressures

Although amplitude-based trimming was used to improve maser coherence times and output power, it was decided in the fall of 1998 to make a series of cells filled with lower noble gas pressures than had been used historically. Estimates indicated that the reduction of noble gas densities would result in smaller levels of steady-state noble gas magnetization (reducing the size of B_{ng}), while more rapid gas diffusion would leave the magnetization flux (and thus the maser power) effectively unchanged and would also reduce the spatial variation of the magnetization (and hence the gradient of B_{ng}).

For example, much of the symmetry test data presented in this thesis were

taken using such a cell, SE3, which was filled with noble gas at reduced pressures: 150 Torr ^{129}Xe and 1100 Torr ^3He . As desired, the measured T_2 for the ^{129}Xe and ^3He ensembles in cell SE3 was not a strong function of the polarization level of either species. For example, the best-attainable ^{129}Xe T_2 varied by less than 10% when α of both species was varied from 0 to 1 (compare with Figure 3.24). Given this insensitivity of T_2 to noble gas magnetization levels, it was not surprising that amplitude-based trimming for cell SE3 did not result in any increase of maser amplitudes. As a further test of the insensitivity of T_2 to magnetization levels in the reduced-pressure cells, the ^{129}Xe T_2 of cell SE3 was trimmed using the FID methods of Section 3.5.5. The resonator was next turned on to resonance, and the system allowed to attain maser equilibrium. The resonator was then disengaged and the T_2 of the subsequent ^{129}Xe ringdown was measured to be 299 seconds, essentially unchanged from the initial FID value with both species fully polarized and the resonator off.

Although lower gas fill pressures appear to have reduced greatly the contribution of magnetization-induced field gradients to the transverse dephasing rate, we are considering lowering the ^{129}Xe pressure even further for future work. In current cells, the ^{129}Xe storage time in the maser bulb ($> 2,000$ sec) is substantially longer than the ^{129}Xe T_2 (~ 300 sec). This difference between storage time and T_2 is not ideal, as depolarized ^{129}Xe atoms contribute nothing to the maser output power, but do impede the flux (energy transport) of polarized atoms into the interaction region, and may degrade the DNGM's co-magnetometry by inhibiting motional averaging of atoms in the maser bulb. Increasing the diffusion rate of noble gas polarization from the pump chamber to the maser chamber by lowering the ^{129}Xe pressure could result in greater maser powers for both species, and improved co-magnetometry. Future work on the DNGM should include a thorough test of cells with ^{129}Xe pressures in

the range 20 - 150 Torr.

3.5.7 Choke Coils

Good solenoid design and proper use of the gradient trim coils were crucial for producing the long transverse coherence times T_2 required for stable ^{129}Xe and ^3He maser oscillation. To further improve T_2 , and also to improve the effectiveness of the ^{129}Xe co-magnetometer (Section 3.6), a simple attempt has been made to improve the spatial uniformity of the masing (and freely precessing) noble gas ensembles. The lowest portion of the transfer tube of each DNGM cell is wrapped with a series of four adjacent “choke coils,” each one consisting of six turns of 25 AWG copper magnet wire wound in a single layer, as shown in Figure 3.25. The segmented design allows the reactive magnetic fields produced by the choke coils to adopt (to some extent) a profiled spatial dependence, thus providing more effective flux exclusion.

Although a quantitative theoretical description of the interaction of the choke coils with the noble gas spins and with the resonant pickup coil has not been carried out, the qualitative effect is clear. Reactive back-currents (due to Lenz’s Law) are induced in the choke coils by the time varying magnetic fields produced by the resonant pickup coil and also by the precessing noble gas magnetizations. The magnetic fields produced by these choke coil currents tend to reduce the net transverse tipping field B_\perp in the transfer tube. This reactive field also tends to reduce the contribution of precessing magnetization in the transfer tube to the mean magnetization signal sensed by the detection coil. Reducing contributions from atoms in the transfer tube should improve the effective homogeneity of B_z , and hence T_2 , of the masing ensembles. It should also improve the spatial uniformity of both maser ensembles, thereby improving the DNGM co-magnetometry. Table 3.7 shows the

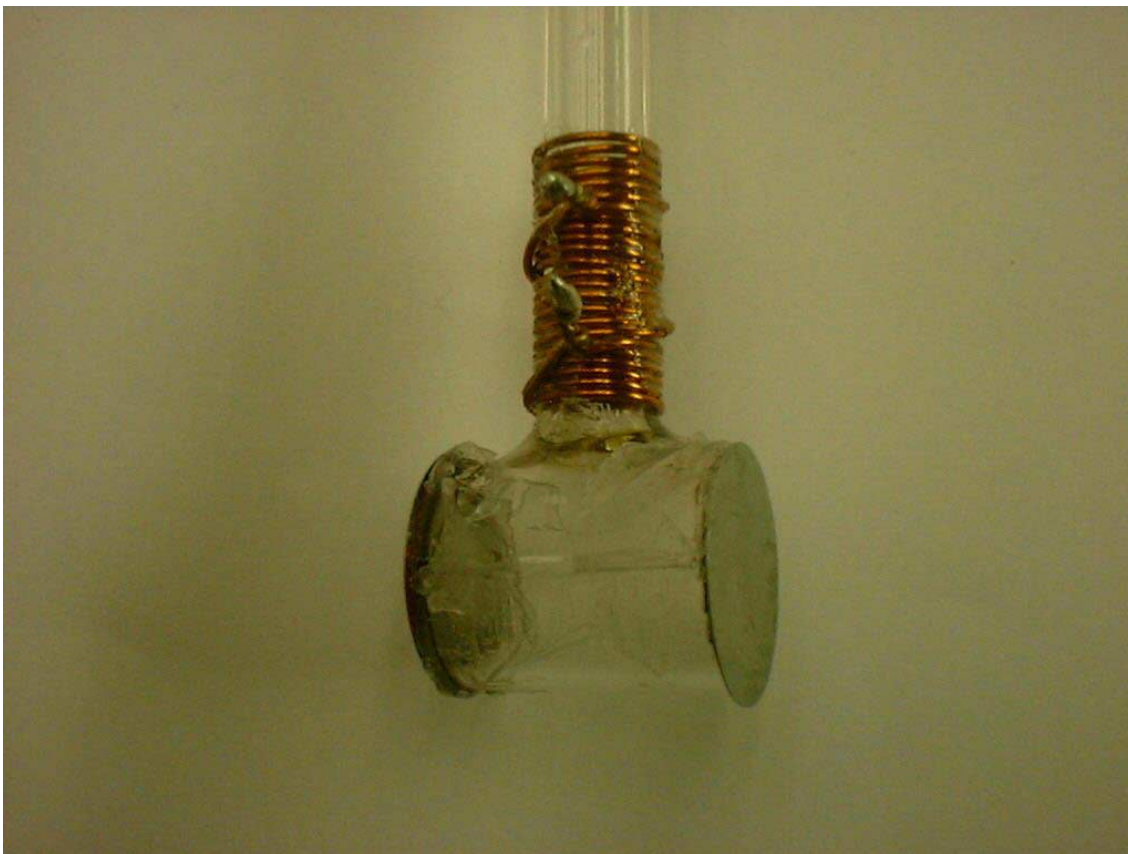


Figure 3.25: Photograph of a typical DNGM EDM cell, with “choke coils” installed, as described in Section 3.5.7.

best attainable values of T_2 for a typical full-pressure DNGM cell, with and without choke coils installed. A direct comparison of co-magnetometer effectiveness with and without choke coils has not been carried out.

3.5.8 Magnetic Field Stabilization

The solenoid and gradient trim coils are driven by a four-channel, homemade current controller box. The output current on each channel is stable to approximately 10 ppm when free-running. In order to further stabilize the magnetic field environment and provide real-time co-magnetometry, the solenoid field is controlled by phase-

Species	T_2 without choke coils (s)	T_2 with choke coils (s)
^{129}Xe	146	185
^3He	99	132

Table 3.7: The best attainable values of T_2 for DNGM cell 37, with and without choke coils installed, DNGM 10, pages 117, 124, and 127.

locking the higher SNR ^{129}Xe maser to an ultra-stable reference oscillator, as shown in Fig. 3.1. For example, in the recent data runs of May 2000, the ^{129}Xe maser was locked at a frequency $\nu_{xe} = 1709.42$ Hz. Section 3.7 describes in detail the signal detection and processing systems in the DNGM. Here we focus on the operation of the phase-lock loop (PLL), assuming other components are properly implemented.

After being buffered and multiplied 5000x by a low noise pre-amplifier (Sec. 3.7), the ^{129}Xe maser signal is sent to a Stanford Research System (SRS) digital lockin-amplifier. This control lockin serves as a low-pass filter as well as a phase-sensitive detector (PSD) used in the operation of the loop, with an output of 10 Volts per 180 degrees of phase difference between the measured ^{129}Xe signal and the stable reference oscillator (a Wavetek model synthesizer phase-locked to a 5 MHz signal derived from a hydrogen maser in our laboratory). The output signal from the PSD is then processed by a high-performance Linear Research 130 (LR130) PID (Proportional-Integral-Differential) controller, the output of which is used as the feedback adjustment to the solenoid current.

The performance of the magfield PLL is assessed and optimized by examining ^{129}Xe phase-residuals (Sec. 2.5) over a 500 second interval, and then adjusting loop parameters until the ^{129}Xe phase data acquired with the monitor lockin amplifier (Sec. 3.7) are as stable as possible. In practice, three parameters are adjusted in order to improve lock loop performance. The low-pass filter on the PSD is always op-

erated with a roll-off of 12 db/octave, while the high-frequency cutoff on the LR130 output is always set to a frequency of 333 Hz. The differentiation time constant is kept at one-third the value of the integration time, as specified in the instrument documentation. The remaining adjustable parameters are thus the time constant of the PSD low-pass filter, and the integration time and DC gain of the LR130 PID controller. Table 3.8 shows example measurements of the standard deviation of the ^{129}Xe phase residuals (σ_ϕ) for several different settings of the adjustable loop parameters. The DNGM is generally operated using the loop parameters that yield the smallest value for σ_ϕ . If two sets of parameters yield roughly the same value for σ_ϕ over 500 second intervals, then longer ($\sim 6,000$ seconds) scans are compared to determine the parameter set that results in the smallest Allan deviation in ν_{he} . Typically, proper trimming of the PLL improves the short-term phase stability of the ^{129}Xe maser by $\sim 50\%$ after initial installation of the DNGM, although it is not uncommon for PLL trimming to result in ten-fold improvements in ^{129}Xe maser phase noise. The frequency stability of the free-running ^3He maser can be improved by a factor of ~ 2 through proper lock loop optimization.

3.6 Co-magnetometer Effectiveness

The average z -component of the magnetic field seen by each maser is not static in time. Fluctuations in B_z can result from changes in polarization distributions, from the penetration of slowly-varying ambient magnetic fields into the interaction region, or from the presence of small DC currents flowing through the high voltage leads in an EDM cell (as described in Chapter 6). This section quantifies the effectiveness of the phase-locked maser in nulling out free-running maser frequency shifts due to such magnetic field fluctuations.

σ_ϕ (mrad)	PID Gain	PID integration time constant (sec)	PSD time constant (msec)
.257	.1	.1	3
.251	.1	.1	10
.248	.1	.1	30
no capture	.1	.1	100
4.40	.1	.3	1
2.5	.1	.3	3
.944	.1	.3	10
.280	.1	.3	30
.357	.1	.3	100
.350	.3	.1	3
.246	.3	.1	10
2.61	.3	.1	30
no capture	.3	.1	100

Table 3.8: Example measurements of the standard deviation of ^{129}Xe maser phase residuals over a 500 second interval as a function of adjustable magnetic field lock-loop parameters (lab book DNGM-16, p. 73). The data were sampled at 1 Hz with a lockin filter bandwidth of 125 mHz and a roll-off of 12 dB/octave.

3.6.1 Theoretical Description

For a noble gas species with gyromagnetic ratio γ_{ng} , the instantaneous detected maser frequency²³ takes the form

$$2\pi\nu_{ng} = \frac{\int \gamma_{ng}\eta(\mathbf{r})B_z(\mathbf{r})P_\perp(\mathbf{r})dV}{\int \eta(\mathbf{r})P_\perp(\mathbf{r})dV}, \quad (3.10)$$

where $B_z(\mathbf{r})$ is the z-component of the magnetic field, $P_\perp(\mathbf{r})$ is the noble gas transverse polarization, and $\eta(\mathbf{r})$ is a geometry-dependent factor which accounts for the relative degree of magnetic flux coupling between atomic spins at position \mathbf{r} and the resonant detection coil.

Suppose the DNGM is initially operating in a magnetic field $B_z(\mathbf{r}) = B_0(\mathbf{r})$,

²³We are only considering the contributions to the maser frequency that are magnetic in origin.

with average maser frequencies ν_{xe} and ν_{he} given by Eqn. 3.10. Suppose further that the z -component of the magnetic field changes by a small amount $\Delta B(\mathbf{r})$. With the ^{129}Xe maser phase-locked, the PID servo will adjust the solenoid current to produce a change ΔB_{sol} in the z -component of the solenoid field such that the average detected ^{129}Xe maser frequency does not change:

$$\Delta\nu_{xe} = \frac{\gamma_{xe} \int \eta(\mathbf{r}) P_{\perp,xe}(\mathbf{r}) (\Delta B(\mathbf{r}) + \Delta B_{sol}(\mathbf{r})) dV}{\int \eta(\mathbf{r}) P_{\perp,xe}(\mathbf{r}) dV} = 0 \quad (3.11)$$

The change in the mean detected ^3He frequency is then given by

$$\Delta\nu_{he} = \frac{\gamma_{he} \int \eta(\mathbf{r}) P_{\perp,he}(\mathbf{r}) (\Delta B(\mathbf{r}) + \Delta B_{sol}(\mathbf{r})) dV}{\int \eta(\mathbf{r}) P_{\perp,he}(\mathbf{r}) dV} \quad (3.12)$$

If the ^3He and ^{129}Xe polarization ensembles have identical spatial distributions, $P_{\perp,he}(\mathbf{r}) \propto P_{\perp,xe}(\mathbf{r})$, then the ^3He maser frequency shift is also zero. In reality, ^{129}Xe and ^3He have quite different physical and chemical properties (see Table 1.1), hence the masing ensembles for each species are distributed differently through the cell and the ^{129}Xe maser co-magnetometer will not function perfectly to isolate the ^3He maser frequency from variations in B_z .

3.6.2 Experimental Measurements

We now describe a series of measurements²⁴ done to estimate the effectiveness of the ^{129}Xe maser co-magnetometer in response to different types of magnetic field changes $\Delta B(\mathbf{r})$. In the first set of measurements, the gradient trim coils described in section 3.5.4 were used to generate magnetic fields with three different spatial

²⁴Lab books DNGM-14 and DNGM-15

gradient coil	$\delta\nu_{he}/\delta I_{trim}$ (Hz/A)	$\delta\nu_{he}/\delta I_{trim}$ (Hz/A)	nulling ratio
	^{129}Xe maser free-running	^{129}Xe maser phase-locked	
x -trim	290	.034	8520
y -trim	236	.275	859
z -trim	110	.192	572

Table 3.9: Results of co-magnetometer measurements carried out in April, 1999.

dependencies:²⁵

$$\begin{aligned}
z - trim : \quad \Delta B_{1z}(x, y, z) &\approx \Delta B_{1z}(z) \approx B_{1z}(0) + z \cdot \partial B_{1z}(0)/\partial z + \dots \\
y - trim : \quad \Delta B_{2z}(x, y, z) &\approx \Delta B_{2z}(y) \approx B_{2z}(0) + y \cdot \partial B_{2z}(0)/\partial y + \dots \\
x - trim : \quad \Delta B_{3z}(x, y, z) &\approx \Delta B_{3z}(x) \approx B_{3z}(0) + x \cdot \partial B_{3z}(0)/\partial x + \dots \quad (3.13)
\end{aligned}$$

With both masers free-running, a single trim coil was turned on to induce a measurable frequency shift in both species. The ^{129}Xe maser was then phase-locked, and the measurement was repeated. The results shown in Table 3.9 reveal that the ^{129}Xe maser co-magnetometer is not perfect, likely due to different spatial distributions of the ^{129}Xe and ^3He masing ensembles. Subsequent measurements were thus performed to assess the potential impact of imperfect co-magnetometry on the LLI and EDM tests reported in this thesis.

The sensitivity of the *CPT* and Lorentz symmetry tests detailed in Chapter 5 would be most compromised by magnetic field fluctuations with diurnal (sidereal) periodicity. Because the longitudinal shielding ratio (see Sec. 3.5.1) of the μ -metal shields is approximately 20 times worse than the transverse shielding ratio, the

²⁵Recall that in our coordinate system the z -axis (quantization axis) points along the maser chamber symmetry axis; the y -axis points along the direction of the transfer tube; and the x -axis points in the direction of $\hat{\mathbf{y}} \times \hat{\mathbf{z}}$.

co-magnetometer response of the DNGM to an applied longitudinal external field would set a strong upper bound on the systematic error caused by *all* ambient field fluctuations. With both masers free-running, current was passed through a square coil (circumference = 25 feet) looped around the center of the shield and solenoid setup, resulting in a .510 Hz shift in the ^3He frequency. The measurement was repeated with the ^{129}Xe maser phase-locked, resulting in a ^3He maser frequency shift of 4.1 μHz . The co-magnetometer nulling ratio for longitudinal (east-west) fluctuating fields in the laboratory was thus determined to be $\approx 124,000$. The typical measured drift in the laboratory magnetic field over a day is ~ 1 mG. Assuming a longitudinal shielding ratio of 900 (Sec. 3.5.1) and a co-magnetometer nulling ratio of 124,000, the ^3He frequency drift over a day would be ~ 26 nHz. The diurnal components of such drift effects are typically much less than 10% of the total drift, resulting in a conservative bound of 3 nHz on a co-magnetometer systematic error in the LLI measurement reported in Chapter 5. This error is well below the present sensitivity of the DNGM to *CPT* and Lorentz violation.

For the ^{129}Xe EDM search, the most serious systematic maser frequency shift would be one whose signature correlated linearly with the applied electric field. A magnetic field resulting from current flow through the high voltage leads and across the surface of an EDM cell could cause such a shift. We now describe a measurement to assess the effectiveness of the ^{129}Xe maser co-magnetometer at nulling out frequency shifts due to leakage currents.

Six strands of 25 AWG copper wire were spaced equally and then laid longitudinally along the maser chamber surface of cell S3 (see Fig. 3.26). The wires were brought to a point at the ends of the maser chamber and braided to form a multi-strand single wire which was then attached to the high voltage leads typically used in the EDM measurements described in Chapter 6. With the ^{129}Xe maser

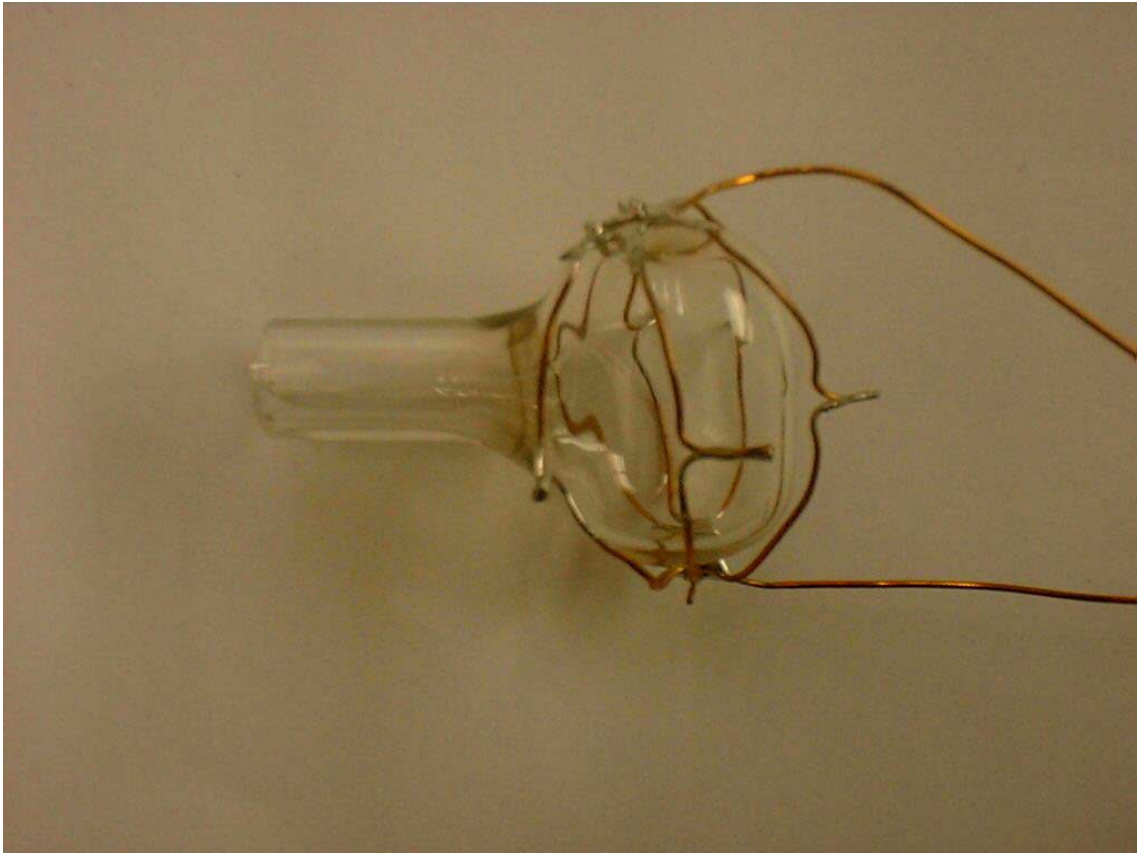


Figure 3.26: A photograph of DNGM cell S3, wired in such as way as to permit generation of a magnetic field at least as inhomogeneous as that which would result from the flow of leakage currents from the high voltage supply.

phase-locked, a current was passed through the leads, thus simulating the magnetic field shape that could result from the flow of leakage currents across the cell surface. The result was a normalized frequency shift $\Delta\nu_{he}/\Delta I_{leak} \approx 1.14$ Hz/Amp. Using a Keithley electrometer, the electrical resistance of several EDM cells was measured to be $\sim 5 \times 10^{13}$ Ω . Assuming a potential difference of 10 kV across an EDM cell, the resulting systematic frequency shift from likely leakage currents was thus estimated to be ~ 0.20 nHz, which is well below the current frequency sensitivity of the experiment.

3.7 Signal Detection System

Figure 3.27 shows a schematic of the DNGM signal detection system. Time-varying magnetic fields produced by precessing noble gas atoms are detected by an inductive pickup coil (L_2, R_2) located in proximity to the DNGM maser bulb. When doing FID measurements, the system is operated off-resonance, with switch S_1 open.²⁶ Closing switch S_1 provides positive feedback to both noble gas species via a dual-resonance tank circuit, formed by an external inductor coil (L_1, R_1) and ultra-stable tuning capacitors (C_1, C_2). Transverse Rabi pulses are applied to the system by closing switch S_2 and introducing a programmable function generator into the circuit. Detected atomic signals are taken as sinusoidally varying voltages across the capacitor C_2 .²⁷ The following sections describe in detail the design and operation of components of the DNGM signal detection system introduced above.

²⁶ C_2 is sufficiently small that the single resonance formed when S_1 is opened is ≥ 15 kHz, well above the operating frequencies of either maser.

²⁷Although the signal is now read across C_2 , it could in principle be taken across C_1 or L_1 . The choice is determined by matching the circuit output impedance to the low-noise preamplifier. At present, good matching is obtained at the atomic resonances when extracting the signal across C_2 . Simultaneous comparison of signals taken across L_1 and C_2 has not yielded significant differences for the SNR of either noble gas species.

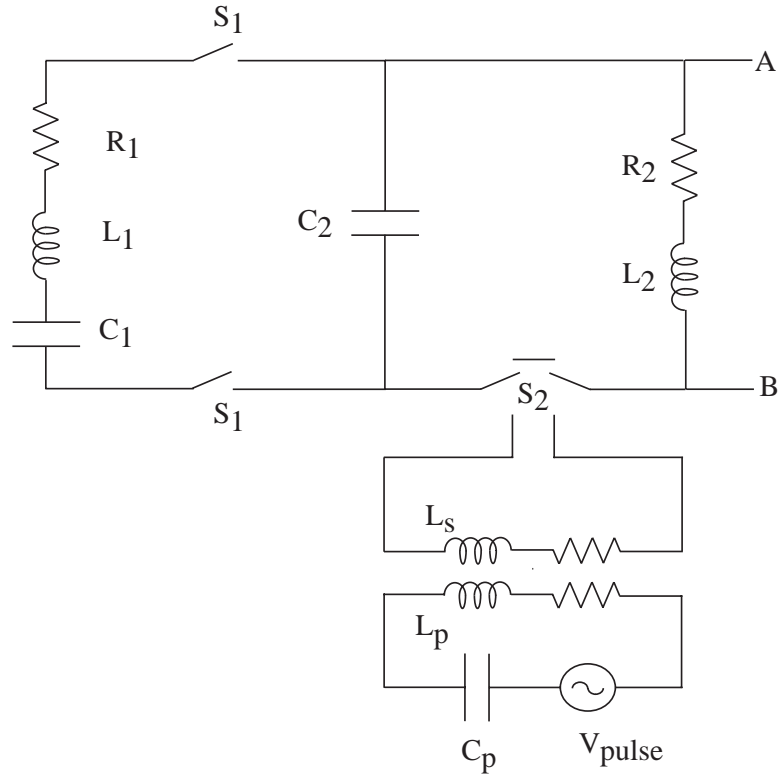


Figure 3.27: A schematic of the DNGM signal detection system. L_2, R_2 are from the inductive pickup coil inside the maser oven, while C_1, L_1, R_1 are contained in a smaller set of magnetic shields separate from the maser oven. C_2 is a fine-tuning capacitor which resides in the external aluminum junction box. The pulse coil is coupled into the circuit by closing switch S_2 , and is driven by inductive coupling between L_s (secondary) and L_p (primary), as shown.

3.7.1 Measuring Coil Q , L , and R_{ac}

Design and implementation of resonant circuitry for the DNGM experiment involved the fabrication of several home-made inductive coils. Here we describe the procedure used to measure the inductance, quality factor, and AC resistance of such coils.²⁸

Consider a simple $R-L-C$ series circuit where R and L are distributed together, as in an inductive coil of the type used in the DNGM. C is an adjustable, low-loss capacitor whose value is known with good precision. An AC voltage is induced across L by bringing into proximity a low-inductance broadcast coil driven by a variable frequency function generator. In order to measure the maximum current passing through the $R-L-C$ circuit as a function of drive frequency, it is usually easiest (when possessing only voltage-sensing lockin amplifiers) to measure the voltage V_{mon} across a very small monitor resistor $r \sim 0.5 \Omega$ inserted in series with the capacitor C .²⁹

The value of the drive frequency at which $|V_{mon}|$ attains its maximum value $|V_{max}|$ is the resonant frequency ν_0 of the circuit. Knowing C , the value of L is obtained from the relationship $L^{-1} = 6\pi^2\nu_0 C$. The quality factor Q_{coil} of the inductor is measured by locating the “half-power” points of the circuit:

$$Q_{coil} = \frac{\nu_0}{\nu_+ - \nu_-}, \quad (3.14)$$

where ν_{\pm} are the frequencies at which $|V_{mon}| = |V_{max}|/\sqrt{2}$. Recalling the expression

$$Q_{coil} = \frac{2\pi\nu_0 L}{R_{eff}}, \quad (3.15)$$

²⁸During these measurements, we kept the inductor several coil diameters away from metallic objects with which it might experience substantial inductive or capacitive coupling.

²⁹In general, all system measurements should be performed for several values of the monitor resistor r and then extrapolated to zero r . In practice, corrections for small, finite r were found to be insignificant.

we can write the AC resistance of the circuit as

$$R_{ac} = \frac{2\pi\nu_0 L}{Q_{coil}} - R_{dc}, \quad (3.16)$$

where R_{dc} is the simple DC resistance of the circuit ($R_{dc} \gg r$). Figure 3.28 shows a plot of Q_{coil} and R_{ac} as a function of frequency for the external resonator coil ($L = 104$ mH) presently in use (Section 3.7.3).

It should be mentioned that measuring Q_{coil} is not equivalent to measuring the effective coupling ηQ_{eff} of the noble gas polarization vector P_{\perp} to the resonant tank circuit. In practice, the strength of the effective coupling of P_{\perp} to the dual resonator is assessed by measuring the radiation damping time τ_{rd} of each noble gas species (Section 4.3). A measurement of ηQ_{eff} could, however, be performed by fabricating a small drive coil whose free current distribution duplicated the bound current distribution of the precessing noble gas ensembles, and then measuring the drive coil's coupling to the pickup coil/resonator circuit.

Q_{eff} is defined in Appendix A as the modulus of the pickup coil inductor impedance over the total impedance of the dual resonator circuit, as seen by the atoms. Measurement of the on-resonance Q_{eff} (and hence η , once ηQ_{eff} has been measured as described above) is straightforward. To determine its value, one must: (i) drive the resonator at resonance with a drive coil in proximity to the pickup coil; (ii) measure the current in both the drive coil and in the pickup coil (using small witness resistors); (iii) measure the mutual inductance of the coils; and (iv) measure the self-inductance of the pickup coil. Knowing the mutual inductance and the drive coil current determines the voltage induced in the pickup coil. Knowing the induced voltage and the induced current determines the total circuit impedance at resonance. Knowing the pickup coil self-inductance determines its impedance at

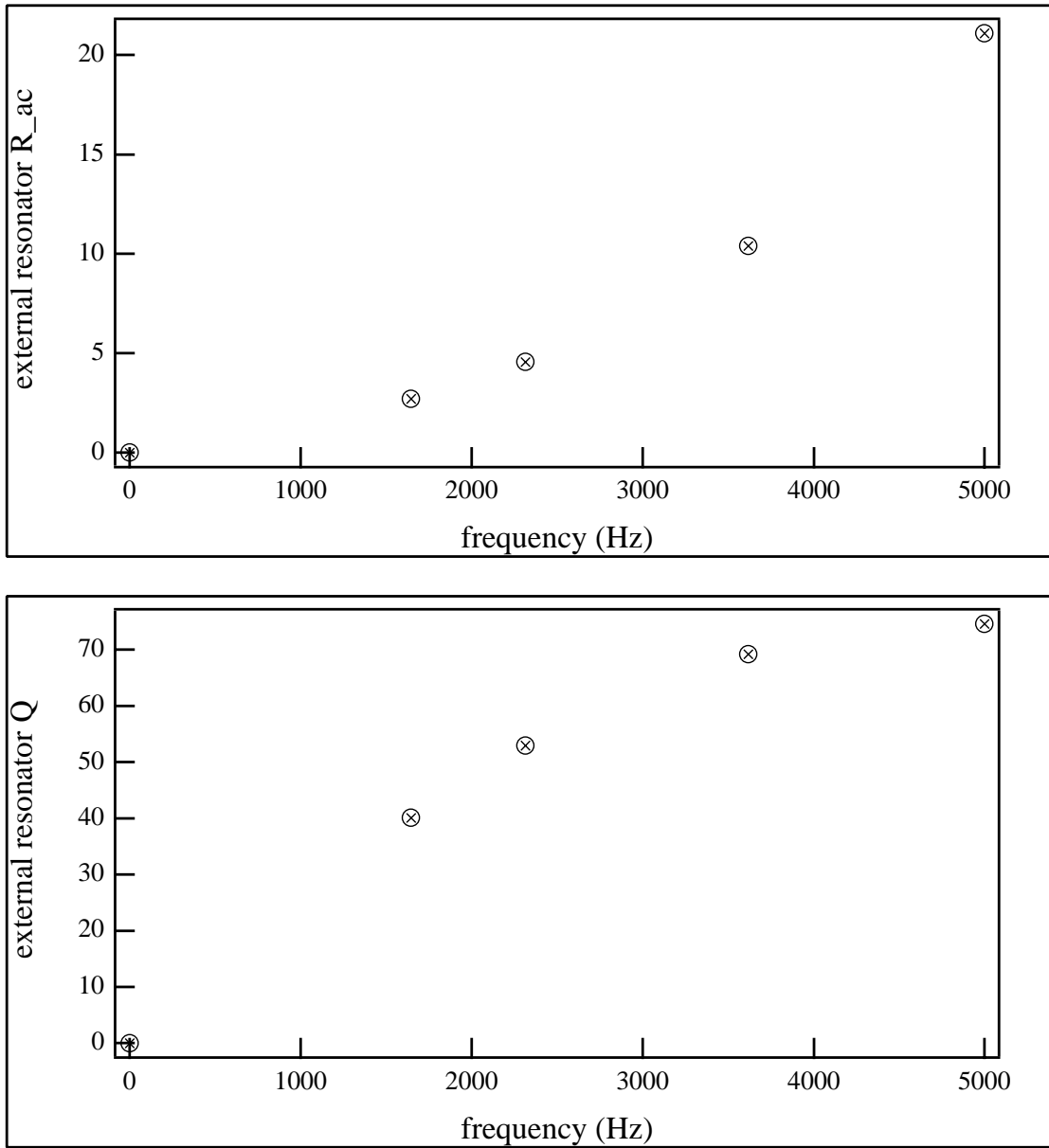


Figure 3.28: Plot of Q_{coil} and R_{ac} as a function of frequency for the external resonator coil ($L = 104$ mH, $R_{dc} = 21.4\Omega$) presently in use (Section 3.7.3). DNGM-15, page 108.

resonance, thus determining Q_{eff} is now determined.

3.7.2 Cabling and Grounding

The DNGM cabling and grounding schemes follow standard principles laid out in the literature (for example, [60]). Electronic instruments used in the DNGM experiment are mounted in three steel equipment racks, each of which has its own six outlet surge/power strip which is in turn plugged into one of four outputs on a 110 VAC Ferrups Uninterruptable Power Supply (UPS). Each output of the UPS is grounded, with 4 AWG copper welding cable connecting the power strip ground on each rack directly to the nearest earth ground. All maser signals are measured differentially, and are routed between points by shielded, twisted-pair or semi-rigid coaxial cable. The shield of each cable is connected to signal ground, which is floated via a 10 k Ω resistor to earth ground. The 10 k Ω resistor was added in 1997 to break ground loops, and has greatly reduced the presence of small bleedthrough signals on the maser traces.

The signal from the the maser pickup coil (L_2, R_2) is carried by a low capacitance (≤ 20 pF/foot) semi-rigid coaxial copper cable from the interaction region to a home-made aluminum junction box located just outside of the DNGM's magnetic shields. The cable is housed inside 5/8" inner diameter hollow copper tubing, which provides mechanical rigidity as well as electrical shielding. The junction box (shown in Figure 3.29) houses the tuning capacitors (C_2) and also serves as a shielded environment wherein electrical connections between the external resonator, signal processing pre-amplifier, and maser pickup coil are made to achieve the circuit topology depicted in Figure 3.27. The A and B differential inputs on a low-noise, voltage pre-amplifier (Ithaco model 1201) mate directly to BNC bulkhead fittings on the junction box,

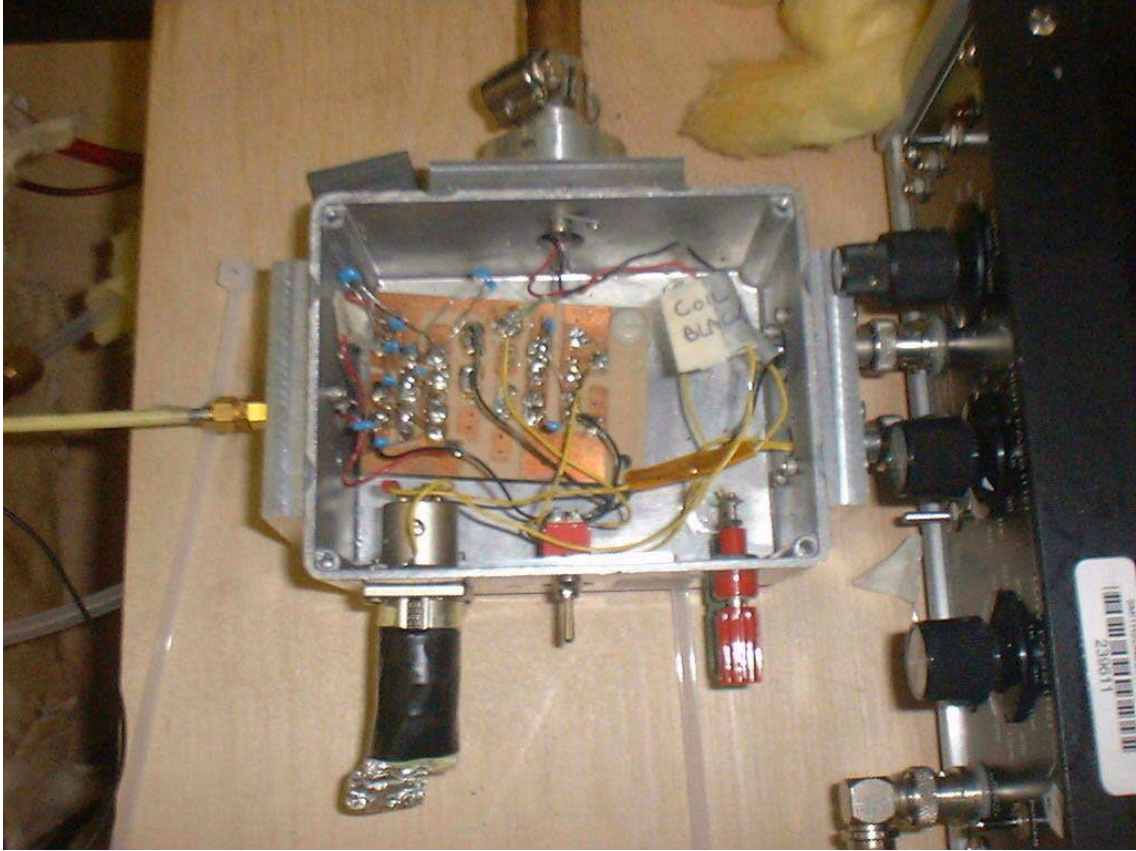


Figure 3.29: A photograph of the aluminum junction box described in Section 3.7.2. The lid has been removed to provide a view of the tuning capacitors C_2 . Notice the connections to the pre-amplifier, external resonator, and maser chamber pickup coil.

while the semi-rigid coaxial from the external resonator (L_1, R_1) is attached to the junction box via a standard bulkhead SMA fitting. The magnetic shields housing the DNGM oven and solenoid are of course connected to signal ground, as are the junction box case and the shielding on all signal-carrying cables including the 5/8" copper tubing. Also connected to signal ground are a smaller set of μ -metal shields (wrapped in fiberglass insulation), in which reside the external resonator coil and its associated tuning capacitor (C_1). The shields help isolate the external resonator from electromagnetic noise and thermal fluctuations in the DNGM laboratory.

3.7.3 Design and Construction of Pickup Coil and External Resonator Circuit

The DNGM pickup coil and double-tuned resonant circuit are comprised of three parallel elements, as shown in Figures 3.1 and 3.27: the pickup coil inductance L_2 and its associated DC resistance R_2 ; a tuning capacitor C_2 ; and an external inductor coil L_1 and its associated DC resistance R_1 , connected in series with another tuning capacitor C_1 . Previous experiments in dual noble gas magnetometry [20, 36] have detected the ^{129}Xe and ^3He signals using separate, orthogonally-oriented pickup coils whose resonances could be trimmed independently. In this section we present the rationale for using a single, double-resonance pickup coil and describe its implementation. Table 3.10 lists important characteristics of the pickup coil and external resonator presently in use in the DNGM system.

One purpose of the single pickup coil resonator configuration is to ensure a cell-pickup coil magnetic field distribution and resulting fill factor η (Equation 2.24) that are as similar as possible for both noble gas species. As shown in Section 3.6, this is very important for effective co-magnetometer operation. A second purpose is to maintain as large a fill factor as possible while also attaining the furthest proximity possible of the pickup coil to the high voltage electrodes used in the EDM experiments described in Chapter 6. A third purpose is to simplify the electrical and mechanical design of the DNGM oven (Section 3.2), and also limit equipment overhead by requiring only one low-noise preamplifier to buffer and pre-process both maser signals. It should be noted that for given frequencies it is impossible to achieve Q_{eff} -values in a double-resonance circuit which are as large as Q_{eff} -values in single-resonance $R - L - C$ circuits. In applications where the masing threshold $\tau_{rd} \leq T_2$ is difficult to attain, the approach described here is not advised. For our dual ^{129}Xe

and ^3He masers, however, the masing threshold is easily attained for a variety of operating temperatures and gas pressures.

Design of the DNGM resonator subsystem begins with the pickup coil, whose shape and size are dictated by fill factor and cell proximity considerations. The wire gauge must then be determined, balancing competing effects. Smaller gauge wire wound on a form of fixed size results in a larger number of turns and inductance, and a correspondingly larger raw signal. Unfortunately, more turns and a larger resistance also cause the pickup and Johnson noise signals to be larger, respectively. Because smaller wire gauge has a larger fractional content of AC lossy insulation to copper, the ratio of a coil's AC resistance to its DC resistance increases with decreasing wire size for a fixed frequency. This effect is potentially important because the AC resistance appears to be more temperature sensitive than the DC resistance of the copper windings, potentially affecting the DNGM's long-term frequency stability. Finally, a practical concern is mechanical strength of the wire. Excessively fine wire is hard to work and difficult to lay down with precision. Because so many considerations go into a choice of wire gauge, a detailed optimization may only be achieved by direct comparison of a series of pickup coils in a range of wire gauges. Such studies have not yet been conducted. Nevertheless, using our best estimates, all pickup coils used thus far in the DNGM experiment have been wound of 32 AWG wire on a Nylatron form such as that depicted in Figure 3.30. Note the pickup coil is oriented with its normal vector pointing along the direction of the cell transfer tube, referred to as the \hat{y} direction in this thesis.

Other components of the DNGM resonator system are designed around the pickup coil and its inductance (L_2) and DC resistance (R_2). Table 3.10 gives important characteristics of the external resonator coil which has been used since 1999 in the DNGM. The coil is wound of 25 AWG copper magnet wire on the Nylatron form

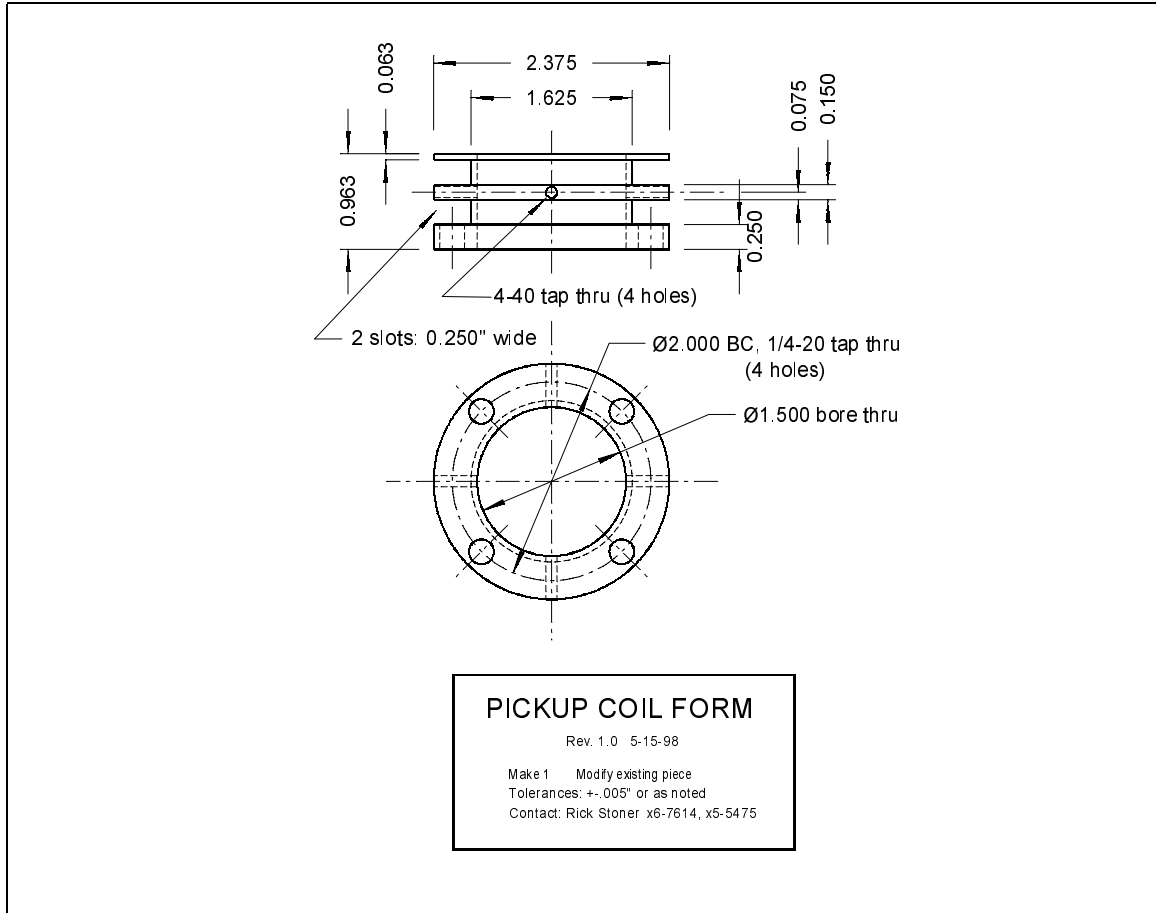


Figure 3.30: A design drawing of the pickup coil form, fabricated from Nylatron GSM. Notice the split coil design, required for passage of the 4-40 plastic screws which secure the high voltage electrodes against the cell endplates.

parameter	pickup coil	external resonator
wire gauge	32	25
inductance	145 mH	103.9 mH
DC resistance	140.1 Ω	21.4 Ω
Q_{coil} at 1.7 kHz	11.5	46
Q_{coil} at 4.7 kHz	29	73
AC resistance at 1.7 kHz	144.6 Ω	2.7 Ω
AC resistance at 4.7 kHz	149.6 Ω	21.1 Ω

Table 3.10: Room-temperature characteristics of the pickup and external resonator coils presently used in the DNGM, depicted in Figures 3.30 and 3.31.

shown in Figure 3.31. Once the value for the external inductor L_1 is established, the values of the tuning capacitors C_1 and C_2 are chosen to establish resonances at the ^{129}Xe and ^3He Zeeman frequencies (Appendix A):

$$\frac{1}{C_1} = 2L_1 \left(\omega_{he}^2 + \omega_{xe}^2 - \sqrt{(\omega_{he}^2 + \omega_{xe}^2)^2 - 4\omega_{he}^2 \omega_{xe}^2 (1 + L_2/L_1)} \right)$$

$$\frac{1}{C_2} = 2L_2 \left(1 + L_2/L_1 \left(\omega_{he}^2 + \omega_{xe}^2 - \sqrt{(\omega_{he}^2 + \omega_{xe}^2)^2 + 4\omega_{he}^2 \omega_{xe}^2 (1 + L_2/L_1)} \right) \right) \quad (3.17)$$

C_1 and C_2 are each the equivalent capacitance of an array of individual ultra-stable capacitors (fractional temperature sensitivity ≤ 30 ppm) soldered to copper circuit boards.³⁰ C_1 resides in a temperature stabilized and noise shielded environment with the external resonator L_1, R_1 , while the bank of C_2 capacitors resides in the external junction box, permitting easy and accurate tuning of the resonator peaks, as described in Section 3.7.4. Typical values of the capacitances presently in use are $C_1 \approx 2.6 \times 10^4$ pf and $C_2 \approx 2.7 \times 10^4$ pf.

The ratio L_1/L_2 establishes the relative strength of the effective Q at the two resonances, with a larger ratio corresponding to a larger effective Q for the higher ^3He resonance. The Q of the lower resonance is determined largely by the properties of the pickup coil only. The present values of the effective quality factors (see Appendix A) are $Q_{eff,xe} = 9.9$ and $Q_{eff,he} = 9.3$. Requiring that the capacitances in Equation 3.17 be real establishes a condition required for the existence of a double resonance:

$$\frac{L_2}{L_1} \leq \frac{1}{4} \cdot \left[\frac{\omega_{xe}}{\omega_{he}} + \frac{\omega_{he}}{\omega_{xe}} \right]^2 - 1. \quad (3.18)$$

³⁰We have a selection of ~ 20 capacitor values in the range 20 pF to 1 μF , enabling precise trimming of the values C_1 and C_2 .

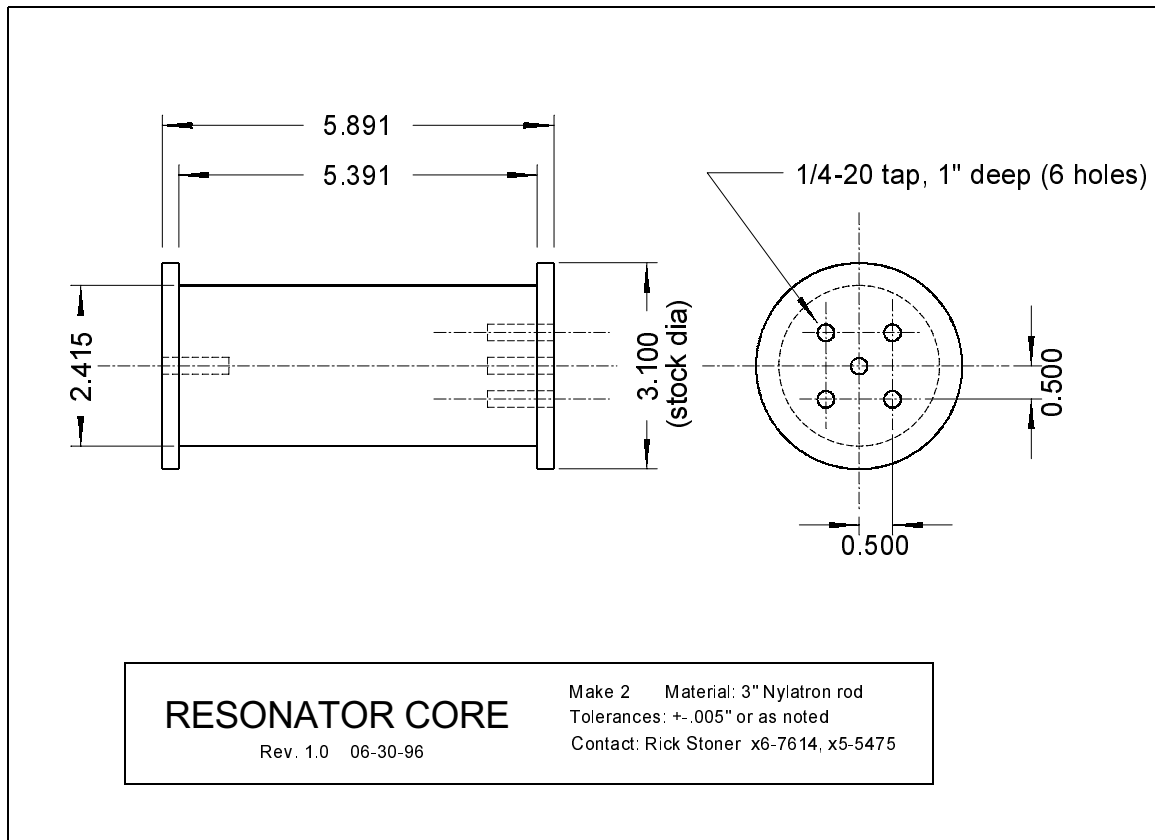


Figure 3.31: A design drawing of the external resonator form, fabricated from Ny-latron GSM. A small circuit board fastened to the bottom of the coil incorporates the capacitance C_1 into the circuit.

3.7.4 Resonator Tuning

Fine tuning of the upper and lower double resonator peaks is achieved by modifying the value of the capacitance C_2 . In the discussion that follows, we will refer to the upper and lower resonances as ν_u and ν_l , respectively, while the noble gas frequencies will continue to be written as ν_{ng} . It should be noted that operating either maser at a frequency which is a multiple of 60 Hz must be avoided at all costs.

The first step in resonator trimming is to choose the desired detuning ($\delta_{ng} \equiv \nu_{ng} - \nu_{res}$) of each maser's operating frequency from the nearest resonator peak. To achieve maximal coupling between the precessing spins and the feedback field, the DNGM is presently operated with the detuning of both species as close to zero as possible. Next, the double resonator is scanned using the methods of Section 3.7.1, and the measured values of the upper and lower resonator peaks ν_u, ν_l are recorded. The value of the tuning capacitance is then changed by an amount ΔC_2 (typically ~ 100 pf), and the resonator is scanned again. The new resonances, desired detunings, and coefficients $\beta_{u,l} = \Delta\nu_{u,l}/\Delta C_2$ are used to select the next iterative change in the capacitance C_2 :

$$\Delta C_2 = \frac{g\nu_l - \nu_u + g\delta_{xe} - \delta_{he}}{\beta_u - g\beta_l}, \quad (3.19)$$

where $g = \gamma_{he}/\gamma_{xe} \approx 2.75408$. Typical values of the β are $\beta_u = -2.67$ Hz/pF and $\beta_l = -.224$ Hz/pF. After C_2 is changed according to Equation 3.19, the resonator is re-scanned, the coefficients $\beta_{u,l}$ re-computed, and the next calculated change in C_2 implemented. It typically requires ~ 5 changes in the value of C_2 to converge to resonator frequencies within .5 Hz of zero detuning from the ^{129}Xe and ^3He Zeeman frequencies.

Note that the above tuning procedure locates the peaks of the dual resonator circuit by finding the frequency where the current across a small monitor resistor (≤ 1

Ω) placed in series with the pickup coil is a maximum. However, our goal is to tune the resonator to the frequencies of maximum coupling to the noble gas magnetizations. Such “maximum coupling” is determined by measuring the radiation damping time (Section 4.3) for each species as a function of resonator peak frequency. In the case of no deviation from the nominal $\pi/2$ phase difference between the noble gas transverse magnetizations and the magnetic fields created by current flow in the pickup coil resonant circuit, maximum radiation damping would occur at the same resonator frequencies as given by the “maximum current” technique. Figure 3.32 shows a plot³¹ of typical measured τ_{rd} as a function of resonator detuning. The ^{129}Xe and ^3He “maximum damping frequencies” are displaced by $\Delta_{xe} = 1.33$ Hz and $\Delta_{he} = -1.52$ Hz, respectively, from the resonator tunings given by the “maximum current” technique. Because these frequency displacements are approximately constant over a wide range of C_2 values, resonator fine-tuning to achieve maximal coupling can be performed by measuring the displacements Δ_{ng} once, incorporating them into Equation 3.19, and then following the tuning procedure based on maximizing current flow through the pickup coil. Of course, changes in the pickup coil or external resonator would necessitate re-measuring of the maximum damping frequency displacements Δ_{ng} .

3.7.5 Effect of Temperature Fluctuations on the Double Resonator

The temperature control systems for the pickup coil and external resonator are described in detail in Section 3.3. Good temperature stability of both coils is important, as variations in the properties of the double resonator system can change the

³¹See logbook DNGM-17, p.86.

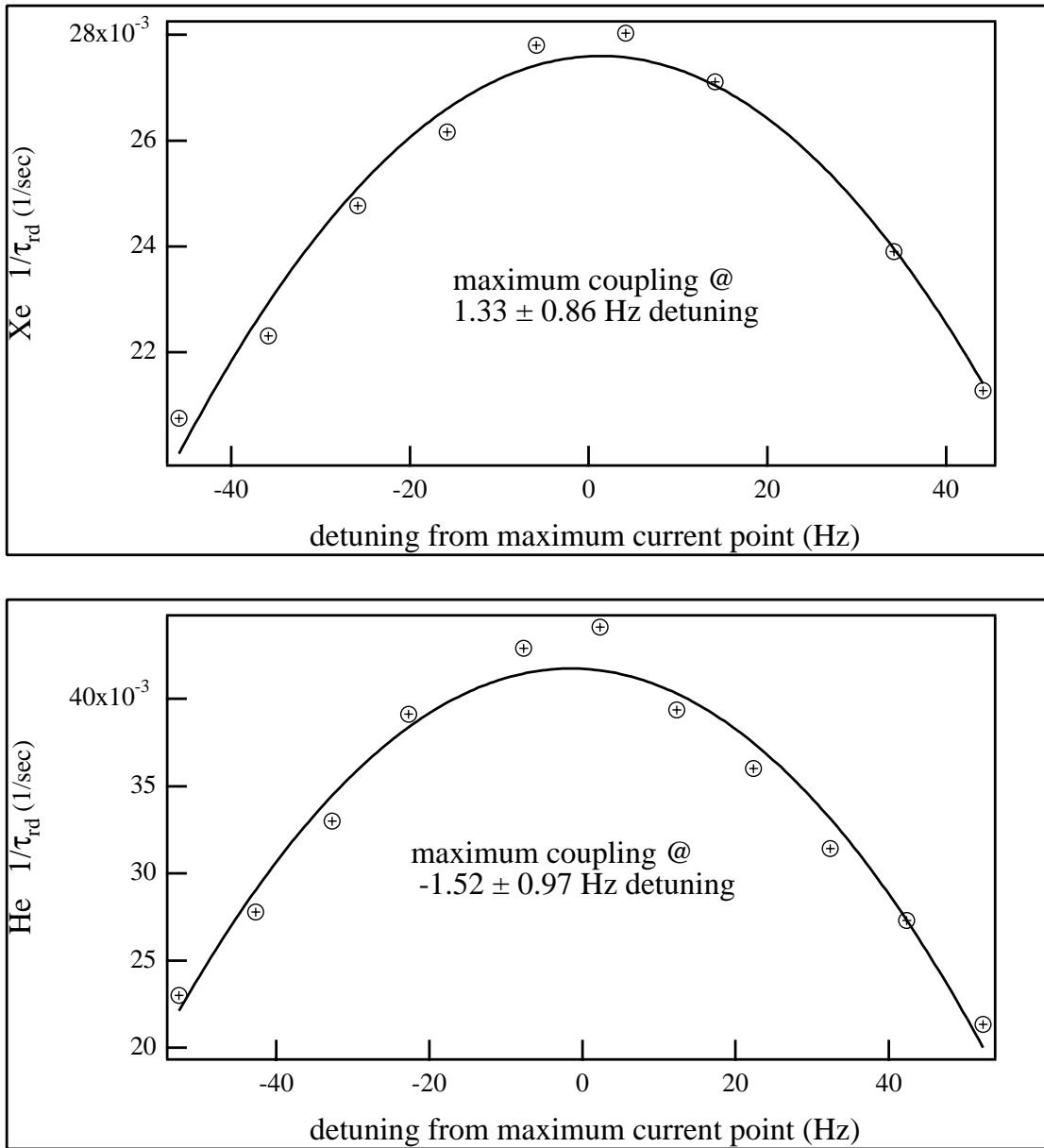


Figure 3.32: A plot of the radiation damping rate τ_{rd}^{-1} for the ^{129}Xe and ^3He species as a function of detuning from the associated resonator peaks where the current through the pickup coil is maximized. See logbook DNGM-17, pages 77-93.

contribution of cavity pulling (Equation 2.28) to the noble gas Zeeman frequencies:

$$\Delta\nu_{ng} \approx \nu_0 + (\nu_{coil} - \nu_0) \left[\frac{Q_{eff}}{\pi\nu_0} \right] \left[\frac{1}{T_2} \right]. \quad (3.20)$$

With the ^{129}Xe maser phase-locked, controlled temperature changes were applied separately to the DNGM pickup coil, external resonator, coaxial cables, and junction box.³² The resulting normalized ^3He maser frequency shifts $\Delta\nu_{he}/\Delta T$ are given in Table 3.11. Under normal operating conditions, and over timescales of several hours,

component	$\frac{\Delta\nu_{he}}{\Delta T} \left(\frac{\mu\text{Hz}}{^\circ\text{C}} \right)$
pickup coil	-3.9
external resonator	-18
semi-rigid coax	$\leq .2$
junction box	$\leq .2$

Table 3.11: Normalized ^3He maser frequency shifts $\Delta\nu_{he}/\Delta T$ when controlled temperature changes were applied to the DNGM pickup coil, external resonator, coaxial cables, and junction box.

the temperatures of the junction box and coaxial cables exhibit fluctuations ~ 100 mK RMS, with typical sidereal variations of $\sim .4$ mK. Temperature fluctuations in L_1 and L_2 are 3 mK and 11 mK, respectively, with sidereal variations of .04 mK and .8 mK. Resulting estimates of the effects of resonant circuit temperature instability on DNGM frequency resolution are given in Table 3.12. None of the systematic temperature shifts are correlated with the applied electric field, and all are substantially smaller than the Allan deviation of the ^3He maser over a typical 5000 second EDM dwell or over a day. We thus conclude that thermal fluctuations

³²The coil temperatures were changed by increasing the setpoint temperatures of the thermal control systems described in Section 3.3. Temperature changes of the coaxial cables and junction box were achieved by applying a heater tape covered in aluminum foil (to distribute the heat as evenly as possible), and measuring the temperature change with temporarily attached RTDs.

in the DNGM dual resonator system do not limit the sensitivity of the symmetry tests described in this thesis.

component	$\delta\nu_{LLI}$ nHz	$\delta\nu_{edm}$ nHz
pickup coil	3.1	43
external resonator	.72	54
semi-rigid coax	.08	20
junction box	.08	20

Table 3.12: Upper bounds on the limitations imposed by thermal fluctuations of the resonator system on the LLI and EDM tests described in this thesis. Note that the RMS fluctuations are not correlated with the applied electric field and will thus average away as $\tau^{-1/2}$. Note that diurnal variations in temperature are not phase-coherent over periods of several days, and the upper bounds in the table for $\delta\nu_{LLI}$ are thus approximate bounds on the single-day LLI measurement resolution of the DNGM.

3.7.6 Pulse Coil Operation and an Estimate of B_1 Homogeneity

Many of the measurements required to characterize and optimize performance of the DNGM (see Chapter 4) require application of a resonant transverse tipping (Rabi) field to the noble gas atoms (Figure 2.2). Depending on the measurement being performed, the double-resonator may or may not be engaged. Closing switch S_2 (see Figure 3.29) places the voltage output of a Wavetek³³ programmable function generator across the pickup coil L_2 , which serves also as the DNGM pulse coil. Note that the Wavetek is actually coupled into the circuit inductively, as shown in Figure 3.27. The pre-amplifier is gated off during pulsing. A pulse consists of a gated sinusoidal waveform at the ^{129}Xe or ^3He Zeeman resonance frequency, typically of duration 80 ms and amplitude ~ 1 Volt RMS. Section 4.6 describes in detail the

³³Wavetek Model 29, 10 MHz DDS Programmable Function Generator. Wavetek Corporation, 9045 Balboa Avenue, San Diego, CA 92123, (619) 279-2200.

method for calibrating the effective magnetization tip angle for a pulse of a particular duration and voltage. A numerical estimate of the tipping field (B_1) homogeneity for the typical DNGM parameters was carried out in June, 2000, by computing³⁴ the volume average over the maser bulb of the RMS deviation of the tipping field from its value at the coil center, $B_1(0, 0, 0)$:

$$\frac{1}{V \cdot B_1(0, 0, 0)} \cdot \sqrt{\int_V (B_1(x, y, z) - B_1(0, 0, 0))^2 dV} \approx .21 \quad (3.21)$$

Note that in the lab frame the B_1 field field is oriented in the \hat{y} direction (in the direction of the cell transfer tube) because of the orientation of the pickup/pulse coil (see Section 3.7.3).

3.7.7 Signal Processing and Data Storage

The detected maser signals are read as sinusoidally varying voltages across the capacitor C_2 . Typical raw signal levels are $3 \mu\text{V}$ for ^3He and $5 \mu\text{V}$ for ^{129}Xe . The signals are buffered and pre-processed by an Ithaco³⁵ 1201 low-noise, voltage preamplifier. The amplifier is set with a wide frequency passband (30 Hz - 100 kHz) and a gain of 5000.

The amplified signals are sent to three separate SRS digital lockin amplifiers. An SRS-830 lockin serves as a prefilter and phase-sensitive detector for the magnetic field phase-lock loop (Section 3.5.8). Two SRS-850 lockins monitor and record the phase and amplitude of the ^{129}Xe and ^3He masers. The data are typically sampled at $1/4$ Hz, as triggered by an ultra-stable signal derived from a reference hydrogen maser. The SRS-850 digital low-pass filters are set with bandwidth = 125 mHz and

³⁴Thanks to Marius Popa for performing the calculation.

³⁵Ithaco 1201 Low Noise Voltage Preamplifier. Now made by DL Instruments, PO Box 1086, 176 Lake Road, Dryden, NY 13053, (607) 844-3725.

12 db/octave roll-off. Varying the bandwidth and sampling rate of the detection lockins in regimes near their present values has never yielded improvement in the frequency stability of DNGM data (see Section 2.5). All timebase and reference signals used in the DNGM experiment are derived from the same hydrogen maser clock, thus eliminating concerns about unstable phase and frequency differences between the reference oscillators. Finally, data stored in the lockin buffers are downloaded via a GPIB interface to a computer for analysis (Section 2.5) and archiving, typically once every 24 hours.

3.8 Appendix to Chapter 3: Assembly and Optimization

The preceding sections of Chapter 3 have described the fabrication and experimental realization of all noble gas maser subsystems. The data contained in graphs and tables in those sections reflect typical parameter values and behavior for the DNGM as it is presently configured. We also note that graphs of the Allan deviation and free-running ^3He maser phase for the optimized DNGM are presented at the end of Section 2.5. Chapter 4 presents methods not described in Chapter 3 for measuring various operational parameters of the DNGM.

The present section is intended to serve as a concise resource for scientists who are continuing the DNGM research program at the Smithsonian Astrophysical Observatory. Here we describe our procedure for assembling the DNGM and achieving maser oscillations with good frequency stability. These steps may (and undoubtedly will) be modified as development and improvement of the DNGM continues. For now, however, we hope that the list that follows, as well as the tables of typical instrument settings, serve as a good starting point for new researchers in our laboratory.

- Assemble oven. Make sure all glass windows are clean, tubing is well-insulated. Place in center of shields. Check continuity of all cables. Check for shorts between leads and to the solenoid core.
- Check 5 MHz signal and operation of timebase system.
- Set mass flow controller (MFC) $\approx 70\%$. Turn on pump chamber heat. Verify with HP spectrum analyzer that noise profile looks normal after attaching all grounding clips. Make sure pump heater interlock box is working and actively in use.
- After pump chamber is heated up, turn on LDA. Steer LDA by eye. Make sure LCVR is set for maximal pumping into σ^+ state (LCVR drive voltage depends on solenoid magfield direction). For Coherent LDA, set $I = 37$ Amperes, $T = 19$ °C.
- Set up photodetectors. Find Rb Zeeman resonance.
- Use Rb magnetization signal to steer laser better. Adjust collection mirror to maximize detected signal. Be sure to record DC signal out of Rb detector.
- De-Gauss shields. Let system spin up overnight into σ^+ state. The dual resonator should not be engaged, and the current in each trim coil should be zero.
- Find ^{129}Xe FID signal. Set main magfield value so that ν_{xe} is roughly where you plan to operate. SRS 850s will be set with fs = 10 mV, 12 db/octave, bandwidth = 1.2 Hz.
- Trim z -position of oven.

- Adjust trim 2, trim 3, and trim 1 (i.e., y -trim, z -trim, and x -trim).
- Reduce air flow rate to the value you will use when running. Turn on maser chamber and external resonator heaters.
- Reduce the LCVR voltage so that the Rb signal is approximately 10% less than its maximum value.
- Lock LDA broadband power. Make sure photodiode (PDD) temperature control systems are functioning.
- Let system spin up until ^{129}Xe and ^3He are fully polarized. Apply small tips (with double resonator not engaged) to ^{129}Xe and ^3He . Record T_2 of each species as well as initial amplitudes of the FIDs.
- Turn on double resonator. When ^{129}Xe maser is alive and well, engage the magnetic field lock loop.
- Set SRS 850s for maser detection: $f_s = 50$ mV, 12 db/octave, bandwidth = 125 mHz, display and store only x and y traces. Sample rate is set by the trigger from the pulse-per-second box.
- Let masers equilibrate. Re-scan Rb Zeeman resonance, make sure that LCVR is driven at 10% below maximum magnetization value. Lock Rb magnetization using the LCVR feedback loop
- The system is driftier in the first few days of operation. Thus you will need to re-lock the LCVR every ~ 24 hours.
- Assess system performance by looking at short term phase noise and Allan deviation as a function of τ . Decide whether to re-optimize any settings:

magnetic field lock loop parameters, flow rate (competing effects of reduced phase noise versus poorer temperature control), temperature control circuits, and the like.

description	GPIB	fs (mV)	tc (sec)	Ch. 1	Ch. 2	ν_{ref}
maser temp	1	1	1	X	-	850 Hz
resonator temp	2	1	1	X	-	950 Hz Hz
pump temp	3	5	0.3	X	-	1000 Hz
^3He monitor	4	1	1	X	Y	4343.27 Hz
^{129}Xe monitor	5	1	1	X	Y	1709.40 Hz
magfield PLL ctrl	6	50	1	-	θ	1709.42 Hz
room temp	7	1	1	X	-	1000 Hz
Rb magnetization ctrl	8	2	0.3	R	-	450 Hz
LDA bband pwr ctrl	9	500	30	R	-	100 Hz

Table 3.13: Table of typical settings for SRS 830 and 850 lockin amplifiers, as of June 2000.

description	Gain	T_{int} (sec)	T_{diff} (sec)	T_{HF} (sec)	R_{out} (k Ω)
maser temp	10	220	100	.01	5.1
resonator temp	3	300	.003	100	0.0
pump temp	10	10	10	0.1	0.062
Magn. field PLL	0.01	0.1	0.003	0.1	0.0
Laser power PLL	10	.3	0.003	0.3	3.3
LCVR PLL	30	30	0.01	0.0	1000

Table 3.14: Table of typical settings for PID boxes, as of June 2000.

description	DC gain	R_{set} (Ω)	T_{set} ($^{\circ}\text{C}$)
maser temp	81.8	115.9	41
resonator temp	92.1	111.3	29
pump temp	83.6	144.2	115
room temp**	1	111.3	29

Table 3.15: Settings for the temperature monitor/control bridges depicted in Figure 3.14. The ** indicates monitor function only, no control.

Chapter 4

Measurement of Operational Parameters and Verification of the Bloch Theory

In this chapter we present methods for measuring the primary operational parameters of the dual noble gas maser. In Section 4.7 we use data from near equilibrium oscillations to verify the correctness of the Bloch theory for the ^{129}Xe maser.

4.1 Rb Frequency Shift Measurement of ^{129}Xe Polarization in the Pump Bulb

Section 2.6 describes the shift of the noble gas Zeeman frequencies induced by polarized Rb atoms (the collisional contact shift and the bulk Rb magnetization shift). There is also a reciprocal shift induced on the Rb Zeeman frequency by the presence

of polarized noble gas atoms. In a spherical cell this shift takes the form

$$2\pi \cdot \delta\nu_{rb} = (\kappa_{ng} - 1)\gamma_{rb} \cdot \frac{8\pi}{3}\hbar\gamma_{ng}[ng]P_{ng}, \quad (4.1)$$

where $[ng]$ is the noble gas number density in the pump bulb, γ_{rb} and γ_{ng} are the Rb and noble gas gyromagnetic ratios, P_{ng} is the average longitudinal noble gas polarization, and κ_{ng} is the Rb contact shift enhancement factor due to the presence of noble gas [48].

In the pump bulb, estimating P_{ng} by measuring $\delta\nu_{rb}$ is straightforward in principle. First, the center frequency of the Rb Zeeman transition is measured (Section 3.4) with the pump bulb noble gas polarization at its canonical operating value. For typical DNGM cells, the SNR of the Rb magnetization diagnostic permits determination of the center line (≈ 700 kHz at 1.5 G) to within ~ 100 Hz. A very strong depumping drive tuned to the noble gas Zeeman resonance is then applied to the pump bulb, rapidly bringing the noble gas polarization to zero in ~ 10 seconds. The Rb Zeeman frequency is then measured again. From these measurements, the mean noble gas polarization under normal operating conditions is given by

$$P_{ng} = 2\pi \cdot \delta\nu_{rb} \left((\kappa_{ng} - 1)\gamma_{rb} \cdot \frac{8\pi}{3}\hbar\gamma_{ng}[ng] \right)^{-1}. \quad (4.2)$$

In practice, the largest uncertainty in determining P_{ng} using this technique comes from uncertainty in the value of $[ng]$. For a cell in which the pump and maser chambers have the same volume and the volume of the transfer tube is negligible,

$$[ng] = \frac{2[ng]_{room}}{1 + T_p/T_m}, \quad (4.3)$$

where $[ng]_{room}$ is the noble gas number density at 293 K (determined during cell

filling), and T_p and T_m are the pump and maser bulb temperatures, respectively. Because the sensors that measure T_p and T_m are located outside the cell volume, with resultant inaccuracies of ~ 10 K in the determination of the gas temperature for each chamber, the true value of T_p/T_m is probably certain to no better than 5%.

In July, 1999 we used the above technique to determine $P_{xe} \approx .0835$ from a frequency shift of $\delta\nu_{rb} = 2.76$ kHz in cell S3, filled at room temperature (298 K) with 106.9 Torr of ^{129}Xe and operated with $T_p = 373$ K and $T_m = 306$ K (DNGM-15, p. 138). In practice, the much smaller contact shift enhancement factor for ^3He ($\kappa_{he} \approx 5, \kappa_{xe} \approx 726$ [20]) and the estimated small values of $P_{he} \approx 2\%$ make it impractical to measure the level of ^3He polarization in the pump bulb using the methods described in this section.

4.2 Measurement of Noble Gas Decoherence

Decoherence of the noble gas ensembles is measured with the DNGM detection coil off-resonance (i.e., with no active maser oscillation). A transverse Rabi field is applied to the maser bulb using the pulse/pickup coil described in Section 3.7.6, creating a transverse noble gas magnetization that undergoes free induction decay (FID). The induced voltage across the pickup coil is amplified, buffered, and sent to a phase-sensitive lockin amplifier for detection and digitization. The stored voltage traces are then downloaded to a computer for analysis. Figure 4.2 shows a typical FID ringdown for the ^{129}Xe species after application of a $\theta \approx 10^\circ$ Rabi field tipping pulse. Curvefitting to a function of the form

$$V_{xe}(t) = c_0 + c_1 \cos(c_2 \cdot t + c_3) \cdot e^{-c_4 \cdot t} \quad (4.4)$$

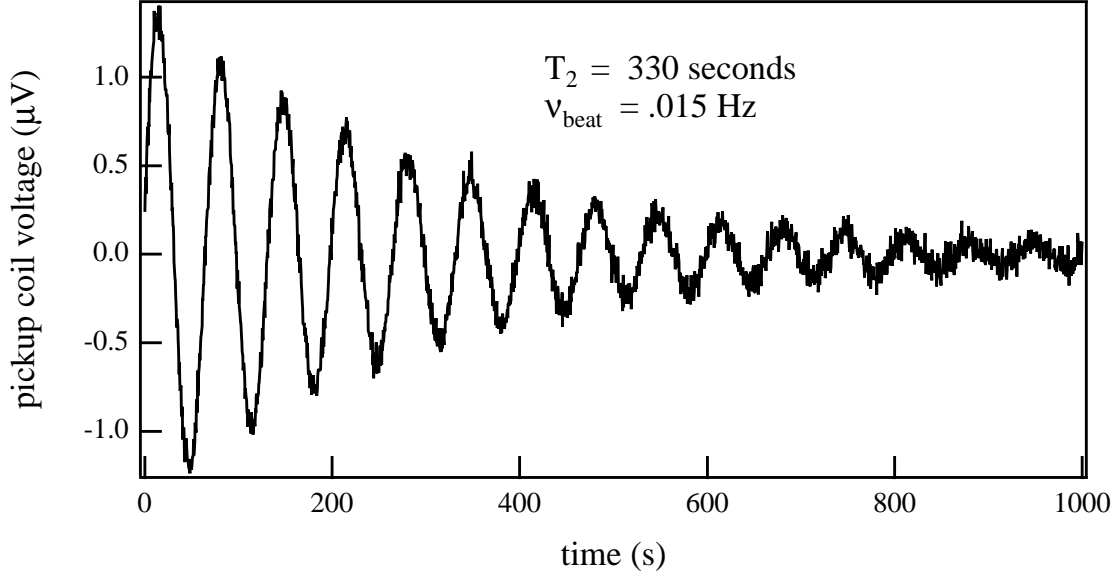


Figure 4.1: A typical free-induction-decay (FID) ringdown for the ^{129}Xe species in EDM cell SE3. The oscillation beat frequency is the difference between the noble gas Zeeman frequency (≈ 1700 Hz) and the frequency of the ultra-stable oscillator used as a reference for the lockin detector.

yields the noble gas ensemble decoherence time $T_2 = 1/c_4$, and the noble gas Zeeman frequency $\nu_{ng} = \nu_{ref} + c_2/(2\pi)$.

Section 3.5.5 describes the method for maximizing T_2 by adjusting the z -position of the DNGM oven assembly (with respect to the solenoid) and the current through each of the gradient trim coils. Section 3.5.6 details the effects of noble gas magnetization-induced field gradients on the ^3He and ^{129}Xe decoherence times. As a reminder, typical optimized T_2 values for the most recent DNGM cell SE3 are 330 seconds for ^{129}Xe and 170 seconds for ^3He .

4.3 Measurement of the Radiation Damping Time and Estimation of the Resonator Fill Factor

Measurement of the radiation damping time τ_{rd} (Equation 2.24) is performed with the noble gas atoms pumped into the negative energy state and with both species maximally polarized. The damping time is obtained by measuring the free-induction decay rate T_2^{-1} with the dual resonator tuned both on and off the noble gas Zeeman frequencies (Section 2.4.1). From Equation 2.25, τ_{rd} for each species can be deduced from the difference of these two measurements:

$$\frac{1}{\tau_{rd}} = \frac{1}{T_{2,on}} - \frac{1}{T_{2,off}}. \quad (4.5)$$

For example, the most recent measurements of τ_{rd} for cell SE3 yield damping times of $\tau_{rd,xe} = 76$ seconds and $\tau_{rd,he} = 15.9$ seconds.¹

4.4 Measurement of the Longitudinal Polarization Lifetime in the Maser Chamber

Measurement of the effective lifetime of the noble gas longitudinal polarization (P_z) in the maser chamber is performed with the double resonator tuned far above the noble gas Zeeman frequencies. In the absence of spin-circuit coupling, $P_z(t)$ after the optical pumping laser is turned off is given approximately² by

$$P_z(t) \approx P_o \cdot e^{-t/T_1^*} \quad (4.6)$$

¹DNGM-18, 5/30/00).

²See Appendix A for the full theory.

where T_1^* is the effective longitudinal polarization lifetime, incorporating wall relaxation, bulk relaxation, and inter-bulb transport effects.

Figure 4.2 shows plots of the ratio $P_z(t)/P_{z,max}$ for typical ^{129}Xe and ^3He T_1^* measurements, made with glass cell S1. The measurements were performed by turning off the optical pumping laser at $t = 0$, applying small tips to the spinning-down polarization ensembles at time intervals t_n , and measuring the initial amplitude of the detected NMR FID $\propto P_z(t_n) \sin \theta_{tip}$. Each tip was of the same size and sufficiently small ($\theta_{tip} \leq 5^\circ$) that pulsing did not contribute significantly to the rate of longitudinal polarization depletion. The values of T_1^* were obtained by fitting a decaying exponential to the ratio $P_z(t)/P_{z,max}$ for each ensemble. It should be noted that the T_1^* values of 532 seconds for ^{129}Xe and 7.12 hours for ^3He are typical for all-glass cells. Our EDM cells had a smaller surface area to volume ratio and thus generally longer decay times because of the reduced rate of wall collisions: $T_1^* \sim 800 - 1000$ seconds for ^{129}Xe and 8 - 12 hours for ^3He .

4.5 Measurement of the Ratio $P_{z,o}/P_o$

A key operational parameter for a Zeeman maser is the ratio of the steady state longitudinal polarization with active maser oscillation ($P_{z,o}$) to that without active maser oscillation (P_o). When the maser is operated at zero resonant circuit detuning ($\omega_{ng} = \omega_o$), $P_{z,o}/P_o$ is given by the simplified Bloch equations (see the first of Equations 2.31):

$$\frac{P_{z,o}}{P_o} = \frac{\tau_{rd}}{T_2}. \quad (4.7)$$

Comparison of measured values of τ_{rd} and T_2 (Sections 4.2 and 4.3) to the measured ratio $\frac{P_{z,o}}{P_o}$ thus provides one test of the correctness of the Bloch theory.

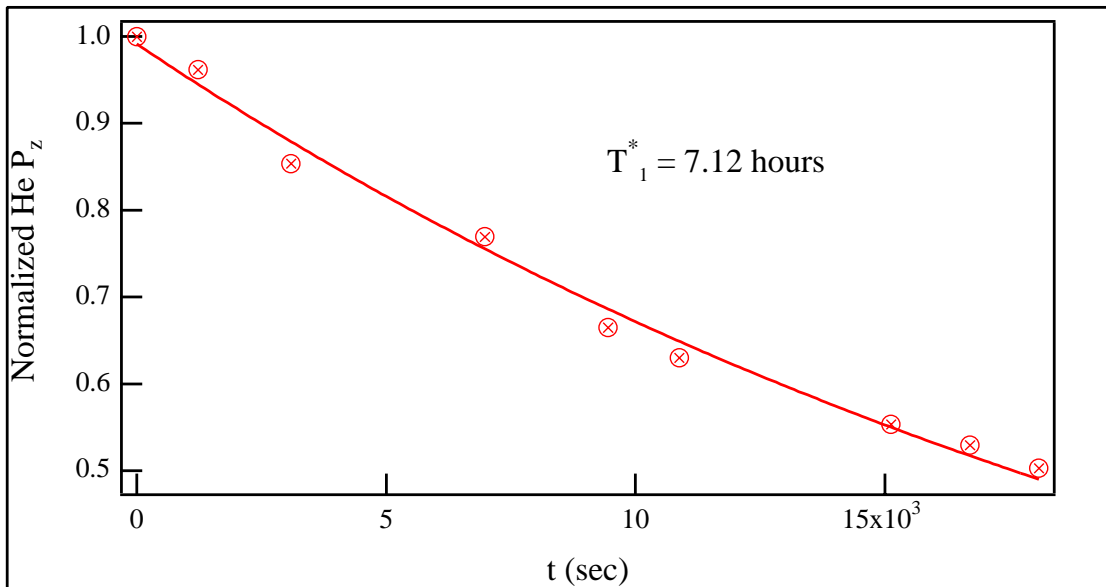
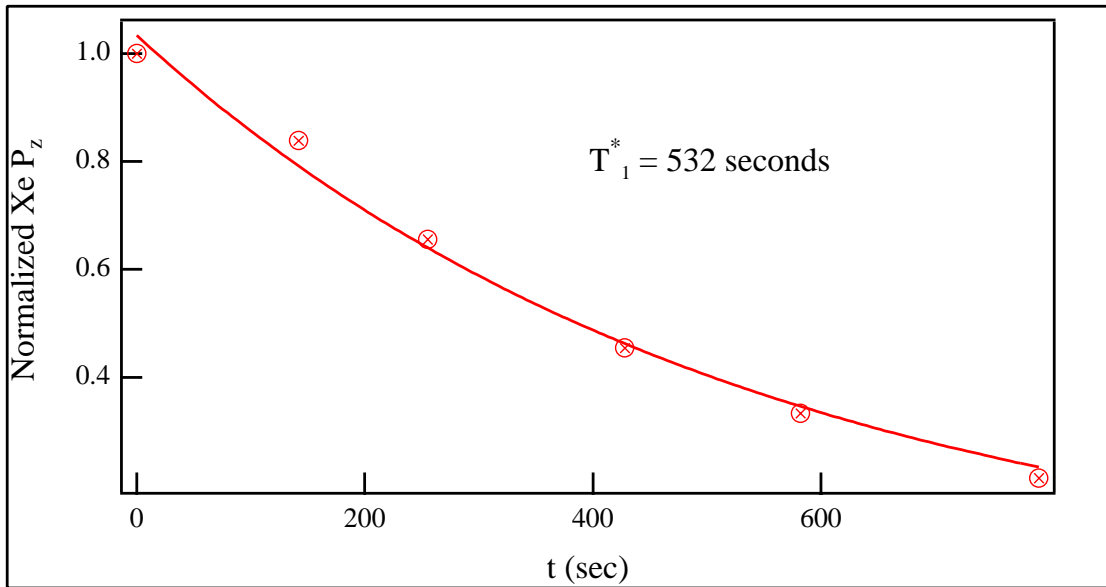


Figure 4.2: Typical measurements of the ratio $P_z(t)/P_{z,max}$ used to determine T_1^* for ^{129}Xe and ^3He . Made with glass cell S1; DNGM-14, page 119.

Measuring $P_{z,o}/P_o$ is straightforward. First, with the atoms fully polarized and the dual resonator far detuned, a small tip angle is applied to the noble gas ensemble. The resulting coefficient c_1 from the FID (Section 4.2) is proportional to $P_o \cdot \sin \theta_{tip}$. The second step is performed with the masers fully equilibrated. The resonator is again far detuned, and a strong magnetic field gradient is applied to dephase the atoms' transverse polarization. (These manipulations leave the longitudinal polarization largely unaffected if performed in less than \sim one minute.) The same tipping angle as used in the first step is then applied to the ensemble, and the coefficient $C_1 \propto P_{z,o} \cdot \sin \theta_{tip}$ is extracted from the measured FID. $P_{z,o}/P_o$ is then given by the ratio C_1/c_1 . For example, table 4.1 shows a comparison of the ratios $P_{z,o}/P_o$ and τ_{rd}/T_2 for cell S1 data. The ratios agree remarkably well given the inhomogeneity of the tipping field (Section 3.7.6), and support one of the major predictions of the Bloch theory (see the first of Equations 2.31).

Species	$P_{z,o}/P_o$	τ_{rd}/T_2
^{129}Xe	.10	.12
^3He	.082	.071

Table 4.1: Comparison of the ratios $P_{z,o}/P_o$ and τ_{rd}/T_2 for cell S1 data, DNGM-14, pages 1, 19, 61, 66, and 67.

4.6 Measurement of the Equilibrium Orientation Angle of the Maser Polarization

In this section we describe a method for measuring the equilibrium polarization (i.e. Bloch vector) orientation angle θ_o of a noble gas masing ensemble. This angle is defined by the relation $\tan \theta_o \equiv P_{\perp,o}/P_{z,o}$, as shown in Figure 4.3. It might seem that

θ_o could be measured easily as follows: first, take an equilibrated maser and turn off the resonator coupling (i.e., detune the resonator far above the noble gas Zeeman frequency). The initial amplitude of the resultant ringdown gives $P_{\perp,o}$. After the ringdown has decayed, the remaining polarization vector will be $P_{z,o}$. Applying a $\pi/2$ pulse to the ensemble should thus produce an FID whose initial amplitude is $P_{z,o}$ (in the same relative units as $P_{\perp,o}$). Unfortunately, the homogeneity of the tipping magnetic field (Section 3.7.6) produced by the DNGM pulse coil is not adequate for quantitative measurements using large tip angles. We now describe a method for measuring θ_o that is based upon the application of small tips to the equilibrium noble gas ensemble of the phase-locked species.

Referring to Figure 4.3, we assume that at $t = 0$ the transverse polarization of the phase-locked maser points along the y -axis and that a resonant Rabi tipping pulse, indicated as \mathbf{B} in the drawing, is applied. The Rabi field is actually the co-rotating component of a linearly oscillating magnetic field.³ The counter-rotating term is far off-resonance and does not contribute to the tipping process [34, 37, 43]. The strength of the tipping field is characterized by a (small) tip angle α (to be measured), and it is offset by a phase δ from P_{\perp} , as shown.

If $\delta = \pi/2$, the phase variable $\Phi(t) = \tan(P_y(t)/P_x(t))$ (Equation 2.22) of the maser vector will not change⁴, but the orientation angle of the maser will increase to $(\theta_o + \alpha)$ at $t = 0^+$. Such a tip is referred to in our laboratory as a “proper” tip. However, because of electronic phase shifts δ_{stray} induced by various circuit components and the proximity of metal shields to the pulsing coil, it is not possible to produce a proper tip to the phase-locked maser simply by placing the phase of the

³ $\hat{y} \cdot B_o \cos \omega t = .5 \times (\hat{y} \cdot B_o \cos \omega t + \hat{x} \cdot B_o \sin \omega t) + .5 \times (\hat{y} \cdot B_o \cos \omega t - \hat{x} \cdot B_o \sin \omega t)$.

⁴Note that there is no requirement that the tipping pulse time be much shorter than a Larmor period, as the tipping field is generated by the same synthesizer which references the phase-locked maser, and is stationary with respect to the Bloch vector in the rotating frame.

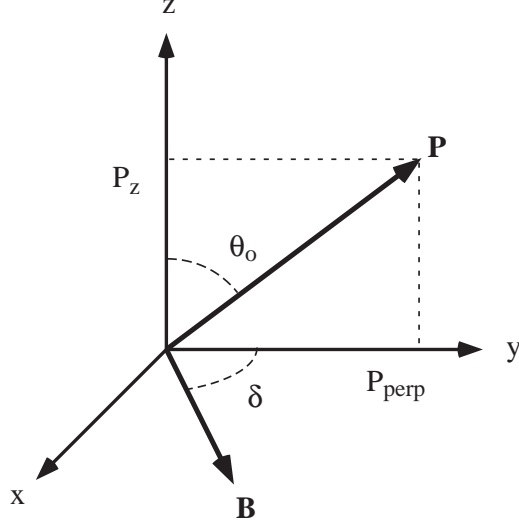


Figure 4.3: A figure depicting the maser polarization vector \mathbf{P} . P_{\perp} (P_{perp}) is taken to point along the y -axis at time $t = 0$. The equilibrium orientation angle is given by $\tan \theta_o \equiv P_{\perp,o}/P_{z,o}$. The angle δ gives the phase difference between a resonant tipping field \mathbf{B} and P_{\perp} in the $x - y$ plane.

Rabi pulse generator in quadrature with the phase of the function generator that references the magnetic field phase lock loop. Instead, one must perform several small on-resonant tips and FID measurements at several different relative phase settings $\delta_{lab} \equiv (\delta_{stray} + \delta)$. For each tip, the dynamical maser phase variable $\Phi(t)$ will change by a different amount $\Delta\Phi(0)$.⁵ For a proper tip (i.e., $\delta_{lab} = \delta_{stray} + \frac{\pi}{2}$), the phase of the maser will not change at all. We found that locating this zero-crossing via linear interpolation is quite accurate, as long as one brackets the zero phase change with at least two points on either side of the zero-crossing.

Once the δ_{lab} to achieve a proper tip is determined, the DNGM is allowed to equilibrate. Then, a proper tip of a small angle α is applied; and the ratio $P_{\perp,+}/P_{\perp,o}$ of the transverse component of polarization after ($P_{\perp,+}$) and before ($P_{\perp,o}$) the tip

⁵We determine $\Delta\Phi(0)$ as follows. For the ≈ 30 seconds before the tip is applied, we fit a line $\Phi_{<}(t) = m_{<}t + b_{<}$ to the phase curve. For the ≈ 30 seconds after the tip is applied, we fit a line $\Phi_{>}(t) = m_{>}t + b_{>}$ to the phase curve. We then have $\Delta\Phi(0) = b_{>} - b_{<}$.

is determined from measurements of the maser amplitude after and before the tip. $P_{\perp,+}$ and $P_{\perp,o}$ are related to the orientation angles θ_o and α as follows:

$$\begin{aligned} \frac{P_{\perp,+}}{P_{\perp,o}} &= \frac{\sin \theta_o \cos \alpha + \cos \theta_o \sin \alpha}{\sin \theta_o} \\ &= \cos \alpha + \cot \theta_o \sin \alpha. \end{aligned} \quad (4.8)$$

For example, Figure 4.4 shows the R -trace (Equation 2.36) of the phase-locked ^{129}Xe maser using cell S1 before and after a proper tip α was applied at $t = 0$. Fitting a line $R(t) = mt + b$ to the region $t \leq 0$, and a decaying sinusoid $R(t) = A_{\perp} e^{-\gamma_{ring} t} \sin(\omega_{ring} t - \phi)$ to the region $t \geq 0$ gives the ratio $P_{\perp,+}/P_{\perp,o} = A_{\perp}/b$. For the data shown in Figure 4.4, the applied tip α was of duration $\tau_o = 80$ msec.

To obtain the values of the parameters α and θ_o , we note that the size of the tip angle is proportional to the duration of the pulse. By repeating the procedure described above, but for several different pulse durations (and hence tip angles), it is possible to extract α and θ_o . Figure 4.5 shows a plot of $P_{\perp,+}/P_{\perp,o}$ as a function of varying pulse durations τ (in msec) for fixed drive voltage 15 mV RMS. Curvefitting the measured ratios $P_{\perp,+}/P_{\perp,o}$ to the function

$$\frac{P_{\perp,+}(\tau)}{P_{\perp,o}(\tau)} = \cos \left(c_1 \cdot \frac{\tau}{80} \right) + c_0 \cdot \sin \left(c_1 \cdot \frac{\tau}{80} \right) \quad (4.9)$$

yields the equilibrium orientation angle $\cot \theta_o = c_0$ as well the value of the tip angle $\alpha = c_1$ for an 80 ms pulse. A similar series of measurements was carried out with the ^3He maser phase-locked, also with cell S1. For both species, Table 4.2 lists the values for θ_o (the equilibrium polarization orientation angle) and α , as well as the near-equilibrium ringdown parameters γ_{ring} and ω_{ring} , that were deduced from the ensemble of measurements performed with cell S1 in December, 1998.

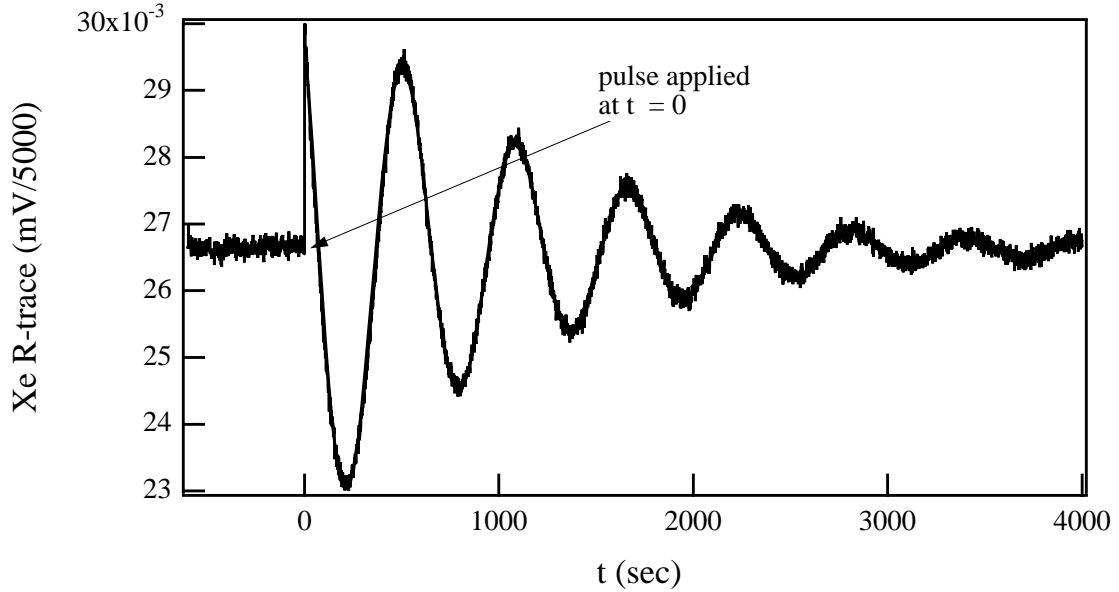


Figure 4.4: The R -trace of the phase-locked ^{129}Xe maser before and after a proper tip α was applied at $t = 0$. Fitting a line $R(t) = mt + b$ to the region $t \leq 0$, and a decaying sinusoid $R(t) = A_{\perp} e^{-\gamma_{ring} t} \sin(\omega_{ring} t - \phi)$ to the region $t \geq 0$ gives the ratio $P_{\perp,+}/P_{\perp,o} = A_{\perp}/b$. For the data shown, the applied tip was of duration $\tau_o = 80$ ms. DNGM 14, page 50.

Parameter	^{129}Xe	^3He
θ_o	51.9°	28.52°
α	10.5°	7.7°
γ_{ring}	$9.2 \times 10^{-4} \text{ sec}^{-1}$	$4.31 \times 10^{-4} \text{ sec}^{-1}$
ω_{ring}	$10.84 \times 10^{-3} \text{ rad/sec}$	$4.3 \times 10^{-3} \text{ rad/sec}$

Table 4.2: Summary of the values θ_o and α , as well as the near-equilibrium ringdown parameters γ_{ring} and ω_{ring} that were deduced from the ensemble of measurements performed with cell S1 in December, 1998 (DNGM-14, pages 1 - 73). Recall that the near-equilibrium oscillations of P_{\perp} are underdamped sinusoids, with $1/e$ decay time given by $1/\gamma_{ring}$ and oscillation period given by $2\pi/\omega_{ring}$ (Equation 2.35).

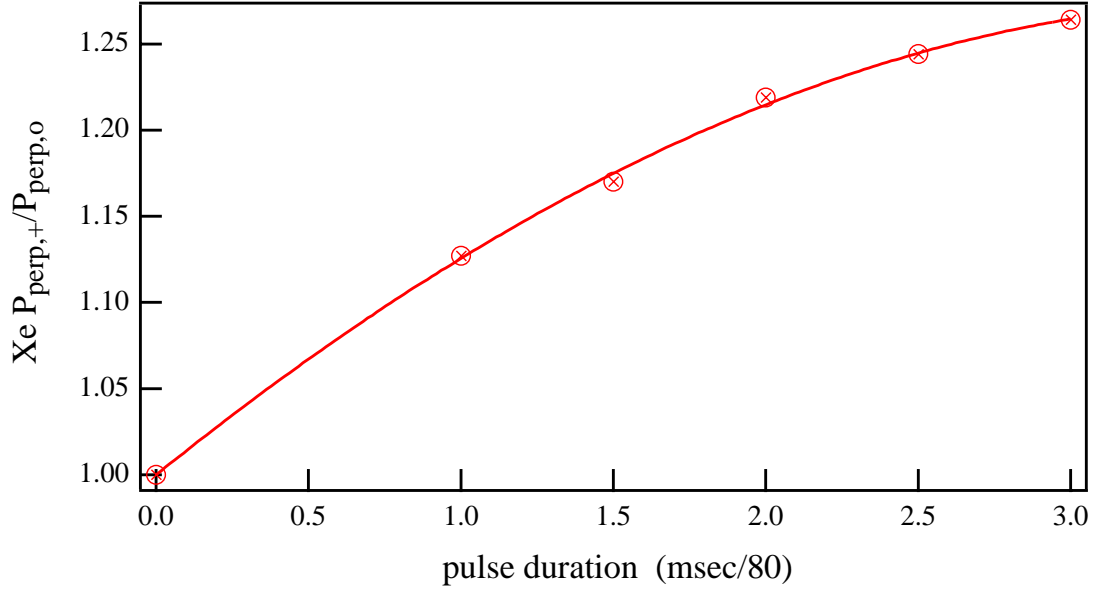


Figure 4.5: ^{129}Xe plot of the measured ratio $P_{\perp,+}/P_{\perp,o}$ as function of varying pulse durations τ for fixed drive voltage 15 mV RMS. Curvefitting to the function in Equation 4.8 yields the equilibrium orientation angle $\cot \theta_o = c_0$ as well the value of the tip angle $\alpha = c_1$ for an 80 ms pulse (see also Equation 4.9).

4.7 Verification of the Bloch Theory for Near-Equilibrium Oscillations of the ^{129}Xe Maser

In Section 2.4.2 we used the simplified Bloch theory of the DNGM to predict that the near-equilibrium oscillations of the transverse and longitudinal polarization vectors are related by

$$\delta \dot{P}_{\perp} = \left(\frac{P_{\perp,o}}{P_o \tau_{rd}} \right) \cdot \delta P_z(t), \quad (4.10)$$

where we have assumed that the resonator is tuned to the noble gas Zeeman frequency, $\omega_{ng} = \omega_o$, and we have ignored polarization transport effects. Suppose that the masers are well-equilibrated, and that at $t = 0^-$ we apply a “proper” tip (Section 4.6) which increases the orientation angle of the maser polarization by a small

amount α .

A near-equilibrium oscillation of the form $\delta P_{\perp}(t) = A_{\perp} e^{-\gamma_{ring} t} \sin(\omega_{ring} t - \phi)$ will ensue. If Equation 4.10 is correct, the oscillations in $\delta P_z(t)$ will be given by

$$\delta P_z(t) = \frac{P_o \tau_{rd}}{P_{\perp,o}} A_{\perp} e^{-\gamma_{ring} t} (-\gamma_{ring} \sin(\omega_{ring} t - \phi) + \omega_{ring} \cos(\omega_{ring} t - \phi)). \quad (4.11)$$

Just after the tip is applied, the above relations can be combined to give

$$\begin{aligned} \frac{\delta P_z(0)}{\delta P_{\perp}(0)} &= -\frac{P_o \tau_{rd}}{P_{\perp,o}} (\gamma + \omega \cot \phi) \\ &= -\cot \theta_o \frac{P_o \tau_{rd}}{P_{z,o}} (\gamma + \omega \cot \phi) \\ &\equiv R_{theory}, \end{aligned} \quad (4.12)$$

where θ_o is the maser polarization orientation angle before the pulse occurs, such that $\tan \theta_o = \frac{P_{\perp,o}}{P_{z,o}}$ (see Figure 4.3).

But we can also say something about this ratio using geometry. If P is the length of the polarization vector before the proper tip α is applied, then we can write $P_{z,o} = P \cos \theta_o$ and $P_{\perp,o} = P \sin \theta_o$. Just after the small tip is applied we have

$$\begin{aligned} \delta P_z(0) &= P[\cos(\theta_o + \alpha) - \cos(\theta_o)] \\ \delta P_{\perp}(0) &= P[\sin(\theta_o + \alpha) - \sin(\theta_o)]. \end{aligned} \quad (4.13)$$

Expanding and keeping terms to order α^2 only, we obtain

$$\begin{aligned} \frac{\delta P_z(0)}{\delta P_{\perp}(0)} &= -\frac{\tan \theta_o + \frac{\alpha}{2}}{1 - \frac{\alpha}{2} \tan \theta_o} \\ &\equiv R_{exp}. \end{aligned} \quad (4.14)$$

In Section 4.6 we applied a proper tip with $\alpha = .184$ (10.5°) and measured for the ^{129}Xe maser in cell S1: $\theta_o = 51.9^\circ$, $\omega_{ring} = .01084$, and $\gamma_{ring} = .000920/\text{sec}$. Measurements of τ_{rd} and the ratio $P_{z,o}/P_o$ for the same cell (DNGM 13, pages 140-150) yielded values of 27.9 seconds and .158, respectively. Plugging into Equations 4.12 and 4.14 gives $R_{theory} = -1.549$ and $R_{exp} = -1.512$. These results show that the simplified Bloch theory describes the near-equilibrium behavior of the ^{129}Xe maser quite well. Similar measurements were attempted for the ^3He maser, but the agreement between R_{theory} and R_{exp} was poor. This failure was expected, as the simplified Bloch equations (discussed in Section 2.4.2) neglect the coupling of the maser and pump chamber polarization dynamics, an assumption that is very poor for the rapidly diffusing ^3He atoms (See Appendix A for a discussion of the extended Bloch theory and polarization transport effects).

Chapter 5

Testing Lorentz and CPT

Symmetry Using a Two-Species

Noble Gas Maser

5.1 Overview

The standard model of particle physics successfully describes known particle interactions and has predicted *a priori* the existence of new particles, notably the W and Z gauge bosons and the top quark. At the foundation of this successful theory is the assertion that the physics of particles must be exactly invariant under simultaneous application of charge conjugation, parity inversion, and time reversal (CPT). CPT invariance is in turn based on the symmetry called local Lorentz invariance (LLI). LLI states that the result of any local non-gravitational experiment is independent of that (freely falling) experiment's orientation or velocity. Not only does LLI lie at the foundation of CPT and hence the standard model; but it also forms the basis for most single-metric theories of gravitation, and, along with the weak equivalence

principle, comprises the equivalence principle first stated by Einstein [62].

The fundamental nature of CPT and LLI symmetries provides motivation for their being tested experimentally with increasing exactness. However, recent theoretical developments have provided additional impetus for new experimental tests of LLI and CPT. Kostelecký and coworkers have devised the first comprehensive quantum field theory that admits possible violations of CPT and LLI [6, 23–30, 63–66] which are not countenanced by the minimal standard model. We used the $^{129}\text{Xe}/^3\text{He}$ dual noble gas maser (DNGM) to test Lorentz symmetry by monitoring the relative phases and Larmor frequencies of the co-located ^3He and ^{129}Xe masers as the laboratory reference frame rotated with respect to the distant stars. A sidereally varying frequency shift would be a signature of LLI violation, as emphasized pictorially in Figure 5.1.

The minimal standard model is believed to be the low energy limit of a more fundamental theory that may also incorporate gravity. This fundamental theory could possess the properties of Lorentz and CPT symmetries, which could be spontaneously broken to yield apparent Lorentz and CPT violation at the level of the standard model. (For example, a class of string theories has been shown to have such spontaneous Lorentz and CPT violation [6].) The standard model extension of Kostelecký et al. treats the effects of spontaneous Lorentz symmetry breaking in the context of a low-energy effective theory, in which terms can be induced that violate Lorentz invariance explicitly [6, 23–25, 27–30, 64]. Lorentz symmetry remains a property of the underlying fundamental theory, because the breaking is spontaneous. Thus the effective low energy theory possesses many desirable properties, such as the usual $\text{SU}(3)\times\text{SU}(2)\times\text{U}(1)$, microcausality, energy positivity, and momentum and energy conservation. Also, standard quantization methods are retained, so that Dirac and Schrödinger equations emerge at the appropriate limits.

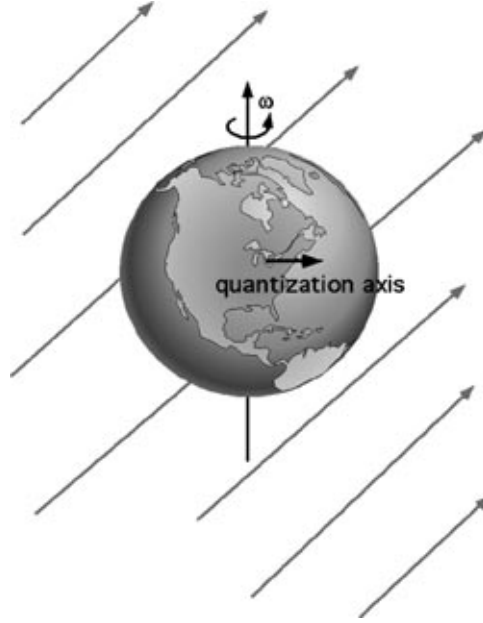


Figure 5.1: Bounds on CPT- and Lorentz-violation can be obtained by comparing the frequencies of co-located clocks as they rotate with respect to the fixed stars. The standard-model extension described in [6, 23–25, 27–30, 63, 64, 64, 66] admits Lorentz-violating coupling of the unpaired neutron in both ^{129}Xe and ^3He nuclei to expectation values of tensor fields. Each of these fields may have an unknown magnitude and orientation in space, to be limited by experiment. The background arrows in Figure 5.1 illustrate one such field.

A natural scale for a fundamental theory including gravity is the Planck mass M_p , which is roughly 10^{17} times larger than the characteristic electroweak mass m_w of the low energy standard model. If the origin of spontaneous Lorentz violation lies at the Planck scale, experimental signals resulting from the fundamental theory could be strongly suppressed by some power of the ratio m_w/M_p . Other substantial suppressions could also be present, such as factors arising from Yukawa couplings to the Higgs scalar field [6]. The calculable phenomenon predicted by the extended theory are arrived at perturbatively, but no assumptions are made about the nature of the Lorentz violating parameters, other than that they are suppressed strongly and hence are extremely small. Very sensitive experiments are thus required to

observe such potential effects. Kostelecký et al. have studied several classes of experiments which might eventually resolve these very small possible violations of LLI and CPT, and determined that clock comparisons provide some of the most sensitive probes. The beauty of their theory is to provide a single coherent framework at the level of the standard model that can be used to analyze and compare a great variety of experimental tests.

Application of the standard model extension to atoms, molecules, and ions is stated in terms of an effective low-energy Lagrangian which includes small LLI-violating interactions associated with the coupling of massive spin- $1/2$ Dirac fermions to remnant vacuum fields [6,67]. All these couplings violate Lorentz symmetry; some also violate CPT. The strengths of the couplings are stated in terms of parameters which are in general different for each fermion type. Thus, couplings of the electron, neutron, and proton to these possible remnant fields must each be constrained (or measured) separately by experiment. As a consequence, only certain linear combinations of parameters, rather than individual parameters themselves, can be constrained by clock tests. Kostelecký and Lane have derived a non-relativistic Hamiltonian appropriate for perturbative calculations, and computed the net effect of LLI-violating couplings of the electron, proton, and neutron on the energy levels of selected atoms and ions. These calculations rely on simplifying assumptions, such as the validity of Schmidt model descriptions of nuclei, but nevertheless provide an approximate basis for comparing the sensitivities of various LLI/CPT tests.

5.2 Limit on Lorentz and CPT Violation Using the DNGM

We now present a paper¹ which (i) provides an overview of, and context for, the standard model extension developed by Kostelecký et al.; (ii) describes our experimental search for LLI and CPT violation using the DNGM; and (iii) compares our results on LLI violation to other noteworthy tests of LLI and CPT. Our paper is rich in references - listed at the end of the thesis - and we particularly recommend the paper by Kostelecký and Lane [6] as a starting point. This article describes thoroughly the standard model extension and also provides an excellent survey and interpretation of all completed and proposed clock-comparison tests of LLI and CPT symmetries.

Note that Chapters 1 – 4 of this thesis contain a thorough discussion of the theory and operation of the DNGM. Many of the sections in those chapters are particularly germane to the test of Lorentz and CPT symmetry reported here. In particular, we emphasize the following:

Section 2.5 Methodology of measuring maser phase and frequency.

Section 2.6 Phase and frequency shift mechanisms in the DNGM. Included are discussions of drift extraction analysis methods for LLI and EDM experiments.

Section 3.4.3 Stabilization of Rb magnetization in pump bulb.

Section 3.6 Co-magnetometer experiments bound the size of potential sidereally varying frequency shifts caused by magnetic field fluctuations.

¹Our paper was recently submitted to *Physical Review Letters*, and is reproduced here with the permission of all co-authors.

Section 3.7.5 Resonator temperature coefficient measurements bound the size of potential sidereally varying frequency shifts caused by temperature fluctuations.

Section 3.7.7 Data acquisition, processing and storage.

Note also that Section 5.3 presents additional tables and graphs that are not included in our paper of Section 5.2 but might be of interest to the reader.

Limit on Lorentz and CPT Violation of the Neutron Using a Two-Species Noble Gas Maser

D. Bear, R.E. Stoner, and R.L. Walsworth

Harvard-Smithsonian Center for Astrophysics, Cambridge, MA 02138

V. Alan Kostelecký and Charles D. Lane

Physics Department, Indiana University, Bloomington, IN 47405

Abstract

A search for sidereal variations in the frequency difference between co-located ^{129}Xe and ^3He Zeeman masers sets the most stringent limit to date on leading-order Lorentz and *CPT* violation involving the neutron, consistent with no effect at the level of 10^{-31} GeV.

Lorentz symmetry is a fundamental feature of modern descriptions of nature, including both the standard model of particle physics and general relativity. However, these realistic theories are believed to be the low-energy limit of a single fundamental theory at the Planck scale. Even if the underlying theory is Lorentz invariant, spontaneous symmetry breaking might result in small apparent violations of Lorentz invariance at an observable level. Experimental investigations of the validity of Lorentz symmetry therefore provide valuable tests of the framework of modern theoretical physics.

Clock-comparison experiments [7–10, 68–70] serve as sensitive probes of rotation invariance and hence of Lorentz symmetry, essentially by bounding the frequency variation of a clock as its orientation changes. In practice, the most precise limits are obtained by comparing the frequencies of two different co-located clocks as they rotate with the Earth. Typically, the clocks are electromagnetic signals emitted or absorbed on hyperfine or Zeeman transitions.

Here, we report on a search for sidereal variations in the frequency of co-located ^{129}Xe and ^3He masers, both operating on nuclear spin-1/2 Zeeman transitions. In the context of a general standard-model extension allowing for the possibility of Lorentz and CPT violation [23, 63, 66], the $^{129}\text{Xe}/^3\text{He}$ -maser experiment sets the most stringent limit to date on leading order Lorentz and CPT violation of the neutron: about 10^{-31} GeV, or more than six times better than the best previous measurements [6].

The standard-model extension motivating this experiment emerges from any underlying theory that generates the standard model and contains spontaneous Lorentz violation [67]. For example, this might occur in string theory [71]. The standard-model extension maintains theoretically desirable properties of the usual standard model [66]. Its formulation at the level of the known elementary particles is a key feature enabling quantitative comparison of a wide array of tests of Lorentz and CPT symmetry. In this context, theoretical studies have been performed to investigate the sensitivity of clock-comparison experiments [6], tests of QED in Penning traps [64], experiments with a spin-polarized torsion pendulum [72], hydrogen-antihydrogen spectroscopy [30], studies of photon birefringence in the vacuum [27, 66, 73], observations of muons [74], measurements of neutral-meson oscillations [23, 24, 63], studies of the baryon asymmetry [29], and observations of cosmic rays [75].

In the context of the standard-model extension, the most sensitive prior clock-

comparison experiment is the $^{199}\text{Hg}/^{133}\text{Cs}$ comparison of Hunter, Lamoreaux *et al.* [6, 8, 9]. Recent experimental work motivated by the standard-model extension includes Penning trap tests by Gabrielse *et al.* on the antiproton and the H^- ion [76] and by Dehmelt *et al.* on the electron and positron [77, 78]. A reanalysis by Adelberger, Gundlach, Heckel, and co-workers of existing data from a spin-polarized torsion pendulum experiment [79, 80] sets the most stringent bound to date on Lorentz and CPT violation of the electron, at about 10^{-29} GeV [81]. A recent Lorentz-symmetry test using hydrogen masers has searched for Zeeman-frequency sidereal variations, placing a bound on Lorentz violation at the level of 10^{-27} GeV [82]. Together with the results of Ref. [81], this implies an improved clean limit of 10^{-27} GeV on Lorentz-violating couplings involving the proton. Also, the KTeV experiment at Fermilab and the OPAL and DELPHI collaborations at CERN have constrained possible Lorentz- and CPT-violating effects in the K and B_d systems [83, 84].

The standard-model extension predicts that the leading-order Lorentz- and CPT-violating correction to the ^3He -maser frequency, using the ^{129}Xe maser as a co-magnetometer, is [6]:

$$2\pi |\delta\nu_J| = \left| -3.5\tilde{b}_J^n + 0.012\tilde{d}_J^n + 0.012\tilde{g}_J^n \right|. \quad (5.1)$$

Here, \tilde{b}_J^n , \tilde{d}_J^n , and \tilde{g}_J^n are small parameters characterizing the strength of Lorentz-violating couplings of the neutron to possible background tensor fields that may arise from spontaneous symmetry breaking in a fundamental theory. The couplings associated with \tilde{b}_J^n and \tilde{g}_J^n also violate CPT. All three parameters are linear combinations of more basic quantities in the underlying relativistic Lagrangian of the standard-model extension [6].

In the analysis leading to Eq. (1), the Lorentz-violating coupling of either the ^3He or ^{129}Xe nucleus has been taken as that of a single $^1S_{1/2}$ valence neutron in a Schmidt model [6]. The parameters appearing in Eq. (1) are therefore associated only with neutron couplings, as indicated by the superscript n on \tilde{b}_J^n , \tilde{d}_J^n , \tilde{g}_J^n . Equation (1) also assumes that the applied magnetic field, which sets the quantization axis of the experiment, is directed east-west in the Earth’s reference frame. The subscript $J = X, Y$ indicates components in the sidereal reference frame that are orthogonal to the Earth’s axis of rotation.

The design and operation of the two-species $^{129}\text{Xe}/^3\text{He}$ maser has been discussed in recent publications [2,3]. Here, we give a brief review. The two-species maser contains dense co-located ensembles of ^3He and ^{129}Xe atoms. Each ensemble performs an active maser oscillation on its nuclear spin-1/2 Zeeman transition at approximately 4.9 kHz for ^3He and 1.7 kHz for ^{129}Xe in a static magnetic field of 1.5 gauss. This two-species maser operation can be maintained indefinitely. The population inversions for the two maser ensembles are created by spin-exchange collisions between the noble-gas atoms and optically pumped Rb vapor [18,19]. The $^{129}\text{Xe}/^3\text{He}$ maser has two glass chambers, one acting as the spin exchange “pump bulb” and the other serving as the “maser bulb.” This two chamber configuration permits the combination of physical conditions necessary for a high flux of spin-polarized noble gas atoms into the maser bulb, while also maintaining ^3He - and ^{129}Xe -maser oscillations with good frequency stability: stability of about 100 nHz is typical for measurement intervals larger than about an hour [3]. Either noble-gas species can serve as a precision magnetometer to stabilize the system’s static magnetic field, while the other species is employed as a sensitive probe for Lorentz- and CPT-violating interactions.

We used the $^{129}\text{Xe}/^3\text{He}$ maser to search for a Lorentz-violation signature by monitoring the relative phases and Larmor frequencies of the co-located ^3He and

^{129}Xe masers as the laboratory reference frame rotated with respect to the fixed stars. The system was operated with the ^{129}Xe maser as the co-magnetometer, the ^3He maser free-running, and the quantization axis directed east-west in the Earth's reference frame. To leading order, the standard-model extension predicts that the Lorentz-violating frequency shifts for the ^3He and ^{129}Xe maser are the same size and sign. Hence, the resultant sidereal variation of the ^3He maser frequency observed in the laboratory frame takes the form

$$\delta\nu_{He} = \delta\nu_X \cos(\Omega_s t) + \delta\nu_Y \sin(\Omega_s t), \quad (5.2)$$

where Ω_s is the angular frequency of the sidereal day [85], and the parameters $\delta\nu_J$ given by Eq. (1) represent the net effect of the Lorentz- and CPT-violating couplings on the ^3He maser frequency with the ^{129}Xe maser acting as a co-magnetometer. The time t was measured in seconds from the beginning of the sidereal day in Cambridge, Massachusetts (longitude -71.11°).

Data collection and analysis were performed as follows. The ^{129}Xe - and ^3He -maser signals from an inductive pickup coil were buffered, amplified, and sent to a pair of digital lock-in detectors. Typical raw-signal levels were about 3 to 5 μV . All reference signals used in the experiment were derived from the same hydrogen-maser clock, thus eliminating concerns about unmeasurable electronic phase shifts between the reference oscillators. The hydrogen maser operated on the standard hyperfine clock transition, and thus had no leading-order sensitivity to Lorentz and CPT violation [6, 30]. Active feedback to the solenoid's magnetic field locked the phase of the ^{129}Xe maser to that of a 1.7 kHz reference signal, and thereby isolated the experiment from common-mode systematic effects (such as stray magnetic field fluctuations) that would otherwise shift the frequencies of the noble-gas masers

in proportion to the ratio of their magnetic moments. When phase locked, the short- and long-term frequency stability [3] of the ^{129}Xe maser was several orders of magnitude better than that of the free-running ^3He maser, so the ^{129}Xe Zeeman frequency was treated as constant in the data analysis.

The phase and amplitude of both maser signals were recorded at four-second intervals by the lock-in amplifiers and downloaded for analysis every 23.93 hours. A one-sidereal day run thus contained approximately 21,540 evenly spaced measurements of the relative phases of the two masers. The values of the two coefficients $\delta\nu_X, \delta\nu_Y$ were computed, providing a measure of potential Lorentz-violation for that day's run. Seven additional diagnostic signals were recorded, including the temperatures of the pump bulb, maser bulb, and external resonator; an optical monitor of the Rb magnetization in the pump bulb; the broadband power emitted by the optical-pumping laser-diode array; the ambient room temperature; and the east-west component of the ambient magnetic field. Control loops stabilized the system temperatures to about 10 mK. Two additional control loops were used, feeding back to the optical-pumping laser to reduce systematic effects arising from variations in the density and polarization of Rb in the pump bulb [57].

Small noble-gas polarization-induced frequency shifts were the dominant source of instability (i.e., phase drift) in the free-running ^3He maser. For a typical one-day run, the linear-correlation coefficient between ^3He phase data and the integrated amplitude of either maser was in the range 0.95 - 0.99. We admitted terms to our data-analysis model to account for this polarization-induced phase drift. The effect of potential Lorentz-violating couplings on the evolution of the ^3He phase was expressed in terms of the coefficients $\delta\nu_J$ via integration of Eq. (2), and initial

reduction of each one-day run was performed using the minimal fit model

$$\begin{aligned} \delta\phi_{He} = & \phi_0 + 2\pi\nu_0 t \\ & + 2\pi\Omega_s^{-1}[\delta\nu_X \sin(\Omega_s t) - \delta\nu_Y \cos(\Omega_s t)], \end{aligned} \quad (5.3)$$

where the coefficients ϕ_0 and ν_0 account for absolute phase and frequency offsets between the ^3He maser and the ultra-stable reference oscillator. The reduced χ^2 statistic for this fit model was determined, and then additional terms corresponding to quadratic and maser amplitude-correlated phase drift were incorporated into the model if they significantly improved the reduced χ^2 [86]. The coefficients $\delta\nu_X$ and $\delta\nu_Y$ for each one-day run were extracted using a linear least-squares routine on the best-fitting model for that day, which contained at most seven free parameters and thus at least $(21500 - 7)$ degrees of freedom. See Fig. 1 for an example of the residuals from one day's data. As a final check, a faux Lorentz-violating effect of known phase and amplitude was added to the raw data and the analysis was repeated. Data reduction for a given sidereal day was considered successful if the synthetic physics was recovered and there was no change in the covariance matrix generated by the fitting routine.

Data for this experiment were acquired with three different maser cells over a period of 30 days in April 1999 (cell S3), 24 days in September 1999 (cell E9), and 60 days in February-May 2000 (cell SE3, runs 1 and 2). A total of 90 usable sidereal-day values of $\delta\nu_X$, $\delta\nu_Y$ were obtained. The main magnetic field of the apparatus was reversed about every 10 days to help distinguish possible Lorentz-violating effects from diurnal systematic variations. Field reversal and subsequent re-equilibration of the masers required approximately 24 hours.

Systematic effects resulting from possible diurnally varying ambient magnetic

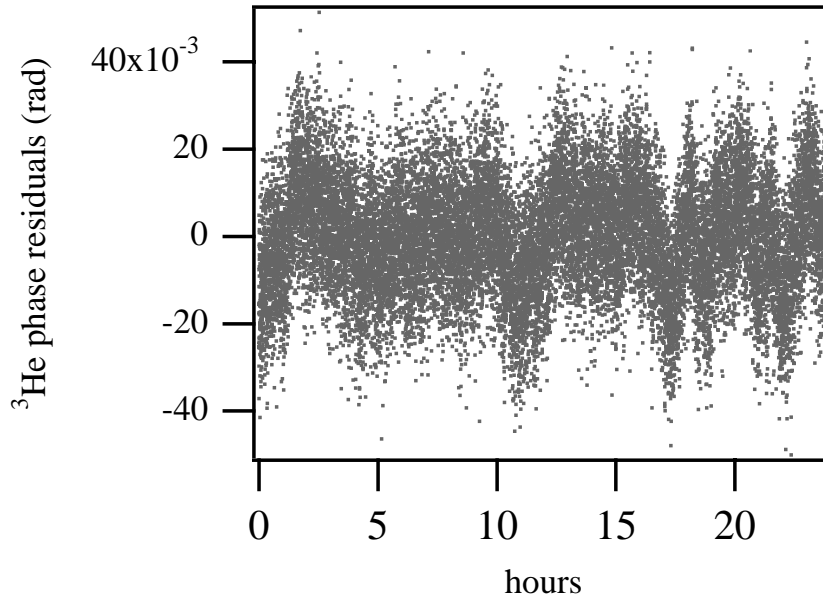


Figure 5.2: Typical residuals for the ^3He phase data from one sidereal day, calculated using the fit model given in Eq. (3).

fields would not average away with field reversals. Thus, the effectiveness of the ^{129}Xe co-magnetometer at eliminating such effects was carefully assessed before beginning data acquisition. Since the two maser ensembles do not have perfect spatial overlap, penetration of external magnetic fields through the nested magnetic shields and into the interaction region could induce small frequency shifts in the free-running ^3He maser despite the presence of the ^{129}Xe co-magnetometer. Large coils (~ 2.4 m diameter) surrounding the $^{129}\text{Xe}/^3\text{He}$ -maser apparatus were used to switch on and off 0.5 G external magnetic fields in the north-south and east-west directions. A bound on the ratio $|\delta\nu_{\text{He}}/\delta B_{\text{external}}|$ was obtained. The drifts in the ambient magnetic field near the apparatus were measured to be about 0.2 mG over a typical 24-hour period, resulting in a worst-case shift on the free-running ^3He maser of less than 8 nHz, well below the present sensitivity of the experiment to Lorentz and CPT violation. It should be noted that the relative phase between the solar and

sidereal day evolved about 2π radians over the course of the experiment (April 1999 to May 2000). Hence, diurnal systematic effects from any source would tend to be reduced by averaging results from all measurement sets.

The measured values of $\delta\nu_J$ exhibited a small dependence on the direction of the solenoidal magnetic field in the laboratory frame. This dependence was most likely due to hysteresis and asymmetry in magnetic interactions between the solenoid and the nested μ -metal shields under field reversal. For each cell, the data for the east and west magnetic-field orientations were analyzed separately to determine mean values and standard errors for $\delta\nu_J$, yielding the results in Table 1. As an example, Fig. 2 shows the single-day values of $\delta\nu_X$ obtained in the first run with cell SE3 in the east field orientation (SE3 E1).

Cell	$\delta\nu_X$ (nHz)	$\delta\nu_Y$ (nHz)
S3 E	95 ± 118	197 ± 114
S3 W	-43 ± 138	88 ± 148
E9 E	-86 ± 234	-194 ± 207
E9 W	-206 ± 186	-60 ± 134
SE3 E1	100 ± 148	9 ± 141
SE3 W1	-1 ± 88	62 ± 109
SE3 E2	-2 ± 180	68 ± 107
SE3 W2	-35 ± 118	197 ± 120

Table 5.1: Means and standard errors for $\delta\nu_X$ and $\delta\nu_Y$. Results are displayed for each of the three cells (S3, E9, and SE3) with both east (E) and west (W) orientations of the magnetic field. Two runs were performed for cell SE3.

The total weighted means and uncertainties for $\delta\nu_X$ and $\delta\nu_Y$ were then formed from all data sets. Finally, the results were used to extract the measured value of $R \equiv \sqrt{\delta\nu_X^2 + \delta\nu_Y^2}$, giving 53 ± 45 nHz (1- σ level).

The size of the coefficients in Eq. (1) indicates that the $^{129}\text{Xe}/^3\text{He}$ -maser experiment is most sensitive to the Lorentz- and CPT-violating coupling associated

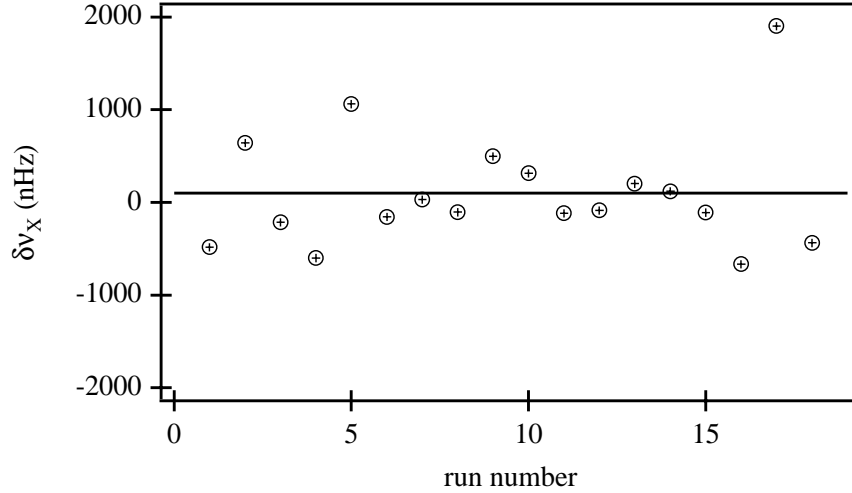


Figure 5.3: Values of the Lorentz-violating parameter $\delta\nu_X$ obtained with cell SE3 in the E1 orientation. The horizontal line indicates the mean value for that data set.

with \tilde{b}_j^n . Under the assumption of negligible \tilde{a}_j^n and \tilde{g}_j^n [6], the above experimental result for R corresponds to a value for $\tilde{b}_\perp^n \equiv \sqrt{(\tilde{b}_X^n)^2 + (\tilde{b}_Y^n)^2} = (4.0 \pm 3.3) \times 10^{-31}$ GeV. This result is consistent with no Lorentz- and CPT-violating effect, given reasonable assumptions about the probability distribution for R [87]. It represents the most stringent limit to date on possible Lorentz- and CPT-violating couplings involving the neutron and is more than six times better than the best previous measurements [6].

We are planning improved Lorentz and CPT tests using noble-gas masers. Upgrading laser and temperature control and acquiring a larger data set could better the present Lorentz and CPT constraint from the $^{129}\text{Xe}/^3\text{He}$ system by up to an order of magnitude. Also, a new two-species Zeeman maser using ^3He and ^{21}Ne might provide even greater improvements to constraints on neutron parameters [6, 88].

David Phillips, Mark Rosenberry, Federico Cané, Timothy Chupp, Robert Vesot and Edward Mattison helped greatly with this project. Development of the $^{129}\text{Xe}/^3\text{He}$ Zeeman maser was supported by a NIST Precision Measurement Grant.

Support for the Lorentz-violation test was provided by NASA grant NAG8-1434, ONR grant N00014-99-1-0501, and the Smithsonian Institution Scholarly Studies Program. This work was supported in part by the DOE under grant DE-FG02-91ER40661.

5.3 Addendum to Chapter 5

In this section we present some additional tables and graphs that are not included in the paper of Section 5.2 but might be of interest to the reader.

Comparison of Experimental Bounds on Lorentz Symmetry

Experiment	$\tilde{b}_{\mathbf{X},\mathbf{Y}}^e$ (GeV)	$\tilde{b}_{\mathbf{X},\mathbf{Y}}^p$ (GeV)	$\tilde{b}_{\mathbf{X},\mathbf{Y}}^n$ (GeV)
anomaly frequency of electron in Penning trap (Dehmelt et. al.)	10^{-25}	–	–
^{199}Hg and ^{133}Cs precession frequencies (Hunter, Lamoreaux et. al.)	10^{-27}	10^{-27}	10^{-30}
spin-polarized torsion pendulum (Adelberger et. al.)	10^{-29}	–	–
Hydrogen maser (Phillips, Humphrey, Walsworth et. al.)	10^{-27}	10^{-27}	–
$^{129}\text{Xe}/^3\text{He}$ DNGM (this work)	–	–	10^{-31}

Table 5.2: Leading experimental bounds on Lorentz violation for the electron, proton and neutron.

Plot of R -distribution function

The probability distribution for $R = \sqrt{\delta\nu_X^2 + \delta\nu_Y^2}$ is formed by multiplying the distributions for $\delta\nu_X$ and $\delta\nu_Y$, converting to polar coordinates, and integrating over the polar angle. In the case where $\delta\nu_X$ and $\delta\nu_Y$ have zero mean value and the same standard deviation σ , the probability distribution takes the form $P(R) = \sigma^{-2}R \exp(-r^2/2\sigma^2)$, with the most probable value of R occurring at $R = \sigma$. Thus our experimental result of $R = 53 \pm 45$ nHz is consistent with no sidereal variation of the ^3He maser frequency, with R differing from the most probable value by less than one standard deviation.

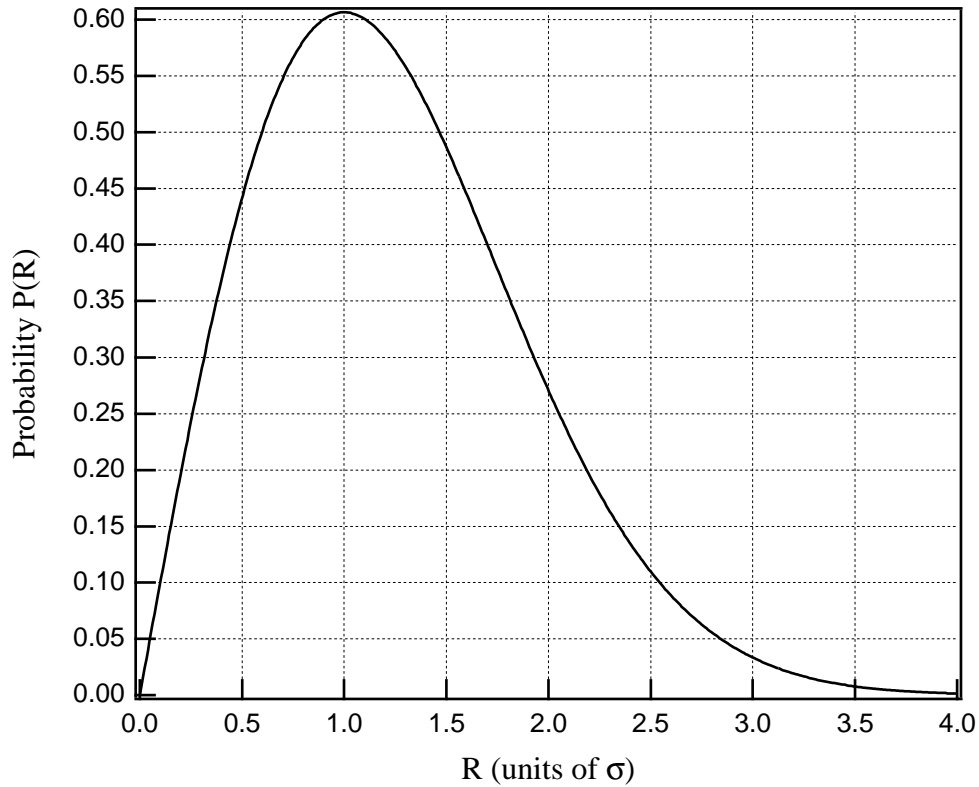


Figure 5.4: A plot of the R -distribution probability function.

Chapter 6

Toward a Test of Time Reversal Symmetry Using the DNGM

In this chapter we describe a preliminary search for a permanent electric dipole moment (EDM) of the ^{129}Xe atom, as evidence of time reversal (T) symmetry violation in elementary particle interactions. We emphasize that the EDM work presented here is strictly preliminary in nature. The null result of $d_{xe} < 1 \times 10^{-26}$ e-c.m. is not yet competitive with the current best EDM limits [15] in atomic systems, and thus does not provide new information on possible sources of T -violation posited by extensions to the standard model (Equation 6.1). Nevertheless, we expect that the capability of the DNGM for performing sensitive differential measurements of the ^{129}Xe and ^3He nuclear Zeeman transition frequencies should permit a measurement of the ^{129}Xe EDM at a sensitivity of $\sim 1 \times 10^{-28}$ e-c.m. within a few years. Such a result would be the most sensitive absolute EDM search made in any system to date and would provide a theory-dependent sensitivity to proposed T -violating interactions that is roughly comparable to the recent ^{199}Hg EDM search [15], but with the important advantage of having a co-magnetometer. Here we provide moti-

vation for performing an EDM search in ^{129}Xe . We also describe the experimental apparatus and procedures implemented thus far in obtaining our preliminary result of $d_{xe} < 1 \times 10^{-26}$ e-c.m.

6.1 Theoretical Overview and Motivation

Time reversal was long assumed to be a fundamental, perfect symmetry of elementary particle interactions. In 1964, however, a single, indirect¹ example of a violation of T -symmetry was discovered in the decay of neutral K -mesons [31]. During the past 30 years much theoretical effort has been devoted to understanding T -symmetry violation in nature, and many experiments have been performed to search for failures of T -symmetry beyond that originally observed in the K -meson system. The theoretical work has posited various possible sources of T -asymmetry beyond the standard model, but no new experimental examples have been found, thus preventing confirmation of a correct theory and leaving T -symmetry violation as an important problem in elementary particle physics. In addition, the inferred matter/antimatter asymmetry in the universe may be a consequence of T -asymmetry in the laws of elementary particle interactions [32]. Thus an understanding of T -symmetry violation is important both for high energy physics and cosmology. Further experimentation, especially the discovery of additional examples of T non-conservation, is essential to understand this fundamental symmetry breakdown.

Several experimental approaches have been used in the search for additional failures of T -symmetry [33]. The two most sensitive are: (i) the investigation of interactions and decays of high energy particles (e.g. the K and B mesons); and (ii)

¹This experiment measured CP violation, which implies T violation if CPT holds. Recent work on the CPLEAR experiment at CERN has made direct observation of T -symmetry violation in the same system.

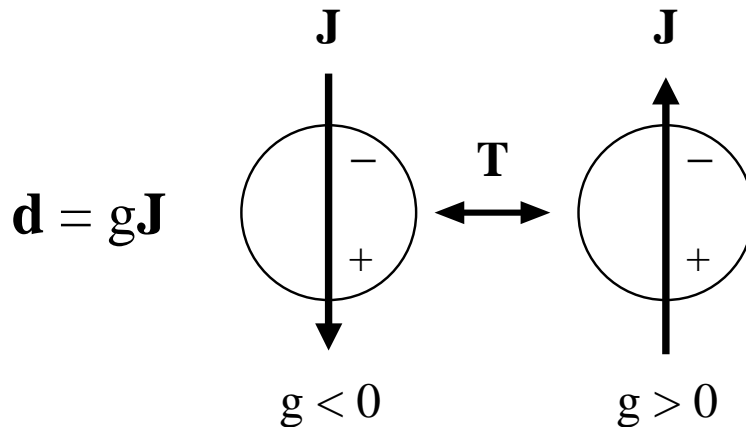


Figure 6.1: Illustration of how for an atom, molecule, or elementary particle to have a permanent EDM, T symmetry must be violated.

the search for EDMs of atoms, molecules, and the neutron. To date, no examples of T -symmetry violation in high energy particle decays have been uncovered that are inconsistent with the standard model. Similarly, no evidence of an EDM has yet been found. Nevertheless, the experimental EDM sensitivity has improved by a factor of $\sim 10^{10}$ over the last 30 years, and is now at a level to test many theories that purport to explain T -asymmetry in nature. For example, experiments with cold stored neutrons [11,89] have set the most stringent direct limits to date on the EDM of a free particle by setting a bound on the neutron EDM (d_n at the level of 10^{-25} e-cm). The limit on d_n has directly disproved or constrained several theories that include T -symmetry violation [17,33]. In particular, Weinberg's 3-Higgs model [90] is effectively ruled out because it predicts $10^{-25}\text{e-cm} \leq d_n \leq 10^{-22}$ e-cm.

Theories of particle interactions that are asymmetric (or odd) under T generally predict that free particles like the neutron, proton, and electron have non-zero EDMs. Composite systems like atoms and molecules may also have EDMs due to the intrinsic EDMs of their sub-atomic constituents as well as T -odd interactions

among these constituents [17, 33]. In the absence of degeneracies, Wigner-Eckart selection rules require an electric dipole moment \mathbf{d} to be parallel or antiparallel to the system's total angular momentum \mathbf{F} . But \mathbf{d} is a polar vector (T -even, P -odd) while \mathbf{F} is an axial vector (T -odd, P -even). Thus the relative orientations of \mathbf{d} and \mathbf{F} change under time reversal or spatial inversion, as illustrated pictorially in Figure 6.1.² Calculations indicate that atomic EDM magnitudes increase rapidly with atomic number Z [35]. Thus precision experimental EDM searches using high Z atoms serve as important complements to EDM measurements on the neutron.

In recent years, precision experimental searches for atomic EDMs have used the high- Z diamagnetic atoms ^{129}Xe [20, 91] and ^{199}Hg [14, 92] and the high- Z paramagnetic atoms ^{133}Cs [12] and ^{205}Tl [16, 93]. EDMs of ^{129}Xe and ^{199}Hg are most sensitive to T -odd interactions in the nucleus as well as tensor electron-nuclear interactions; whereas ^{133}Cs and ^{205}Tl EDMs are most sensitive to a possible EDM of the electron. Each of the EDM measurements performed to date sets a stringent limit, consistent with zero, on the magnitude of the atomic or molecular EDM in question. These null results already impose significant constraints on theories that incorporate T -asymmetry in extensions of the standard model [17, 90, 94]. For example, there has recently been great interest in models in which neutral-Higgs-boson exchange mediates T -symmetry violation [90, 94]. Such models predict atomic EDMs to be of the order of magnitude of the best limits coming from present experiments, although the theoretical connection between elementary particle theory and atomic experiment is difficult (providing order of magnitude reliability [17]). Thus the challenge to experimental atomic physicists is to improve the EDM measurement sensitivity of their techniques, so that the predictions of finite atomic EDMs can be definitively

²For a spin- $1/2$ atom such as ^{129}Xe , this fact follows trivially from Kramer's theorem [34], which asserts that the energy levels of a T -even Hamiltonian are doubly degenerate.

Parameter	limit	experiment	reference
d_e	4×10^{-27}	^{205}Tl	[16]
C_S	7×10^{-7}	^{199}Hg	[15]
C_T	1.3×10^{-8}	^{199}Hg	[15]
η	1.6×10^{-3}	^{199}Hg	[15]

Table 6.1: Table of the most stringent present experimental limits on the T -violating parameters in Equation 6.1.

tested.

Calculations by Khriplovich [95,96], Martensson-Pendril [97], and Flambaum [98] estimate the value of an atomic EDM in ^{129}Xe to be approximately given by

$$d_{xe} = \overbrace{10^{-3} \cdot d_e + 7.5 \times 10^{-23} \cdot C_S}^{\text{Khriplovich}} + \overbrace{10^{-21} \cdot C_T}^{\text{Martensson-Pendril}} + \overbrace{10^{-26} \cdot \eta}^{\text{Flambaum}}. \quad (6.1)$$

Here, d_e is the value of the electron EDM; C_S and C_T are coupling constants reflecting the strength of pseudo-scalar and pseudotensor T -violating interactions between the electrons and nucleons; and η is a dimensionless scale factor proportional to the size of the atomic Schiff moment, which reflects contributions to an atomic EDM arising from intrinsic nucleon EDMs and T -violating nucleon-nucleon interactions. Table 6.1 gives the most stringent present limits on these parameters, as well the experiments which have established those limits. The theoretical values are uncertain at approximately the 50% level, but it is still possible to deduce that for a ^{129}Xe EDM search to provide new information, d_{xe} will need to be measured at a level $\sim 1 - 2 \times 10^{-28}$ e-c.m. or better.

6.2 Experimental Procedure and Apparatus

As described in Section 6.1, an atomic EDM must point along the total angular momentum vector \mathbf{F} . In ^{129}Xe and ^3He , the electronic angular momentum \mathbf{J} is equal to zero, and \mathbf{F} points along the direction of the nuclear spin \mathbf{I} . We can thus write the Hamiltonian for a ^{129}Xe or ^3He atom in external electric and magnetic fields as

$$\hat{H} = \frac{-(d_{ng}\mathbf{E} + \mu_{ng}\mathbf{B}) \cdot \mathbf{I}}{I}, \quad (6.2)$$

where d_{ng} is the magnitude of the noble gas EDM, \mathbf{E} is the electric field, \mathbf{B} is the magnetic field, and \mathbf{I} is the nuclear spin ($I = 1/2$). The dual noble gas maser EDM search consisted of sequential applications of an electric field \mathbf{E} across the interaction region. The electric field was oriented parallel to the experiment's static magnetic field, and its direction was reversed regularly (\sim every 5000 seconds).

The DNGM was operated with the ^{129}Xe species phase-locked and the ^3He maser free-running. Coupling to a ^{129}Xe EDM would produce a frequency shift linear in the magnitudes and signs of both the ^{129}Xe EDM and the applied electric field. A ^{129}Xe EDM coupling would change the magnetic field required to maintain a constant ^{129}Xe maser frequency: this EDM-induced alteration of the magnetic field would cause a frequency shift in the free-running ^3He maser. Calculations indicate that d_{ng} should scale as Z^2 or Z^3 [35], so that $d_{xe} \geq \left(\frac{54}{2}\right)^2 d_{he}$. The value of the ^{129}Xe EDM is then given by

$$d_{xe} = \frac{h}{2\gamma\Delta E} \delta\nu_{he}, \quad (6.3)$$

where $\gamma \approx 2.75408$ is the ratio of the ^3He and ^{129}Xe magnetic moments and $\delta\nu_{he}$ is the change in the free-running ^3He maser frequency when the electric field changes by ΔE . We will apply this result when analyzing our preliminary data in Section

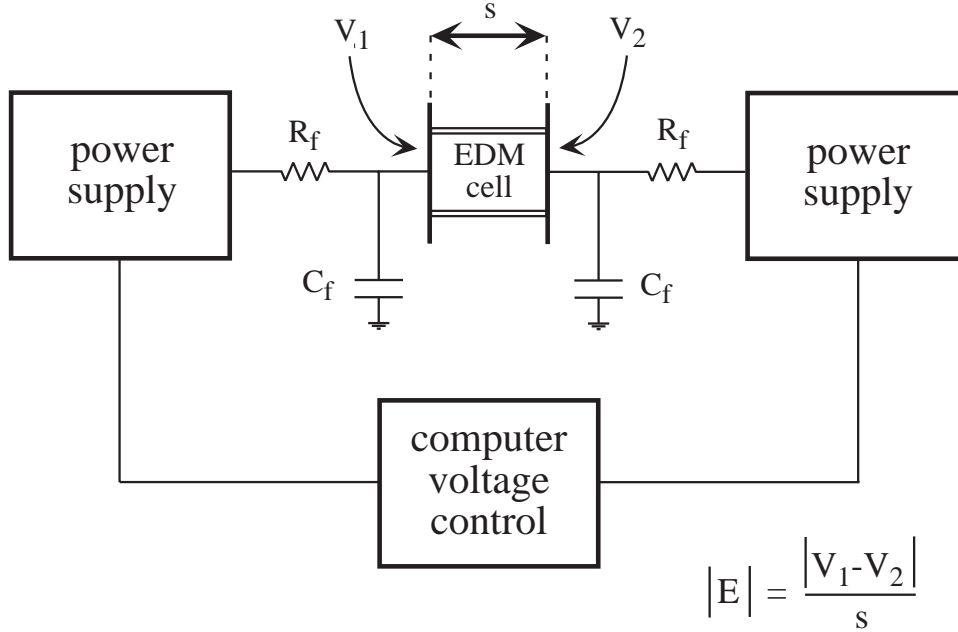


Figure 6.2: Schematic of the DNGM high voltage system used to create the applied electric field necessary for a ^{129}Xe EDM search.

6.3.

A schematic of the electric field control system is shown in Figure 6.2. The field across the EDM cell (typically ~ 2 kV/cm) was generated by a pair of polarity-switching high voltage DC power supplies.³ Polished brass tabs were soldered to high voltage hookup wire coming from the power supply outputs. Electrical connection from the high voltage to the cell was achieved by pressing the tabs against the molybdenum cell endplates using 4-40 nylon screws, as shown in Figure 6.3. The value of the electric field across the cell is given by $E = \frac{V_+ - V_-}{s}$, where the endplate separation s was 2 cm for the preliminary measurements reported in this thesis.

The resistances $R_f = 10$ M Ω and capacitances $C_f \sim 20$ pf shown in Figure 6.2 provided low-pass filtering of each power supply output, with an approximate

³CE1001 30 kV supplies, available from K and M Electronics, 11 Interstate Drive, West Springfield, MA 01089.

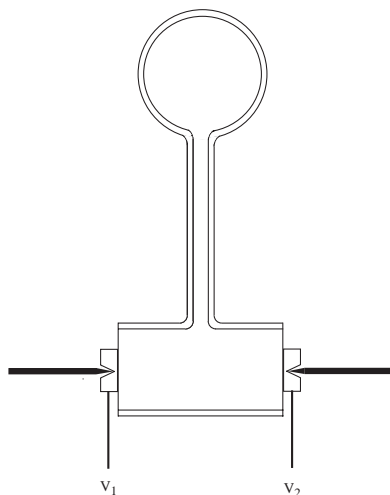


Figure 6.3: Electrical connection from the high voltage to the cell was achieved by pressing polished brass tabs against the molybdenum cell endplates using 4-40 nylon screws. See Section 3.1 for a description of surface preparation of the electrodes.

breakpoint at 5 kHz. As will be described in Section 6.3, increasing the value of C_f by a factor 10^5 should provide immediate, large improvements in the EDM measurement resolution of the DNGM.⁴ The polarity and output levels of both high voltage supplies were controlled by a dedicated computer located in the DNGM laboratory. Note that in the EDM experiments reported in [15, 20, 36], precision electrometers capable of sensing currents at the level of ~ 1 pA were part of the high voltage systems. Although our co-magnetometer measurements in Section 3.6 indicate that leakage currents will not play a role even in a sub- 1×10^{-28} e-c.m. ^{129}Xe EDM measurement, we plan on implementing real-time leakage current monitoring instrumentation in the near future.

⁴ $1 - 10\mu\text{f}$ high voltage capacitors are commercially available for a cost of \sim \$200 each.

6.3 Preliminary Results

As described in Section 6.2, a ^{129}Xe EDM measurement consisted of looking for a frequency shift on the ^3He Zeeman frequency as the electric field across the DNGM cell was reversed from E to $-E$.⁵ With no electric field applied across the cell, the DNGM ^3He maser Allan deviation over time intervals $\tau \sim 5$ ks was typically 200 nHz. Making two consecutive such measurements while reversing the applied electric field ± 5 kV/cm would yield a one-standard-deviation sensitivity to a ^{129}Xe EDM of $\sim 14 \times 10^{27}$ e-c.m. per field reversal. If 15 field reversals were performed per day of running, the single-day EDM resolution of the DNGM would be given approximately by 3.6×10^{27} e-cm. In 300 days of running, the DNGM could place a limit of $\sim 2.0 \times 10^{28}$ e-c.m. on the value of a ^{129}Xe EDM. As described in Section 6.1, a result of this sensitivity could provide meaningful information on proposed sources of T -violation in various extensions of the standard model.

To date, operation of the high voltage power supplies at electric fields ≥ 2 kV/cm in the maser bulb has degraded the DNGM frequency stability (i.e., Allan deviation) by as much as a factor of 5 – 10. This degradation is caused by two different effects. One is a steady bleed-through of RF noise from the power supply electronics. The magnitude of this noise source appears to be proportional to the voltage applied to the high voltage electrodes. Addition of large filtering capacitors to the supply electronics should abate this noise source considerably. The second source of noise occurs only for cell electric fields higher than ~ 2.2 kV/cm. These noise events are discrete in nature and probably arise from arcing from the high voltage electrodes

⁵A alternating dwell pattern $+E, -E, +E, -E, \dots$ provides the most efficient duty cycle for an EDM measurement. For our preliminary measurements, we restricted our dwell patterns to be strictly alternating. Most EDM measurements [15], however, are performed with some dwell patterns incorporating zero electric field in order to search for a variety of possible systematic effects associated with high voltage polarity switching, imperfect field reversal, effects which might scale as E^2 , etc. See [15, 36] for a thorough discussion.

to the resonant pickup coil. They result in bursts of RF voltage which perturb the maser and can also overload the pre-amplifier. In addition, the rate and intensity of these discrete noise events increase rapidly for cell electric fields beyond 2.2 kV/cm. Although the origin of these noise bursts is not understood precisely, better surface preparation, a larger separation between the electrodes and the pickup coil, and the addition of a dielectric medium around the electrodes should abate the noise bursts substantially.

With this still non-optimized system, we have taken approximately 25 days of preliminary EDM data over the last several months, with the primary goals of debugging the high voltage control software and also of testing our data analysis routines. We now briefly describe how our preliminary ^{129}Xe EDM data were analyzed. Note that our methods are similar to those laid out in [15].

The phase and amplitude of both maser signals were recorded at four-second intervals by the lock-in amplifiers (Section 3.7) and downloaded for analysis once every 24 hours. We performed initial reduction of the ^3He phase trace for each EDM run by fitting to the minimal fit model

$$\phi_{He}(t) = \phi_0 + 2\pi\nu_o t, \tag{6.4}$$

where the coefficients ϕ_0 and ν_o accounted for absolute phase and frequency offsets between the ^3He maser and the ultra-stable reference oscillator (Section 2.5). The reduced χ^2 statistic for this fit model was determined, and then additional terms corresponding to quadratic and maser amplitude-correlated phase drift (see Section 2.6) were incorporated into the model if they significantly improved the reduced χ^2 [86]. The ^3He phase residuals from the least-squares regression were then analyzed for a ^{129}Xe EDM signature.

With the ^{129}Xe maser phase-locked and the ^3He maser free-running, a ^{129}Xe EDM signature would consist of a signed frequency shift linear in the value of the applied electric field (Equation 6.3). Each one-day run consisted of dwells during which the electric field across the cell had constant (signed) values E_i separated by dead-times T_o during which the field was reversed by linearly ramping the power supply voltages from V to $-V$. Typical field reversal dead times were ~ 700 seconds, and typical dwell times were ~ 5000 seconds.⁶ A single day run thus contained approximately 16 evenly spaced measurements of the free-running ^3He frequency. Additional diagnostic signals were also recorded during data taking. In addition to monitoring the voltages V_1 and V_2 of the EDM cell electrodes, we monitored the temperatures of the pump bulb, maser bulb, and external resonator; the relative value of the Rb magnetization in the pump bulb (Section 3.4.2); the broadband power emitted by the optical-pumping laser-diode array; and the ambient room temperature.

Let $\{\nu_i\}$ represent the sequence of N minimum-variance estimates of the ^3He maser frequency (see Equation 2.39) corresponding to the electric field dwell pattern $\{E_i\}$. We can then form $\{d_i\}$, the sequence of $(N - 1)$ measurements of the ^{129}Xe EDM:

$$d_i = \frac{h}{2\gamma} \left(\frac{\nu_i - \nu_{i+1}}{E_i - E_{i+1}} \right), \quad (6.5)$$

where h is Planck's constant and $\gamma \approx 2.75408$ is the ratio of the ^3He and ^{129}Xe magnetic moments. The estimated mean for a one-day measurement of the ^{129}Xe EDM is given by the mean of the set $\{d_i\}$, and the estimated error is equal to the standard deviation of the set $\{d_i\}$ divided by $\sqrt{N - 1}$, and then multiplied by $\sqrt{2}$ to correct for cross-correlations between adjacent d_i .

⁶As stated earlier, all preliminary runs had strictly alternating electric field dwell patterns.

Usable data for this experiment were acquired for 25 days with two different maser cells over the period September, 1999 to April, 2000. Although no systematic checks were carried out for the preliminary data runs,⁷ we remark here that an electric-field correlated frequency shift could arise from a magnetic field produced by the flow of leakage currents along the surface of the EDM cell [15,20]. Such shifts could give false positive or false negative EDM results, and are thus of particular concern. We showed in Section 3.6, however, that the ^{129}Xe co-magnetometer should limit the size of such a shift to $\leq .02$ nHz/(kV/cm), well below even the most optimistic estimate for ^{129}Xe EDM sensitivity of the DNGM, even in several years of running.

Weighted averaging of the the estimated means and errors of all single-day EDM runs were used to extract a value for the ^{129}Xe EDM [86] from our preliminary data. Our null result of $d_{xe} = (.84 \pm 1.1) \times 10^{-26}$ e-c.m. ($1\text{-}\sigma$ level) indicates no evidence of T -symmetry violation in the ^{129}Xe atom at the present level of statistical sensitivity. The last two columns of Table 6.2 enumerate the single-day EDM results, with estimated errors. These data are plotted in Figure 6.4.

The excellent frequency resolution (in the absence of electric fields) of the DNGM has enabled us to establish the most stringent limit to date on Lorentz and CPT violation involving the neutron, as described in Chapter 5. Attainment of comparable resolution in the presence of electric fields of ~ 5 kV/cm would permit a ^{129}Xe EDM search with a sensitivity of $1 - 2 \times 10^{-28}$ e-c.m. in ≈ 300 days of running. Such a limit would constrain T -symmetry violating mechanisms (Section 6.1) at a level comparable to the the best present experimental limits (see Table 6.1), but with the important advantage of a co-magnetometer. We believe that straightforward im-

⁷It was clear that the noise from the high voltage supplies would need to be overcome before meaningful EDM work could continue.

cell	dwel time (s)	dead time (s)	d_{xe} (10^{-26} e-c.m.)	σ_d (10^{-26} e-c.m.)
E9 West	5000	232	2.69	10.2
E9 West	5000	232	8.5	10.6
E9 West	5000	232	6.5	7.2
E9 West	5000	170	-3.11	3.54
E9 West	5000	170	10.1	5.3
E9 West	5000	170	5.21	4.48
E9 West	5000	170	-3.1	4.9
SE3 West	7000	2960	2.98	4.69
SE3 West	7000	833	-4.7	10
SE3 West	7000	833	2.12	1.6
SE3 West	5000	700	3.64	8.68
SE3 West	5000	700	2.92	8.18
SE3 East	5040	700	-12.8	7.96
SE3 East	5040	700	-12.98	10.4
SE3 East	5040	700	-0.1037	5.72
SE3 East	5040	700	-8.44	11.6
SE3 East	5040	700	-14.66	8.8
SE3 East	5040	700	10	9.5
SE3 West	5040	700	-8.41	9.65
SE3 West	5040	700	-17.1	9.58
SE3 West	5040	700	2.62	5.53
SE3 West	5040	200	-45.1	20.4
SE3 West	5040	700	-10.8	10.7
SE3 West	7000	700	-3.9	9.4
SE3 West	5040	700	6.95	7.62
SE3 West	5040	700	8.358	11

Table 6.2: Table enumerating the 25 usable single-day EDM results (d_{xe}), with estimated errors (σ_d). Also indicated are the cell used, the direction of the solenoid magnetic field (East or West), the duration of each high voltage dwell, and the field-reversal dead time for each single-day measurement.

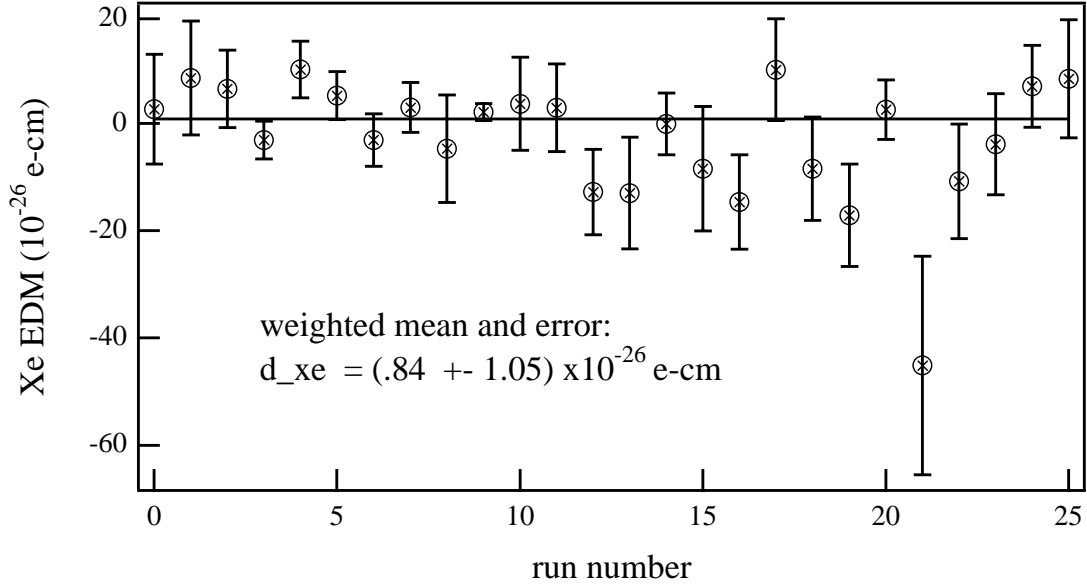


Figure 6.4: Estimated mean values and standard errors of the 25 usable single-day EDM runs. The weighted mean and error provide a null-result of $d_{xe} = (.84 \pm 1.1) \times 10^{-26}$ e-c.m. ($1\text{-}\sigma$ level) for the value of a ^{129}Xe EDM.

provements to the high voltage power supplies⁸ should enable such a measurement to be performed within the next 1 – 2 years.

⁸Immediate plans include improving the RC filter shown in Figure 6.2 by incorporating very large ($\sim 1\mu\text{f}$) high voltage capacitors into the circuit, thereby reducing the low-pass breakpoint to $1/RC \sim 100$ Hz. We also plan to assess the effects of adding a dielectric medium around the cell electrodes. Preliminary studies involving sulfur-hexafluoride (SF_6) have shown great promise.

Bibliography

- [1] T. Chupp, R. Hoare, R. Walsworth, and B. Wu, Phys. Rev. Lett. **72**, 15 (1994).
- [2] R. Stoner, M. Rosenberry, J. Wright, T. Chupp, E. Oteiza, and R. Walsworth, Phys. Rev. Lett. **77**, 3971 (1996).
- [3] D. Bear, T. Chupp, K. Cooper, S. DeDeo, M. Rosenberry, R. Stoner, and R. Walsworth, Phys. Rev. A **57**, 6 (1998).
- [4] A. Abragham, *Principles of Magnetic Resonance* (Oxford University Press, Oxford, 1961).
- [5] W. Farr and E. Otten, Appl. Phys. **3**, 367 (1974).
- [6] V.A. Kostelecký and C.D. Lane, Phys. Rev. D **60**, 116010 (1999); J. Math. Phys. **40**, 6425 (1999).
- [7] J. Prestage, Phys. Rev. Lett. **54**, 2387 (1985).
- [8] C. Berglund, L. Hunter, D. K. Jr., E. Prigge, M. Ronfeldt, and S. Lamoreaux, Phys. Rev. Lett. **75**, 10 (1995).
- [9] L. Hunter, C. Berglund, M. Ronfeldt, E. Prigge, D. Krause, and S. Lamoreaux, in *CPT and Lorentz Symmetry*, edited by V. Kostelecky (World Scientific, Singapore, 1999).

- [10] T. Chupp, Phys. Rev. Lett. **63**, 1541 (1989).
- [11] K. Smith, Phys. Lett. B **234**, 191 (1990).
- [12] S. Murthy, D. Krause, Z. Li, and L. Hunter, Phys. Rev. Lett. **63**, 965 (1989).
- [13] D. Cho, K. Sangster, and E. Hinds, Phys. Rev. Lett. **63**, 2559 (1989).
- [14] J. Jacobs, W. Klipstein, S. Lamoureaux, B. Heckel, and E. Fortson, Phys. Rev. Lett. **71**, 3782 (1993).
- [15] J. Jacobs, W. Klipstein, S. Lamoureaux, B. Heckel, and E. Fortson, Phys. Rev. A **52**, 3521 (1995).
- [16] E. Commins, S. Ross, D. DeMille, and B. Regan, Phys. Rev. A **50**, 2960 (1994).
- [17] S. Barr, Int. J. Mod. Phys. A **8**, 209 (1993).
- [18] T. Chupp, E. Oteiza, J. Richardson, and T. White, Phys. Rev. A **38**, 3998 (1988).
- [19] G. Cates, R. Fitzgerald, A. Barton, P. Bogorad, M. Gatzke, N. Newbury, and B. Saam, Phys. Rev. A **49**, 4631 (1992).
- [20] E. R. Oteiza, Ph.D. thesis, Harvard University, 1992.
- [21] T. G. Walker and W. Happer, Reviews of Modern Physics **69**, 2 (1997).
- [22] J. Vanier and C. Audoin, *The Quantum Physics of Atomic Frequency Standards* (IOP Publishing, Ltd., Bristol, 1989).
- [23] V. Kostelecky and R. Potting, in *Gamma Ray-Neutrino Cosmology and Planck Scale Physics*, edited by D. Cline (World Scientific, Singapore, 1993).

- [24] D. Colladay and V.A. Kostelecký, Phys. Lett. B **344**, 259 (1995); Phys. Rev. D **52**, 6224 (1995); V.A. Kostelecký and R. Van Kooten, Phys. Rev. D **54** 5585 (1996); V.A. Kostelecký, Phys. Rev. Lett. **80** 1818 (1998); Phys. Rev. D **61**, 16002 (2000).
- [25] V. Kostelecky, Phys. Rev. Lett. **80**, 259 (1998).
- [26] R. Bluhm, V. Kostelecky, and N. Russell, Phys. Rev. Lett. **79**, 1432 (1997).
- [27] S. Carroll, G.B.Field, and R. Jackiw, Phys. Rev. D **41**, 1231 (1990).
- [28] R. Jackiw and V. Kostelecky, Phys. Rev. Lett. **82**, 3572 (1999).
- [29] O. Bertolami, D. Colladay, V. Kostelecky, and R. Potting, Phys. Rev. B **395**, 178 (1997).
- [30] R. Bluhm, V. Kostelecký, and N. Russell, Phys. Rev. Lett. **82**, 2254 (1999).
- [31] J. Christenson, J. Cronin, V. Fitch, and R. Turlay, Phys. Rev. Lett. **13**, 138 (1964).
- [32] A. Sakharov, JETP Lett. **44**, 460 (1967).
- [33] L. Hunter, Science **252**, 73 (1991).
- [34] J. Sakurai, *Modern Quantum Mechanics* (Addison Wesley, New York, 1985).
- [35] A. Martenson-Pendrill, in *Methods in Computational Chemistry, Volume 5: Atomic and Molecular Properties*, edited by S. Wilson (Plenum Press, New York, 1992).
- [36] M. A. Rosenberry, Ph.D. thesis, University of Michigan, 1999.

- [37] H. Haken and H. Wolf, *The Physics of Atoms and Quanta* (Springer-Verlag, New York, 1993).
- [38] W. Happer and W. Wijngaarden, *Hyperfine Interactions* **38**, 435 (1987).
- [39] A. Baranga, S. Appelt, M. Romalis, C. Erickson, A. Young, G. Cates, and W. Happer, *Phys. Rev. Lett.* **80**, 13 (1998).
- [40] M. V. Romalis, Ph.D. thesis, Princeton University, 1997.
- [41] E. Condon, *Physical Review* **43**, 648 (1933).
- [42] T. Stein, J. Carrico, E. Lipworth, and M. Weisskopf, *Physical Review* **2**, 1093 (1970).
- [43] C. Cohen-Tannoudji, B. Diu, and F. Laloe, *Quantum Mechanics* (John Wiley and Sons, New York, 1977).
- [44] D. McGregor, *Phys. Rev. A* **41**, 2631 (1990).
- [45] D. Howe, D. Allan, and J. Barnes, *Proceedings of the 35th Annual Symposium on Frequency Control* (1981).
- [46] S. R. Stein, *Proceedings of the 35th Annual Symposium on Frequency Control* (1981).
- [47] Y. Chibane, S. Lamoreaux, J. Pendlebury, and K. Smith, *Meas. Sc. Technol.* **6**, 1671 (1995).
- [48] S. Schaefer, G. Cates, and W. Happer, *Phys. Rev. A* **39**, 5613 (1989).
- [49] N. Ramsey, *Physical Review* **100**, 1191 (1955).

- [50] G. Cates, D. White, T. Chien, S. Schaefer, and W. Happer, *Phys. Rev. A* **38**, 5092 (1988).
- [51] D. Sindord and G. Maciel, *Journal of the American Chemical Society* **105**, 3767 (1983).
- [52] X. Zeng, E. Miron, W. V. Winjngaarden, D. Schreiber, and W. Happer, *Physics Letters* **96A**, 191 (1983).
- [53] R. Maoz and J. Sagiv, *Journal of Colloid and Interference Science* **100**, 465 (1984).
- [54] T. Giorgi, B. Ferrario, and B. Storey, *Journal of Vacuum Science Technology* **3**, 2 (1985).
- [55] M. S. Rosen, Ph.D. thesis, University of Michigan, 2000.
- [56] J. Moore, C. Davis, and M. Coplan, *Building Scientific Apparatus* (Addison-Wesley, New York, 1989).
- [57] D. Phillips, G. Wong, D. Bear, R. Stoner, and R. Walsworth, *Rev. Sci. Inst.* **70**, 2905 (1999).
- [58] C. Alcock, V. Itkin, and M. Horrigan, *Canadian Metallurgical Quarterly* **23**, 309 (1984).
- [59] R. Hanson and F. Pipkin, *Rev. Sci. Inst.* **36**, 179 (1965).
- [60] H. Ott, *Noise Reduction Techniques in Electronic Systems* (John Wiley and Sons, New York, 1988).
- [61] R. Noble, *Electronics World and Wireless World* **Sept**, 726 (1991).

- [62] C. Will, *Theory and Experiment in Gravitational Physics* (Cambridge University Press, New York, 1981).
- [63] V.A. Kostelecký and R. Potting, Phys. Rev. D **51**, 3923 (1995).
- [64] R. Bluhm, V.A. Kostelecký and N. Russell, Phys. Rev. Lett. **79**, 1432 (1997); Phys. Rev. D **57**, 3932 (1998).
- [65] D. Colladay and V. Kostelecky, Phys. Rev. D **55**, 6760 (1997).
- [66] D. Colladay and V.A. Kostelecký, Phys. Rev. D **55**, 6760 (1997); Phys. Rev. D **58**, 116002 (1998).
- [67] V.A. Kostelecký and S. Samuel, Phys. Rev. Lett. **63**, 224 (1989); Phys. Rev. D **40**, 1886 (1989); Phys. Rev. Lett. **66**, 1811 (1991).
- [68] V. Hughes, H. Robinson, and V. Beltran-Lopez, Phys. Rev. Lett. **4**, 342 (1960).
- [69] R. Drever, Philos. Mag. **6**, 683 (1961).
- [70] S. Lamoreaux, Phys. Rev. **39**, 1082 (1989).
- [71] V.A. Kostelecký and S. Samuel, Phys. Rev. D **39**, 683 (1989); V.A. Kostelecký and R. Potting, Nucl. Phys. **B359**, 545 (1991); Phys. Lett. B **381**, 89 (1996); V.A. Kostelecký, R. Potting, and M. Perry, Phys. Rev. Lett. **84**, 4541 (2000).
- [72] R. Bluhm and V.A. Kostelecký, Phys. Rev. Lett. **84**, 1381 (2000).
- [73] R. Jackiw and V.A. Kostelecký, Phys. Rev. Lett. **82**, 3572 (1999). See also M. Pérez-Victoria, Phys. Rev. Lett. **83**, 2518 (1999); J.M. Chung, Phys. Lett. B **461**, 138 (1999).
- [74] R. Bluhm, V. Kostelecky, and C. Lane, Phys. Rev. Lett. **84**, 1098 (2000).

- [75] S. Coleman and S. Glashow, *Phys. Rev. D* **56**, 116008 (1999).
- [76] G. Gabrielse, A. Khabbaz, D. Hall, C. Heimenn, H. Kalinowski, and W. Jhe, *Phys. Rev. Lett.* **82**, 3198 (1999).
- [77] R. Mittleman, I. Ioannou, H. Dehmelt, and N. Russell, *Phys. Rev. Lett.* **83**, 2116 (1999).
- [78] H. Dehmelt, R. Mittleman, J. R.S. Van Dyck, , and P. Schwinberg, *Phys. Rev. Lett.* **83**, 4694 (1999).
- [79] E. Adelberger, in *Physics Beyond the Standard Model*, edited by P. Herczeg (World Scientific, Singapore, 1999).
- [80] M. Harris, Ph.D. thesis, University of Washington, 1998.
- [81] B. Heckel, in *Quantum Gravity, Generalized Theory of Gravitation and Superstring Theory Based Unification* (International Conference on Orbis Scientiae, Fort Lauderdale, 1999).
- [82] D.F. Phillips *et al.*, submitted for publication, preprint physics/0008230.
- [83] KTeV Collaboration, presented by Y.B. Hsiung at the KAON 99 conference, Chicago, June 1999.
- [84] OPAL Collaboration, R. Ackerstaff *et al.*, *Z. Phys. C* **76**, 401 (1997); DELPHI Collaboration, M. Feindt *et al.*, preprint DELPHI 97-98 CONF 80 (July 1997).
- [85] One sidereal day is approximately one solar day scaled by $(1 - 1/364.24)$, or about 23.93 hours.
- [86] P. R. Bevington, *Data Reduction and Error Analysis for the Physical Sciences* (McGraw-Hill, Boston, 1992).

- [87] The probability distribution for R is formed by multiplying the distributions for $\delta\nu_X$ and $\delta\nu_Y$, converting to polar coordinates, and integrating over the polar angle. In the case where $\delta\nu_X$ and $\delta\nu_Y$ have zero mean value and the same variance σ , the probability distribution takes the form $P(R) = \sigma^{-2}R \exp(-r^2/2\sigma^2)$, with the most probable value of R occurring at $R = \sigma$.
- [88] R. Stoner, in *CPT and Lorentz Symmetry*, edited by V. Kostelecky (World Scientific, Singapore, 1999).
- [89] I. Altarev, JETP Letters **44**, 460 (1986).
- [90] S. Weinberg, Phys. Rev. D **42**, 860 (1990).
- [91] T. Vold, Phys. Rev. Lett. **52**, 2229 (1984).
- [92] S. Lamoreaux, J. Jacobs, , B. Heckel, F. Raab, and N. Fortson, Phys. Rev. Lett. **59**, 2275 (1987).
- [93] K. Abdullah, C. Carlberg, E. Commins, H. Gould, and S. Ross, Phys. Rev. Lett. **65**, 2347 (1990).
- [94] S. Barr and G. Segre, Phys. Rev. D **48**, 302 (1993).
- [95] I. Khriplovich, in *Atomic Physics*, edited by S. Harouche (World Scientific, Teaneck, NJ, 1989).
- [96] I. Khriplovich, *Parity Nonconservation in Atomic Phenomena* (Gordon and Breach Science Publishers, Philadelphia, 1991).
- [97] A. Martensson-Pendril, Phys. Rev. Lett. **54**, 1153 (1985).
- [98] V. Flambaum, I. Khriplovich, and O. Sushkov, Phys. Lett. B **162**, 213 (1985).

Appendix A

Extended Bloch Theory of the Dual Zeeman Maser

An extended Bloch theory of the dual noble gas maser was developed by Dr. Richard Stoner, a research scientist in our laboratory at the Harvard-Smithsonian Center for Astrophysics. We present in this appendix, at his request and with his permission, Dr. Stoner's (as yet) unpublished manuscript on this extended Bloch theory.

Extended Bloch theory of the dual Zeeman maser

Richard E. Stoner

Harvard-Smithsonian Center for Astrophysics, Cambridge, MA 02138

(July 16, 2000)

A dual Zeeman maser is a device in which ensembles of two different spin-polarized gases are co-located in the same glass cell and perform continuous and simultaneous maser oscillations on their respective Zeeman transitions. Being at present the only two-species maser technology, it is a unique tool for differential magnetometry. Recent experiments have demonstrated phenomena in Zeeman masers that cannot be described by existing theory. Accordingly, an extended Bloch theory of the Zeeman maser is presented in this paper. This paper first provides a brief review of the development of Zeeman masers. A description of the diffusive transport of polarization between separated pumping and interaction regions is then presented. The equations of motion are solved exactly via Laplace transforms. This model accounts for wall loss effects and finite transport times, and is of general applicability, including polarized gas targets for nuclear and particle physics studies. A Bloch model of the Zeeman maser incorporating the new polarization transport results is presented. Solutions for the equations of motion are presented for steady state and threshold conditions as well as near-steady-state polarization and frequency oscillations. Fundamental limitations of the Bloch theory description of Zeeman masers are discussed.

84.40.Ik, 32.80.Bx, 32.60.+i, 67.65.+z

I. INTRODUCTION

The dual Zeeman maser is a new device of considerable usefulness for precision measurement and fundamental symmetry tests [1–3]. Two noble gas ensembles simultaneously and continuously oscillate while occupying the same volume; thus, one of the masers can be used to stabilize the magnetic field to high precision, leaving the other maser free to respond to subtle physical effects. The demonstration of a dual noble gas Zeeman maser has been recently reported [4,5]. Single-species Zeeman masers were first operated by Myint and Robinson [6], and subsequently by Richards *et. al.* [7]. Both these experiments employed ^3He as the maser gain medium, spin polarized via metastable-state optical pumping. In contrast, Chupp *et. al.* showed that spin exchange with optically-pumped Rb could serve as a means of polarizing noble gas ensembles sufficiently to support a Zeeman maser, and operated single-species Zeeman masers employing ^3He and ^{129}Xe [8]. The employment of spin exchange with optically-pumped Rb makes possible the simultaneous polarization of multiple species; this fact has been exploited in several fundamental symmetry tests using freely-precessing polarized ensembles, including a study of local Lorentz invariance (LLI) [9], the linearity of quantum mechanics [10], and a search for a permanent electric dipole moment (EDM) in ^{129}Xe [11]. A spin-exchange-pumped ^3He maser was recently operated by Romalis and Happer [12] in the so-called inhomogeneous broadening regime, characterized by large magnetic field gradients and slow diffusion. If we define the maser Larmor frequency by ω_L and its gradient (due to magnetic field variation) as $\nabla\omega_L$, and the characteristic diffusion constant and cell dimension by D and R , respectively, the inhomogeneous broadening regime is characterized by $D/R^2 \ll R\nabla\omega_L$ [12]. This condition can be interpreted as a situation in which the diffusion rate across the cell is much less than the spread in Larmor frequency across the cell due to field gradients. In this case, diffusion is not rapid enough to suppress the broadening effect of field gradients. The dual Zeeman maser described here (and all Zeeman maser systems reported to date, excepting [12]) operates in the regime of fast diffusion and small field gradients, wherein diffusion is rapid enough to average out the effects of field gradients: i.e., $D/R^2 \gg R\nabla\omega_L$ (motional narrowing [12]). Operating in the motional narrowing regime is crucial for precision comagnetometry in the dual Zeeman maser; in order that the two species sense the same average magnetic field in a given volume, the spatial distribution of the masing ensembles should be identical in shape [24,26]. This ideal is most closely attained in the regime of rapid diffusion, where the masing ensembles are nearly uniform.

The dual noble gas Zeeman maser was first proposed by Walsworth [13]. He observed that a device capable of continuous oscillation would have significant advantages over the use of freely precessing ensembles, including the maintainance of stable polarizations and the reduction of required measurement duration permitted by coherent frequency averaging.

A qualitative discussion of the physics of the Zeeman maser is presented in this Section, along with a brief description of an existing experimental apparatus. As of this writing, noble gas Zeeman masers have been implemented using ^3He (nuclear spin 1/2), ^{129}Xe (nuclear spin 1/2), and ^{21}Ne (nuclear spin 3/2) [3–5,24]. This paper will focus on describing

a dual Zeeman maser system using ^3He and ^{129}Xe , as implemented in our laboratory and the laboratory of Chupp and co-workers [4,5]. This is an interesting case study because the interactions of these noble gases with alkali atoms and with their glass cell enclosure are very different, leading to significant differences in the dynamics of the ^3He and ^{129}Xe masers. These differences affect how well the two masers function as co-magnetometers, as will be discussed in Section IV below.

Section II presents new equations of motion of diffusive transport of polarization, in a system where atoms are polarized in a "pump" region and are transported by diffusion to an interaction region. In previous work, a simple linear gradient model was used to describe ^3He diffusion in noble gas masers [7,8] as well as in polarized ^3He targets for nuclear physics research [14]. The new model incorporates a 1-d diffusion field to describe the transport region, and incorporates polarization destruction effects in the pump, interaction, and transfer regions via phenomenological polarization lifetimes T_1 . This model has applicability to polarized ^3He targets used in nuclear physics applications [14], as well as to the dual Zeeman maser. These equations of motion are solved exactly by use of Laplace transforms. It will be seen that polarization losses in the transfer region are not important to Zeeman maser operation in the diffusive transport of ^3He , but will be shown to be important in transport of ^{129}Xe . This distinction arises because diffusion of ^{129}Xe is much slower than that of ^3He , and the polarization wall loss rate of ^{129}Xe is much greater than that of ^3He . The time-dependent solutions will be useful in extracting polarization lifetimes from experimental data. The solutions to the equations of motion in steady state will serve as a tool in the design of polarization systems.

Section III presents a Bloch model of the Zeeman maser that incorporates the diffusive transport formalism of Section II. This extended Bloch model also explicitly presents the maser oscillation frequency as a dynamical variable, which permits detailed theoretical description of frequency phenomena that were not experimentally resolvable prior to the advent of the dual Zeeman maser. These extended Bloch equations are solved in the steady state to derive startup conditions, an energy balance condition, and the cavity-pulling relation. The Bloch equations of motion are then linearized about the steady state, and the linearized equations are solved exactly using Laplace transforms. These solutions permit measurements of near-equilibrium behavior to be used to determine the values of maser operating parameters.

Having worked out the near-equilibrium dynamics of the Zeeman maser polarizations, we will then investigate the effects of these variations on the maser frequency in Section IV. In addition, we will describe the frequency dynamics of the two-species Zeeman maser. One species is phase locked to an external reference clock by feedback to the main magnetic field B_o . It will be shown that effects which would, in the absence of the phase lock loop, tend to shift the phaselocked maser, will produce frequency shifts on the other [free-running] maser. The demonstration of the dual Zeeman maser included effects wherein it was obvious that the polarizations (and associated magnetizations) of the noble gases were strongly coupled to the frequency of oscillation [4], and were a significant cause of frequency instability for measurement intervals longer than 500 sec. The fundamental reason for this coupling is that unlike other maser technologies, the Zeeman maser's frequency of oscillation is first-order in the longitudinal magnetic field. The magnetization of the polarized gases contribute to this field to induce polarization-proportional frequency shifts. These shifts must be understood in order to specify the requirements for polarization stability needed to attain a given frequency stability. Section IV presents a description of these effects.

We will then present a scheme for minimizing the variation of the oscillation frequency with longitudinal polarization. It will be shown that operating the maser at a selected detuning from the peak of the resonator response will result in a cavity-pulling shift that is equal in magnitude and opposite in sign of the frequency shift due to other frequency shifts proportional to the longitudinal polarization P_z . The result is that maser frequency oscillations resulting from near-equilibrium oscillations of the maser polarization components are greatly reduced. This detuning scheme might be useful in applications like an atomic gyroscope, wherein the maser system might be subjected to perturbations; however, it has not yet proven to be beneficial in precision measurement applications. The detuning scheme is analogous in concept to that of Crampton for the hydrogen maser [15], in which operation of the maser at a selected detuning results in a cavity-pulling shift that cancels the spin-exchange shift, leaving the maser frequency independent of the flux of polarized H atoms into the maser bulb. Finally, in Section IV we will cite some limitations of the extended Bloch theory in describing dual Zeeman masers. Since the Bloch theory deals in volume-averaged dynamical variables, it cannot account for effects due to changes in the shape of the distributions over which the averaging is done. Recent measurements in our laboratory suggest that such effects are important [5].

We now present a brief qualitative discussion of Zeeman maser operation, which should aid in the understanding of the formal mathematical discussions to follow. Certain processes must be present for any oscillator to operate: a population inversion; an energy source to sustain that inversion; feedback; and energy dissipation. Population inversion in a Zeeman maser is attained when the atoms have a net spin polarization, such that their Zeeman energy in the axial magnetic field is positive. The inversion condition is sustained by providing a continuous source of polarized atoms. As earlier mentioned, this has been achieved experimentally via optical pumping of metastable noble gas atoms, or via spin exchange of noble gas atoms with optically pumped alkali atoms. Feedback in a Zeeman maser is provided by placing the polarized sample of noble gas atoms in proximity with the inductor of a tuned

resonant circuit, called the pickup coil. Energy dissipation results from dephasing of the atoms' Larmor precession and from ohmic energy losses in the pickup coil.

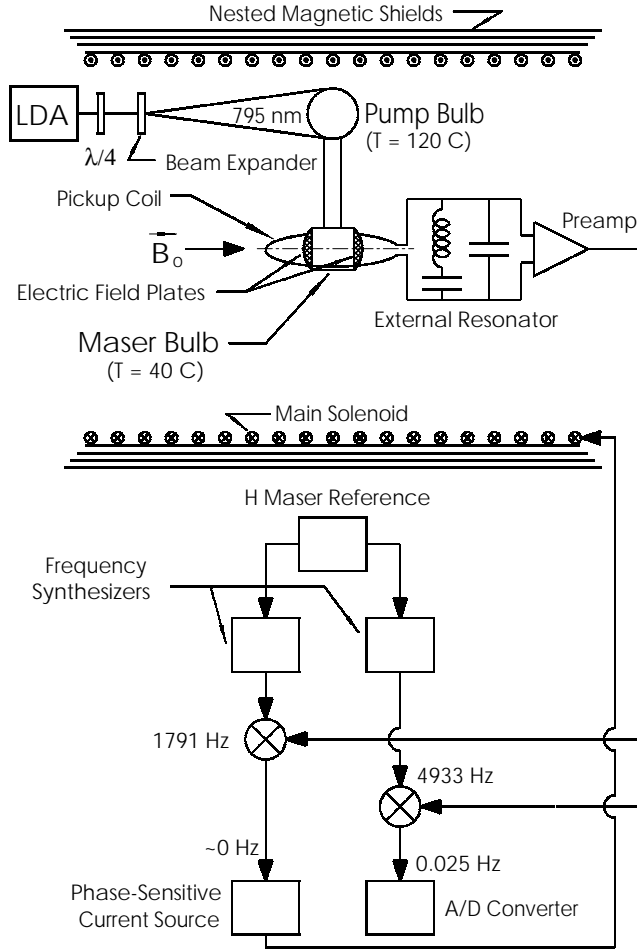


FIG. 1. The $^{129}\text{Xe}/^3\text{He}$ dual Zeeman maser. Co-located ensembles of noble gas atoms are polarized by spin exchange collisions with optically pumped Rb atoms. A laser diode array is used to provide resonant light for optical pumping. The static magnetic field of 1.5 G is produced by a solenoid residing inside nested layers of μ -metal shielding. Polarized noble gas atoms diffuse down the transfer tube to the maser bulb, where the noble gas atoms' nuclear spins precess in the static field. The precession excites current in nearby inductive pickup coils, which are part of a circuit tuned with resonances near the Larmor precession frequencies of the two noble gas species (see Appendix E). The current induces resonant alternating magnetic fields which act back on the precessing atoms, providing feedback for maser oscillation. (The cell shown has electric field plates; all-glass cells have also been used.) The signals from the resonant circuit are presented to a low-noise preamp; the amplified signals are analyzed and digitally sampled using lockin amplifiers. The lockin amplifiers' reference signals, and the A/D conversion trigger signal, are all synchronized to one 5 MHz reference signal derived from an H maser.

Figure 1 is a schematic diagram of a Zeeman maser operated in our laboratory [4,5]. Atoms are polarized in the "pump bulb" and diffuse to the "maser bulb", which is placed near the pickup coil. As the polarized atoms precess in the static magnetic field, they produce in their vicinity an oscillating magnetic field, which is the field induced by the atoms' component of magnetization normal to the static magnetic field. The oscillating flux through the pickup coil excites an oscillating current in the resonant circuit. The circuit's resonance is tuned to the nuclear spin Larmor frequency, so that the current is phased so as to create a field in the rotating frame that "tips" the atoms to the lower energy state. Figure 2 is an illustration of the maser polarization and magnetization vectors in the frame rotating with the precessing nuclear spins, along with the magnetic fields "seen" by the spins and the $\vec{M} \times \vec{B}$ torques induced by those magnetic fields. The polarization and magnetization vectors, as well as the static field vector, are

in the plane of the paper. The magnetization is shown as oppositely directed to the polarization: all noble gases used thus far in Zeeman masers have negative gyromagnetic ratios. The principal torque is that driving the Larmor precession, and is directed into the paper. The pickup coil magnetic field is static in the rotating frame. The pickup coil magnetic field is directed into the paper when the Larmor precession frequency is at the peak of the resonator response function, and can have a small component in the plane of the paper for detuned operation. The effect of this small component of the pickup coil field in the plane of the paper is described below. It is the component of the pickup coil field directed into the paper that "tips" the atoms, i.e. torques the polarization vector towards the lower energy state (the lower energy state is realized when a spin's polarization vector is antiparallel to the static field). The tipping process always transitions the spins to a state of lower energy, regardless of whether the atoms' longitudinal polarization is aligned to the upper or lower energy state. This is because the pickup coil is a passive device that cannot add energy to the polarized atoms. This tipping process is observed generally in nuclear magnetic resonance (NMR) and is termed radiation damping [16], because in many NMR experiments the atoms' polarization is due to a Boltzmann distribution in a magnetic field, so that the atoms are in the lower energy (i.e. non-inverted) state. The atoms' precession is then observed to be damped by the feedback effect. Radiation damping is the *primum mobile* of the Zeeman maser. It continuously converts longitudinal polarization into transverse polarization, thus allowing for attainment of a steady state transverse polarization, i.e. continuous Larmor precession. Figure 2 shows the balance of processes that must occur for steady state operation of a Zeeman maser: the longitudinal polarization must be replenished (by diffusion of polarized atoms) to compensate for losses due to radiation damping and cell wall collisions; and the transverse polarization is replenished (by radiation damping) to compensate for losses due to ensemble dephasing and spin depolarization. The oscillation threshold conditions derived below in Sec. III will quantitatively describe these balance conditions.

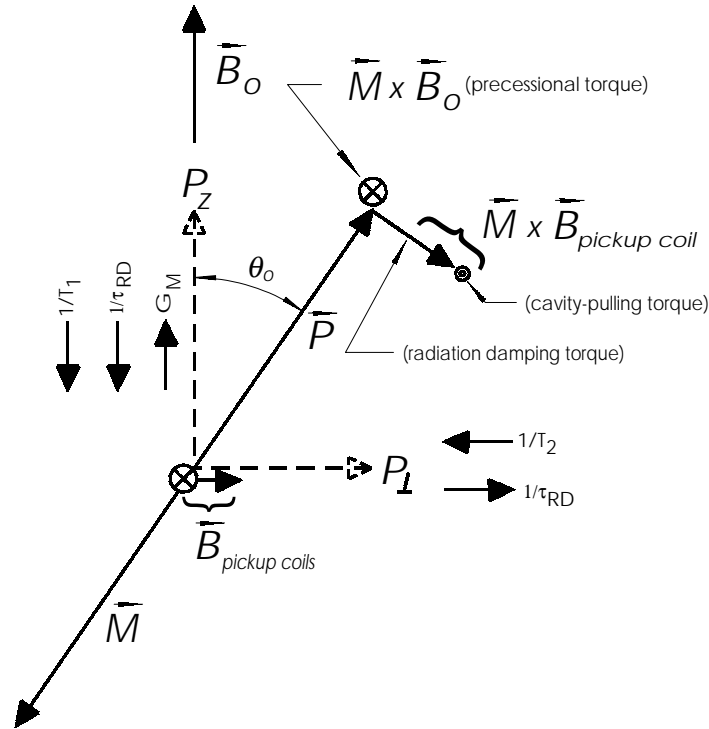


FIG. 2. The Zeeman maser polarization and magnetization vectors as seen in the frame rotating at the Larmor precession frequency. For the noble gas species described in this work, the magnetization is oppositely directed to the polarization. Static and AC magnetic fields are also shown, along with the resultant torque vectors. Under the correct conditions, both longitudinal and transverse components of polarization exist in steady state. Longitudinal polarization P_z is replenished by diffusive loading, and dissipated by wall loss and radiation damping. Transverse polarization is replenished by radiation damping, and destroyed by magnetic field gradient dephasing, wall loss, and escape from the interaction region.

We can also identify from Fig. 2 the physical mechanism by which cavity pulling, a general property of maser oscillators [17], manifests itself in the Zeeman maser. When the maser precession frequency differs from the resonant frequency of the resonator circuit, the radiation damping field (which co-rotates with the transverse polarization) created by the pickup coil is not precisely $\pi/2$ out of phase with the precessing polarization vector, so that there is a small component of the damping field that lies parallel to the transverse polarization. This damping field component then couples to the longitudinal polarization P_z to exert a torque which alters the precession frequency. Figure 2 shows the case where the maser frequency lies above the RLC resonance. The resultant torque, directed out of the paper, reduces the net precession frequency, consistent with the expected action of a cavity pulling mechanism. It will be shown in Sec. III that this mechanism is indeed cavity-pulling, and that the shift is proportional to the detuning of the maser frequency from the RLC resonance, and to the longitudinal polarization P_z . The shift can then take on either positive or negative sign, and thus could be combined with other P_z -proportional frequency shifts to reduce or eliminate the net dependence of the maser frequency on P_z .

II. DIFFUSIVE TRANSPORT OF POLARIZATION IN TWO-BULB CELLS

In this section we derive a system of equations relating the mean polarization in the pump and maser chambers to the polarization in a one-dimensional transfer tube connecting them (see Fig. 1). This analysis describes polarization along the field direction only (field is directed along z , see Fig. 2), and will be extended in Section III to include a [precessing] transverse polarization due to maser action. We will subsequently carry out an exact solution to these equations using parameter values derived from existing dual noble gas masers.

It is assumed that the magnetizations are nearly uniform in both the pump chamber and maser chamber. The mean polarization is related to mean magnetization (magnetic dipole moment per unit volume) via

$$M_P = -\frac{\hbar\gamma}{2} [ng] P_P; \quad M_z = -\frac{\hbar\gamma}{2} [ng] P_z \quad (1)$$

in the pump and maser chambers, respectively. γ is the gyromagnetic ratio, and $[ng]$ is the number of noble gas atoms per unit volume. The minus sign is to account for the fact that for all the polarized noble gas atoms to be considered in this paper, the magnetic moment is antiparallel to the particle spin; thus, $\gamma > 0$ describes the antialigned case. The polarization in the transfer tube (of length L), is modelled as a 1-d field in variables x and t , $0 \leq x \leq L$. This field is related to the volume-averaged pump and maser bulb polarizations (P_P and P_z , respectively) via

$$P_P(t) = \Pi(0, t); \quad P_z(t) = \Pi(L, t) \quad (2)$$

Polarization is exchanged between the transfer tube and the pump and maser bulbs via diffusion. Polarization flux from the pump and maser bulbs into the transfer tube is proportional to the gradient of the transfer tube polarization at the endpoints. The total dipole moment in, e.g., the pump chamber, is the average pump bulb magnetization M_P times the bulb volume V_P . The rate of change of *total* dipole moment due to diffusion into/out of the transfer tube is then

$$\frac{d}{dt} \{M_P V_P\} = A_{tt} \cdot D \cdot \frac{\partial}{\partial x} M_P \quad (3)$$

where A_{tt} is the cross-sectional area of the transfer tube (assumed uniform throughout the transfer tube) and V_P is the pump chamber volume. The rate of change of the polarizations due to diffusion to/from the transfer tube is now obtained by use of Equation (1):

$$\dot{P}_P \Big|_{diffusion} = \frac{A_{tt} \cdot D \cdot \frac{\partial}{\partial x} \Pi(x, t) \Big|_{x=0}}{V_P}; \quad \dot{P}_z \Big|_{diffusion} = \frac{-A_{tt} \cdot D \cdot \frac{\partial}{\partial x} \Pi(x, t) \Big|_{x=L}}{V_M} \quad (4)$$

The minus sign included in the maser chamber diffusion exchange rate accounts for the location of the maser chamber at $x = L$.

Parameter	Description	^{129}Xe	^3He
A_t	Transfer tube cross-sectional area	$\pi(0.232 \text{ cm})^2 = 0.170 \text{ cm}^2$	
L	Transfer tube length	4.14 cm	
V_M	Maser bulb volume	$\pi(0.629 \text{ cm})^2(2.06 \text{ cm}) = 2.55 \text{ cm}^3$	
V_P	Pump bulb volume	$\frac{4}{3}\pi(0.944 \text{ cm})^3 = 3.52 \text{ cm}^3$	
T_M	Maser bulb temperature	45° C	
T_P	Pump bulb temperature	120° C	
$[Rb]$	Pump bulb Rb density	$2.03 \times 10^{-13} \text{ cm}^{-3}$	
P_{Xe}	^{129}Xe fill pressure	114 torr	
P_{He}	^3He fill pressure	1100 torr	
P_{N_2}	N_2 fill pressure	78 torr	
P_{Rb}	Rb polarization (pump)	0.7	
η	Resonator fill factor	2.31×10^{-2}	
B_0	Static magnetic field	1.5 gauss	
D	Diffusion constant (maser bulb, transfer tube)	$1.65 \times 10^{-1} \frac{\text{cm}^2}{\text{sec}}$	$8.48 \times 10^{-1} \frac{\text{cm}^2}{\text{sec}}$
D	Diffusion constant (pump)	$2.42 \times 10^{-1} \frac{\text{cm}^2}{\text{sec}}$	$1.21 \frac{\text{cm}^2}{\text{sec}}$
G_M	Transfer rate (maser)	$2.65 \times 10^{-3} \text{ sec}^{-1}$	$1.36 \times 10^{-2} \text{ sec}^{-1}$
G_P	Transfer rate (pump)	$2.82 \times 10^{-3} \text{ sec}^{-1}$	$1.41 \times 10^{-2} \text{ sec}^{-1}$
γ_{SE}^{-1}	Spin exchange time (pump)	137 sec	$3.08 \times 10^5 \text{ sec}$
κ	Wall loss parameter (maser bulb, transfer tube)	$2.8 \times 10^{-4} \frac{\text{cm}}{\text{sec}}$	$1.6 \times 10^{-5} \frac{\text{cm}}{\text{sec}}$
κ	Wall loss parameter (pump bulb)	$1.40 \times 10^{-4} \frac{\text{cm}}{\text{sec}}$	$1.6 \times 10^{-5} \frac{\text{cm}}{\text{sec}}$
T_1	Polarization lifetime (maser)	860 sec	$1.50 \times 10^4 \text{ sec}$
$T_{1,P}$	Polarization lifetime (pump)	$2.25 \times 10^3 \text{ sec}$	$1.97 \times 10^4 \text{ sec}$
$T_{1,t}$	Polarization lifetime (transfer tube)	415 sec	$7.26 \times 10^3 \text{ sec}$
γ	Gyromagnetic ratio	$2\pi \times 1.177 \frac{\text{kHz}}{\text{gauss}}$	$2\pi \times 3.242 \frac{\text{kHz}}{\text{gauss}}$
ω	Operating frequency	$2\pi \times 1791 \text{ Hz}$	$2\pi \times 4933 \text{ Hz}$
Q	Resonator quality factor	9.9	9.3
T_2	Coherence time	333 sec	170 sec
τ_{RD}	Radiation damping time	76 sec	15.9 sec

TABLE I. Physically reasonable parameter values used in computing solutions to the equations of motion. Notes: i) the cell gas pressures are given at a temperature of roughly 24°C; ii) Xe wall loss parameters in pump and maser bulbs are related according to [20]; iii) Appendix A is used to compute polarization lifetimes from the wall loss parameters.

It is assumed that the diffusion process can be described everywhere in the transfer tube by a single constant diffusion rate D . This is not strictly in accordance with the experimental conditions in the dual noble gas maser cell. Table 1 lists typical parameter values for the dual noble gas maser [4]; it indicates that the pump and maser bulbs are maintained at different temperatures, 120° and 40° C respectively. This is a $\sim 25\%$ difference in absolute temperature, corresponding to roughly 37% change in D over the length of the transfer tube (since $D \propto T^{3/2}$ [18]). However, much of the temperature drop in the transfer tube probably occurs within ~ 1 cm of the pump chamber in both the SAO [5] and Michigan apparatus [4]; and the transfer tubes typically in use are about 4 cm in length (Table 1). In addition to the effects of diffusion, the transfer tube polarization evolves under a polarization loss rate characterized by a constant $T_{1,tt}^{-1}$. This loss rate is also expected to decrease exponentially with temperature (for a recent study of polarization wall loss in ^{129}Xe , see [20]) and is thus not constant over the length of the transfer tube; however, as in the case of the diffusion constant the bulk of the variation occurs near the pump chamber. Thus, in attempting to extract maser parameters using the model in this paper, it would appear necessary to account for the non-uniform temperature, but it may be possible to do so approximately in a simple way. For example, the simulations reported in this paper take the diffusion constant and polarization wall loss rate in the pump chamber to be different from the assumed common values of the transfer tube and maser chamber (Table 1).

The pump bulb polarization is continually replenished via spin-exchange collisions with optically-pumped, polarized Rb atoms, at a rate of $P_{Rb}\gamma_{SE}$ per noble gas atom; a phenomenological loss rate, $T_{1,P}^{-1}$, accounts for polarization loss due to effects such as wall collisions and magnetic field inhomogeneities [22,28]. The maser bulb polarization loss rate is characterized by T_1^{-1} . These phenomenological loss rates can be related to one another in terms of a common parameter, by solving the diffusion equation in the various regions of the cell and assuming that noble gas polarization destruction is dominated by wall collisions. This analysis is carried out in Appendix A.

In terms of these parameters, the coupled equations of motion for the polarizations are given by

$$\begin{aligned}\dot{P}_P(t) &= P_{Rb}\gamma_{SE} - \frac{P_P(t)}{T_{1,P}} + G_P L \frac{\partial}{\partial x} \Pi(0, t) \\ \dot{P}_z(t) &= -\frac{P_z(t)}{T_1} - G_M L \frac{\partial}{\partial x} \Pi(L, t) \\ \left(D \frac{\partial^2}{\partial x^2} - \frac{\partial}{\partial t} - \frac{1}{T_{1,tt}} \right) \Pi(x, t) &= 0\end{aligned}\tag{5}$$

where G_M, G_P are defined as

$$G_P = \frac{A_{tt}D}{V_P L}; \quad G_M = \frac{A_{tt}D}{V_M L}\tag{6}$$

The transfer tube polarization $\Pi(x, t)$ can be expressed in terms of the polarizations P_P and P_z by means of a Fourier series expansion and the method of Green's functions, in conjunction with boundary conditions of eqn (2). The derivation is outlined in Appendix B. The result is a reduction of eqns (5) to a set of 2 coupled equations in terms of P_P and P_z alone. Substitution of results (B12), (B13), and (B14) into the first two of Eqns (5) yields

$$\dot{P}_P(t) = P_{Rb}\gamma_{SE} - P_P(t) \left(\frac{1}{T_{1,P}} + \gamma_{SE} \right) + G_P \left[\begin{aligned} &(P_z(t) - P_P(t)) + \sqrt{\frac{2}{L}} \sum_{m=1}^{\infty} b_m \cdot \pi m \cdot \exp(-k_m^2 D t) \\ &+ P_z(t) \cdot \Sigma_2 - P_P(t) \cdot \Sigma_1 \\ &- 2 \cdot \sum_{m=1}^{\infty} (-1)^m \left[\frac{1}{k_m^2 D T_{1,tt}} - 1 \right] \int_0^{\infty} du \exp\left(-\left(k_m^2 D + \frac{1}{D T_{1,tt}}\right) u\right) \dot{P}_z(t-u) \\ &+ 2 \cdot \sum_{m=1}^{\infty} \left[\frac{1}{k_m^2 D T_{1,tt}} - 1 \right] \int_0^{\infty} du \exp\left(-\left(k_m^2 D + \frac{1}{D T_{1,tt}}\right) u\right) \dot{P}_P(t-u) \end{aligned} \right]\tag{7}$$

$$\dot{P}_z(t) = -\frac{P_z(t)}{T_1} - G_M \left[\begin{aligned} &(P_z(t) - P_P(t)) + \sqrt{\frac{2}{L}} \sum_{m=1}^{\infty} b_m \cdot \pi m \cdot \exp(-k_m^2 D t) \\ &+ P_z(t) \cdot \Sigma_1 - P_P(t) \cdot \Sigma_2 \\ &- 2 \cdot \sum_{m=1}^{\infty} \left[\frac{1}{k_m^2 D T_{1,tt}} - 1 \right] \int_0^{\infty} du \exp\left(-\left(k_m^2 D + \frac{1}{D T_{1,tt}}\right) u\right) \dot{P}_z(t-u) \\ &+ 2 \cdot \sum_{m=1}^{\infty} (-1)^m \left[\frac{1}{k_m^2 D T_{1,tt}} - 1 \right] \int_0^{\infty} du \exp\left(-\left(k_m^2 D + \frac{1}{D T_{1,tt}}\right) u\right) \dot{P}_P(t-u) \end{aligned} \right]$$

These are the [integro-differential] equations of motion for the pump and maser bulb polarizations. Note that (as expected) these equations reduce to those of references [8,14] in the limit of infinite D . The steady-state pump and maser bulb polarizations in the absence of masing action (defined as $P_{P,o}$ and P_o , respectively) are found by setting $\dot{P}_P = \dot{P}_M = 0$ in Equations (7). The result is

$$\begin{aligned} P_{P,o} &= \Delta_o^{-1} \cdot \left(\frac{1}{T_1} + G_M (1 + \Sigma_1) \right) \cdot P_{Rb} \gamma_{SE} \\ P_o &= \Delta_o^{-1} \cdot G_M (1 + \Sigma_2) \cdot P_{Rb} \gamma_{SE} \end{aligned} \quad (8)$$

where Δ_o is defined as

$$\Delta_o \equiv \left(\gamma_{SE} + \frac{1}{T_{1,P}} + G_P (1 + \Sigma_1) \right) \cdot \left(\frac{1}{T_1} + G_M (1 + \Sigma_2) \right) - G_M G_P (1 + \Sigma_2)^2 \quad (9)$$

Remember that Σ_1 and Σ_2 are defined by equation (B15). The above results can then be used to find the steady-state polarization profile $\Pi_o(x)$ in the transfer tube by substitution of equations (8), (9) into eqn. (B12). Note also that we take the initial condition transients of (B12) as having damped out. The result is

$$\Pi_o(x) = P_{P,o} + \frac{x}{L} \cdot (P_o - P_{P,o}) + P_o \cdot 2 \sum_{m=1}^{\infty} \frac{\sin(k_m x)}{\pi m} (-1)^m \frac{1}{k_m^2 D T_{1,tt} + 1} - P_{P,o} \cdot 2 \sum_{m=1}^{\infty} \frac{\sin(k_m x)}{\pi m} \frac{1}{k_m^2 D T_{1,tt} + 1} \quad (10)$$

The effect of transfer tube polarization loss is manifested by the presence of the Σ_1, Σ_2 terms (see (B15)) in (9) and the summation terms in (10). All of these terms vanish in the limit of large $T_{1,tt}$ or large D . This is reasonable because even if there is a finite transfer tube loss rate, little loss occurs if the diffusion is rapid since the atoms then spend little time in the transfer tube.

Calculations using (9) and (10) show that accounting for transport effects does not alter the polarizations of ^3He beyond the \sim percent level (either in a Zeeman maser or a typical polarized target). However, ^{129}Xe polarization in a double-bulb cell is significantly affected by polarization loss in the transfer tube. Figure 3 is a plot of the calculated steady state Xe polarization profile and the Xe polarization gradient in the transfer tube assuming the system parameter values of Table I. We have assumed that the wall loss parameter (see Appendix A) in the maser bulb and transfer tube are the same. The polarization profile deviates discernably from the strict linear variation that would be expected in the limit of zero transfer tube loss. This is obvious from the gradient plot; the gradient decreases in absolute value by 43% over the length of the transfer tube. The polarization profile is concave upward: because of transfer tube losses, more polarization must be supplied from the pump bulb, leading to a more negative gradient at $x = 0$, and less polarization is delivered from the transfer tube into the maser bulb, leading to a less negative gradient at $x = L$. It can be shown that the effect of transfer tube loss on the pump bulb polarization is small, whereas the maser bulb polarization is more strongly affected as compared to the loss-free transfer tube case. For the case displayed in Fig. 3, a maser bulb polarization of 0.36 is attained; it can be shown that in the case of infinite $T_{1,tt}$ that the steady state maser bulb polarization is 0.41.

In summary, the steady state maser bulb polarization is significantly reduced by transfer tube losses in conjunction with a finite value of D , in comparison with the loss-free case. These conditions are realized in currently operating ^{129}Xe Zeeman masers. The steady-state solutions (8) provide explicit relations for the dependence of the maser and pump chamber polarizations on the transfer tube polarization loss rate and the polarization diffusion constant (in addition to the other system parameters), and are therefore a useful tool for the design of double-bulb cell systems in which atoms are polarized in one bulb, and a physics experiment using the atoms is carried out in the other. The necessity of these results for analyzing existing ^3He polarized targets is admittedly limited; however, these results can guide possible future experiments in which large standoff distances between the polarizing region and the interaction region is desired. Given a wall loss rate, diffusion constants (calculable with good accuracy from cell gas pressures and temperatures [18,19]), laser power, cell geometry parameters, and the required polarization delivery, this theory determines the maximum permissible length of the transfer tube.

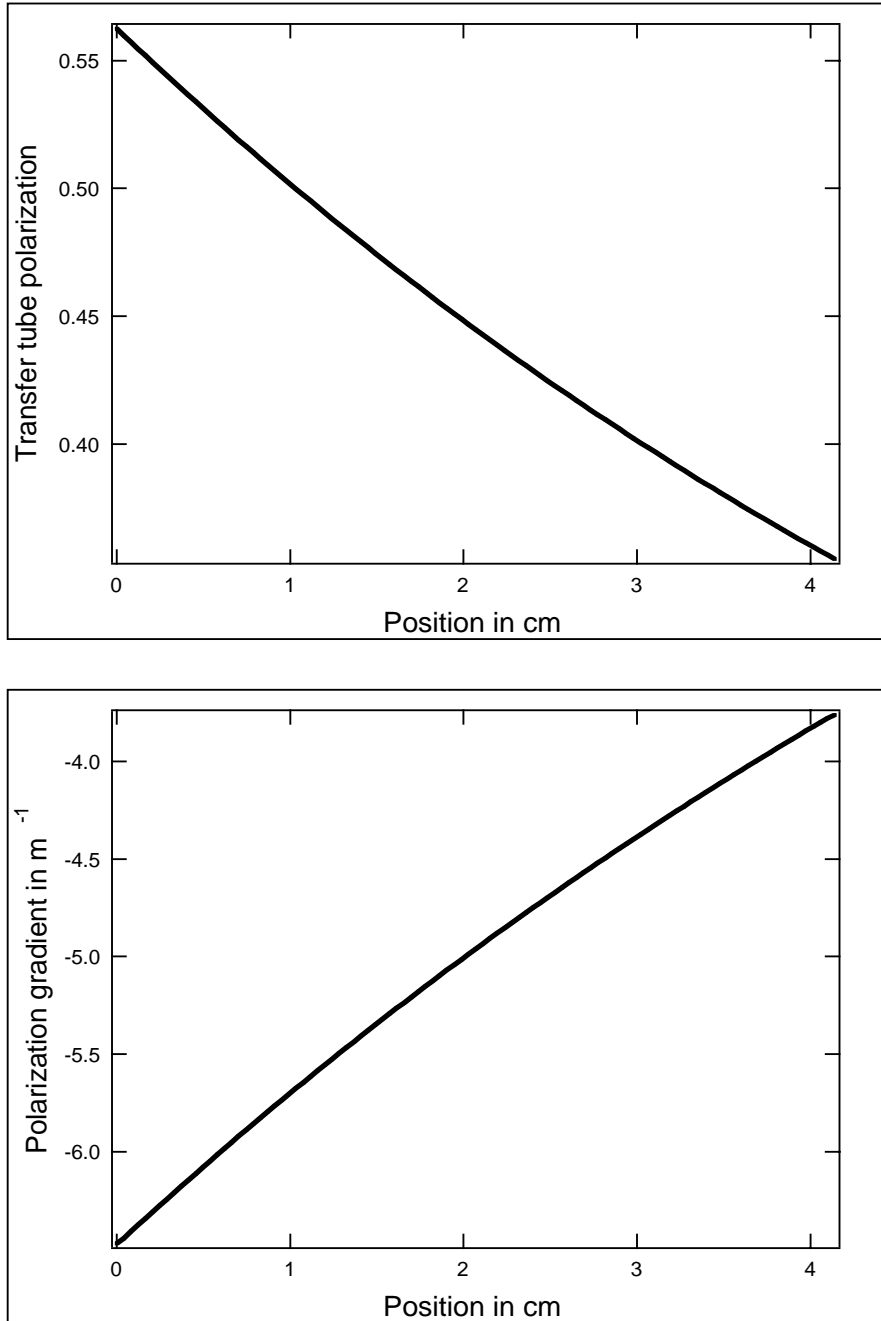


FIG. 3. Polarization and polarization gradient as a function of position in the transfer tube, calculated from eqn (10) using parameter values given in Table I. The endpoint values correspond to the values of the polarization in the pump ($x = 0$) and maser ($x = L$) bulbs. The endpoint gradients are proportional to the flux of polarization from the pump and maser bulbs. In the limit of small polarization loss in the transfer tube, the polarization gradient would be constant.

An exact solution to eqns (7) can be obtained for a time-dependent problem of interest. This solution can be used to extract the wall loss parameter for both the maser and pump bulbs. Again, the model is principally applicable to

the slowly diffusing, high wall loss rate ^{129}Xe case. Consider an experiment wherein the initial Xe polarizations are zero, and wherein the spin-exchange polarization source term is suddenly turned on to its full value $P_{Rb}\gamma_{SE}$ at $t = 0$. The Rb polarization loss rate is almost completely determined in the pump bulb by the very high rate of Xe-Rb spin rotation collisions [21]; the rate of these collisions per Rb atom depends only on the Xe density, not the polarization, so that the Rb polarization can be taken to be constant in time. Also, the Rb polarization will attain its peak value in less than a msec, so that the Rb polarization can be considered to be turned on instantaneously. Under the initial conditions given above, Laplace transforms can be applied straightforwardly to equations (7): in terms of the Laplace transforms defined by

$$\begin{aligned} Q_P(s) &\equiv \int_0^{\infty} dt \cdot \exp(-st) P_P(t) \\ Q_M(s) &\equiv \int_0^{\infty} dt \cdot \exp(-st) P_M(t) \end{aligned} \quad (11)$$

the solutions are

$$\begin{aligned} Q_P(s) &= \Delta(s)^{-1} \cdot \left(s(G_M\sigma_1(s) - 1) - \left(\frac{1}{T_1} + G_M(1 + \Sigma_1) \right) \right) \cdot P_{Rb}\gamma_{SE} \\ Q_M(s) &= \Delta(s)^{-1} \cdot (sG_M\sigma_2(s) - G_M(1 + \Sigma_2)) \cdot P_{Rb}\gamma_{SE} \end{aligned} \quad (12)$$

$$\Delta(s) = s \cdot \left\{ \left\{ \left[s(1 - G_P\sigma_1(s)) + \left(\frac{1}{T_{1,P}} + \gamma_{SE} + G_P(1 + \Sigma_1) \right) \right] \cdot \right\} + \left\{ \left[s(G_M\sigma_1(s) - 1) - \left(\frac{1}{T_1} + G_M(1 + \Sigma_1) \right) \right] \right\} \right\} + \left\{ \left\{ \left[sG_P\sigma_2(s) - G_P(1 + \Sigma_2) \right] \cdot \right\} \right\} \left\{ \left[sG_M\sigma_2(s) - G_M(1 + \Sigma_2) \right] \right\} \right\} \quad (13)$$

and

$$\begin{aligned} \sigma_1(s) &\equiv 2 \sum_{m=1}^{\infty} \left[\left(\frac{1}{k_m^2 D T_{1,tt}} - 1 \right) \frac{1}{s + k_m^2 D + \frac{1}{T_{1,tt}}} \right] \\ \sigma_2(s) &\equiv 2 \sum_{m=1}^{\infty} (-1)^m \left[\left(\frac{1}{k_m^2 D T_{1,tt}} - 1 \right) \frac{1}{s + k_m^2 D + \frac{1}{T_{1,tt}}} \right] \end{aligned} \quad (14)$$

The solution to the original problem is the sum of residues of this transform (multiplied by an exponential time dependence):

$$\begin{aligned} P_P(t) &= \sum_{i=0}^{\infty} C_{P,n} \exp(\Omega_i t) = P_{Rb}\gamma_{SE} \sum_{i=0}^{\infty} \exp(\Omega_i t) \left[\frac{\Omega_i (G_M\sigma_1(\Omega_i) - 1) - \left(\frac{1}{T_{1,M}} + G_M(1 + \Sigma_1) \right)}{\frac{d}{ds} \Delta(s) \Big|_{s=\Omega_i}} \right] \\ P_z(t) &= \sum_{i=0}^{\infty} C_{M,n} \exp(\Omega_i t) = P_{Rb}\gamma_{SE} \sum_{i=0}^{\infty} \exp(\Omega_i t) \left[\frac{\Omega_i G_M\sigma_2(\Omega_i) - \left(\frac{1}{T_{1,M}} + G_M(1 + \Sigma_1) \right)}{\frac{d}{ds} \Delta(s) \Big|_{s=\Omega_i}} \right] \\ &[\Omega_i \equiv \text{ith root of } \Delta(s)] \end{aligned} \quad (15)$$

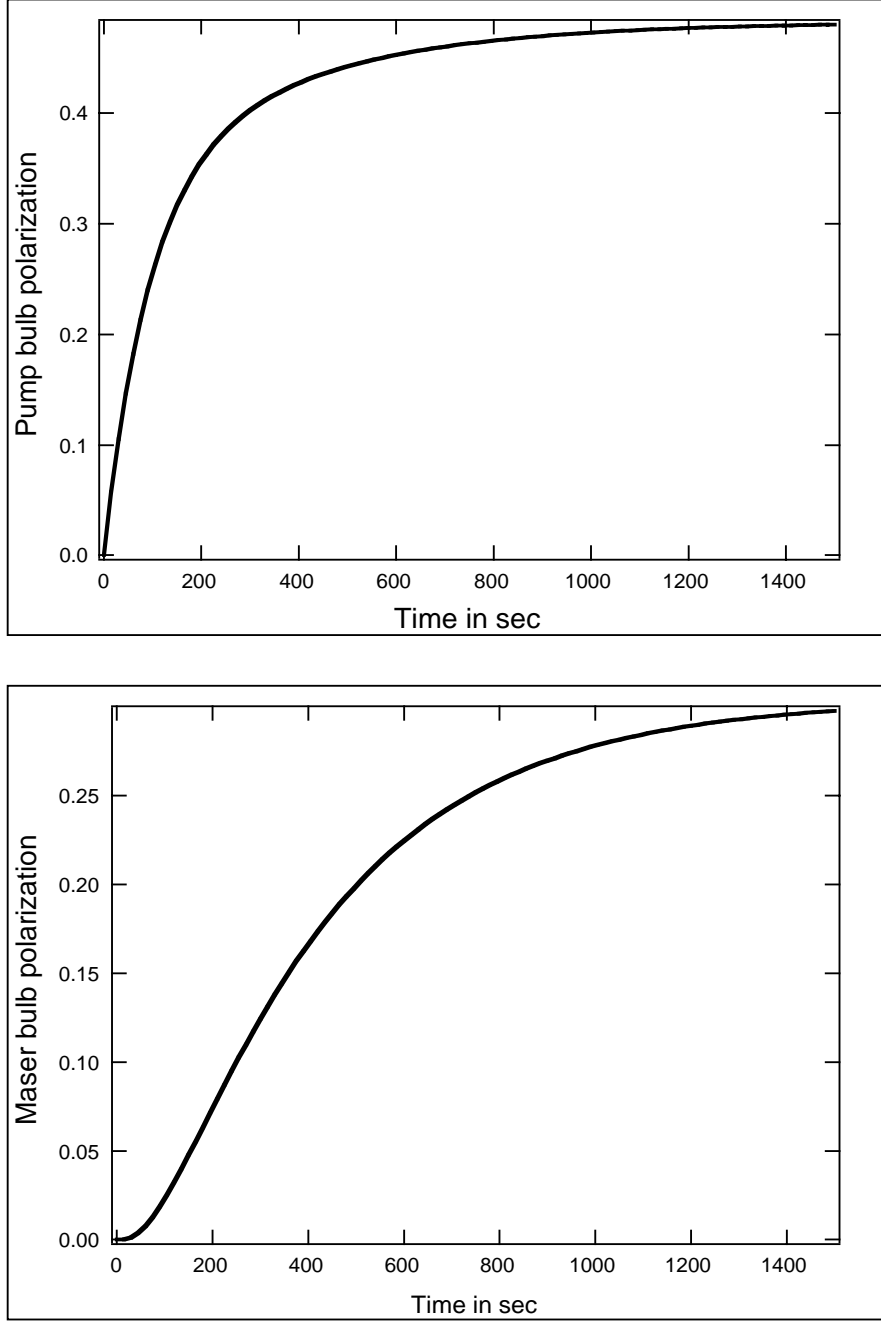


FIG. 4. Pump and maser bulb Xe polarizations as a function of time after turning on the optical pumping laser, computed from eqn (15) and using the parameter values of Table I. There is a propagation delay time before the maser chamber polarization starts to increase from zero, resulting from finite length of the transfer tube.

The residues result from simple poles at the zeros of the determinant function $\Delta(s)$. There is an infinitude of such poles. Note that even though the points $s = -k_m^2 D - 1/T_{1,tt}$ are removable singularities of the overall integrand, $\Delta(s)$ changes sign near these points, i.e. has roots, thus contributing simple poles at these points. The residues can

be found numerically. The first root is at $s = 0$ (which yields the equilibrium solutions). The next two roots Ω_1 and Ω_2 are given approximately by the solutions to the quadratic equation

$$0 = \left\{ \begin{array}{l} s^2 \left[(1 - G_P \sigma_1(0)) (G_M \sigma_1(0) - 1) + G_P G_M \sigma_2(0)^2 \right] \\ + s \left[\begin{array}{l} (G_P \sigma_1(0) - 1) \left(\frac{1}{T_1} + G_M (1 + \Sigma_1) \right) \\ + (G_M \sigma_1(0) - 1) \left(\frac{1}{T_{1,P}} + \gamma_{SE} + G_P (1 + \Sigma_1) \right) \\ - 2G_P G_M \sigma_2(0) (1 + \Sigma_2) \end{array} \right] \\ + \left[\begin{array}{l} - \left(\frac{1}{T_{1,P}} + \gamma_{SE} + G_P (1 + \Sigma_1) \right) \left(\frac{1}{T_1} + G_M (1 + \Sigma_1) \right) \\ + G_P G_M (1 + \Sigma_2)^2 \end{array} \right] \end{array} \right\} \quad (16)$$

These are the late-time exponential decay rates. The remaining roots serve to describe the early time behavior of the system and are approximately

$$\Omega_i|_{i \geq 3} \cong -k_{i-2}^2 D - \frac{1}{T_{1,tt}} \quad (17)$$

The solution (obtained with 15 terms of the sums in (15) is plotted in Fig. 4. It is interesting to note that the onset of P_z is delayed, with respect to P_P , by a time $\sim (k_1^2 D)^{-1}$, the diffusion time of the lowest-order transfer tube diffusion mode. P_P and P_z can each be approximately described as linear combinations of a constant term, and exponential terms $\exp(\Omega_1 t)$ and $\exp(\Omega_2 t)$ (i.e., a double exponential plus constant). Thus, for the purposes of parameter extraction from experimental data, one can simultaneously fit the two profiles to double exponentials (having the same time constants), and then equate the decay rates of eqn. (15) to the time constants extracted from the fit. The time constants in the calculations shown in Fig. 4 are $-\Omega_1^{-1} = 91$ sec, and $-\Omega_2^{-1} = 357$ sec, which are much shorter than the polarization lifetimes. The time constants are determined by the diffusion constants, the spin exchange rate, and the cell geometry as well as the polarization lifetimes.

It can be shown that in the case of ^3He , the fractional difference between maser and pump bulb polarizations is only $\leq 1\%$. Thus, the ratio P_P/P_z for ^{129}Xe can be measured in cells containing both ^3He and ^{129}Xe , by comparing Xe and He signals measured in the pump and maser bulbs. Knowledge of that ratio alone allows the determination of the polarization lifetimes T_1 and $T_{1,tt}$, given that the diffusion rate D has been determined independently from cell gas pressures and temperatures [18,19], that the cell geometry is known in detail, and assuming that the wall loss rate κ in the maser chamber and transfer tube are the same (see Appendix A). This seems to be a reasonable assumption since the temperature in these regions is for the most part the same, but this approach remains to be tested experimentally. Measurement of the polarizations P_P and P_z as a function of time then provides an independent determination of the polarization lifetimes T_1 and $T_{1,tt}$, as well as a determination of the pump chamber polarization lifetime $T_{1,P}$.

In conclusion, a simple model for polarization transport in two-bulb cells leads to a set of differential equations which admit exact solutions. While the exact solutions are complicated in form, approximate expressions for exponential decay rates can be used for extraction of cell polarization lifetimes from experimental data. The steady state solutions to the equations of motion illustrate the effect of transfer tube polarization loss on the net transport of polarization, and are a valuable tool for the design of cells in which atoms are polarized in a region separate from where they will be used.

III. ZEEMAN MASER DYNAMICS IN TWO-BULB CELLS

This section presents a Bloch model of the Zeeman maser that incorporates the results of the previous section, along with a description of the maser frequency as an independent dynamical variable. The frequency is seen to depend directly on the longitudinal polarization P_z , through the mechanism of cavity-pulling; this theory also permits the easy introduction of [P_z -proportional] shifts due to fields induced by the polarized atoms' magnetization. These effects are subtle, causing fractional frequency shifts of less than 0.1 ppm, and were made observable only by the advent of the two-species Zeeman maser [4].

This section considers the dynamics of single species Zeeman masers using simple RLC resonators. However, the equations of motion are formulated so as to permit their use in describing dual Zeeman masers with a more realistic resonator configuration (see Appendix E).

The equations of motion are derived by first writing down the Bloch equations, extended to include polarization transport effects, in terms of Cartesian variables P_P , P_z , P_x , P_y . The resulting system is then transformed into a cylindrical representation in terms of variables P_P , P_z , P_\perp , Φ . The maser oscillation frequency ω is the time derivative

of Φ ; P_{\perp} is the magnitude of the polarization component perpendicular to the longitudinal (z -) axis. Conditions required for the existence of a steady state solution will be discussed. The equations can be linearized about a steady state solution (when it exists), and the resulting system of equations describing the near-steady-state oscillations is solved using Laplace transforms. A simple description of the cavity-pulling mechanism in Zeeman masers is then presented.

Prior to writing the maser equations of motion, it is necessary to introduce formally the effect of the pickup coil feedback described qualitatively in Sec. I. The description of this feedback must account for the coupling of the pickup coil to the polarized ensemble, and also the characteristics of the resonant circuit to which the pickup coil is attached. We assume for simplicity that the resonant circuit is a simple RLC circuit, with resonant frequency inductance L , capacitance C , $\omega_o = 1/\sqrt{LC}$, resistance R , and quality factor defined as $Q = \omega_o L/R$. The response of the resonant circuit to the time-varying flux induced by the magnetization precessing at frequency ω is described in terms of the following definitions of a resonator phase α and amplitude response function ρ (see Appendix C):

$$\rho(\omega) = \frac{Q}{\sqrt{Q^2 \left(1 - \left(\frac{\omega_o}{\omega}\right)^2\right)^2 + \left(\frac{\omega_o}{\omega}\right)^2}}$$

$$\cos \alpha = \left(1 - \left(\frac{\omega_o}{\omega}\right)^2\right) \rho(\omega) \quad \sin \alpha = \frac{\omega_o}{\omega} \frac{\rho(\omega)}{Q} \quad (18)$$

Note that these definitions are not consistent with those of reference [8]; the change is made here to more simply accommodate resonator implementations other than simple RLC circuits (see Section IV and Appendix E).

As remarked, ω is a dynamical variable in the theory, so in principle the functions α and ρ are time-dependent. However, it will be seen that deviations of ω from the Larmor precession frequency are roughly seven orders of magnitude smaller than the feedback RLC resonance frequency ω_o . A typical resonator Q is of order 10^1 ; thus, the changes induced in the values of α and ρ by frequency variations are negligible as far as the behavior of the polarizations are concerned. α and ρ can be assigned the values which they take on at the atoms' Larmor precession frequency γB_o .

We can write the components of the polarization P_x, P_y in terms of a maser phase Φ and a maser amplitude P_{\perp} :

$$P_x = P_{\perp} \cos(\Phi(t)) \quad P_y = P_{\perp} \sin(\Phi(t)) \quad (19)$$

The maser oscillation frequency ω is defined in terms of the phase Φ as

$$\Phi(t) = \int^t dt' \omega(t') \quad (20)$$

As remarked earlier, the precessing atoms excite current in the the resonant circuit which flows through the pickup coil; the magnetic field induced by this current flow torques the magnetization of the precessing ensemble. The time derivative of the noble gas polarization due to magnetic field torque is

$$\left. \frac{d}{dt} \vec{P} \right|_{\text{Magnetic field torque}} = \gamma \vec{B} \times \vec{P} \quad (21)$$

The components of the magnetic field due to the main axial field, along with that due to the pickup coil, are shown in Appendix C to be

$$\begin{aligned} \gamma B_x &= \frac{P_{\perp}}{\tau} \cos(\Phi(t) + \alpha) = \frac{1}{\tau} (P_x \cos \alpha - P_y \sin \alpha); \\ \gamma B_y &= \frac{P_{\perp}}{\tau} \sin(\Phi(t) + \alpha) = \frac{1}{\tau} (P_y \cos \alpha + P_x \sin \alpha); \\ \gamma B_z &= \gamma B_o \end{aligned} \quad (22)$$

where τ is defined as

$$\tau^{-1} = \frac{\hbar \gamma^2}{2} [ng] \mu_o \eta \rho(\omega) \quad (23)$$

η is a dimensionless parameter proportional to the strength of the inductive coupling between the pickup coil and the magnetization of the polarized ensemble, and its value is computed for a typical geometry in Appendix C. The Bloch equations in Cartesian coordinates for P_x and P_y can be written as

$$\begin{aligned}\dot{P}_x &= \gamma B_y P_z - \gamma B_z P_y - \frac{P_x}{T_2} \\ \dot{P}_y &= \gamma B_z P_x - \gamma B_x P_z - \frac{P_y}{T_2}\end{aligned}\quad (24)$$

where T_2 is a phenomenological damping time.

Equations (24) can be transformed into equations in P_\perp , P_z and ω via linear combination. First, multiply the first equation by $(-P_y)$, multiply the second equation by (P_x) , and add the results. Using relations (19), (20), and (22) yields the equation governing the deviation of the maser frequency from the Larmor precession frequency:

$$\omega - \gamma B_o = -\frac{P_z}{\tau} \cos \alpha \quad (25)$$

Important effects resulting from magnetic fields due to the magnetization of polarized atoms are not included here, but will be discussed later. It will also be shown that the frequency deviation shown here is, in steady state, a cavity-pulling frequency shift. The equation in \dot{P}_\perp can be obtained by multiplying the first equation of (24) by (P_x) , the second by (P_y) , and adding the results. Use of relations (19), (20), and (22) yields

$$\dot{P}_\perp = \frac{P_z P_\perp}{\tau} \sin \alpha - \frac{P_\perp}{T_2} \quad (26)$$

It remains to show how the equation in \dot{P}_z transforms: for brevity, consider the portion of the time derivative due to the torque exerted by the magnetic field. It is simple to derive the relation

$$\dot{P}_z \Big|_{\text{magnetic torque}} = -\frac{1}{\tau} P_\perp^2 \sin \alpha \quad (27)$$

We can now write down the equations of motion for the Zeeman maser in which all variables P_\perp , P_z , Φ , P_P , are slowly varying, i.e. $dx/dt \ll \omega x$. We have essentially achieved a transformation of the equations into a frame rotating at the maser precession frequency. Prior to writing the equations, let us define the radiation damping time τ_{RD} :

$$\tau_{RD}^{-1} = \frac{1}{2} \frac{\hbar \gamma^2}{2} \mu_o \eta Q [ng] P_o \quad (28)$$

In this definition, P_o is the noble gas polarization in the maser chamber that would be attained in the absence of masing, given by equation (8). The definition is cast in these terms so as to make τ_{RD} a readily measurable quantity. Using this definition in the expression for the quantity τ of eqn. (23), we obtain the transformed Bloch equations of motion for the Zeeman maser:

$$\begin{aligned}\dot{P}_P(t) &= P_{Rb} \gamma_{SE} P_P(t) \left(\frac{1}{T_{1,P}} + \gamma_{SE} \right) + G_P \left[\begin{aligned} & (P_z(t) - P_P(t)) + \sqrt{\frac{2}{L}} \sum_{m=1}^{\infty} b_m \cdot \pi m \cdot \exp(-k_m^2 D t) \\ & + P_z(t) \cdot \Sigma_2 - P_P(t) \cdot \Sigma_1 \\ & - 2 \cdot \sum_{m=1}^{\infty} (-1)^m \left[\frac{1}{k_m^2 D T_{1,tt}} - 1 \right] \int_0^{\infty} du \exp\left(-\left(k_m^2 D + \frac{1}{D T_{1,tt}}\right) u\right) \dot{P}_z(t-u) \\ & + 2 \cdot \sum_{m=1}^{\infty} \left[\frac{1}{k_m^2 D T_{1,tt}} - 1 \right] \int_0^{\infty} du \exp\left(-\left(k_m^2 D + \frac{1}{D T_{1,tt}}\right) u\right) \dot{P}_P(t-u) \end{aligned} \right] \\ \dot{P}_z(t) &= -\frac{1}{P_o \tau_{RD}} P_\perp^2 \frac{\rho(\omega)}{Q} \sin \alpha - \frac{P_z(t)}{T_1} - G_M \left[\begin{aligned} & (P_z(t) - P_P(t)) + \sqrt{\frac{2}{L}} \sum_{m=1}^{\infty} b_m \cdot \pi m \cdot \exp(-k_m^2 D t) \\ & + P_z(t) \cdot \Sigma_1 - P_P(t) \cdot \Sigma_2 \\ & - 2 \cdot \sum_{m=1}^{\infty} \left[\frac{1}{k_m^2 D T_{1,tt}} - 1 \right] \int_0^{\infty} du \exp\left(-\left(k_m^2 D + \frac{1}{D T_{1,tt}}\right) u\right) \dot{P}_z(t-u) \\ & + 2 \cdot \sum_{m=1}^{\infty} (-1)^m \left[\frac{1}{k_m^2 D T_{1,tt}} - 1 \right] \int_0^{\infty} du \exp\left(-\left(k_m^2 D + \frac{1}{D T_{1,tt}}\right) u\right) \dot{P}_P(t-u) \end{aligned} \right] \\ \dot{P}_\perp &= \frac{P_z P_\perp}{P_o \tau_{RD}} \frac{\rho(\omega)}{Q} \sin \alpha - \frac{P_\perp}{T_2} \\ \omega - \gamma B_o &= -\frac{P_z}{P_o \tau_{RD}} \frac{\rho(\omega)}{Q} \cos \alpha\end{aligned}\quad (29)$$

This form of the Bloch equations is very useful for studying maser operation in which frequency stability is a critical consideration. Before attempting to find steady state or near-steady-state solutions for the dynamical variables, we again observe that in the first three equations of (29) we can assume a fixed maser frequency $\omega \cong \gamma B_o$ in computing the evolution of P_\perp , P_z , P_P . The result for P_z thus obtained can be used to determine the deviations of the maser frequency ω from the Larmor frequency γB_o using the last equation of (29).

Also, the use of a phenomenological damping time T_2 should be discussed and justified. The term $(-P_\perp/T_2)$ must account for all processes that destroy transverse polarization. These processes include collisions with the cell wall that depolarize the atoms (and indeed, all other processes that destroy P_z) [20,22], dephasing due to nonuniformities in the main magnetic field B_o [22,23], and escape of atoms from the maser bulb via diffusion. The net T_2 is the inverse of the sum of all rates of destruction of transverse polarization by various processes. Thus, in any attempt to model a real system using this theory, one is constrained in the selection of T_2 values by $T_2 < T_1$.

Moreover, in considering the dephasing effects of P_\perp diffusing out of the maser bulb, one might ask whether it can be properly accounted for with such a simplistic treatment. After all, in our study of P_z transport in Section II, we explicitly modelled the diffusion process in the transfer tube using a large number of diffusion modes. The description of dephasing due to diffusive escape that we are proposing here is really one in which transverse polarization in the transfer tube linearly decreases to zero over some effective length scale L_{eff} up the transfer tube from the maser bulb. The rate of diffusion into the transfer tube is then proportional simply to P_\perp . This simplistic approach should be valid as long as $L_{eff} \ll L$ where L is the transfer tube length. This amounts to requiring that transverse polarization is rapidly destroyed in the transfer tube. No transverse polarization has been seen in the pump chamber during masing in experiments in our laboratory, so that at the very least, the transverse polarization does reach zero somewhere in the transfer tube and thus the weaker condition $L_{eff} \leq L$ is satisfied. There is also no experimental observation of more than one exponential time constant in free induction decay of transverse polarization in either ^{129}Xe or ^3He , in cells described by the parameters of Table 1. This indicates that there is no significant excitation of transfer tube P_\perp diffusion modes beyond the linear. Thus, while a system might exist in which a more comprehensive description of diffusive escape of P_\perp from the maser bulb would be required, this appears not to be the case for a system described by Table 1.

Let us first consider the required conditions for attaining a maser steady state, and the steady state values of the dynamical variables. Setting all time derivatives to zero, and assuming all initial condition terms with decaying exponential time dependence are damped to zero, one obtains the following set of equations:

$$\begin{aligned}
0 &= P_{Rb}\gamma_{SE} - P_{P,o} \left(\frac{1}{T_{1,P}} + \gamma_{SE} \right) - G_P [P_{P,o}(1 + \Sigma_1) - P_{z,o}(1 + \Sigma_2)] \\
0 &= -\frac{1}{P_o\tau_{RD}} \frac{\rho(\omega)}{Q} P_{\perp,o}^2 \sin \alpha - \frac{P_{z,o}}{T_1} - G_M [P_{z,o}(1 + \Sigma_1) - P_{P,o}(1 + \Sigma_2)] \\
0 &= \frac{P_{z,o}P_{\perp,o}}{P_o\tau_{RD}} \frac{\rho(\omega)}{Q} \sin \alpha - \frac{P_{\perp,o}}{T_2} \\
\omega_{ss} - \gamma B_o &= -\frac{P_{z,o}}{P_o\tau_{RD}} \frac{\rho(\omega)}{Q} \cos \alpha
\end{aligned} \tag{30}$$

In solving these equations, it is permissible to set $\omega = \gamma B_o$ everywhere except the left hand side of the last equation. The solutions are

$$\begin{aligned}
\omega_{ss} &= \gamma B_o + \frac{\cot \alpha}{T_2} \\
P_{z,o} &= \frac{P_o\tau_{RD}}{T_2} \frac{1}{\frac{\rho(\gamma B_o)}{Q} \sin \alpha} \\
P_{P,o} &= \frac{P_{Rb}\gamma_{SE} + \frac{P_o\tau_{RD}}{T_2} \frac{1}{\frac{\rho(\gamma B_o)}{Q} \sin \alpha} G_P (1 + \Sigma_2)}{\gamma_{SE} + \frac{1}{T_{1,P}} + G_P (1 + \Sigma_1)}
\end{aligned}$$

$$P_{\perp,o} = \left(\frac{P_o \tau_{RD}}{\frac{\rho(\gamma B_o)}{Q} \sin \alpha} \right)^{\frac{1}{2}} \left\{ \begin{array}{l} \left(P_{Rb} \gamma_{SE} + \frac{P_o \tau_{RD}}{T_2 \frac{\rho(\gamma B_o)}{Q} \sin \alpha} - G_P (1 + \Sigma_2) \right) G_M (1 + \Sigma_2) \\ \gamma_{SE} + \frac{1}{T_{1,P}} + G_P (1 + \Sigma_1) \\ - \frac{P_o \tau_{RD}}{T_2 \frac{\rho(\gamma B_o)}{Q} \sin \alpha} \left(\frac{1}{T_1} + G_M (1 + \Sigma_1) \right) \end{array} \right\}^{\frac{1}{2}} \quad (31)$$

Each of these results will now be discussed in turn. First consider the frequency equation: using the definitions of $\sin \alpha$, $\cos \alpha$ as given in (18), and assuming that the resonator $Q \ll \gamma B_o T_2$, it is easy to show that the steady state maser oscillation frequency ω_{ss} is given by

$$\omega_{ss} = \gamma B_o - \frac{Q}{Q_{line}} (\gamma B_o - \omega_o) \quad (32)$$

where the line quality factor Q_{line} is defined as

$$Q_{line} \equiv \frac{\gamma B_o T_2}{2} \quad (33)$$

This is precisely the general result for the cavity pulling frequency shift in an oscillator [17].

Equation (28) shows that the product $P_o \tau_{RD}$ is dependent only on fixed properties of the system such as cell and resonator geometry, resonator Q , gas density, etc. Thus, the second of eqns (31) shows that the maser interaction tends to naturally fix the longitudinal polarization even as the maser amplitude changes with changing polarization flux from the pump chamber. In light of the dependence of the maser frequency on P_z , this is an important property for applications requiring high frequency stability. Also, the second of eqns (31) determines a threshold condition for maser operation. We know on physical grounds that the ratio $(P_{z,o}/P_o)$ must be less than unity, since the maser interaction cannot add polarization (i.e. energy) to the maser bulb. This leads to the threshold condition

$$\tau_{RD} \leq \left(\frac{\rho(\gamma B_o)}{Q} \sin \alpha \right) T_2 \quad (34)$$

which is a generalization of the threshold condition derived in [8] to include the effects of possible maser operation away from the resonator peak frequency ω_o . For a given coherence time T_2 , a smaller damping time τ_{RD} (i.e. stronger cell/pickup coil coupling) is needed to attain threshold as the detuning $(\omega - \omega_o)$ increases in absolute magnitude. That this is a threshold condition is also indicated by substituting the value $P_{z,o} = P_o$ in the fourth of equations (31); it can be shown that in that situation the equilibrium transverse polarization $P_{\perp,o}$ is zero. For $P_{z,o} > P_o$, it can be shown that $P_{\perp,o}$ becomes imaginary, which is physically impermissible.

The third of equations (31) represents a simple balance of polarization creation and loss in the pump bulb, with the maser chamber polarization fixed as described above by the maser interaction. The fourth equation of (31) can be shown to be equivalent to an energy balance condition. To see this, we first write down the rate at which energy enters the maser bulb via diffusion of polarized atoms:

$$\dot{E}_{diffusion} = \frac{\hbar \gamma B_o}{2} [ng] V_{cell} \left[P_{P,o} G_M (1 + \Sigma_2) - P_{z,o} \left(\frac{1}{T_1} + G_M (1 + \Sigma_2) \right) \right] \quad (35)$$

The first term in brackets represents the influx of polarized atoms into the maser chamber. The second term represents polarization destruction and escape of polarized atoms from the maser chamber. Energy is lost to the maser chamber via the interaction with the pickup coil resonator of the radiation field generated by the atoms:

$$\dot{E}_{radiation} = - \langle I_{pu}^2 \rangle_{avg} R \quad (36)$$

Using relation (C13), we can rewrite this as

$$\dot{E}_{radiation} = - \frac{1}{2} \frac{\xi^2 V_{cell}^2}{L^2} Q^2 M_{\perp,o}^2 \cdot R \quad (37)$$

where we have assumed for simplicity that the maser is operating with zero detuning, i.e. $\omega = \omega_o$. Let us now use the third equation of (31) in relation (35) to obtain

$$\dot{E}_{diffusion} = \frac{\hbar\gamma B_o}{2} [ng] V_{cell} \frac{P_{\perp,o}^2}{P_o\tau_{RD}} \quad (38)$$

It is now easy to see that the sum $\dot{E}_{radiation} + \dot{E}_{diffusion}$ vanishes, which we demonstrate by computing the ratio of absolute values:

$$\left| \frac{\dot{E}_{radiation}}{\dot{E}_{diffusion}} \right| = \frac{\frac{1}{2} \frac{\xi^2 V_{cell}^2}{L^2} Q^2 M_{\perp,o}^2 \cdot R}{\frac{\hbar\gamma B_o}{2} [ng] V_{cell} \frac{P_{\perp,o}^2}{P_o\tau_{RD}}} = \frac{1}{2} \xi^2 V_{cell} Q^2 \frac{\hbar\gamma}{2} [ng] \frac{R}{L^2} P_o\tau_{RD} \quad (39)$$

We now apply to this result the definition (28) for τ_{RD} , definition (C14) for η , and the definition of the resonator quality factor $Q = \omega_o L/R$:

$$\left| \frac{\dot{E}_{radiation}}{\dot{E}_{diffusion}} \right| = \frac{\omega}{2} \left(\frac{\xi^2 V_{cell}}{\mu_o L} \right) Q^2 \frac{\hbar\gamma}{2} [ng] \frac{1}{Q} \left(\frac{1}{2} \frac{\hbar\gamma^2 B_o}{2} [ng] \eta Q \right)^{-1} = \frac{\omega}{\gamma B_o} \left(\frac{\xi^2 V_{cell}}{\mu_o L} \right) \frac{1}{\eta} = 1 \quad (40)$$

The energy balance result is precisely analogous to that derived for the hydrogen maser [25].

The equations of motion (29) can be linearized about the equilibrium solutions (31), and the linearized equations can be solved via Laplace transforms in a fashion very similar to that employed in solving the equations of motion in Section II. As remarked earlier, we need not account for frequency variations in studying the dynamics of the polarization. We will proceed by assuming a fixed frequency and solving for the polarizations as a function of time; the behavior of the frequency can then be determined using our knowledge of the behavior of P_z . First, we express the polarizations as their steady state values plus time-dependent deviations:

$$\begin{aligned} \omega &= \omega_{ss} + \delta\omega(t) \\ P_{\perp}(t) &= P_{\perp,o} + \delta P_{\perp}(t) \\ P_z(t) &= P_{z,o} + \delta P_z(t) \\ P_P(t) &= P_{P,o} + \delta P_P(t) \end{aligned} \quad (41)$$

The deviation functions are assumed small in the sense that any term higher than first order in the deviation functions can be neglected. Substituting definitions (41) into equations of motion (29), using steady state solutions (31), and neglecting terms of higher than linear order in the deviation functions yields the following coupled equations of motion:

$$\begin{aligned} \delta\omega &= -\frac{\delta P_z}{P_o\tau_{RD}} \left[\frac{\rho(\omega)}{Q} \cos \alpha \right]_{\omega=\gamma B_o} \\ \frac{d}{dt} \delta P_{\perp}(t) &= \left(\frac{P_{\perp,o}}{P_o\tau_{RD}} \frac{\rho(\omega)}{Q} \sin \alpha \right) \cdot \delta P_z(t) \\ \frac{d}{dt} \delta P_z(t) &= \left\{ \begin{aligned} &\left(\frac{-2P_{\perp,o}}{P_o\tau_{RD}} \frac{\rho(\omega)}{Q} \sin \alpha \right) \cdot \delta P_{\perp}(t) + G_M (1 + \Sigma_2) \delta P_P(t) - \left(\frac{1}{T_1} + G_M (1 + \Sigma_1) \right) \cdot \delta P_z(t) \\ &+ G_M \cdot 2 \sum_{m=1}^{\infty} \left[\frac{1}{k_m^2 D T_{1,tt+1}} - 1 \right] \int_0^{\infty} du \exp \left(-D \left(k_m^2 + \frac{1}{D T_{1,tt}} \right) u \right) \delta \dot{P}_z(t-u) \\ &- G_M \cdot 2 \sum_{m=1}^{\infty} (-1)^m \left[\frac{1}{k_m^2 D T_{1,tt+1}} - 1 \right] \int_0^{\infty} du \exp \left(-D \left(k_m^2 + \frac{1}{D T_{1,tt}} \right) u \right) \delta \dot{P}_P(t-u) \end{aligned} \right\} \\ \frac{d}{dt} \delta P_P(t) &= \left\{ \begin{aligned} &- \left(\gamma_{SE} + \frac{1}{T_{1,P}} + G_P (1 + \Sigma_1) \right) \cdot \delta P_P(t) + G_P (1 + \Sigma_2) \cdot \delta P_z(t) \\ &+ G_P \cdot 2 \sum_{m=1}^{\infty} \left[\frac{1}{k_m^2 D T_{1,tt+1}} - 1 \right] \int_0^{\infty} du \exp \left(-D \left(k_m^2 + \frac{1}{D T_{1,tt}} \right) u \right) \delta \dot{P}_P(t-u) \\ &- G_P \cdot 2 \sum_{m=1}^{\infty} (-1)^m \left[\frac{1}{k_m^2 D T_{1,tt+1}} - 1 \right] \int_0^{\infty} du \exp \left(-D \left(k_m^2 + \frac{1}{D T_{1,tt}} \right) u \right) \delta \dot{P}_M(t-u) \end{aligned} \right\} \end{aligned}$$

(42)

The first equation is in a sense already solved, in that once we have obtained an expression for δP_z , the frequency deviation is determined. As already remarked, the frequency deviation is small and does not appreciably affect the dynamics of δP_P , δP_\perp , and δP_z . Before proceeding further, let us note that we measure phase, not frequency, in laboratory maser systems [5]. We can define a phase deviation function by $\delta\omega \equiv d(\delta\Phi)/dt$. Substituting this relation into the first of equations (42), and also substituting the second of equations (42) into the first, we integrate both sides to obtain

$$\delta\Phi(t) = -\frac{\delta P_\perp(t)}{P_{\perp,o}} \cot \alpha \quad (43)$$

Note that a trivial constant of integration has been omitted from this relation. This form is useful for interpreting experimental data, and will be generalized in Section IV to include the effects of magnetization fields and realistic multiple-species resonators. We see that the maser phase deviation from linear evolution is proportional to the maser amplitude deviation.

We can solve for the polarization deviations using Laplace transforms, defined by

$$\begin{aligned} \delta Q_\perp(s) &\equiv \int_0^\infty dt \cdot \exp(-st) \delta P_\perp(t) \\ \delta Q_z(s) &\equiv \int_0^\infty dt \cdot \exp(-st) \delta P_z(t) \\ \delta Q_P(s) &\equiv \int_0^\infty dt \cdot \exp(-st) \delta P_P(t) \end{aligned} \quad (44)$$

We anticipate that the solutions will behave like that of a damped harmonic oscillator, as has been shown for Zeeman masers both theoretically and experimentally in previous work [4,6–8]. Reminiscent of Section II, the Laplace transform solution will yield information (oscillation frequency and damping rate) describing late time behavior, and an infinitude of damping rates that permit one to match initial conditions. Our primary interest is the late time behavior, i.e. behavior at times where the rapidly decaying exponentials associated with specific initial conditions have damped out. This frequency and damping rate are easy to measure, thus providing another means of determining system parameter values from experiment. Even though early time behavior is not our primary interest, for definiteness we will specify exact initial conditions, which are required to construct Laplace transforms. A problem of interest involves administering a sudden RF "tip" to a maser initially in a steady state, thus perturbing the maser chamber polarizations, but not the pump chamber polarization. This corresponds to the following initial conditions:

$$\begin{aligned} \delta P_\perp(t < 0) &= 0 & \delta P_\perp(t = 0) &= \delta P_{\perp,o} \\ \delta P_z(t < 0) &= 0 & \delta P_z(t = 0) &= \delta P_{z,o} \\ \delta P_P(t \leq 0) &= 0 \end{aligned} \quad (45)$$

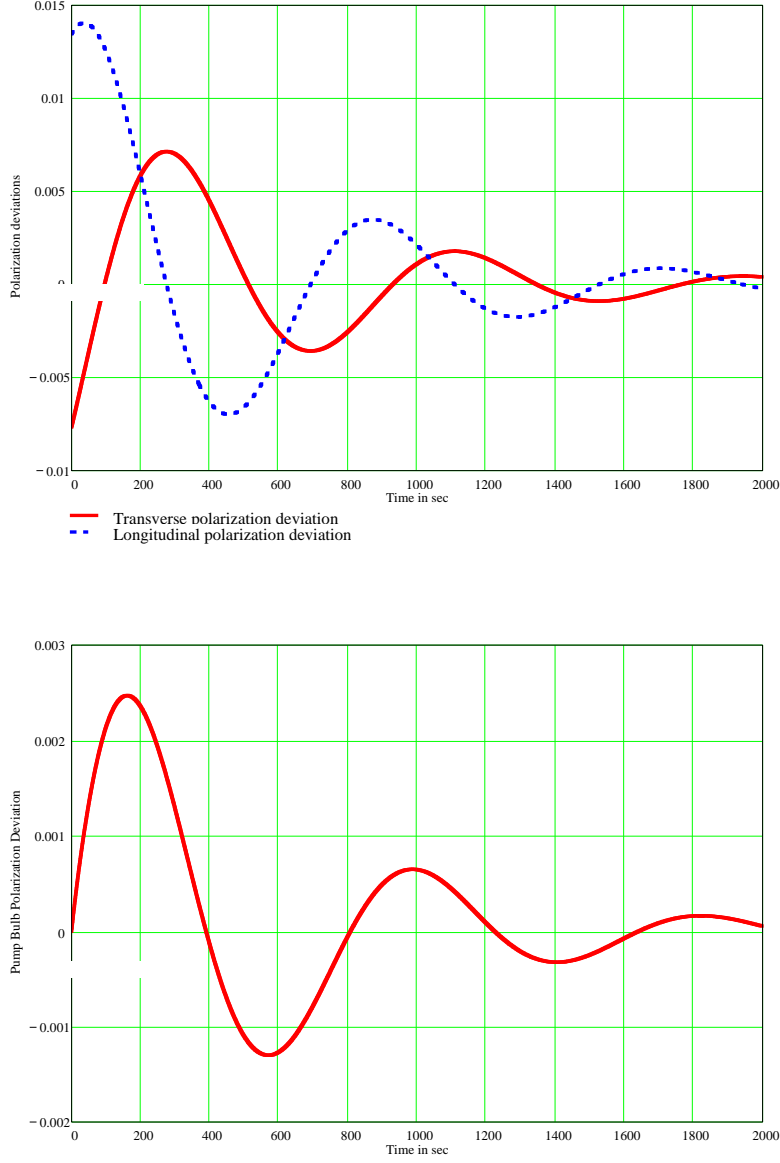


FIG. 5. Near steady-state oscillations for a ^{129}Xe Zeeman maser described by the parameters of Table I. At $t = 0$ the maser was subjected to a 5° "tip" towards the longitudinal axis (see Fig. 2). The maser chamber longitudinal polarization deviation is displayed with the transverse polarization deviation in the upper graph. The pump chamber polarization deviations are plotted in the lower graph. The pump bulb polarization oscillations are significantly smaller in size than those in the maser bulb. The steady state polarizations are: $P_{P,o} = 0.495$, $P_{z,o} = 0.0810$, $P_{\perp,o} = 0.158$. The exponential decay time constant tends to increase with increased polarization lifetimes, and the oscillation frequency tends to increase with decreased radiation damping time.

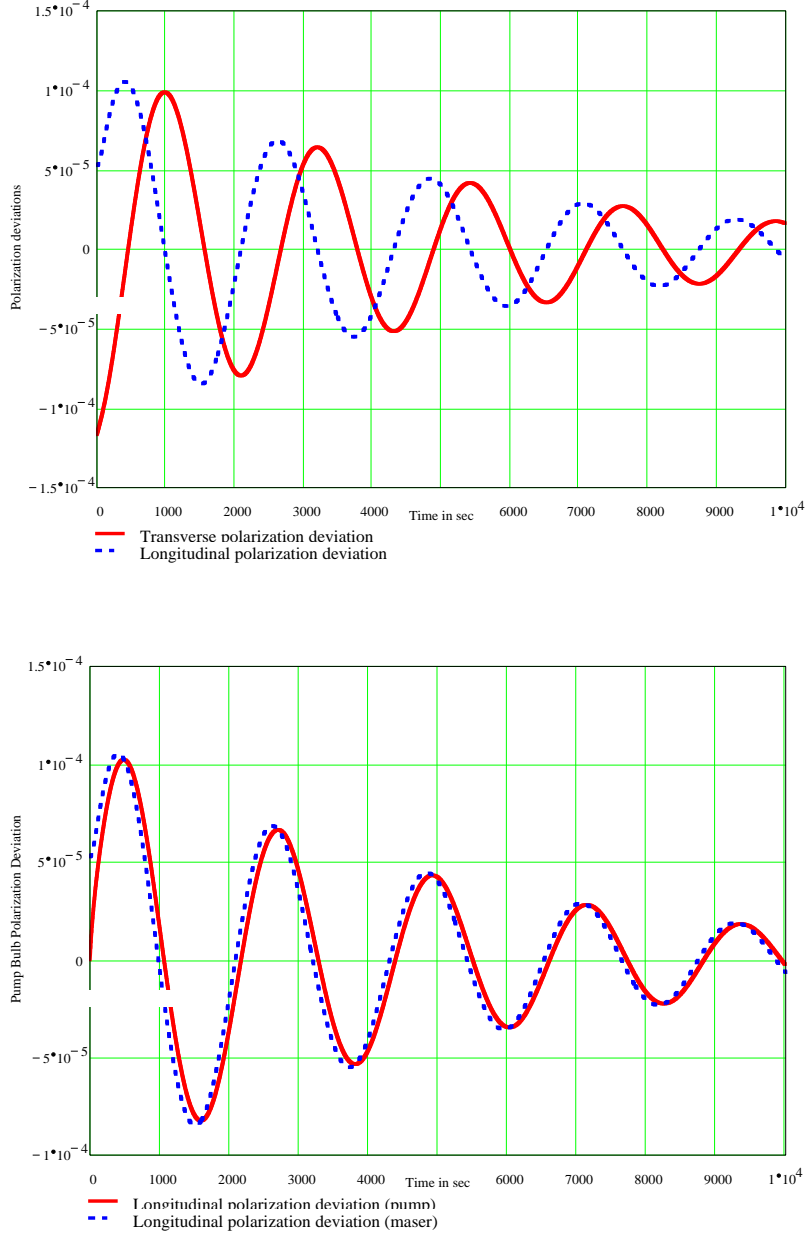


FIG. 6. Near steady-state oscillations for a ^3He Zeeman maser described by the parameters of Table I. At $t = 0$ the maser was subjected to a 5° "tip" towards the longitudinal axis (see Fig. 2). The maser chamber longitudinal polarization deviation is displayed with the transverse polarization deviation in the upper graph. The pump chamber polarization deviation is plotted in the lower graph; for comparison, the maser chamber longitudinal polarization deviation is also shown in the lower graph. The pump bulb polarization oscillations are very similar in size to the maser bulb longitudinal polarization oscillations. The steady state polarizations are: $P_{P,o} = 1.46 \times 10^{-3}$, $P_{z,o} = 1.31 \times 10^{-3}$, $P_{\perp,o} = 6.63 \times 10^{-4}$.

The Laplace transform representation of equations (42) with initial conditions (45) is obtained by multiplying each side of the equations by $\exp(-st)$ and integrating over $-\infty \leq t \leq +\infty$, remembering to apply the initial conditions in evaluating the integrals. An elementary (but long and tedious) calculation leads to a matrix representation of the equations for the Laplace transforms. To write this equation we must first define a matrix $\mathcal{R}(s)$. Note that the functions $\sigma(s)$ are those defined in equation (14):

$$\mathcal{R}(s) = \begin{bmatrix} \frac{\gamma_{SE} + s + \frac{1}{T_{1,P}} + G_P(1+\Sigma_1) - sG_P\sigma_1(s)}{G_P\sigma_2(s)} & \frac{-G_P(1+\Sigma_2) + sG_P\sigma_2(s)}{G_P\sigma_2(s)} & 0 \\ \frac{-G_M(1+\Sigma_2) + sG_M\sigma_2(s)}{1-G_M\sigma_1(s)} & \frac{\frac{1}{T_1} + G_M(1+\Sigma_1) - sG_M\sigma_1(s) + s}{1-G_M\sigma_1(s)} & \frac{2P_{\perp,o} \frac{\rho(\omega)}{Q} \sin \alpha}{P_o\tau_{RD}(1-G_M\sigma_1(s))} \\ 0 & -\frac{P_{\perp,o} \rho(\omega)}{P_o\tau_{RD} Q} \sin \alpha & s \end{bmatrix} \quad (46)$$

Using this definition, the matrix representation of the transformed equations of motion is

$$\begin{bmatrix} \delta P_{z,o} \\ \delta P_{z,o} \\ \delta P_{\perp,o} \end{bmatrix} = \mathcal{R}(s) \cdot \begin{bmatrix} \delta Q_P(s) \\ \delta Q_z(s) \\ \delta Q_{\perp}(s) \end{bmatrix} \quad (47)$$

The solution to this equation is obtained by simple inversion of the matrix \mathcal{R} . We write the inverse in terms of the matrix $\mathcal{S}(s)$ and the function $\mathcal{D}(s)$ by

$$\mathcal{R}(s)^{-1} = \frac{1}{\mathcal{D}(s)} \mathcal{S}(s) \quad (48)$$

Appendix D shows that the poles of the right hand side of this equation are located at the zeros of the function $\mathcal{D}(s)$. Also, a simple strategy for determining the roots of $\mathcal{D}(s)$, as well as the explicit expressions for the elements of the inverse matrix are presented in that Appendix. The expressions for the solution to the time-dependent problem are

$$\begin{aligned} \delta P_P(t) &= \sum_{i=0}^{\infty} C_{P,n} \exp(\Omega_i t) \\ \delta P_z(t) &= \sum_{i=0}^{\infty} C_{z,n} \exp(\Omega_i t) \\ \delta P_{\perp}(t) &= \sum_{i=0}^{\infty} C_{\perp,n} \exp(\Omega_i t) \\ [\Omega_i &\equiv \text{ith root of } \mathcal{D}(s)] \end{aligned} \quad (49)$$

Appendix D gives expressions for the coefficients C_n . We have plotted the solutions (49) for the ^{129}Xe maser in Fig. 5 and the ^3He maser in Fig. 6. The parameter values of Table I are assumed. The main distinguishing characteristic between the two cases is time scale: the ^3He oscillations take much longer to damp out than do the ^{129}Xe oscillations, and the pump chamber oscillations are much larger in the ^3He case, reflective of the stronger coupling between pump and maser bulbs as compared to the ^{129}Xe maser.

It might appear that the complexity of the expressions for the near-equilibrium oscillation frequency and the damping rate, and for the steady-state maser polarizations, might make maser parameter extraction difficult. However, the theory is sufficiently comprehensive that there are only a few parameters that cannot be well determined *a priori* (the absolute equilibrium polarizations, e.g., are somewhat hard to measure with great accuracy). E.g., if one uses Appendix A to relate the polarization lifetimes of different regions in the cell (as was done for the parameters of Table I), one would only be left with one or two polarization wall loss parameters remaining undetermined. The coherence time T_2 might also need to be a free parameter as well, insofar as T_2 has been found to vary with P_z and is somewhat difficult to measure directly with great accuracy. This is only three unknown or partially known parameters: the near-equilibrium oscillation frequency and damping rates, along with the steady-state orientation angle of the maser, amount to three independent and readily measured quantities. In principle, then, there is reason to hope that a nonlinear least squares determination of the unknown parameters could be easily obtained. Moreover, if one used polarization transport data to determine the wall loss parameters, the near-equilibrium oscillation parameters and the steady-state maser polarization orientation angle actually amount to overconstraint, since there remains only one free parameter of note. This would permit a rigorous test of the Bloch theory. A detailed comparison of this theory to measured maser characteristics will be presented in a future publication [24].

IV. FREQUENCY DYNAMICS IN DUAL ZEEMAN MASERS AND LIMITATIONS OF THE BLOCH THEORY

We now examine the implications of the previous section for Zeeman maser frequency stability. We need to make extensions to eqn (29) to account for the effects of magnetic fields induced by the magnetization of the polarized noble gases. We also must account for the effects of using one maser to stabilize the magnetic field. We will see that influences which would have tended to cause the locked maser's frequency to vary will instead induce frequency changes on the free-running maser. A method for stabilizing maser frequency against changes in P_z will also be described. Finally, we will discuss the fundamental limits of the Bloch theory in describing the dual Zeeman maser.

Magnetic fields due to the magnetization of the polarized noble gases are an important (but largely undesirable) influence in the use of polarized noble gases in precision measurement [11]. One of the important features of Zeeman masers for precision measurement was highlighted by Walsworth [13]. Zeeman maser oscillation fixes the maser's longitudinal polarization even in the presence of [quasistatic] variations in the influx of polarization into the maser bulb from the pump bulb. This can be seen from equation 31, where the steady state longitudinal polarization $P_{z,o}$ is seen to be a function of fixed system parameters and the coherence time T_2 . Uncontrolled changes in the longitudinal polarization of ^3He and ^{129}Xe were the dominant systematic error in the EDM measurement of Oteiza and Chupp [11].

We will account for noble gas magnetization fields in the extended Bloch model in a simple way. We describe the interaction between magnetization fields and the noble gas atoms in terms of volume averaged magnetic fields exerting torques on the volume averaged noble gas magnetizations. We describe the noble gas magnetization fields as proportional to the polarizations, but with one constant of proportionality relating longitudinal components and another constant of proportionality relating transverse components. This description is exactly correct in a cell which is an ellipsoid of revolution filled with uniform noble gas magnetization, if the ellipsoid's axis of revolution is oriented along the magnetic field axis. For other configurations (e.g. a cylindrical cell with symmetry axis parallel to the main magnetic field), this is an approximation.

We will now work out the equation of motion for the frequency of a free-running dual Zeeman maser, assuming the other maser is locked to an external clock. The derivation are omitted, since it is largely identical to that of equation (29). We describe the dual maser system in terms of the definitions of Appendix E. We use the index $j = 1, 2$ to label the two masers; for each maser j , we define the following quantities:

$\eta \equiv$ filling factor of pickup coil (see eqn (E3))

$Q_j \equiv$ quality factor of j th resonance (see eqn (E5))

$\omega_{o,j} \equiv$ frequency of j th resonance (see eqn (E4))

$[j] \equiv$ number of atoms per unit volume of j th noble gas species

$\gamma_j \equiv$ gyromagnetic ratio of j th noble gas species

$\tau_{RD,j} \equiv$ radiation damping time of j th noble gas species (see eqn (E9))

$T_{2,j} \equiv$ coherence time of j th noble gas species

$\vec{M}_j \equiv$ magnetic dipole moment per unit volume (i.e., magnetization) of j th noble gas species

$\vec{P}_j \equiv$ longitudinal spin polarization of j th noble gas species

$P_{o,j} \equiv$ spin polarization of j th noble gas species in the absence of maser effects

$\Phi_j(t) \equiv$ [rapidly-varying] phase of j th noble gas species

$\rho(\omega) \equiv$ amplitude of resonator response (see eqn (E6))

$\alpha(\omega) \equiv$ phase of resonator response (see eqn (E6))

(50)

We also reiterate the following basic definitions for each noble gas species j :

$$\vec{M}_j \equiv -\frac{\hbar\gamma_j}{2} [j] \vec{P}_j$$

$$\omega_j \equiv \dot{\Phi}_j \quad ; \quad \Phi_j(t) = \int dt' \omega_j(t')$$

(51)

We now list all magnetic fields presented to and/or induced by the noble gas spins. First, we define a function describing the co-rotating magnetic field produced by the pickup coil when excited by precessing transverse magnetization M_j of species j . This is a generalization of relation (C17) to account for multiple species:

$$\vec{B}_{pu}(\omega_j, M_{\perp,j}) = -\mu_o \eta \rho(\omega_j) \cdot M_{\perp,j} \cdot \begin{pmatrix} \hat{e}_1 \cos(\Phi_j(t) + \alpha(\omega_j)) + \\ \hat{e}_2 \sin(\Phi_j(t) + \alpha(\omega_j)) \end{pmatrix} \quad (52)$$

We now state the magnetic field induced by the magnetization associated with polarization \vec{P}_i . Note that the proportionality factors β_z and β_{\perp} are both equal to unity in a spherical cell, and that we assume that (β_z, β_{\perp}) are the same set of values for both noble gas species:

$$\vec{B}_{mag,i}(\vec{P}_i) = -\frac{2}{3}\mu_o \frac{\hbar\gamma_i}{2} \cdot [i] \cdot \begin{pmatrix} \hat{e}_3 \beta_z P_{z,i} + \\ \beta_{\perp} P_{\perp,i} (\hat{e}_1 \cos(\Phi_i(t)) + \hat{e}_2 \sin(\Phi_i(t))) \end{pmatrix} \quad (53)$$

Finally, the axial magnetic field is taken to be a slowly varying function of time:

$$\vec{B}_o(t) = \hat{e}_3 \cdot B_o(t) \quad (54)$$

The total magnetic field in the cell can thus be written

$$\vec{B}_t(t) = \begin{bmatrix} \hat{e}_3 \cdot B_o(t) & \{main\ magnetic\ field\} \\ +\vec{B}_{pu}(\omega_1, M_{\perp,1}) + \vec{B}_{pu}(\omega_2, M_{\perp,2}) & \{field\ from\ pickup\ coil\ 1\} \\ +\vec{B}_{mag}(\vec{P}_1) + \vec{B}_{mag}(\vec{P}_2) & \{field\ from\ noble\ gas\ magnetizations\} \end{bmatrix} \quad (55)$$

In computing the $\vec{M}_i \times \vec{B}_t(t)$ torque terms, we neglect the torque exerted by non-resonant fields. For example,

$$\vec{M}_1 \times \vec{B}_t(t) \cong \vec{M}_1 \times \begin{bmatrix} \hat{e}_3 B_o(t) \\ +\vec{B}_{pu}(\omega_1, M_{\perp,1}) \\ +\vec{B}_{mag}(\vec{P}_1) \\ +\hat{e}_3 (\hat{e}_3 \cdot \vec{B}_{mag}(\vec{P}_2)) \end{bmatrix} \quad (56)$$

and a similar relation can be found for $\vec{M}_2 \times \vec{B}_t(t)$ torque term by reversing the subscripts 1,2 in the above relation. We now write the equations of motion for the polarizations $P_{x,j}, P_{y,j}$:

$$\begin{aligned} \dot{P}_{x,j} &= -\gamma_j \left(P_{y,j} (\vec{B}_t(t) \cdot \hat{e}_3) - P_{z,j} (\vec{B}_t(t) \cdot \hat{e}_2) \right) - \frac{P_{x,j}}{T_{2,j}} \\ \dot{P}_{y,j} &= -\gamma_j \left(P_{z,j} (\vec{B}_t(t) \cdot \hat{e}_1) - P_{x,j} (\vec{B}_t(t) \cdot \hat{e}_3) \right) - \frac{P_{y,j}}{T_{2,j}} \end{aligned} \quad (57)$$

We now proceed exactly as in equations (21)-(29), for each species, to transform from a Cartesian to a cylindrical representation. After a lengthy (but elementary) analysis, we obtain the following relation for the frequency ω_1 of masing species 1 (the corresponding equation for ω_2 of masing species 2 is obtained by exchanging indices 1 and 2 in the following equation):

$$\gamma_1 B_o(t) - \omega_1 = \begin{bmatrix} \frac{\beta_z - \beta_{\perp}}{\tau_{RD,1}} \cdot \frac{2}{3\eta Q_1} \cdot \frac{P_{z,1}}{P_{o,1}} \\ + \frac{\beta_z}{\tau_{RD,2}} \cdot \frac{2\gamma_1}{3\gamma_2 \eta Q_2} \cdot \frac{P_{z,2}}{P_{o,2}} \\ + \frac{P_{z,1}}{P_{o,1} \tau_{RD,1}} \frac{\rho(\omega_1)}{Q_1} \cos \alpha(\omega_1) \\ - \delta\omega_{1,other} \end{bmatrix} \quad (58)$$

Note that in addition to effects from cavity-pulling and magnetization field effects, we have included a term $\delta\omega_{j,other}$ to account for other frequency shifts. These include a possible inertial (gyroscopic) frequency shift and a possible shift due to exotic physics.

We note that in the equations of motion for the longitudinal polarizations $P_{z,j}$ and $P_{\perp,j}$, there are no terms relating to the magnetization-induced magnetic field. The equations have exactly the form of the first two equations of (29), with the inclusion of subscripts to identify parameters associated with each species. Magnetization fields have no

first-order effect on the dynamics of the polarizations. This is not the case for the system of Romalis and Happer [12], where magnetization fields can be as large as those from the pickup coil, and thus play a large role in the dynamics of the polarizations.

In dual masers presently in operation, one of the masers is used to stabilize the magnetic field. Thus, to compute $B_o(t)$, we can take the frequency ω_1 to be fixed to a constant value by a lockloop that adjusts the external magnetic field $B_o(t)$. Equation (58) can then be solved for $B_o(t)$; the result can be substituted into the equation for ω_2 . The result is the equation of motion for the frequency of the free-running maser in a dual Zeeman maser system:

$$\frac{\gamma_2}{\gamma_1}\omega_1 - \omega_2 = \left[\begin{array}{l} \frac{-P_{z,1}}{P_{o,1}\tau_{RD,1}} \frac{\gamma_2}{\gamma_1} \left[\begin{array}{l} \frac{-2}{3\eta Q_1} \cdot \beta_{\perp} \\ + \frac{\rho(\omega_1)}{Q_1} \cos \alpha(\omega_1) \end{array} \right] \\ + \frac{P_{z,2}}{P_{o,2}\tau_{RD,2}} \left[\begin{array}{l} \frac{-2}{3\eta Q_2} \cdot \beta_{\perp} \\ + \frac{\rho(\omega_2)}{Q_2} \cos \alpha(\omega_2) \end{array} \right] \\ + \frac{\gamma_2}{\gamma_1} \delta\omega_{1,other} - \delta\omega_{2,other} \end{array} \right] \quad (59)$$

It is easy to show that equation (59) holds if either maser is locked, or indeed if the field is stabilized by some other means. This relation highlights an obvious (but important) property of the dual Zeeman maser (or any dual magnetometer): perturbations to either maser manifest themselves in the frequency of the free-running maser, regardless of which maser is locked (by varying the main magnetic field), or manifest themselves in the frequency difference (59) if neither maser's frequency is locked. Thus, when the dual maser system is used to detect small energy shifts due to exotic physics (e.g., due to a possible EDM of the ^{129}Xe atom, or the coupling of the spins to a possible preferred reference frame, in violation of local Lorentz invariance), the maser system retains sensitivity to such effects regardless of which species is used to stabilize the magnetic field [4]. We also note that the dual maser system frequency is not sensitive to possible exotic physics frequency shifts if they are proportional to the gyromagnetic ratios.

The frequency dependence on polarization can easily be studied experimentally by inducing near-equilibrium oscillations of the longitudinal polarizations. We record the phase, not the frequency, of the masers during measurement [5,24]. Thus, we would like to derive an equation analogous to eqn (43) from eqn (59), that relates the near-steady-state phase oscillation $\delta\Phi_2$ to near-steady-state oscillations $\delta P_{\perp,j}$. The derivation is totally analogous to that of eqn (43) and is thus omitted: assuming that maser 1 is locked, the result is

$$\delta\Phi_2 = \left[\begin{array}{l} \frac{\gamma_2}{\gamma_1} \frac{\delta P_{\perp,1}}{P_{\perp,1}|_{steady\ state} \frac{\rho(\gamma_1 B_o)}{Q_1} \sin \alpha(\gamma_1 B_o)} \left[\begin{array}{l} \frac{-2}{3\eta Q_1} \cdot \beta_{\perp} \\ + \frac{\rho(\gamma_1 B_o)}{Q_1} \cos \alpha(\gamma_1 B_o) \end{array} \right] \\ - \frac{\delta P_{\perp,2}}{P_{\perp,2}|_{steady\ state} \frac{\rho(\gamma_2 B_o)}{Q_2} \sin \alpha(\gamma_2 B_o)} \left[\begin{array}{l} \frac{-2}{3\eta Q_2} \cdot \beta_{\perp} \\ + \frac{\rho(\gamma_2 B_o)}{Q_2} \cos \alpha(\gamma_2 B_o) \end{array} \right] \end{array} \right] \quad (60)$$

We should emphasize the correct interpretation of eqn (60): it relates the phase oscillations caused by oscillations in the longitudinal polarizations, to the amplitude oscillations correlated to the longitudinal polarization oscillations. The variations δP_{\perp} do not *cause* the phase oscillations $\delta\Phi$. We emphasize this because we will discuss recently observed *frequency* drifts that are correlated to slow changes in the maser amplitude, induced by a different mechanism than described by eqn (60).

Examination of eqn (59) shows that it might be possible, in principle, to choose operating frequencies for the masers such that there is no net shift in frequency due to noble gas longitudinal polarizations: those operating frequencies are given by

$$\frac{2}{3\eta} \cdot \beta_{\perp} = \rho(\omega_j) \cos \alpha(\omega_j) \quad (61)$$

Using the parameter values of Table 1, however, it would appear problematic to satisfy these conditions. Near the peaks of the resonator response functions at $\omega_{o,j}$, the function ρ takes on the values Q_j (see equations (E5) and (E6)). For the typical values of $\eta = 0.023$, $\beta_{\perp} \approx 1$, $Q_j \approx 10^4$, we see that we require $\cos \alpha > 1$ to achieve cancellation of P_z -proportional frequency shifts, which is of course not realizable.

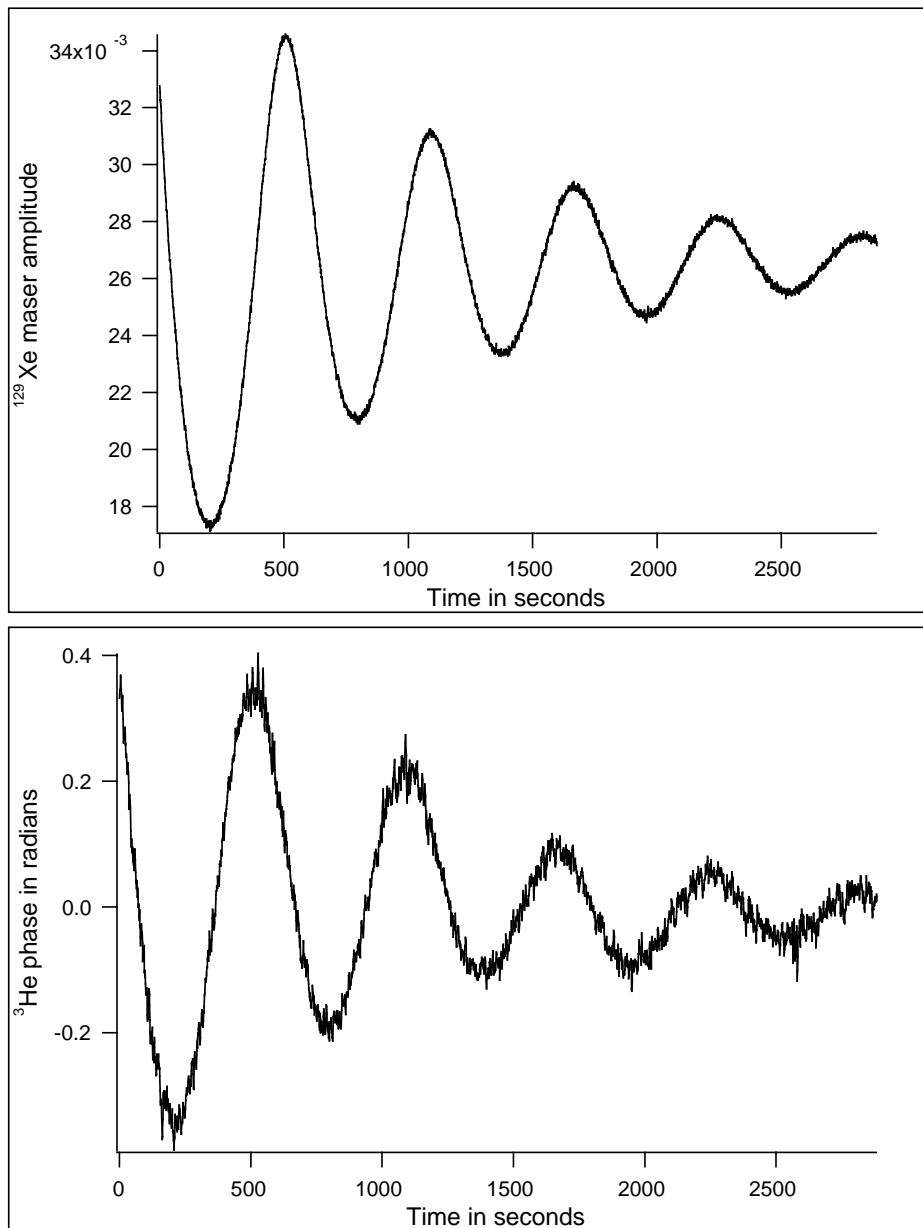


FIG. 7. Maser amplitude and phase oscillations. The top plot shows measured ^{129}Xe maser amplitude as a function of time during maser polarization oscillations. The bottom plot shows the simultaneously observed ^3He maser phase deviations from linear phase evolution, as a function of time. The ^{129}Xe maser was phaselocked. The two profiles are very strongly correlated, as per equations (43) and (60).

However, we have experimentally demonstrated such a cancellation effect. We have carried out experiments in which the net dual maser phase (60) was measured during near-equilibrium P_{\perp} and P_z oscillations induced on each of the masers in turn [24]. An example is shown in Figure 7, which is a plot of the [phaselocked] ^{129}Xe maser amplitude and a plot of the deviation from linear evolution of the [free-running] ^3He maser's precession phase. The profiles are very highly correlated as per the prediction of eqns (43) and (60). We have measured the amplitude of phase deviations in near-equilibrium oscillations as a function of maser operating frequency. Remarkably, in spite of the fact that eqn (61) evaluated with the parameter values of Table I suggests that it should not be possible, we found that there is an operating frequency for each maser that results in zero net phase deviations during near-equilibrium

oscillation of the polarizations. Figure 8 is a plot of measured phase deviations per unit maser amplitude deviation, vs. maser operating frequency, for both the ^{129}Xe and ^3He masers. The data are clearly linear, and the fit lines cross zero, denoting an operating frequency for each maser for which there is no phase (and thus frequency) change due to near-equilibrium polarization oscillations. In each maser, we see that the zero-cross frequency is very close to the measured peak in $\rho(\omega)$. While there were potentially significant systematic errors (of order 10^0 degrees) in the measurements of the resonator phase response, we know that $\cot \alpha$ was much less than unity at the operating frequencies of the zero-crossings.

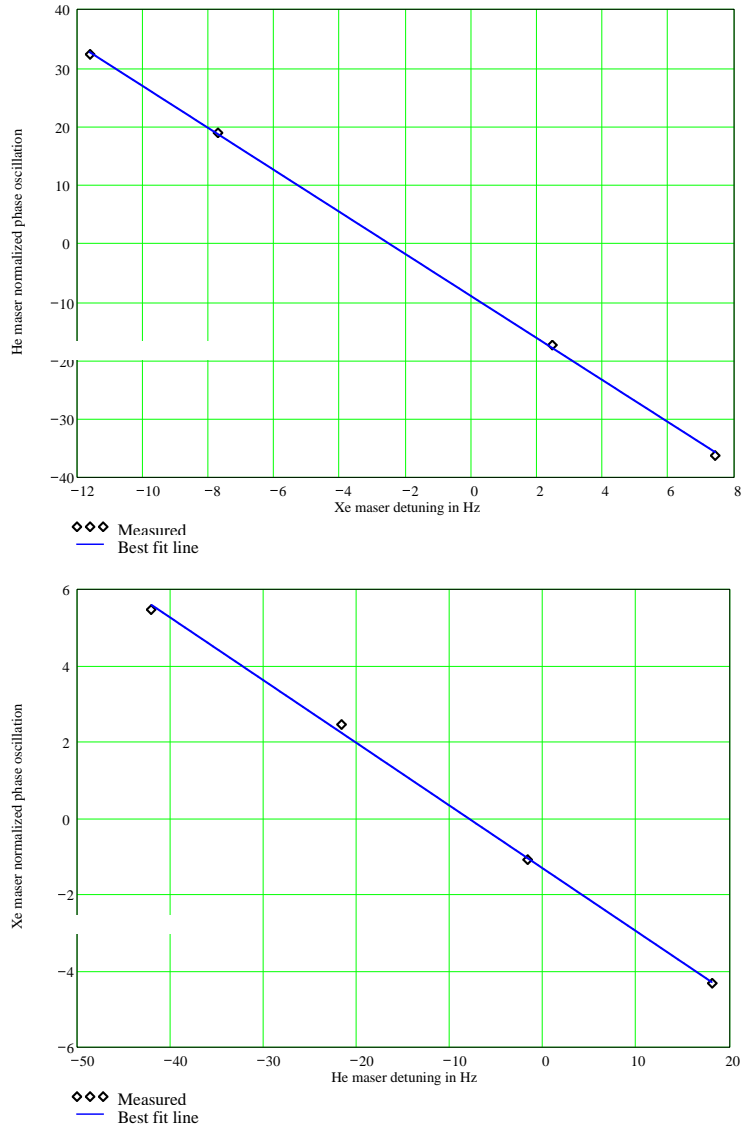


FIG. 8. Amplitude of maser phase oscillations as a function of maser operating frequency. The top figure shows the measured amplitude of free-running ^3He maser phase oscillations induced by the phaselocked ^{129}Xe maser undergoing near-equilibrium polarization oscillations, at several ^{129}Xe maser operating frequencies. The operating frequencies are expressed as deviations from the frequency at which $\rho(\omega)$ has a [local] maximum value, i.e., in terms of detuning from maximum resonator "gain". The bottom figure shows the measured amplitude of free-running ^{129}Xe maser phase oscillations induced by the phaselocked ^3He maser undergoing near-equilibrium polarization oscillations, at several ^3He maser operating frequencies. Again, the operating frequencies are expressed as deviations from the frequency at which $\rho(\omega)$ has a [local] maximum value. The data show that when the ^{129}Xe maser is operated with frequency 2.5 Hz below the Xe resonator peak, polarization oscillations of the ^{129}Xe maser induce no frequency shifts on the free running maser. Similarly, the data show that when the ^3He maser is operated with frequency 8.3 Hz below the He resonator peak, polarization oscillations of the ^3He maser induce no frequency shifts on the free running maser.

The ability to suppress the effect of near-equilibrium oscillations on the masers' phase would be useful in situations where a device is being operated in poorly controlled environments in which the masers are subject to perturbations (e.g., in an atomic gyroscope application). However, in our symmetry test experiments, the environmental control is adequate to prevent excitation of near-equilibrium maser oscillations [5,24]. Thus, operating the masers at the zero-cross frequencies of Fig. 8 has not discernably improved the usefulness of the dual Zeeman maser for precision measurement.

The data of Fig. 8 highlight the fact that equation (61) apparently does not describe some significant physical effects associated with near-equilibrium phase oscillations. There is an obvious fundamental limit to the Bloch theory description of the dual Zeeman maser: the Bloch theory cannot account for effects that result from changes in the shape of polarization distributions, since it deals expressly with volume averages over the maser polarization distributions. However, we have found that shape changes could have significant effects on the maser frequency. We have constructed a theory of precessing/masing three-dimensional ensembles of spin-1/2 particles, including the effects of diffusion, wall collisions, magnetic field gradients, etc. [26], applicable to the motional averaging regime of Zeeman maser operation [12]. The details of that theory are beyond the scope of this paper. However, the most important result of the theory is a simple first integral of the frequency/phase equation. Described by that first integral is how the masers measure an ensemble-average magnetic field. The magnetic field "seen" by the masing ensemble can be written in terms of variables defined in Appendix C: defining $B_z(\vec{r}', t)$ as the z-component of the magnetic field from all sources, we have

$$B_{z,total}(t) = \frac{\int_{cell} d^3\vec{r}' B_z(\vec{r}', t) \mathcal{P}_\perp(\vec{r}', t)}{\int_{cell} d^3\vec{r}' \mathcal{P}_\perp(\vec{r}', t)} \quad (62)$$

which is a volume average of the field, weighted by the transverse polarization distribution (for simplicity, we have assumed here that the magnetic field produced by the pickup coil is spatially uniform). This is intuitively reasonable. The magnetic field $B_z(\vec{r}', t)$ is significantly non-uniform in dual Zeeman maser systems. Magnetic field gradients in our system are of order $20\mu\text{G}/\text{cm}$. In the presence of such a field gradient, even a change of $2\mu\text{m}$ in the "center of mass" position of the \mathcal{P}_\perp distribution would induce a $1\mu\text{Hz}$ frequency shift (which is large in relation to the frequency resolution needed for precision measurements). Such "center-of-mass" shifts occur in a 2-bulb noble gas maser system when there is a change in the flux of polarized noble gas atoms into the interaction region; the shifts are larger for smaller diffusion constant and larger wall loss rate, so that they would be larger for a ^{129}Xe maser than for a ^3He maser. We have observed maser frequency variations that were very strongly correlated to ^{129}Xe maser amplitude changes, and we speculate that "center-of-mass" shifts in the presence of a non-uniform B_z was a contributing mechanism. These amplitude-proportional frequency drifts are an important systematic effect in the $^{129}\text{Xe}/^3\text{He}$ dual Zeeman maser; they cannot be described by the extended Bloch theory presented in this paper. Thus, while the extended Bloch theory would appear to provide a useful description of polarization transport and the gross dynamics of the maser polarizations, it cannot account for some subtle frequency shift mechanisms that play an important role in precision measurement applications of dual Zeeman masers.

APPENDIX A: RELATING POLARIZATION LIFETIMES IN DIFFERENT REGIONS OF THE CELL

In the limit that wall collisions dominate the noble gas polarization destruction, it is possible to express the polarization lifetimes in the three regions of the cell in terms of their geometry along with a wall loss parameter. The lifetimes are computed as the inverse rate constants associated with the fundamental diffusion modes in each of the cell regions. The diffusion equation

$$D\nabla^2 P - \frac{\partial}{\partial t} P = 0$$

and the associated boundary condition

$$-D\nabla P \cdot \hat{n} + \kappa P = 0$$

is solved in the pump chamber (assumed spherical), and the transfer tube and maser chamber (assumed cylindrical). The wall loss parameter κ may or may not be assumed to have a common value in the three regions of the cell. \hat{n} is the normal to the cell wall surface, and D is the diffusion constant. This form of boundary condition has been used previously to model polarization destruction by wall collisions [27,28]. Note that the wall loss parameter κ is only weakly dependent on the cell gas pressure [28], then the wall loss rate is essentially independent of pressure in the limit of small κ . There exist mechanisms other than interaction with cell walls that disorient spins. E.g., diffusion of polarized atoms through magnetic field gradients can induce spin flips [22]. However, in noble gas Zeeman maser cells, wall collisions dominate the polarization lifetime because the cells tend to have small volumes ($\sim\text{cm}^3$). This is not the case with polarized ^3He targets, which have much larger volumes and smaller surface-to-volume ratios [14].

It is elementary to find the fundamental diffusion mode in the spherical pump bulb, of radius a_P : the fundamental mode varies as

$$P \propto \frac{\sin(kr)}{kr} \exp(-\gamma t)$$

and k is related to the polarization lifetime via

$$T_{1,P}^{-1} = \gamma = k^2 D$$

k is found by use of the boundary condition: the resulting transcendental equation is

$$\frac{\tan(ka_P)}{ka_P} = \frac{D}{D - \kappa a_P}$$

The relations for the cylindrical maser chamber, assumed to have radius a_M and length L_M , are found similarly: the fundamental mode varies as

$$P \propto \cos(k_z z) J_0(k_r r) \exp(-\gamma t)$$

and the lifetime is

$$T_{1,M}^{-1} = (k_r^2 + k_z^2) D$$

The transcendental equations determining k_r and k_z are

$$\frac{J_1(k_r a_M)}{J_0(k_r a_M)} = \frac{\kappa}{k_r D}; \quad \tan\left(k_z \frac{L_M}{2}\right) = \frac{\kappa}{k_z D}$$

The polarization lifetime in the transfer tube, $T_{1,tt}$, is determined similarly to that in the cylindrical maser chamber, except that polarization loss is restricted to the side walls; polarization is free to diffuse from the transfer tube ends. Then

$$T_{1,tt}^{-1} = k_{r,tt}^2 D$$

and the transcendental equation determining the transfer tube lifetime, taken to have length L and radius r_{tt} , is

$$\frac{J_1(k_{r,tt} r_{tt})}{J_0(k_{r,tt} r_{tt})} = \frac{\kappa}{k_{r,tt} D}$$

In general, the wall loss parameter might have a different value in the three regions of the cell, particularly since in many circumstances the cell regions are deliberately kept at different temperatures. The wall loss parameter depends exponentially on temperature [20]. Nevertheless, some simplification might be attainable in that often it is the case that most of the transfer tube is at the same temperature as the maser chamber, in which case a common value of κ could be used for those regions. Also, the diffusion constant D has a $T^{3/2}$ dependence which could be used to relate diffusion constants in the different regions of the cell [18].

APPENDIX B: SOLUTION FOR THE TRANSFER TUBE POLARIZATION FUNCTION

The solution of the diffusion equation in terms of the time-dependent boundary values is elementary (see, e.g., [29]), and will only be briefly outlined here. The problem is

$$\left(D \frac{\partial^2}{\partial x^2} - \frac{\partial}{\partial t} - \frac{1}{T_{1,tt}} \right) \Pi(x, t) = 0 \quad (\text{B1})$$

with boundary and initial conditions

$$\begin{aligned} P_P(t) &= \Pi(0, t) \\ P_z(t) &= \Pi(L, t) \\ \Pi(x, 0) &= F(x) \end{aligned} \quad (\text{B2})$$

It is assumed that neither D nor $T_{1,tt}$ is a function of x . The problem can be recast in terms of a function $U(x, t)$, related to $\Pi(x, t)$ via

$$\Pi(x, t) = P_P(t) + \frac{x}{L} (P_z(t) - P_P(t)) + U(x, t) \quad (\text{B3})$$

$U(x, t)$ can easily be shown to satisfy

$$\left(D \frac{\partial^2}{\partial x^2} - \frac{\partial}{\partial t} - \frac{1}{T_{1,tt}} \right) U(x, t) = \frac{\partial}{\partial t} S(x, t) + \frac{1}{T_{1,tt}} S(x, t) \quad (\text{B4})$$

where $S(x, t)$ is defined by

$$S(x, t) \equiv P_P(t) + \frac{x}{L} (P_z(t) - P_P(t)) \quad (\text{B5})$$

and $U(x, t)$ satisfies the homogeneous boundary conditions

$$U(0, t) = U(L, t) = 0 \quad (\text{B6})$$

We seek a particular solution to the inhomogeneous problem eqn. (B4) of the form

$$U_p(x, t) = \sum_{n=1}^{\infty} a_n(t) \sqrt{\frac{2}{L}} \sin\left(\frac{\pi n}{L} x\right) \quad (\text{B7})$$

Substituting (B7) into (B4), multiplying each side of that result by $\sqrt{\frac{2}{L}} \sin\left(\frac{\pi m}{L} x\right)$, and integrating each side over $[0, L]$ yields the relation governing the time-dependent Fourier coefficients $a_n(t)$:

$$\left(-\left(\frac{\pi m}{L}\right)^2 - \frac{1}{DT_{1,tt}} \right) a_m(t) - \frac{\dot{a}_m}{D} = \sqrt{\frac{2}{L}} \frac{1}{D} \frac{L}{\pi m} \left\{ \frac{1}{T_{1,tt}} (P_P - (-1)^m P_z) + (\dot{P}_P - (-1)^m \dot{P}_z) \right\} \quad (\text{B8})$$

These equations can be solved by the method of Green's functions: the result is

$$a_m(t) = \sqrt{\frac{2}{L}} \frac{L}{\pi m} \int_0^{\infty} du \exp\left(-\left(D\left(\frac{\pi m}{L}\right)^2 + \frac{1}{T_{1,tt}}\right)u\right) \left\{ \frac{1}{T_{1,tt}} ((-1)^m P_z(t-u) - P_P(t-u)) \right. \\ \left. + ((-1)^m \dot{P}_z(t-u) - \dot{P}_P(t-u)) \right\} \quad (\text{B9})$$

The substitution of this equation into (B7), the subsequent use of (B4), and the inclusion of a homogeneous solution (necessary for satisfying the initial condition) yields the solution to problem (B1) with conditions (B2):

$$\Pi(x, t) = \left[\begin{aligned} &P_P(t) + \frac{x}{L} (P_z(t) - P_P(t)) + \sqrt{\frac{2}{L}} \sum_{m=1}^{\infty} b_m \sin(k_m x) \exp(-k_m^2 D t) \\ &+ 2 \sum_{m=1}^{\infty} \frac{\sin(k_m x)}{\pi m} \int_0^{\infty} du \exp\left(-\left(D\left(\frac{\pi m}{L}\right)^2 + \frac{1}{T_{1,tt}}\right)u\right) \left\{ \frac{1}{T_{1,tt}} ((-1)^m P_z(t-u) - P_P(t-u)) \right. \\ &\left. + ((-1)^m \dot{P}_z(t-u) - \dot{P}_P(t-u)) \right\} \end{aligned} \right] \quad (\text{B10})$$

where

$$k_m \equiv \frac{\pi m}{L}; \quad b_m \equiv \sqrt{\frac{2}{L}} \int_0^L dx \sin(k_m x) F(x) \quad (\text{B11})$$

The $\{P_z, P_P\}$ dependence can be converted to dependences on $\{\dot{P}_z, \dot{P}_P\}$ via integration by parts. As an alternative, one may be tempted to convert the dependence on the time derivatives $\{\dot{P}_z, \dot{P}_P\}$ to $\{P_z, P_P\}$ in the same fashion. However, that operation is not legitimate since it results in expressions which are differences between two divergent terms. In any case, the integration by parts on the $\{P_z, P_P\}$ dependence in the integral yields

$$\Pi(x, t) = \left[\begin{aligned} & P_P(t) + \frac{x}{L} \cdot (P_z(t) - P_P(t)) + \sqrt{\frac{2}{L}} \sum_{m=1}^{\infty} b_m \sin(k_m x) \exp(-k_m^2 D t) \\ & + P_z(t) \cdot 2 \sum_{m=1}^{\infty} \frac{\sin(k_m x)}{\pi m} (-1)^m \frac{1}{k_m^2 D T_{1,tt} + 1} - P_P(t) \cdot 2 \sum_{m=1}^{\infty} \frac{\sin(k_m x)}{\pi m} \frac{1}{k_m^2 D T_{1,tt} + 1} \\ & - 2 \sum_{m=1}^{\infty} \frac{\sin(k_m x)}{\pi m} (-1)^m \left(\frac{1}{k_m^2 D T_{1,tt} + 1} - 1 \right) \int_0^{\infty} du \exp\left(-\left(k_m^2 D + \frac{1}{T_{1,tt}}\right) u\right) \dot{P}_z(t-u) \\ & + 2 \sum_{m=1}^{\infty} \frac{\sin(k_m x)}{\pi m} \left(\frac{1}{k_m^2 D T_{1,tt} + 1} - 1 \right) \int_0^{\infty} du \exp\left(-\left(k_m^2 D + \frac{1}{T_{1,tt}}\right) u\right) \dot{P}_P(t-u) \end{aligned} \right] \quad (\text{B12})$$

The gradients of this function at the endpoints $x = 0$ and $x = L$ are

$$\left. \frac{\partial}{\partial x} \Pi(x, t) \right|_{x=0} = \left[\begin{aligned} & \frac{1}{L} \cdot (P_z(t) - P_P(t)) + \sqrt{\frac{2}{L}} \sum_{m=1}^{\infty} b_m k_m \exp(-k_m^2 D t) \\ & + P_z(t) \cdot \frac{1}{L} \Sigma_2 - P_P(t) \cdot \frac{1}{L} \Sigma_1 \\ & - \frac{2}{L} \sum_{m=1}^{\infty} (-1)^m \left(\frac{1}{k_m^2 D T_{1,tt} + 1} - 1 \right) \int_0^{\infty} du \exp\left(-\left(k_m^2 D + \frac{1}{T_{1,tt}}\right) u\right) \dot{P}_z(t-u) \\ & + \frac{2}{L} \sum_{m=1}^{\infty} \left(\frac{1}{k_m^2 D T_{1,tt} + 1} - 1 \right) \int_0^{\infty} du \exp\left(-\left(k_m^2 D + \frac{1}{T_{1,tt}}\right) u\right) \dot{P}_P(t-u) \end{aligned} \right] \quad (\text{B13})$$

$$\left. \frac{\partial}{\partial x} \Pi(x, t) \right|_{x=L} = \left[\begin{aligned} & \frac{1}{L} \cdot (P_z(t) - P_P(t)) + \sqrt{\frac{2}{L}} \sum_{m=1}^{\infty} b_m k_m \exp(-k_m^2 D t) \\ & + P_z(t) \cdot \frac{1}{L} \Sigma_1 - P_P(t) \cdot \frac{1}{L} \Sigma_2 \\ & - \frac{2}{L} \sum_{m=1}^{\infty} \left(\frac{1}{k_m^2 D T_{1,tt} + 1} - 1 \right) \int_0^{\infty} du \exp\left(-\left(k_m^2 D + \frac{1}{T_{1,tt}}\right) u\right) \dot{P}_z(t-u) \\ & + \frac{2}{L} \sum_{m=1}^{\infty} (-1)^m \left(\frac{1}{k_m^2 D T_{1,tt} + 1} - 1 \right) \int_0^{\infty} du \exp\left(-\left(k_m^2 D + \frac{1}{T_{1,tt}}\right) u\right) \dot{P}_P(t-u) \end{aligned} \right] \quad (\text{B14})$$

where we have used the definitions

$$\Sigma_1 \equiv 2 \cdot \sum_{m=1}^{\infty} \frac{1}{k_m^2 D T_{1,tt} + 1} \quad \Sigma_2 \equiv 2 \cdot \sum_{m=1}^{\infty} \frac{(-1)^2}{k_m^2 D T_{1,tt} + 1} \quad (\text{B15})$$

APPENDIX C: POSITION-DEPENDENT POLARIZATION DISTRIBUTIONS AND CELL/PICKUP COIL COUPLING

Here we define position-dependent polarization distribution functions, and in terms of those functions derive the parameters which serve as a measure of the coupling strength between the maser bulb and pickup coil resonator. The coupling strength parameters are applicable to the Bloch maser theory of Sec. III. The current induced in the pickup coil by the precessing magnetization, and the resultant magnetic field acting back on the atoms, will be found. Approximations used in obtaining parameter values for the Bloch model of Sec. III will be clearly identified. Note that we have derived equations of motion for the position-dependent polarization distribution functions. These coupled, nonlinear partial differential equations of motion and their approximate solutions will be described in a future publication.

First we define the functions that describe the polarization as a function of position in the cell. These are designated with scripted names to distinguish them from the spatially averaged quantities used in the Bloch model. They are $\mathcal{P}_x(\vec{r}, t)$, $\mathcal{P}_y(\vec{r}, t)$, and $\mathcal{P}_z(\vec{r}, t)$. Just as in the case of the spatially averaged Bloch model variables, we transform the Cartesian variable set into polar variables $\mathcal{P}_\perp(\vec{r}, t)$, $\mathcal{P}_z(\vec{r}, t)$, $\Phi_{total}(\vec{r}, t)$ via

$$\mathcal{P}_x = \mathcal{P}_\perp \cos(\Phi_{total}(\vec{r}, t)) \quad \mathcal{P}_y = \mathcal{P}_\perp \sin(\Phi_{total}(\vec{r}, t)) \quad (C1)$$

We define the instantaneous phase $\Phi_{total}(\vec{r}, t)$ of the precessing polarization at position \vec{r} and time t in the cell. It is written as a sum of two functions, a global phase $\Phi(t)$ which depends on time only, plus a function $\delta\Phi(\vec{r}, t)$ which describes the local deviations of the phase from the global value:

$$\Phi_{total}(\vec{r}, t) = \Phi(t) + \delta\Phi(\vec{r}, t) \quad (C2)$$

The global phase $\Phi(t)$ is the same as that appearing in eqn (20) and is related to the maser precession frequency in the same way.

We take the pickup coil to be a loop of radius a oriented in the y - z plane. The windings are assumed to be of an extent small compared to the coil radius. The magnetization associated with the polarization $\vec{\mathcal{P}}$ is

$$\vec{\mathcal{M}}(\vec{r}, t) = -\frac{\hbar\gamma}{2} [ng] \vec{\mathcal{P}}(\vec{r}, t) \quad (C3)$$

We define the magnetic field produced by the pickup coil as having the form

$$\vec{B}_{pu}(\vec{r}, t) = \vec{\xi}(\vec{r}) I_{pu}(t) \quad (C4)$$

so that $\vec{\xi}(\vec{r})$ is the magnetic field per unit current produced by the pickup coil. We can write the voltage induced in the pickup coil by the precessing magnetization in terms of $\vec{\xi}$ and the magnetization distribution function $\vec{\mathcal{M}}$ [7]:

$$V_{pu}(t) = -\frac{\partial}{\partial t} \int_{cell} d^3\vec{r}' \left\{ \vec{\xi}(\vec{r}') \cdot \vec{\mathcal{M}}(\vec{r}', t) \right\} \quad (C5)$$

In systems which are axially symmetric about the z -axis, only the x -component of the polarization contributes to the flux through the pickup coil. Substituting eqns (C1), (C2), and (C3) into (C5), the pickup coil voltage becomes

$$V_{pu}(t) = \frac{\hbar\gamma}{2} [ng] \frac{\partial}{\partial t} \int_{cell} d^3\vec{r}' \left\{ \xi(\vec{r}') \mathcal{P}_\perp(\vec{r}', t) \cos(\Phi(t) + \delta\Phi(\vec{r}', t)) \right\} \quad (C6)$$

Expanding the cosine term in the integrand yields

$$V_{pu}(t) = \frac{\hbar\gamma}{2} [ng] \frac{\partial}{\partial t} \left\{ \begin{array}{l} \cos\Phi(t) \int_{cell} d^3\vec{r}' \left\{ \xi(\vec{r}') \mathcal{P}_\perp(\vec{r}', t) \cos(\delta\Phi(\vec{r}', t)) \right\} \\ - \sin\Phi(t) \int_{cell} d^3\vec{r}' \left\{ \xi(\vec{r}') \mathcal{P}_\perp(\vec{r}', t) \sin(\delta\Phi(\vec{r}', t)) \right\} \end{array} \right\} \quad (C7)$$

Remember that we require the net ensemble phase for the precessing magnetization to be $\Phi(t)$, so that the coefficient of the $\sin\Phi(t)$ in eqn (C7) must vanish: this determines a condition on the phase deviation function $\delta\Phi(\vec{r}', t)$:

$$\int_{cell} d^3\vec{r}' \left\{ \xi(\vec{r}') \mathcal{P}_\perp(\vec{r}', t) \sin(\delta\Phi(\vec{r}', t)) \right\} = 0 \quad (C8)$$

The expression for the voltage induced in the pickup coil then becomes

$$V_{pu}(t) \cong -\frac{\hbar\gamma}{2} [ng] \cdot \omega \cos\Phi(t) \cdot \int_{cell} d^3\vec{r}' \left\{ \xi(\vec{r}') \mathcal{P}_\perp(\vec{r}', t) \cos(\delta\Phi(\vec{r}', t)) \right\} \quad (C9)$$

where we have neglected the time derivative of the [slowly varying] terms under the integral in comparison to the derivative of the [rapidly varying] $\cos\Phi(t)$ term. At this point, note that the voltage induced in the pickup coil depends on the details of both the polarization and phase distribution as well as the variation of the pickup coil magnetic field across the cell.

We now define the transverse polarization of the Bloch theory, $P_{\perp}(t)$, in terms of the voltage induced in the pickup coil. First, we note the relationship between M_{\perp} , the Bloch magnetization, and P_{\perp} is

$$M_{\perp} = -\frac{\hbar\gamma}{2} [ng] \cdot P_{\perp} \quad (\text{C10})$$

We proceed by rewriting eqn (C9) in the following form:

$$V_{pu}(t) = -\frac{\hbar\gamma}{2} [ng] \cdot \omega \sin \Phi(t) \cdot \left[\int_{cell} d^3\vec{r}' \xi(\vec{r}') \right] \cdot \frac{\int_{cell} d^3\vec{r}' \{ \xi(\vec{r}') P_{\perp}(\vec{r}', t) \cos(\delta\Phi(\vec{r}', t)) \}}{\int_{cell} d^3\vec{r}' \xi(\vec{r}')}$$

We then define the relationship of $P_{\perp}(t)$ to the transverse polarization distribution function $\mathcal{P}_{\perp}(\vec{r}, t)$

$$P_{\perp}(t) \equiv \frac{\int_{cell} d^3\vec{r}' \{ \xi(\vec{r}') \mathcal{P}_{\perp}(\vec{r}', t) \cos(\delta\Phi(\vec{r}', t)) \}}{\int_{cell} d^3\vec{r}' \xi(\vec{r}')} \quad (\text{C11})$$

and also define the relationship of the volume averaged pickup coil field per unit current to the spatially dependent function describing the pickup coil field (note that V_{cell} is the cell volume):

$$\xi_o \cdot V_{cell} \equiv \int_{cell} d^3\vec{r}' \xi(\vec{r}')$$

In terms of these definitions, the pickup coil voltage is then

$$V_{pu}(t) \cong -\frac{\hbar\gamma}{2} [ng] P_{\perp}(t) \cdot \xi_o V_{cell} \cdot \omega \sin \Phi(t) = M_{\perp} \cdot \xi_o V_{cell} \cdot \omega \sin \Phi(t) \quad (\text{C12})$$

Having calculated the pickup coil flux induced by the precessing magnetization, it remains to determine the current flow in the coil that results from that excitation. The analysis is elementary and will not be shown here; we consider a series RLC circuit driven by the voltage $V_{pu}(t)$. It is easy to show that the current in the pickup coil is, using definition (18),

$$I(t) = \frac{\xi_o V_{cell}}{L_{pu}} M_{\perp} \rho(\omega) \cos(\Phi(t) + \alpha(\omega)) \quad (\text{C13})$$

This current produces a field at the cell in the x-direction. Note that L_{pu} is the inductance of the pickup coil. Prior to writing the expression for the pickup coil magnetic field, we define the dimensionless filling factor η by

$$\eta \equiv \frac{\xi_o^2 V_{cell}}{\mu_o L_{pu}} \quad (\text{C14})$$

The filling factor can take on values between zero and unity. For the case of the small and/or spherical cell placed at the center of a loop pickup coil of radius a and having N windings of extent much smaller than a , the filling factor takes the form

$$\eta = \frac{\mu_o N^2 V_{cell}}{2a^2 L_{pu}} \quad (\text{C15})$$

Note that the N^2 in the numerator is cancelled by N^2 scaling of L_{pu} in the denominator, so that η is indeed dependent only on geometry and not on the specific configuration of the coil windings. In the spirit of the Bloch theory, we use the above definitions along with relation (C13) to write the *volume-averaged* pickup coil magnetic field as

$$B_{x,pu}(t) = -\mu_o \eta \rho(\omega) M_{\perp} \exp(i\Phi(t) + i\alpha) \quad (\text{C16})$$

This can be expressed in terms of a sum of vectors co-rotating and counter-rotating with the precessing magnetization ($\hat{e}_1, \hat{e}_2, \hat{e}_3$ are basis vectors in the $x, y,$ and z directions respectively). Keeping only the co-rotating component, we have

$$\vec{B}_{pu}(t) = -\frac{\mu_o}{2} \eta \rho(\omega) M_{\perp} \cdot \{ \hat{e}_1 \cos(\Phi(t) + \alpha) + \hat{e}_2 \sin(\Phi(t) + \alpha) \} \quad (\text{C17})$$

Substituting eqn (C10) into the above equation, and recalling the definition (23), it is easy to show that

$$\begin{aligned} B_x &= \frac{P_{\perp}}{\gamma\tau} \cos(\Phi(t) + \alpha) \\ B_y &= \frac{P_{\perp}}{\gamma\tau} \sin(\Phi(t) + \alpha) \end{aligned} \quad (\text{C18})$$

which leads to relation (22) above.

APPENDIX D: MATRIX SOLUTION OF THE LAPLACE TRANSFORM EQUATIONS FOR NEAR-EQUILIBRIUM OSCILLATIONS

Here we give explicit expressions for terms used in the solution to the Bloch maser equations of motion discussed in Section III. As stated in Section III, the inverse of the matrix $\mathcal{R}(s)$ defined in equation 47 can be written in terms of a function $\mathcal{D}(s)$ and a matrix $\mathcal{S}(s)$ (remember that the functions $\sigma_1(s)$, $\sigma_2(s)$ are defined by eqn (14):

$$\mathcal{D}(s) = \left\{ \begin{array}{l} 2 \left[\frac{P_{\perp,o}}{P_o \tau_{RD}} \frac{\rho(\omega)}{Q} \sin \alpha \right]^2 \cdot \left(\gamma_{SE} + s + \frac{1}{T_{1,P}} + G_P (1 + \Sigma_1) - s G_P \sigma_1(s) \right) \\ + s \left[\left(\gamma_{SE} + s + \frac{1}{T_{1,P}} + G_P (1 + \Sigma_1) - s G_P \sigma_1(s) \right) \cdot \left(\frac{1}{T_1} + G_M (1 + \Sigma_1) + s (1 - G_M \sigma_1(s)) \right) \right. \\ \left. - G_P G_M (- (1 + \Sigma_2) + s \sigma_2(s))^2 \right] \end{array} \right\} \quad (\text{D1})$$

It is easiest to present the matrix $\mathcal{S}(s)$ element by element:

$$\mathcal{S}_{11} = G_P \sigma_2(s) \cdot \left[s \left(\frac{1}{T_1} + G_M (1 + \Sigma_1) + s (1 - G_M \sigma_1(s)) \right) + 2 \left[\frac{P_{\perp,o}}{P_o \tau_{RD}} \frac{\rho(\omega)}{Q} \sin \alpha \right]^2 \right]$$

$$\mathcal{S}_{21} = -s G_P \sigma_2(s) (-G_M (1 + \Sigma_2) + s G_M \sigma_2(s))$$

$$\mathcal{S}_{31} = G_P \sigma_2(s) \cdot \left(-\frac{P_{\perp,o}}{P_o \tau_{RD}} \frac{\rho(\omega)}{Q} \sin \alpha \right) (-G_M (1 + \Sigma_2) + s G_M \sigma_2(s))$$

$$\mathcal{S}_{12} = -s (1 - G_M \sigma_1(s)) (-G_P (1 + \Sigma_2) + s G_P \sigma_2(s))$$

$$\mathcal{S}_{22} = s (1 - G_M \sigma_1(s)) \left(\gamma_{SE} + s + \frac{1}{T_{1,P}} + G_P (1 + \Sigma_1) - s G_P \sigma_1(s) \right)$$

$$\mathcal{S}_{32} = (1 - G_M \sigma_1(s)) \left(\gamma_{SE} + s + \frac{1}{T_{1,P}} + G_P (1 + \Sigma_1) - s G_P \sigma_1(s) \right) \left[\frac{P_{\perp,o}}{P_o \tau_{RD}} \frac{\rho(\omega)}{Q} \sin \alpha \right]$$

$$\mathcal{S}_{13} = (-G_P (1 + \Sigma_2) + s G_P \sigma_2(s)) \left[2 \frac{P_{\perp,o}}{P_o \tau_{RD}} \frac{\rho(\omega)}{Q} \sin \alpha \right]$$

$$\mathcal{S}_{23} = - \left(\gamma_{SE} + s + \frac{1}{T_{1,P}} + G_P (1 + \Sigma_1) - s G_P \sigma_1(s) \right) \left[2 \frac{P_{\perp,o}}{P_o \tau_{RD}} \frac{\rho(\omega)}{Q} \sin \alpha \right]$$

$$\mathcal{S}_{33} = \left[\left(\gamma_{SE} + s + \frac{1}{T_{1,P}} + G_P (1 + \Sigma_1) - s G_P \sigma_1(s) \right) \left(\frac{1}{T_1} + G_M (1 + \Sigma_1) + s (1 - G_M \sigma_1(s)) \right) \right. \\ \left. - G_P G_M (- (1 + \Sigma_2) + s \sigma_2(s))^2 \right] \quad (\text{D2})$$

By inspection, none of the matrix elements contain common factors with $\mathcal{D}(s)$ and so any singularity in $\mathcal{D}(s)$ will correspond to a pole and not a removable singularity (this assertion should be checked numerically in each case). The roots of $\mathcal{D}(s)$ are found numerically. Note that there is no root at $s = 0$; this simply means that the steady state solution vanishes, i.e. all the displacements must damp out at large times. Again, numerical solution for the roots is simplified if approximate values of the roots can be found in advance. One can obtain a cubic equation in s to estimate the three roots (one real, two complex) which define late time behavior, by writing $\mathcal{D}(s)$ in which functions $\sigma_1(s)$, $\sigma_2(s)$ are evaluated at $s = 0$. Setting this expression to zero and solving for the three roots yields estimates for the late time decay rate and oscillation frequency for the near-equilibrium oscillations:

$$0 = \left\{ \begin{array}{l} 2 \left[\frac{P_{\perp,o}}{P_o \tau_{RD}} \frac{\rho(\omega)}{Q} \sin \alpha \right]^2 \cdot \left(\gamma_{SE} + s + \frac{1}{T_{1,P}} + G_P (1 + \Sigma_1) - s G_P \sigma_1(0) \right) \\ + s \left[\left(\gamma_{SE} + s + \frac{1}{T_{1,P}} + G_P (1 + \Sigma_1) - s G_P \sigma_1(0) \right) \cdot \left(\frac{1}{T_1} + G_M (1 + \Sigma_1) + s (1 - G_M \sigma_1(0)) \right) \right. \\ \left. - G_P G_M (- (1 + \Sigma_2) + s \sigma_2(0))^2 \right] \end{array} \right\} \quad (\text{D3})$$

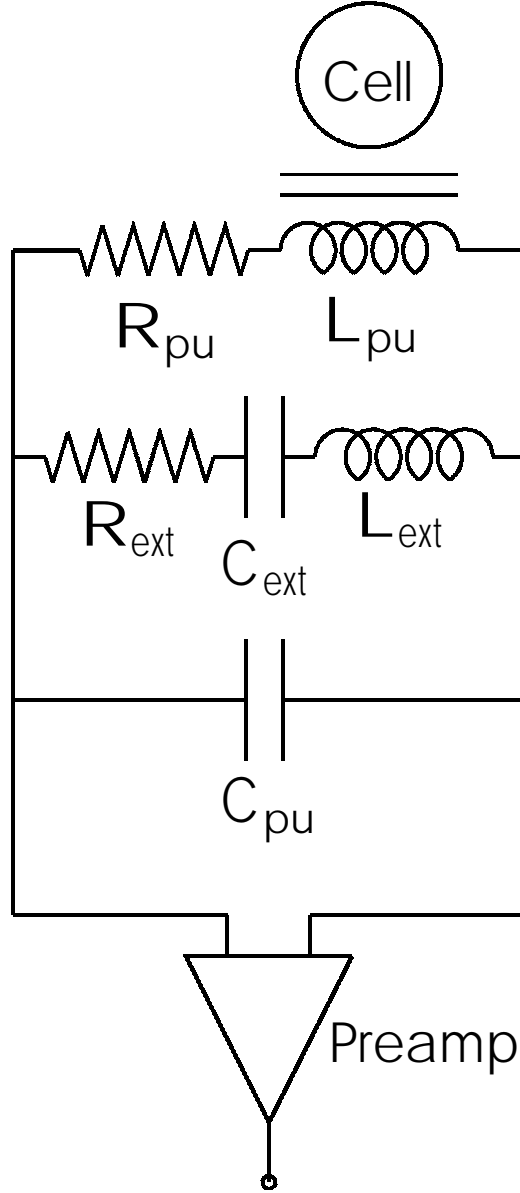


FIG. 9. Schematic diagram for the single pickup coil resonator used in the work of [5]. Precessing magnetizations of noble gases in the cell induce flux through inductor L_{pu} . The resultant voltage across capacitor C_{pu} is presented to a preamplifier. This ideal circuit model fails to account for effects due to eddy current losses and coupling to permeable materials that results from proximity of the inductors to conductors and magnetic shielding, respectively. The component values used to generate the response plots of Fig. 10 are $L_{pu} = 144$ mH, $C_{pu} = 30.5$ nF, $R_{pu} = 143\Omega$, $L_{ext} = 102$ mH, $C_{ext} = 21.1$ nF, $R_{ext} = 32\Omega$.

APPENDIX E: SINGLE-PICKUP COIL RESONATOR FOR DUAL ZEEMAN MASERS

In this section we briefly describe the resonator used in the dual Zeeman maser operated in our laboratory [5]. Figure 9 is a schematic of the resonator circuit. Note that there are two inductors: L_{pu} , which serves as the pickup coil, and L_{ext} , which is located far from the interaction region. Having only a single pickup coil is useful for three reasons: first, maximizing the fill factor η (see eqn (C14)) requires close placement of the pickup coil to the cell,

and this is difficult to achieve with multiple coils for multiple species; second, with a single pickup coil system, it is possible to adjust the effective Q factor of the two resonances by changing the properties of the external coil, without affecting the fill factor η ; and η is [nearly] the same for the two species, which is a considerable system simplification. The two principal drawbacks of the single-pickup coil resonator are: the external coil must reside in a temperature-controlled environment inside magnetic shielding, thus resulting in greater overall system complexity and expense; and energy from the atoms is inevitably dissipated in the external coil, which to some extent must reduce the attainable radiation damping rate (see eqn (28)). The details of resonator design and implementation will be presented in a future publication [24]. Figure 9 defines the circuit components and their typical values. We define effective response functions to relate the precessing noble gas magnetization to the induced magnetic field produced by the pickup coil, in analogy to eqn (18). By an elementary analysis of the circuit of Figure 9, we can obtain an expression for the magnetic field produced by the pickup coil in response to flux induced by precessing magnetization $M_x|_{species\ j} = M_{\perp,j} \cos \Phi_j(t)$ of species j . It is assumed that the pickup coil axis is oriented along the x axis:

$$B_{x,pu}|_{species\ j} = -\mu_o \eta \Re \left[\frac{1}{\frac{Z_{||}(\omega_j) + R_{pu}}{i\omega_j L_{pu}} + 1} M_{\perp,j} \exp(i\Phi_j(t)) \right] \quad (\text{E1})$$

where \Re denotes the real part, and we define

$$\omega_j = \dot{\Phi}_j$$

$$Z_{||}(\omega) = \left(i\omega C_{pu} + \frac{1}{i\omega L_{ext} + \frac{1}{i\omega C_{ext}} + R_{ext}} \right)^{-1} \quad (\text{E2})$$

The fill factor η is that associated with the pickup coil (ξ_{pu} is the volume-averaged magnetic field per unit current produced by the pickup coil):

$$\eta = \frac{\xi_{pu}^2 V_{cell}}{\mu_o L_{pu}} \quad (\text{E3})$$

We further define amplitude and response functions, in order to establish a correspondence of the single pickup coil resonator with the simple LCR resonator presented in Section III. First, it is easy to show that in the limit where the individual coil quality factors are much greater than unity, the circuit of Figure 9 responds resonantly at two frequencies given by

$$\begin{aligned} \omega_{o,1}^2 &= \left[\frac{\frac{1}{2L_{ext}C_{ext}} + \frac{1}{2L_{ext}C_{pu}} - \frac{1}{2L_{pu}C_{pu}}}{-\sqrt{\left(\frac{1}{2L_{ext}C_{ext}} + \frac{1}{2L_{ext}C_{pu}} - \frac{1}{2L_{pu}C_{pu}}\right)^2 + \frac{1}{L_{ext}C_{ext}} \cdot \frac{1}{L_{pu}C_{pu}}}} \right] \\ \omega_{o,2}^2 &= \left[\frac{\frac{1}{2L_{ext}C_{ext}} + \frac{1}{2L_{ext}C_{pu}} - \frac{1}{2L_{pu}C_{pu}}}{+\sqrt{\left(\frac{1}{2L_{ext}C_{ext}} + \frac{1}{2L_{ext}C_{pu}} - \frac{1}{2L_{pu}C_{pu}}\right)^2 + \frac{1}{L_{ext}C_{ext}} \cdot \frac{1}{L_{pu}C_{pu}}}} \right] \end{aligned} \quad (\text{E4})$$

We define effective quality factors Q_j by

$$Q_j = \left| \frac{Z_{||}(\omega_{o,j}) + R_{pu}}{i\omega_{o,j} L_{pu}} + 1 \right|^{-1} \quad (\text{E5})$$

We define the amplitude function $\rho(\omega)$ and phase function $\alpha(\omega)$ by the following relation:

$$\rho(\omega) \exp(i\alpha(\omega)) = \left(\frac{Z_{||}(\omega) + R_{pu}}{i\omega L_{pu}} + 1 \right)^{-1} \quad (\text{E6})$$

This form is chosen so that equations of motion of the same form describe masers using RLC resonators and those using the single pickup coil resonator. Explicitly writing out the function ρ and α in terms of the circuit parameters is complicated and not particularly illustrative. However, Figure 10 shows a plot of the ideal calculated resonator amplitude and phase response function for the resonator circuit of Fig. 9. We see that there are indeed two resonances, with linear phase variation near each; the phase value at each of the resonances is very close to $+\pi/2$. One should note that the resonator response in real resonators is only approximated by Figure 9. The inductors of the resonator circuit are unavoidably placed in proximity to conducting and permeable materials, such that the phase response and quality factors are discernably different from the ideal values realized with the inductors in free space. Another effect is the fact that large, relatively high-Q inductances must necessarily be implemented with multiple-layer coils. These coils inevitably suffer from energy loss processes, which result in real, frequency-dependent AC impedances. The net coil resistances then are frequency-dependent. Measured frequency response curves must be used in applying the theory, and such measured profiles will be presented in a future publication [24].

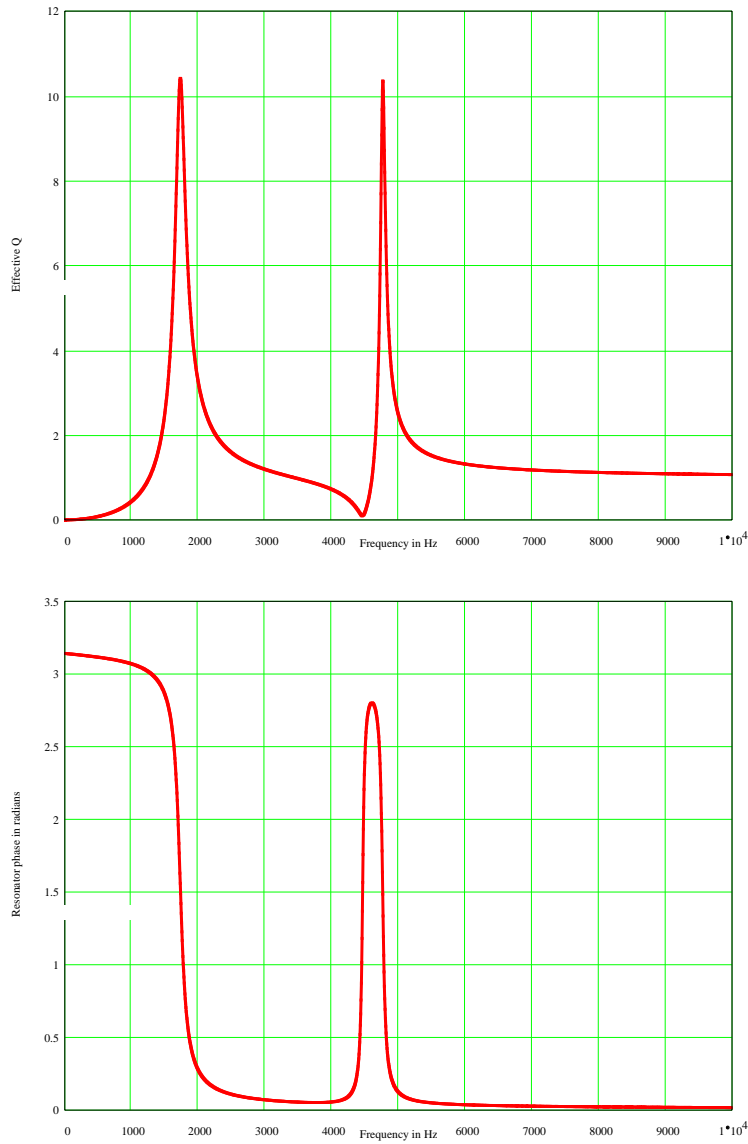


FIG. 10. Resonator response curves for the ideal resonator depicted by Fig. 9. The upper plot is $\rho(\omega)$ as defined by (??); the bottom plot is the phase profile $\alpha(\omega)$.

In any case, these definitions can be used in turn to describe the magnetic fields impressed on the atoms, induced by their precession:

$$\begin{aligned} B_{x,j} &= \frac{P_{\perp,j}}{\gamma_j \tau_j} \cos(\Phi_j(t) + \alpha) \\ B_{y,j} &= \frac{P_{\perp,j}}{\gamma_j \tau_j} \sin(\Phi_j(t) + \alpha) \end{aligned} \quad (\text{E7})$$

In the above relation, the functions τ_j are given by

$$\tau_j^{-1} = \frac{\hbar \gamma_j^2}{2} [j] \mu_o \eta \rho(\omega) \quad (\text{E8})$$

We can now define the radiation damping rates for the two noble gas maser species j :

$$\tau_{RD,j}^{-1} = \frac{1}{2} \frac{\hbar \gamma_j^2}{2} [j] \mu_o \eta Q_j P_{o,j} \quad (\text{E9})$$

where $P_{o,j}$ is the polarization of the j th noble gas species in the absence of masing effects. This completes the definition of the functions used in Section IV.

- [1] R.E. Stoner, in *CPT and Lorentz Symmetry*, V.A. Kostelecky, ed., World Scientific, Singapore (1999), p. 201
- [2] D.Bear, R.E. Stoner, and R. Walsworth, presented at the International Conference on Orbis Scientiae 1999: Quantum Gravity, Generalized Theory of Gravitation and Superstring Theory Based Unification (28th Conference on High Energy Physics and Cosmology Since 1964), Fort Lauderdale, Florida, 16-19 Dec 1999
- [3] R.E. Stoner and R. Walsworth, Phys. Rev. A (submitted for publication)
- [4] R.E. Stoner, M.A. Rosenberry, J.T. Wright, T.E. Chupp, E.R. Oteiza, and R.L. Walsworth, Phys. Rev. Lett. **77**, 3971 (1996)
- [5] D. Bear, T. Chupp, K. Cooper, S. DeDeo, M. Rosenberry, R.E. Stoner, and R.L. Walsworth Phys. Rev. A **57**, 5006 (1998)
- [6] H.G. Robinson and T. Myint, Appl. Phys. Lett. **5**, 116 (1964)
- [7] M.G. Richards, B.P. Cowan, M.F. Secca and K. Machin, J. Phys. B **21**, 665 (1988)
- [8] T.E. Chupp, R.J. Hoare, R.L. Walsworth, and B. Wu, Phys. Rev. Lett. **72**, 2363 (1994)
- [9] T. E. Chupp, R. J. Hoare, R. A. Loveman, E. R. Oteiza, J. M. Richardson, M. E. Wagshul, and A.K. Thompson, Phys. Rev. Lett. **63**, 1541 (1989)
- [10] T.E. Chupp and R.J. Hoare, Phys. Rev. Lett **64**, 2261 (1990)
- [11] E.R. Oteiza, Ph.D. thesis, Harvard University, unpublished (1992)
- [12] M.V. Romalis and W. Happer, Phys. Rev. A **60**, 1385 (1999)
- [13] R.L. Walsworth, unpublished
- [14] T.E. Chupp, R.A. Loveman, A.K. Thompson, A.M. Bernstein, and D.R. Tieger, Phys. Rev. C **45**, 915 (1992)
- [15] Crampton et.al. spin-exchange detuning
- [16] A. Abragam, *Principles of Nuclear Magnetism* (Oxford University Press) p. 73
- [17] J. Vanier and C. Audoin, *The Quantum Physics of Atomic Frequency Standards* (A. Hilger, Bristol, 1989) pp.
- [18] J. Kestin, K. Knierim, E.A. Mason, B. Najafi, S.T. Ro, and M. Waldman, J. Chem. Phys. Ref. Data **13**, 229 (1984)
- [19] J. Bzowski, J. Kestin, E.A. Mason, and F.J. Uribe, J. Chem. Phys. Ref. Data **19**, 1179 (1990)
- [20] B. Driehuys, G.D. Cates, and W. Happer, Phys. Rev. Let. **74**, 4943 (1995)
- [21] X. Zeng, Z. Wu, T. Call, E. Miron, D. Schreiber, and W. Happer, Phys. Rev. A **31**, 260 (1985)
- [22] G.D. Cates, S.R. Schaefer, W.Happer, Phys. Rev. A **37**, 2877 (1988); G.D. Cates, D.J. White, Ting-ray Chien, S.R. Schaefer, W. Happer, Phys. Rev. A **38**, 5092 (1988)
- [23] D.D. McGregor, Phys. Rev. A **41**, 2631 (1990); C.L. Bohler and D.D. McGregor, Phys. Rev. A **49**, 2755 (1994)
- [24] D. Bear, R.E. Stoner, and R.L. Walsworth, to be published
- [25] D. Kleppner, H.M. Goldenberg, and N.F. Ramsey, Phys. Rev. **126**, 605 (1962)
- [26] R.E. Stoner, unpublished
- [27] F. Masnou-Seeuws and M. Bouchiat, J. Phys. (Paris) **28**, 406 (1967)
- [28] Z. Wu, S. Schaefer, G.D. Cates, and W. Happer, Phys. Rev. A **37**, 1161 (1988)
- [29] S.J. Farlow, *Partial Differential Equations for Scientists and Engineers*, (Dover, New York, 1993), p. 46